Université de Strasbourg

Ecole et Observatoire des Science de la Terre

Institut de Physique du Globe de Strasbourg - UMR 7516

Ecole doctorale des Science de la Terre, de l'Univers et de l'Environnement

Thèse de doctorat de l'Université de Strasbourg

Soutenue le : **22 Novembre 2012**

Discipline : Géodésie

Présentée par

Yasser MAHMOUD

Titre

Caractérisation géodésique de la déformation active du point triple d'Hatay (Syrie-Turquie)

Jury

M. Pierre BRIOLE …………….......   *Rapporteur externe*

M. Ziyadin CAKIR ……………......   *Examinateur*

M. Jacques HINDERER ………..…   *Rapporteur interne*

M. Frédéric MASSON   …….….…....   *Directeur de thèse*

M. Mustapha MEGHRAOUI ………   *Co-Directeur de thèse*

M. Philippe VERNANT ….…..........   *Rapporteur externe*
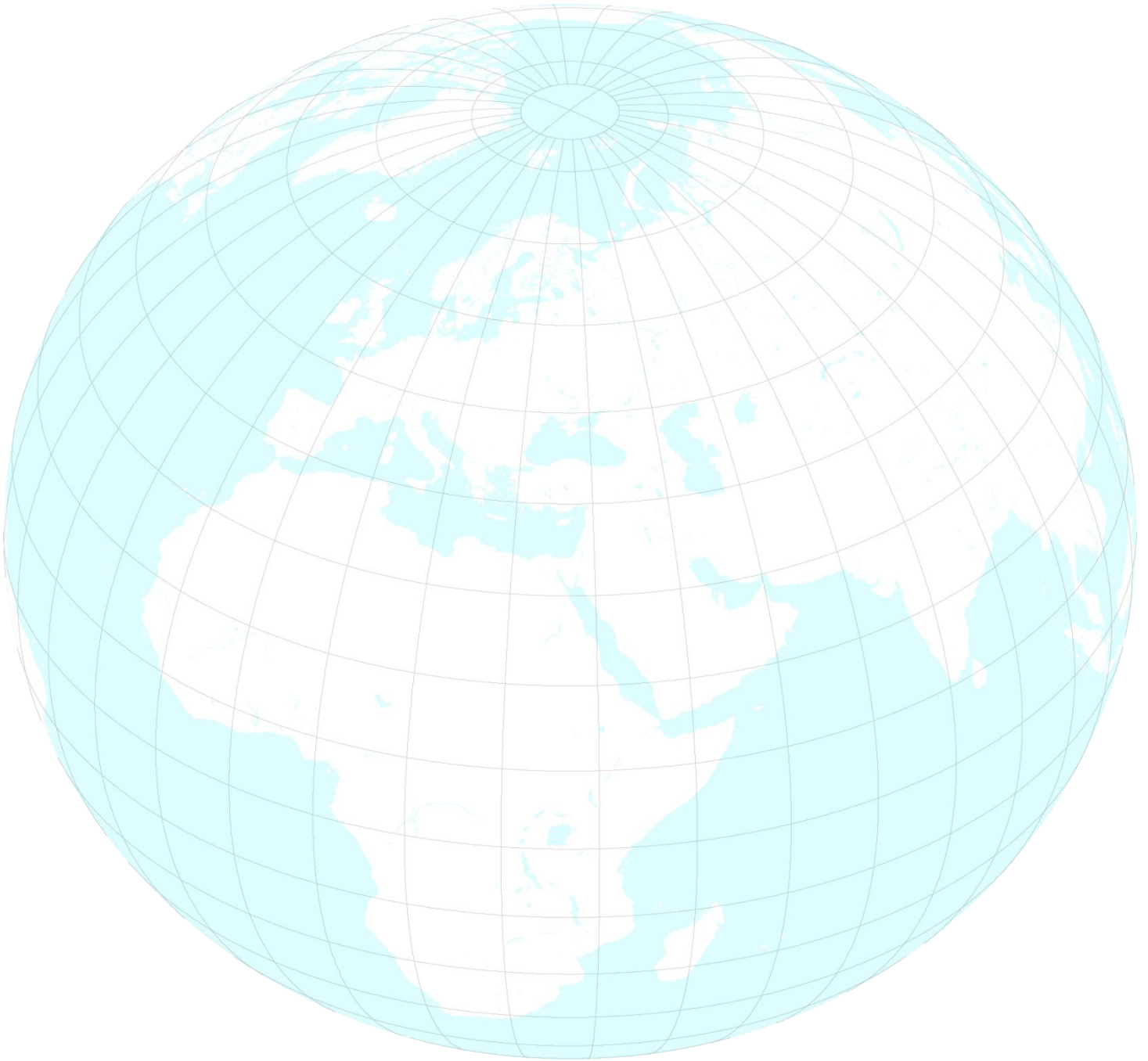
The roots of education are bitter … but the fruit is sweet

(Aristole)

Acknowledgement

At the end of my thesis, I would like to thank all those people who made this work possible and an unforgettable experience for me.

First of all, I would like to express my deepest sense of gratitude to my two supervisors Professors Frédéric MASSON and Mustapha MEGHRAOUI, for accepting to supervise my thesis, for their continuous advices and encouragements throughout the course of this thesis, for their insightful comments and hard questions. I thank them also for the systematic guidance, great effort they put into training me in to the scientific research, for all what I listed and what I did not my sincere gratitude.

I am particularly grateful for the support and encouragement by the "Dynamique Globale et Déformation Active" group at the Institut de Physique du Globe de Strasbourg (IPGS) of University of Strasbourg. It was not only a pleasure to work and study with you, but your suggestions, comments, criticisms, and friendship along the way have been very helpful.

I would like to acknowledge all the members of my thesis Jury for accepting to evaluate and examine my work. I am grateful to Professors Pierre BRIOL, Philippe VERNANT and Jacques HINDERER for reviewing this manuscript and for their constructive criticism. I am also very thankful to Professor Ziyadin CAKIR for examining the present work.

My thanks go also to the National Earthquake Center (NEC, Syria), the Marmara research center (TUBITAK, Turkey) and The Istanbul Technical University for providing permanent GPS data. I thank them also for providing equipment and assistance during data acquisition steps in the field and for the GPS campaigns carried out in Syria and in Turkey. Their supports were much appreciated. Particular thanks to all the teams from these institutions that participated and helped during field work. Thanks to Hakan Yavasoglu, Onder Yonlu, Rahsan Çakmak, Sedat Inan, and Semih Ergintav from Turkey, Abdulmutaleb Alchalbi, Reda Sbeinati, Mohammad Abou Romieh, Adham Alsaoud, Rayan Yassminh, Basel Ballani, Marwan Alkasser, and Mohamad Daoud from Syria, Jacques Durand and Sheldon Warden from France.

My special gratitude goes also to Prof. Ziyadin CAKIR for all his contribution and support to make my PhD experience productive, for the time he spent during the field of this

thesis, and also for providing insightful ideas especially about the block modeling and DEFNODE program.

Special thanks to, Patrice Ulrich for giving the technical assistance for data processing using GAMIT/GLOBK, to EOST's administrative staff.

My thankful to my colleagues Maxime, Pierre, and Julien, for the three years we shared the office as well as the funny and depressed moments, for their care and precious friendship and support during my stay at the EOST. I do not forget my Syrian and other nationalities friends in France, the list is long, thanks to all of you.

I give my sincere thanks to Dr. Samir Belabbes for his support, for his valuable advices and friendly help. He provided all along the thesis encouragements, sound advices, and constructive discussions.

My thesis scholarship was funded by the Syrian Government through the Syrian Ministry of High Education. I would like to express them my gratitude for continuously funding my scholarship especially for the last year where my country confronted many financial difficulties.

I would like to express my heart-felt gratitude to my parents, my brothers, my sister, my sister in law, and my nephew for their continuous care, and support. None of this would have been possible without their love.

Last, but not least, I would like to thank my fiancée Walaa for standing beside me throughout my career and during the different steps of this thesis. She gave me love, support, and encouragement. She was continuously my inspiration and motivation for continuing to improve my knowledge and step forward my career. She is my rock, and I dedicate this work to her.

Table of contents

Abstract

The active deformation at the Hatay Triple Junction (HTJ) in north-western Syria and south-eastern Turkey is a subject of debates essentially because of the tectonic complexity of the region. The HTJ is formed by the relative motion of Arabia, Anatolia, Sinai plates and the intersection of their boundaries represented by left-lateral Dead Sea Fault (DSF), the Cyprus subduction Arc and the left-lateral East Anatolian Fault (EAF). Recent GPS studies provide 18±2 mm/yr for the north-westward motion of Arabia toward Eurasia and 6±2 mm/yr for the northward motion of Africa toward Eurasia in the eastern Mediterranean (McClusky *et al.,* 2003; Reilinger *et al.,* 2006). Similar previous GPS studies indicate a left-lateral strike-slip rate across the DSF varying from 5.0 mm/yr (along the southern part) to ~2 mm/yr (along the northern part). In contrary, the EAF has a roughly constant velocity along strike estimated at 9.7 + 0.9 mm/yr (Reilinger *et al.,* 2006). The HTJ contains several well-identified active fault segments (DSF, EAF, Karatas-Osmaniye fault (KOF), Karasu fault (KF), Lattakia fault, Jisr-al-shuggur fault, Idleb fault and Afrin fault) (Saroglu *et al.*, 1992; Meghraoui *et al.*, 2003; Tatar *et al.*, 2004), the fault-slip rates for which are poorly constrained. Hence we decided to investigate and understand the strain accumulation rate and interseismic behavior across fault zones and related block tectonics in the vicinity of the HTJ.

A network of 57 GPS sites was established in the north-west Syria (33 points) and south-east Turkey (24 points) in the context of this study; our network was reinforced by 14 permanent sites belonging to a regional GPS networks in Syria and Turkey. The density of our GPS sites around the HTJ and the points distribution in 4 main profiles crossing the majority of fault zones in the region, might give the ability to identify at a relative small scale, the strain accumulation and the physical parameters of active faults in the region. Furthermore, our study would imply a better seismic hazard and risk assessment in one of the highly populated regions in the eastern Mediterranean.

In this study, we show that the active deformation and kinematic of the triple junction can be explained by a block model using GPS vectors. Using a block model with finite number of rotating elastic spherical blocks limited by faults, is more efficient to understand the kinematic of the triple junction. In such model, the fault receives a large amount of the deformation caused by the relative blocks movements. We used DEFNODE program to construct a 3D elastic dislocation model in which the tectonic plates are represented as closed

spherical polygons on the lithosphere, limited by the faults which are represented in 3 dimensions by along-strike and down-dip nodes defining the geometry, direction, width, and dip angle of the faults. The block rotation and fault locking parameters are estimated using GPS velocities for inversion in an elastic and homogeneous half-space of Okada (1985).

We found that a simple model with three major plates proposed by previous studies fails to explain the GPS data used in this study, A more complex block model is proposed by adding the Iskenderun block and Amanous micro block, the Karasu fault and Karatas-Osmaniye fault being defined as individual faults not as the extension of other major faults in the region. Our modeling assumes that the Maras triple junction is formed by the connection of KOF with KF and EAF. The KF shows a sinistral slip rate of 4.0±1.0 mm/yr and a compressional behavior with a compression rate of 2.1-2.7 mm/yr which contradicts the extensional nature proposed by previous studies. The EAF shows pure left lateral slip rate of 9.0±0.3 mm/yr with no significant extension or compression; the DSF has a slip rate of 3.5±0.3 mm/yr over the northern and southern segments; the KOF has a 3.6±0.7 mm/yr; the Cyprus arc has a clear compressional deformation with a revers slip rate of 2.0-5.0 mm/yr and with no significant strike-slip component. The relative Euler poles are estimated in this block modeling, we define the Anatolia-Arabia Euler pole at (27.61±0.98 °N, 45.127±2.45 °E, 0.391± 0.056°/Myr), and (31.012±1.51 °N, 46.464±4.44 °E, 0.202±0.067°/Myr) Sinai-Arabia Euler pole.

Keywords: GPS, geodesy, active tectonic, Dead Sea fault, East Anatolian Fault, triple junction.

Résumé

Les déformations actives à la jonction triple d'Hatay (HTJ) dans le nord-ouest de la Syrie et le sud-est de la Turquie est toujours un sujet de débats en raison de la complexité tectonique de cette région. La HTJ est formée par le mouvement relatif des plaques Sinaï, Arabie, et Anatolie, et l'intersection de leurs limites représentées par la faille senestre de la Mer Morte (DSF), l'Arc de subduction de Chypre et la faille senestre Est Anatolien (EAF). Des études GPS récentes indiquent un déplacement de 18±2 mm/an pour le mouvement nord-ouest de l'Arabie vers l'Eurasie, et 6±2 mm/an de déplacement nord de l'Afrique vers l'Eurasie dans l'Est de la Méditerranée (McClusky *et al.,* 2003; Reilinger *et al.,* 2006). Ces mêmes études GPS indiquent un taux décrochement senestre à travers le DSF variant de 5 mm/an (le long de la partie sud) à ~2 mm/an (le long de la partie nord). En revanche, l'EAF a une vitesse à peu près constante le long de la faille estimée à 9.7±0,9 mm/an (Reilinger *et al.,* 2006). La HTJ est composée de plusieurs segments de failles actives bien identifiés (DSF, EAF, Faille Karatas-Osmaniye (KOF), Faille de Karasu (KF), Faille de Lattaquié, Faille de Jisr Al-Shuggur, Faille d'Idleb et la Faille d'Afrin), mais le taux de glissement de ces failles n'est toujours pas bien identifié. Cela nous a poussé à tenter de mieux comprendre et d'évaluer le taux d'accumulation des contraintes et le comportement inter-sismique afin de mieux contraindre les déformations actives et la tectonique de blocs associée dans le voisinage de HTJ. Dans cet objectif, un réseau de 57 sites GPS a été mis en place dans le nord-ouest de la Syrie (33 points) et au sud-est de la Turquie (24 points) dans le cadre des travaux de cette thèse. Notre réseau a été renforcé par 14 sites permanents appartenant à des réseaux GPS régionaux en Syrie et en Turquie. Ainsi, nous considérons que la densité de nos sites GPS autour de la HTJ et la distribution des points en 4 profils principaux qui traversent la majorité des structures tectoniques connus dans la région peuvent fournir des informations utiles permettant ainsi d'identifier, à une échelle relativement petite, les paramètres physiques et l'accumulation de déformations dans la région. En effet, ces résultats permettent une meilleure évaluation du risque sismique dans cette zone à fort densité de population.

Dans cette thèse, nous montrons que la déformation active et cinématique de la jonction triple peut être expliquée par un modèle de blocs en utilisant les vecteurs GPS. L'utilisation d'un nombre fini des blocs sphériques élastiques limités par les failles dans un modèle de bloc est plus efficace pour comprendre la cinématique de la jonction triple.

Dans un tel modèle, les failles acquièrent une quantité importante de la déformation provoquée par les mouvements relatifs des blocs. Nous avons utilisé le programme DEFNODE pour construire un modèle de dislocation élastique 3D dans laquelle les plaques tectoniques sont représentés comme des polygones sphériques sur la lithosphère, et limités par des failles qui sont représentées en 3 dimensions par des nœuds distribuées sur le longueur et la surface de faille qui définissent la géométrie, la direction, la largeur et le pendage des failles. Les paramètres de la rotation des blocs et des profondeurs de blocage de failles sont estimés en utilisant les vitesses GPS pour l'inversion dans un demi-espace élastique et homogène d'Okada (1985).

Nous trouvons qu'un modèle simple à trois grandes plaques proposées par les études précédentes ne permet pas d'expliquer les données GPS utilisées, un modèle de bloc plus complexe est proposé en rajoutant les micros blocs d'Iskenderun et d'Amanous, la faille de Karasu et la faille de Karatas-Osmaniye ont été définies comme des failles individuelles et non pas comme l'extension d'autres failles majeurs dans la région. Notre modélisation assume que la jonction triple de Maras est formé par la connexion de KOF avec KF et EAF. Le KF montre un taux de glissement senestre de 4,0±1,0 mm/an et un comportement de compression, avec un taux de raccourcie de 2.1 à 2.7 mm/an, ce qui contredise la nature extensionnelle proposée par les études précédentes. L'EAF montre un taux pur de glissement latéral gauche de 9,0±0,3 mm/an sans extension ou compression significative, la DSF a un taux de glissement de 3,5±0,3 mm/an sur les segments nord et sud, la KOF a 3,6±0,7 mm/an; l'arc de Chypre a une déformation de compression clair avec un taux de glissement revers de 2.0 à 5.0 mm/an et sans significative dérochement. Les pôles relatifs d'Euler ont été estimés dans cette modélisation de blocs, nous définissons l'Euler pole de l'Anatolie-Arabie à (27.61±0.98 °N, 45.127±2.45 °E, 0.391±0.056 °/Ma), et l'Euler pôle de Sinaï-Arabie à (31.012±1.51 °N, 46.464±4.44 °E, 0.202±0.067 °/Ma).

Mots-Cles: Global positioning System (GPS), geodesy, active tectonic, Dead Sea fault, East Anatolian Fault, triple junction.

Introduction

The study of active deformation and kinematics of the lithosphere showed significant progress in the last years thanks to the important advance in the space geodetic techniques. Among these techniques, the Global Positioning System (GPS) is one of the most useful techniques for the study of the earth's crustal deformation. This technic provides an easy, low-coast, and accurate tool for the identification of active deformation at the large and regional scale.

In this study, we use GPS measurements in order to follow and monitor the active deformation at the Hatay Triple Junction, located in northwest of Syria and southeast of Turkey. The intersection between the Dead Sea fault (DSF), the East Anatolian fault (EAF) and the Cyprus Arc (CA) correspond to the Hatay Triple Junction (HTJ), forming the limits between Arabia, Africa and Anatolia. The Hatay tectonic zone is among the few Fault-Fault-Trench (FFT) triple junctions. Other comparable FFT triple junctions are the Mendocino (North America-Pacific-Juan de Fuca plates) and the Kamchatka-Aleutian (Eurasia-Okhotsk-North America plates) that are mainly in oceanic domains. The HTJ has the unique advantage to be partly intra-continental and offers a visible and accessible intersection between the EAF, the DSF and the Cyprus subduction zone. This region has a moderate seismic activity during the last century. However, the related faults segments experienced large and destructive historical earthquakes with magnitude greater than M = 7; some of these earthquakes like the events of 1114, 1408, 1513, 1822, 1872 are well documented and identified along the DSF and the EAF (Ambraseys and Jackson, 1998; Sbeinati et al., 2005).

The deformation and strain accumulation of the main plate boundary faults (EAF, DSF), between Arabia-Anatolia and Arabia-Africa respectively, have been documented in many and different previous geological (Arpat and Saroglu, 1972; McKenzie, 1976; Saroglu *et al.*, 1992; Meghraoui *et al.*, 2003; Westaway, 2004) and geodetic studies (Gomez *et al.*, 2007a; Alchalbi *et al.*, 2010). The majority of these studies assess the deformation rate in HTJ at a long term scale, from thousands to a few millions of years. The Dead Sea transform fault accommodates the relative motion between the Arabia plate (~20 mm/yr north-westward direction) and the Africa plate (~10 mm/yr northward direction), a differential accumulated left lateral strike-slip of 25-35 km was documented between the north and south parts of DSF which can be explained by the shortening through the Palmyride fold belt or by internal

deformation caused by the fable rigidity of the northeast part of Sinai plate (Ambraseys and Barazangi, 1989; Westaway, 1994). Geological studies along the fault indicate a slip rate of 4-7 mm/yr (Quennell, 1958; Freund *et al.,* 1968; Freund, 1970). Other estimations of slip rate ranging between 3 mm/yr and 10 mm/yr along the DSF were proposed from geomorphological studies for the last few thousands of years (Garfunkel, 1981; Niemi *et al.,* 2001). Paleoseismological studies along different segment of DSF propose a slip rate of 5-7 mm/yr (Meghraoui *et al.*, 2003; Akyuz *et al.*, 2006; Ferry *et al.*, 2011). The major Arabia-Anatolia plate boundary (EAF) has been the site of various geological and seismological studies, the previous long term estimations of slip rate along this plate boundary are also varying between 4 mm/yr and 19 mm/yr (Arpat and Saroglu, 1972; Lyberis *et al.,* 1992; Yurur and Chorowicz, 1998; Westaway, 2003). The few geodetic studies in the region (mainly GPS studies) have been carried out mainly for large scale deformation assessment, such as the study of the geodynamics of the eastern Mediterranean or the convergence between the Arabia and Africa plates from one side and the Eurasia in the other side. GPS measurements were used to infer deformation rate along the DSF and the values proposed were significantly smaller than other long term estimations, especially in the northern part of the DSF. Studies of the Arabia, Africa, and Eurasia relative motions using GPS measurements indicate a slip rate of 4.5 – 6 mm/yr in general for the DSF (McClusky *et al.*, 2003; Reilinger *et al.*, 2006). Other regional geodetic studies agree with these estimations along the southern DSF (Le Béon *et al.*, 2008; Al-Tarazi *et al.*, 2011), but not along the northern segments where Alchalbi *et al.,* (2010) propose a significantly smaller value of 1.8 – 3.3 mm/yr. In contrast, GPS studies agree with long term studies of slip rate of the EAF and no difference in the slip rate is obtained along the different fault segments.

The kinematic and the active deformation pattern of the Hatay triple junction remains unclear, and detailed investigations are necessary to a better understanding of the complex mechanic characteristics at the intersection between the major Arabia, Africa, and Eurasia plates.

Different reasons motivated us to perform this study in this Hatay Triple Junction and they can be summarized in the following.

- Most of the geodetic studies in the region were directed to understand plate motions or the kinematics of the region at large scale. However, the existence of small-scale tectonic features like the Afrin Fault, Idleb Fault, Karasu Fault,

Karatas-Osmaniye Fault, Lattakia fault, Jisr-al-shuggur fault, and other potential micro blocks, makes the triple junction a complex tectonic domain. Previous studies were unable to determine the physical parameters of small faults and then their contribution to the regional deformation.

- The recent geodetic estimations of deformation and strain accumulation along the major faults need to be revised and well identified in details, after taking into account the several active sub-segments in the region. Especially, there is a significant difference in fault slip rate estimations between the short-term studies and other long-term studies (e.g., north of DSF). The slip rate, locking depth, and strain accumulation on all the active faults and sub-faults need to be determined in order to have a better image about the kinematics of this region.

- The seismic quiescence and the significant difference between historical and instrumental seismicity on all the related faults give the motivation to study the strain accumulation on these faults, and try to distinguish the role of each tectonic feature in the junction kinematic. The high-level of historical seismic activity implies that this region can produce destructive earthquakes. Our aim is to identify the major source of strain accumulation on related faults, and predict the magnitude and the return period of future large earthquakes.

A dense regional GPS network is needed in order to address these issues. Thus, we installed a network of 57 GPS sites around the Hatay triple junction in northwest Syria and southeast Turkey with mean inter-site distance of about 15 km. Our GPS network in Hatay region is designed to provide the best assessment of active deformation in the region. The space distribution of our GPS sites and the consistency with the previously existing sites, have been taken into account before installation. We installed 33 sites in Syria and 24 sites in Turkey; altogether, they form 4 main profiles cross the majority of active faults related to the Hatay triple junction. In 2009 and 2010, two campaigns of measurements were achieved where all the GPS points have been measured for 24 hours in each campaign; the last campaign was conducted in September 2011. In this campaign, only the sites in the Turkish side were measured. Unfortunately, political and social unrests appeared in Syria and our planned GPS campaign was impossible to achieve. The regional GPS campaign network was reinforced by 14 permanent GPS sites from the Syrian and Turkish GPS network. The collected data were processed using GAMIT/GLOBK (Feigl et al., 1993a; Dong et al., 1998)

program, together with data of 71 International GPS Service (IGS) points distributed on the major plates around the region of study. Introducing these IGS sites in our processing provide stabilization frame and calibrate our measurements to the global GPS network, it is also used in the determination of the Euler pole and angular velocity of major tectonic plates.

After processing the collected GPS data and calculating the GPS velocity field around the Hatay triple junction, a block model was applied to estimate the strain accumulation along the faults and the blocks rotation parameters. The use of block model was necessary for such complex area, where a simple interpretation of GPS velocity field using 1D or 2D models is not sufficient for the detection of the active deformation. Therefore, we applied 3D elastic dislocation model using DEFNODE program (McCaffrey, 1995; McCaffrey, 2002).

Different model were tested in order to determine the best fit with the GPS data used in this study. We found that two micro blocks called Iskenderun and Amanous blocks are fundamental in the explanation of the active deformation in the triple junction of Hatay and a best fit to the GPS data cannot be obtained without representing the Karasu fault and Karatas-Osmaniye fault as independent faults and not as a continuation of the DSF or the EAF.

This thesis represents our work into five main chapters, we present the previous important studies achieved in our studied region, the GPS measurements and velocity field around Hatay triple junction, the GPS block modeling, and a discussion of our results.

The first and second chapters provide a review of the geodetic and geological studies of the Dead Sea fault and the East Anatolian fault respectively. The N–S trending DSF extends for 1000 km and makes the connection between the Red Sea mid-oceanic ridge (Aqaba Gulf) in the south to the triple junction area to the north where it joins the East Anatolian Fault (EAF) and the Cyprus Arc (CA). Several geological and geodetic studies estimate the rate of displacement along the DSF fault as 2 to 10 mm/yr (Alchalbi *et al.,* 2010; Ferry *et al.,* 2007; Freund *et al.,* 1968; Garfunkel *et al.,* 1981; Gomez *et al.,* 2007; McClusky *et al.,* 2003; Meghraoui *et al.,* 2003; Wdowinski *et al.,* 2004). A difference in slip rate is observed between the northern and southern of DSF. ~105 km of left lateral cumulative slip was documented on the south, while only 70 − 80 km was observed in the north (Quennell, 1958; Freund, 1970; Chaimov *et al.*, 1990; Westaway, 2003). The North-West movement of the Arabia plate with rate of ~20 mm/yr results in 9.7 mm/yr of pure left strike-slip along the East Anatolian fault (McClusky *et al.,* 2000; Reilinger *et al.,* 2006). The EAF extends from Karliova triple junction for 600 km and connect to the HTJ. In these two chapters we compile

all the GPS data available in the region and compare their results with results of other long term studies (geology, paleoseismology, and geomorphology) in order to validate the correlation between long-term and short-term estimations. It is noted that the velocity rates estimated by geodetic studies are in general lower than the slip rates proposed by the geological and geomorphological studies, especially along the DSF.

The third chapter shows and explains our GPS network installed to constrain the active deformation in the region of Hatay by means of GPS processing using GAMIT/GLOBK showing the first order results and velocity field.

We have installed 57 GPS sites in the region (33 in Syria and 24 in Turkey), the sites were selected carefully in order to benefit from other previously existing GPS sites in the region, and to have the best spatial distribution to study such complex area. All GPS sites were measured during two campaigns in 2009 and 2010; a third campaign was lunched only in Turkey in September 2011. The sites in the Turkish side were observed for 24 hours over two sessions of 12 hours using Thales Z Max receivers with Thales Z Max Ashtech antenna. The 33 sites in Syria were observed for one session of 24 hours using Thales DSNP 6502MK receivers and Leica AT504 Choke Ring Antenna. Using "GAMIT" program, the collected data was processed together with other regional and international (IGS) permanent GPS sites (71 sites) in order to construct stabilization frame and connect our network with the international terrestrial reference frame. A GPS velocity field for all points is calculated and represented in different reference frames using "GLOBK" program. Euler poles and rotation rates of major tectonic plates in the region were also estimated using the GPS velocity vectors of permanent sites.

The fourth chapter describes block modeling at the triple junction using GPS velocities from our network and other published solutions (Reilinger *et al.*, 2006; Le Béon *et al.*, 2008; Alchalbi *et al.*, 2010; Al-Tarazi *et al.*, 2011). We show that the active deformation at the triple junction of Hatay can be explained by the use of finite number of rotating elastic spherical blocks limited by faults. The "DEFNODE" program is used to perform a 3D model, in which the tectonic blocks are represented as closed spherical polygons, where faults are represented in 3 dimensions by a long-strike nodes coincide with the blocks boundaries on the earth surface. We apply the dislocation model in an elastic and homogeneous half-space of Okada (1985) by using GPS velocities in order to assess the faults locking and blocks rotations parameters. We test several models with different tectonic configurations and try to

minimize the data misfit of our model. Reduced chi-square statistic and residuals are calculated to determine the best model configuration.

The last fifth chapter discusses the obtained results from block modeling and GPS velocity vectors. An interpretation of the block rotation and fault locking parameters are presented in this chapter, trying to understand the kinematic of the triple junction and how the strain accumulation is going on for the related faults. Furthermore, we use the estimated slip rates of our study in the prediction of the seismic hazard in the region and propose a maximum possible magnitude along the different faults related to the HTJ.

We are aware that our GPS velocity field vectors have relative high uncertainties, but it can provide an important contribution to the understanding of the HTJ kinematic and with future measurements of our GPS network, a better image of the active deformation distribution can be obtained.

Chapter I

I-   The Dead Sea Fault

I.1   Introduction

The Dead Sea fault (DSF) is a north-south trending left lateral strike-slip fault (Garfunkel *et al.,* 1981), known as the Levant fault zone and also documented as a transform fault (Wilson, 1965). The DSF forms the limit between the Arabian and African (Sinai) plates and accommodates the northward motion of Arabia in the east relative to the Sinai subplate in the west (Figure I.1). Both plates show a northward movement toward the Eurasia plate with different rates, the Arabian plate rate being about 18-25 mm/yr and the African plate having a slower movement rate of about 10 mm/yr (Reilinger *et al.,* 1997b; McClusky *et al.,* 2000; Reilinger *et al.,* 2006). The DSF extends for about 1000 km and connects the Red sea mid-oceanic ridge (Aqaba Gulf) in the south to the triple junction area to the north in Turkey where it joins the East Anatolian Fault (EAF) and the Cyprus Arc (CA). The DSF consists in N–S trending fault zone that crosses the Dead Sea and links southward through the Gulf of Aqaba and Tiran Strait to the oceanic spreading zone in the Red Sea. The central segment across Lebanon is oriented N308°E, and the northern segment trends N–S across Syria and bends towards NNE showing several small splays (Figure I.1) in southern Turkey (Tatar *et al.*, 2004; Westaway, 2004). A rate of displacement of 2 to 10 mm/yr has been estimated by several geological and geodetic studies along the DSF fault (Freund *et al.*, 1968; Garfunkel *et al.*, 1981; Pe'eri *et al.*, 2002; McClusky *et al.*, 2003; Meghraoui *et al.*, 2003; Wdowinski *et al.*, 2004; Ferry *et al.*, 2007b; Gomez *et al.*, 2007a; Le Béon *et al.*, 2008; Alchalbi *et al.*, 2010).

Geodetic, Geological and geomorphological studies show that the Dead Sea fault does not slip with the same rate along all its segments. We observe a difference in total motion between the south and the north segments of the fault. A total cumulative sinistral slip of about 105 km has been documented along the southern part of the fault (Wadi Araba) and was accumulated during 15 - 20 Ma, when the DSF was initiated in the Middle Miocene (Quennell, 1958; Freund, 1970; Garfunkel, 1981). In the northern part of the fault (Al-Ghab fault, Figure I.1) the total documented amount of slip is 70 – 80 km (Freund, 1970; Dewey *et al.*, 1986; Chaimov *et al.*, 1990; Westaway, 1995; Westaway, 2003), which suggests 25-35 km of slip missed between the north and south of DSF. Several studies had interest to justify this lake of slip. Freund *et al.,* (1970) suggested that some displacement can be transferred a way to the East and west of the main fault throw faults in the Lebanon range (e.g., Serghaya fault, Roum fault, Yammuneh fault), causing this lower displacement along the northern DSF. Chaimov *et al.,* (1990) and Khair *et al.,* (1997) suggest that the shortening on the Palmyride

9

fold belt (20 -30 km) may be also related to the difference in total slip. Furthermore, Yurtmen *et al.,* (2002) noted, that the estimations of total slip in the northern DSF excludes the slip on the Afrin fault that runs east of Amik basin. Other studies (Butler *et al.*, 1998; Butler and Spencer, 1999) suggested that the northern DSF stopped to be active around the Late Miocene and the slip was accommodated by another hypothetical fault zone located offshore to the west along the coast of Syria and Lebanon. In contrast, Brew *et al.,* (2001) and Heimann (2001) suggested that the Northern DSF became active around the Early Pliocene, therefore it shows a smaller amount of total slip.
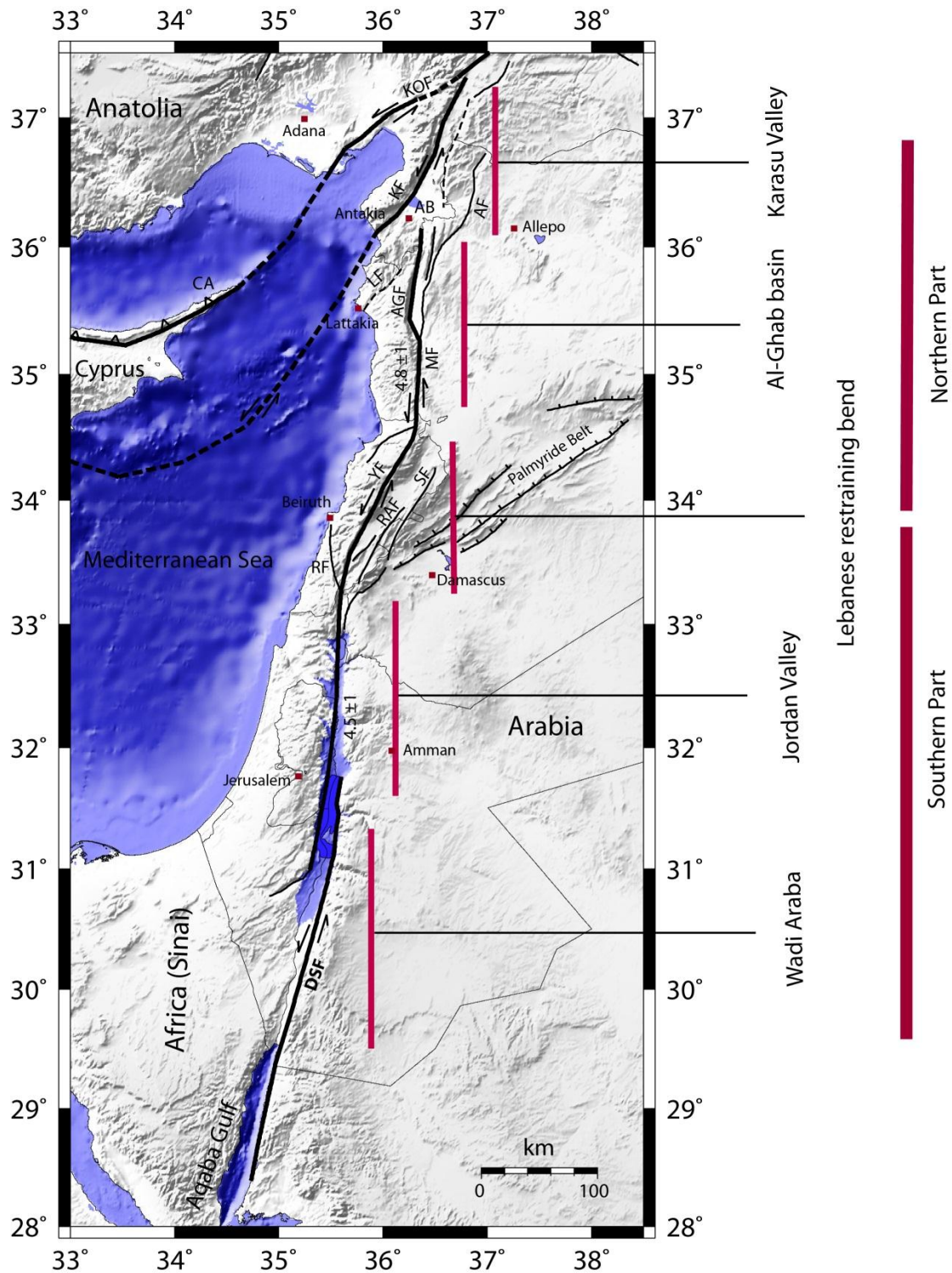
Figure I.1: The Dead Sea fault segments, Fault mapping and slip rates from (Khair et al., 2000; Westaway, 2003; Ferry et al., 2007a; Gomez et al., 2007a; Meghraoui et al., 2011). Abbreviations for some key tectonic features: AGF: Al-Ghab fault, AF: Afrin fault, CA: Cyprus Arc, AB: Amik basin, KF: Karasu fault, KOF: Karatas-Osmaniye fault, LF: Lattakia fault, DSF: Dead Sea fault, EAF: East Anatolian fault, MF: Missyaf fault, SF: Serghaya fault, RF: Roum fault, RAF: Rashaya fault, YF: Yammuneh fault.

I.2   *Tectonic setting of Dead Sea Fault*

I.2.1   *General tectonic setting*

The Dead Sea Fault (Figure I.1) can be subdivided into the north and the south zone connected to each other by the restraining Lebanese bend an active transpressive zone (Griffiths *et al.,* 2000; Gomez *et al.,* 2003). The main difference between its southern and northern zones is the difference in accumulated slip rate (25 - 35 km) between the north (70 - 80 km) and south (~105 km) of the DSF (Freund, 1970; Chaimov *et al.,* 1990; Westaway, 1995; Westaway, 2003). Khair *et al.,* (2000) divided the DSF into five major segments (Wadi Araba, Jordan Valley, Albeqa'a basin, Al-Ghab Basin and Karasu Valley). The segmentation was proposed due to the difference in geometry, geomorphology, geology and seismicity of each fault zone (Figure I.1). Sbeinati *et al.,* (2010) divided the northern DSF into two main parts: 1) a 90±10 km long linear fault zone which is the Missyaf segment, limited by the Lebanese restraining bend and the Al-Ghab pull-apart basin and 2) the Al-Ghab pull-apart basin of ~10km wide and related complex system of fault branches in its northern termination where it reaches the Amik basin. Another division for the DSF was proposed by Ferry *et al.,* (2011) who considered that the DSF is made of a transtensional system to the south (including the Hula, Dead Sea, and Gulf of Aqaba pull-apart basins), the Lebanese restraining bend (the Yamouneh, Rashaya, Serghaya, and Roum faults) in the middle, and a strike-slip system to the north (the Missyaf fault and the Ghab pull-apart basin). All of these segments have N-S trending in general with small deviation to the NNE for the central and the northern segment of the fault.

In this study, we will focus on the northern part of the Dead Sea fault which connects with the triple junction in south-east of Turkey and north-west of Syria. A detailed investigation of strain accumulation using GPS measurements will be carried out to determine the physical parameters of mapped active faults and understand the kinematics of this part of DSF. Furthermore, the new detailed information and more clear view on the kinematics can be used in the analysis of seismic hazard and risk of the region and have a better assessments.

I.2.2   *Eastern Mediterranean geodynamics*

The present-day geodynamics of the eastern Mediterranean region is controlled by the relative motions of three major plates, Eurasia, Africa, and Arabia (Figure I.2). A large part of deformation in the region is due to the interaction between these plates (Jackson and McKenzie, 1984; Spakman *et al.,* 1988; Westaway, 1994; Le Pichon *et al.,* 1995; Barka *et al.,* 1997; Jolivet and Faccenna, 2000; McClusky *et al.,* 2000; Doglioni *et al.,* 2002; Piromallo and Morelli, 2003; Dilek, 2006; Reilinger *et al.,* 2006). The Anatolian continental block which was a part from Eurasia plate, is acting as a micro plate between these three major plates since the middle Miocene, when it collided with Eurasia (Dewey *et al.,* 1986).
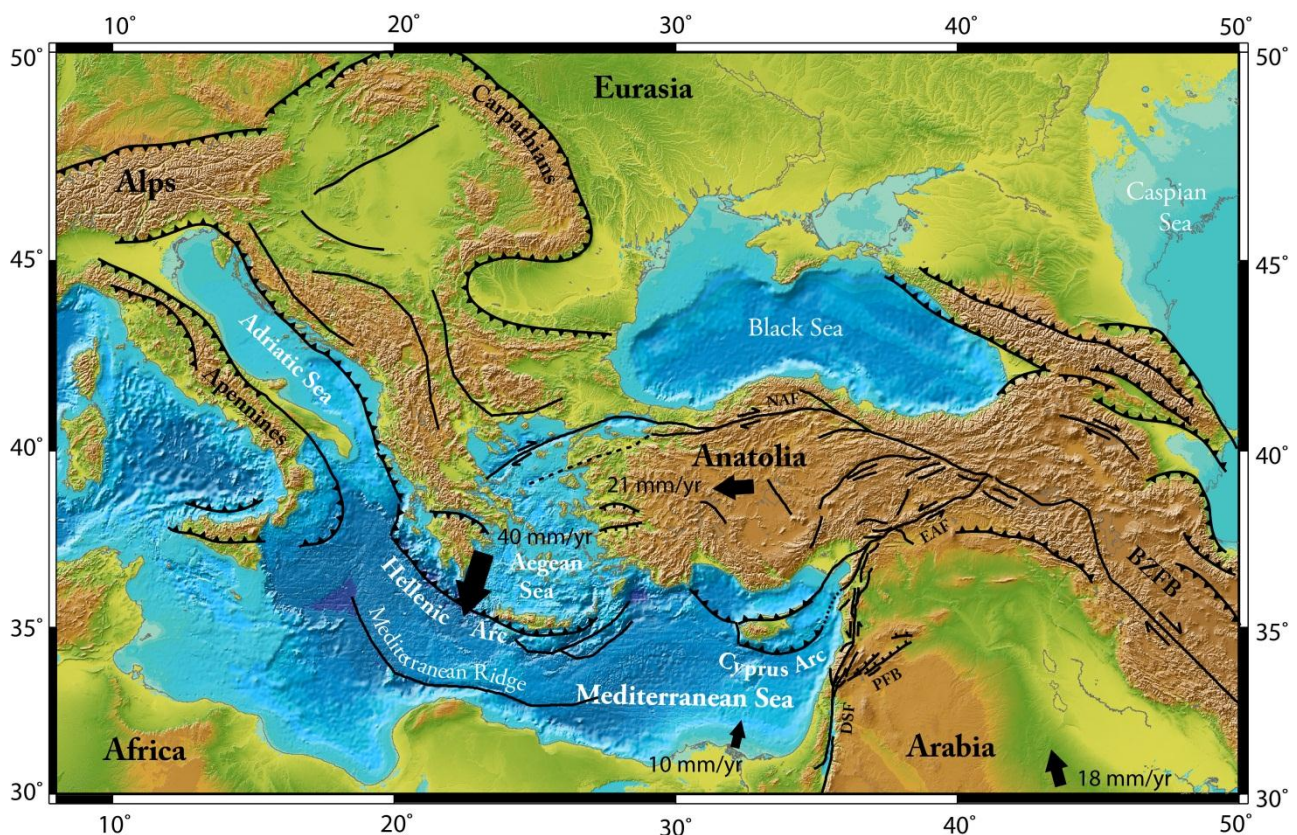
Figure I.2: Map of the eastern Mediterranean region, illustrating the major plates (Africa, Arabia, Eurasia, and Anatolia) and their boundaries and important fault systems. Thick black arrows show the plates convergence directions. Abbreviations for some key tectonic features: EAF: East Anatolian Fault, DSF: Dead Sea Fault, NAF: North Anatolian Fault, PFB: Palmyride Fold Belt, BZFB: Bitlis–Zagros fold and thrust belt. Fault mapping is from (Dilek, 2010). Movement rates are from (McClusky et al., 2003; Reilinger et al., 2006).

The current Anatolian-African plate boundary is represented by a north-dipping subduction zone that has been part of a wide-ranging domain of regional convergence

between Eurasia in the north and Africa and Arabia in the south since the late Mesozoic (Faccenna *et al.,* 2003; van Hinsbergen *et al.,* 2005; Jolivet and Brun, 2010). The convergence rate between Africa and Eurasia is greater than 40 mm/yr across the Hellenic Arc but decreases to ~10mm/yr across the Cyprus Arc. Based on plate-tectonic models (NUVEL-1, De Mets *et al.,* 1990) and the global positioning system of present-day central movements in this collision zone (Reilinger *et al.,* 1997b; McClusky *et al.,* 2000; Reilinger *et al.,* 2006), The Arabia-Eurasia convergence is estimated to ~20 mm/yr with NNW trending movement of the Arabia plate relative to Eurasia. This difference in convergence rate between Arabia, Africa and Eurasia can be translated into a slip rate along the Dead Sea fault. The NNW trending convergence of Arabia towards Anatolia produces thickening of the crust in south-eastern Turkey, implying compressional deformation along the Bitlis–Zagros fold and thrust belt (Saroglu and Yilmaz, 1990), and westward extrusion of the Anatolian block. The Anatolian plate is bounded by the dextral NAF and the sinistral EAF (McKenzie, 1972; Sengor, 1979; Sengor *et al.,* 1985; Dewey *et al.,* 1986; McClusky *et al.,* 2000). GPS data indicate a mean extrusion rate for Anatolia, with respect to Eurasia, of about 25 mm/yr along the NAF (Straub and Kahle, 1994; Le Pichon *et al.,* 1995; Straub and Kahle, 1995; McClusky *et al.,* 2000).

I.2.3   *Dead Sea Fault segments*

I.2.3.1 *Wadi Araba*

Wadi Araba is the southern part of DSF. It starts from the Red Sea (Aqaba Gulf) at 29.5^o N and extends for about 160 km till the Dead Sea basin at 31° N (Figure I.1). This valley is delimited by two plateaus from the east and west, respectively (Klinger *et al.,* 2000b). Along this segment, the fault has a sharp morphological discontinuity that can easily be traced across the Quaternary deposits and alluvium sediments, excluding where the fault is covered with sand dunes or cuts across very recent alluvial terraces. The principal fault is rather straight, striking $N20^oE$, and showing limited structural discontinuities, with a simple geometry reliable with basically pure strike-slip motion (Garfunkel *et al.,* 1981; Klinger *et al.,* 2000b).

The estimations of the slip rate along Wadi Araba segment are varying between 2.5 and 7.5 mm/yr. An estimation based on geodesic study (GPS) of 4.9±1.4 mm/yr was given by (Le Béon *et al.,* 2008), this value relays on 6 years of time span and a locking depth of 12 km. Geodetic studies along this segment and other segments are described in details in paragraph (1.4.2.2), see Table I.3.

Regarding the historical catalogues, a few seismic events are reported during the last 2000 years along the Wadi Araba. The biggest reported events occurred in AD 1068, 1212, 1293 and 1458 (Abou Karaki, 1987; Ambraseys *et al.,* 1994; Klinger *et al.,* 2000b). These events seems to be smaller than the 1995 earthquake which struck the Aqaba Golf with a Mw~7.3 (Klinger *et al.,* 1999) due to lack of seismicity and elapsed time since the most recent historical earthquakes which suggest that a tectonic loading has been accumulating along the fault (Ferry *et al.,* 2011).

I.2.3.2 *Jordan Valley*

The trending N-S Jordan Valley extends ~180 km between the Dead Sea pull-apart basin at 30.7^o N and the Hula Basin in the north before connecting with the Lebanese restraining bend at 33.1^o N. The northern end of this segment attests on the division of the DSF into many fault branches trending toward the NNE, the Serghaya, Rashaya, Hasbaya, and Yammuneh faults (Figure I.1). This segment is connecting the two pull-apart basins of the Dead Sea and the Tabariya and was the object of paleoseismologic and geomorphologic studies which estimate its slip rate a 2.5 to 10 mm/yr (Marco *et al.,* 1997; Galli, 1999). One of the last recent studies along Jordan Valley (Ferry *et al.,* 2011) proposes a slip rate of 5 mm/yr. This study relies on paleoseismic, archaeoseismologic and historical data for 12 destructive earthquakes over the last 25 kyr.

The calculated average magnitude for the paleoearthquakes in the Jordan Valley segment is Mw 6.6 (Hamiel *et al.,* 2009). However, Ferry *et al.,* 2011 suggests that the length of fault segments and thickness of the seismogenic crust agree with Mw 7.2-7.4 as a reasonable maximum magnitude in the region. Studies of macroseismic damage from historical events and archaeological evidence conclude that 1–3 large earthquake (Ms>6) occurred in the northern Jordan Valley segment during the past 2000 yr (Ambraseys *et al.,* 1994; Guidoboni *et al.,* 1994; Marco *et al.,* 2003).

I.2.3.3 *Beqa'a Basin (Lebanese restraining bend)*

The 200-km-long Lebanese restraining bend between 33.1^o N and 34.7^o N is the central part of the Dead Sea fault in Lebanon and southwestern Syria. This segment strikes 25°–30° from the main trend of the transform fault (Gomez *et al.*, 2007a). It shows NNE trending fault branches, i.e., the Serghaya, Rashaya, Hasbaya, and Yammuneh Faults and NW trending Al-Roum Fault in the south and the SE Akkar fault in the north. The Yamouneh

Fault forms the main fault continuation on the Dead Sea Fault to the North and ends at the Lebanese border where the NS section starts in Syria. Al-Roum and Akkar faults are striking oblique to the DSF transform. They seems to serve as the structure linkages between the strike-slip faults of the Lebanese restraining bend and the horizontal shortening of the mountain Lebanon range (Gomez *et al.*, 2006; Nemer and Meghraoui, 2006; Gomez *et al.*, 2007a).

Recent geodesic studies gave a slip rate of 4-5 mm/yr along the main Yamouneh fault (Mahmoud *et al.*, 2005; Reilinger *et al.*, 2006; Gomez *et al.*, 2007a). Other geomorphologic studies propose a slip rate of 5-10 mm/yr (Garfunkel *et al.,* 1981; Daeron *et al.,* 2004a). The historical seismicity of this segment being rich with several historical large events contradicts with the recent time of a general seismic quiescence. The large earthquakes that took place in the Lebanese restraining bend are 551 AD, 1202 AD, 1759 AD and 1837 AD (Ambraseys and Melville, 1988; Ambraseys and Barazangi, 1989; Beydoun, 1997; Sbeinati *et al.*, 2005).

I.2.3.4 Al-Ghab basin

This segment is NS trending and extends along 150 km between 34.7^{o}N and 35.9^{o}N in the NW of Syria (Figure I.1). It is adjacent to the coast range (Brew *et al.,* 2001); it extends from Lebanon to the south of Turkey where it joins the Karasu Valley. This part of the DSF has three main sub-segments from south to north: the Missyaf segment as single linear fault structure; the Al-Ghab fault zone and pull-apart region divides into several fault branches with the main Jisser Al-Shoughur segment west of the basin and the Afamia and Afrin faults to the east of the basin (Sbeinati, 2010). Previous geodetic studies have moderated the slip rate of this DSF segment, most of them determined almost the same rate (4.2 – 4.8 mm/yr) (Mahmoud *et al.*, 2005; Reilinger *et al.*, 2006; Gomez *et al.*, 2007a). (Alchalbi *et al.,* 2010) has proposed a smaller value of 1.8-3.3 mm/yr, this last value have the largest time span (~7.5 year) among the other similar studies. Other archaeoseismologic studies give a slip rate of 5-6.9 mm/yr.

This segment has experienced a considerable historical seismicity. Several large seismic events (with M > 7) took place along the Missyaf fault and the others branches to the north like 859AD, 1349 AD, 1157AD, 1170 AD, 1202AD and 1408AD (Ambraseys and Melville, 1988; Meghraoui *et al.,* 2003; Sbeinati, 2010).

The northern DSF, in Syria and southern Turkey, is regarded as a series of transpressional stepovers, along which the left-lateral slip is apparently slower than the relative plate motion, because this slip is oblique to the relative plate motion (Gomez *et al.,* 2007).

I.2.3.5 Karasu Fault

The Karasu fault limits the northernmost segment of the left lateral DSF and extends for 150 km along the Karasu valley in south east Turkey, between 35.9^o N and 37.1^o N. At this segment, the fault changes its striking direction and continues to the NE. The Karasu Fault joins the southern end of the left lateral East Anatolian fault and the Cyprus arc extension in the north of the valley (Figure I.1). This valley is tectonically complex because of the existence of many small fault segments in the region and it accommodates the deformations of the triple point junction between the Arabia, Africa and Eurasia plates. Previous historical studies show that this segment was the source of many large earthquakes in the past, like the 859AD, 1822AD and 1872AD with M>7 (Sbeinati *et al.*, 2005).

I.3   *Seismicity of Dead Sea Fault*

I.3.1   Historical seismicity

The Middle East is one of the oldest inhabited regions of the world and by consequence it has among the richest written history on earthquakes. The earthquakes as any other well-known natural events were recorded and described carefully. The old documents describe the earthquakes effects on nature and man-made structures, such as faulting rupture, co-seismic deformation, landslide, springs appearing and disappearing, lives losses, houses destruction, ... etc. This allows us to have, nowadays, a very rich earthquake catalogue for more than 3000 year in the Middle East region (Ambraseys *et al.*, 1994; Ambraseys and Jackson, 1998; Sbeinati *et al.*, 2005; Ambraseys, 2009b).

Seismic activity of the DSF has been measured for different magnitudes and timescales: that is tens of thousands of years (Marco *et al.,* 1996; Amit *et al.,* 2002; Begin *et al.,* 2005), thousands of years (Zilberman *et al.,* 2005), hundreds of years (Migowski *et al.,* 2004), and decades (Salamon *et al.,* 2003). These studies have shown that the eastern Mediterranean Sea region was strongly affected by large historical seismic events where

many medieval cities, fortresses, citadels or known archaeological sites were damaged or destroyed by earthquakes. A very good example of large seismic activities along the Dead Sea fault is the event of May 20, 1202 of Ms >7.5 and I = X (Daeron *et al.,* 2004) which has been felt over long distances from Egypt to Greece and Iran (Ambraseys *et al.,* 1994). The earthquake revealed surface ruptures and destroyed a large part of Lebanon and surrounding areas and led to an unprecedented decline in social structures and the local economy. Other earthquakes have struck ancient cities such as Antakya in Turkey, Apamea and Aleppo in Syria, Baalbek in Lebanon and Jarash in Jordan. The traces of these historical events are clearly visible on these sites by the presence of walls damaged or destroyed crumbled and columns. This impressive wealth of archaeological sites and cultural rights is an open archive to study the ancient and historical earthquakes.

Sbeinati *et al.,(2005)* has prepared a historical earthquake catalogue of Syria and neighboring regions where large shocks are represented in Table I.1 and shows the parameters of the destructive historical earthquakes estimated from the textual descriptions of events damage. The catalogue is presented as a list of earthquakes with its parameters ordered by date, time, epicenter, coordinates, estimated maximum intensity, calculated magnitude, intensity at affected localities, and the natural co-seismic features. The historical catalogue of Sbeinati *et al.,* (2005) extends up to 1365 B.C. and contains important information on the occurrence of large earthquakes. Even though the low level of instrumental seismicity and the absence of strong motion records, seismic parameters and fault activity along the Dead Sea Fault related to the historical earthquake data has an important role in estimating the seismic hazard for the region.

No	Date (dd.mm.yyyy)	Long. (E°)	Lat. (N°)	Major affected localities	I0 (EMS-92)	H (km)	Ms
1	37 A.D.	36.30	36.00	Antioch, Dafneh	VII-VIII	15	6.2
2	53	36.50	36.20	Antioch, Afamia, Manbej, Lattakia	VIII	30	6.6
3	303-304	34.30	33.80	Saida, Sur, Syria	VIII-IX	20	7.1
4	494	36.30	35.80	Antioch, Tripoli, Lattakia	VII-VIII	25	6.5
5	22.08.502	34.80	33.00	Akka, Sur, Saida, Beirut, Safad	VIII-IX	30	7.2
6	531-534	37.20	35.50	Area between Aleppo and Homs	VIII	15	6.5
7	09.07.55 1	35.50	34.00	Cities of Lebanese coast, Arwad	IX-X	28	7.2
8	565-571	36.20	36.00	Antioch, Seleucea, Kilikia, Anazrabo	VII-VIII	30	6.0
9	18.01.747	35.60	32.50	Mt. Tabor, Baalbak, Bosra, Nawa, Balqa, Al-Quds, Beit Qubayeh, Tabaryya, Damascus, Daraa	IX	25	7.2
10	24.11.847	36.30	34.40	In and around Damascus, Antioch, Al-Mosel	IX	35	7.5
11	30.12.859-29.01.860	36.40	35.70	Antioch, Lattakia, Jableh, Homs, Palmyra, Tarsus, Balis, Damascus, Adana, Ar-Raqqa	VIII-IX	33	7.4

12	05.04.991	36.40	33.70	Baalbak, Damascus	IX	22	7.1
13	30.07-	36.20	34.40	Tripoli, Lattakia, Akka, Sur	VIII	32	6.9
14	11.1114	38.50	37.30	Maskaneh, Maraash,	VIII-IX	40	7.4
15	11.1114	36.50	37.30	Samsat, Orfa, Harran	IX	40	7.7
16	27.09.1152	36.70	32.60	Bosra, Hauran, Syria	VIII	12	5.8
17	02-	36.50	35.50	Shaizar, Hama, Kafer Tab, Aleppo	VII	22	6.0
18	13.07.1157	36.60	35.20	Hama, Afamia, Kafer Tab, Homs, Tayma	VIII	25	6.6
19	12.08.1157	36.60	35.40	Shaizar, Kafar Tab, Afamia, Hama, Arqa, Aleppo, Homs, Lattakia, Tripoli, Antioch, Qalaat Al-Hosn,	IX-X	15	7.4
20	29.06.1170	36.40	34.80	Damascus, Homs, Hama, Lattakia, Baalbak, Shaizar, Barin, Aleppo	IX	35	7.7
21	20.05.1202	36.10	34.10	Mount Lebanon, Baalbak, Sur, Beit Jin, Banyas, Nablus, Al-Samyra, Damascus, Safita, Akka, Tripoli, Hauran, Beirut, Homs, Tartus	IX	30	7.6
22	02.01.1344	37.40	36.70	Al-Rawendan, Manbej, Aleppo	VIII	30	6.8
23	20.02.1404	36.20	35.70	Blatnes, Bkas, West of Aleppo, Qalaat Al-Marqeb, Tripoli, Lattakia, Jableh	VIII-IX	30	7.4
24	29. 12.1408	36.10	35.80	Shugr, Bkas, Blatnes, Lattakia, Jableh, Antioch, Syrian	IX	25	7.4
25	10.10.1568	35.50	35.50	Lattakia, Famagusta	VIII	12	6.0
26	21.01.1626	37.10	36.50	Aleppo, Gaziantab, Hama	IX	20	7.3
27	22.09.1666	43.00	37.00	Al-Mousel, Sinjar, Sharqat	IX	35	6.9
28	24.11.1705	36.60	33.70	Yabroud, Al-Qastal, Damascus, Tripoli	VIII	35	6.9
29	15.04.1726	36.60	36.30	Jum, Aleppo	VIII	15	6.1
30	25.09.1738	36.50	36.70	Iskenderun, Bellen Bass, Antioch, Jabal Al-Amanus,	VIII	10	6.2
31	30.10.1759	35.60	33.10	Al-Qunaytra, Safad, Akka	VIII-IX	20	6.6
32	25.11.1759	35.90	33.70	Baalbak, Zabadani, Ras Baalbak, Al-Qunaytra, Damascus, Beirut, Saida, Safad, Sur, Tripoli, Homs, Hama, An-Nasra, Lattakia, Al-Quds, Gaza, Antioch	IX	30	7.4
33	26.04.1796	36.20	35.30	Qalaat Al-Marqeb, Al-Qadmous, Nahr Al-Kabir, Jableh, Bkas, Lattakia	VIII-IX	20	6.8
34	13.08.1822	36.75	36.10	Jisr Ash'Shoughour, Quseir, Aleppo, Darkoush, Antioch, Iskenderun, Idleb, Kelless, Armanaz, Sarmada, Lattakia, Homs, Hama, Maraash, Ram	IX	18	7.0
35	01.01.1837	-	-		VIII		>7.0
36	03.04.1872	36.50	36.20	Harem, Armanaz, Lake of Al-Amq, Antioch, Aleppo, Suaidiya, Izaz, Idleb, Iskenderun	VIII-IX	10	7.2

Table I-1: Main destructive earthquakes with Ms > 5.9 along the Dead Sea Fault (Sbeinati et al., 2005).

Most of studies referring to historical earthquakes confirm that almost all of them are associated with a sinistral surface rupture. Figure I.3 shows the historical earthquakes of magnitude greater than 5 associated with the Dead Sea Fault in Syria from 37 A.D. to 1900 A.D. Sbeinati (2010). A repetition of seismic events matching to those of the past, nowadays, will cause enormous damage, because of the increase of modern buildings and the population during the last century.
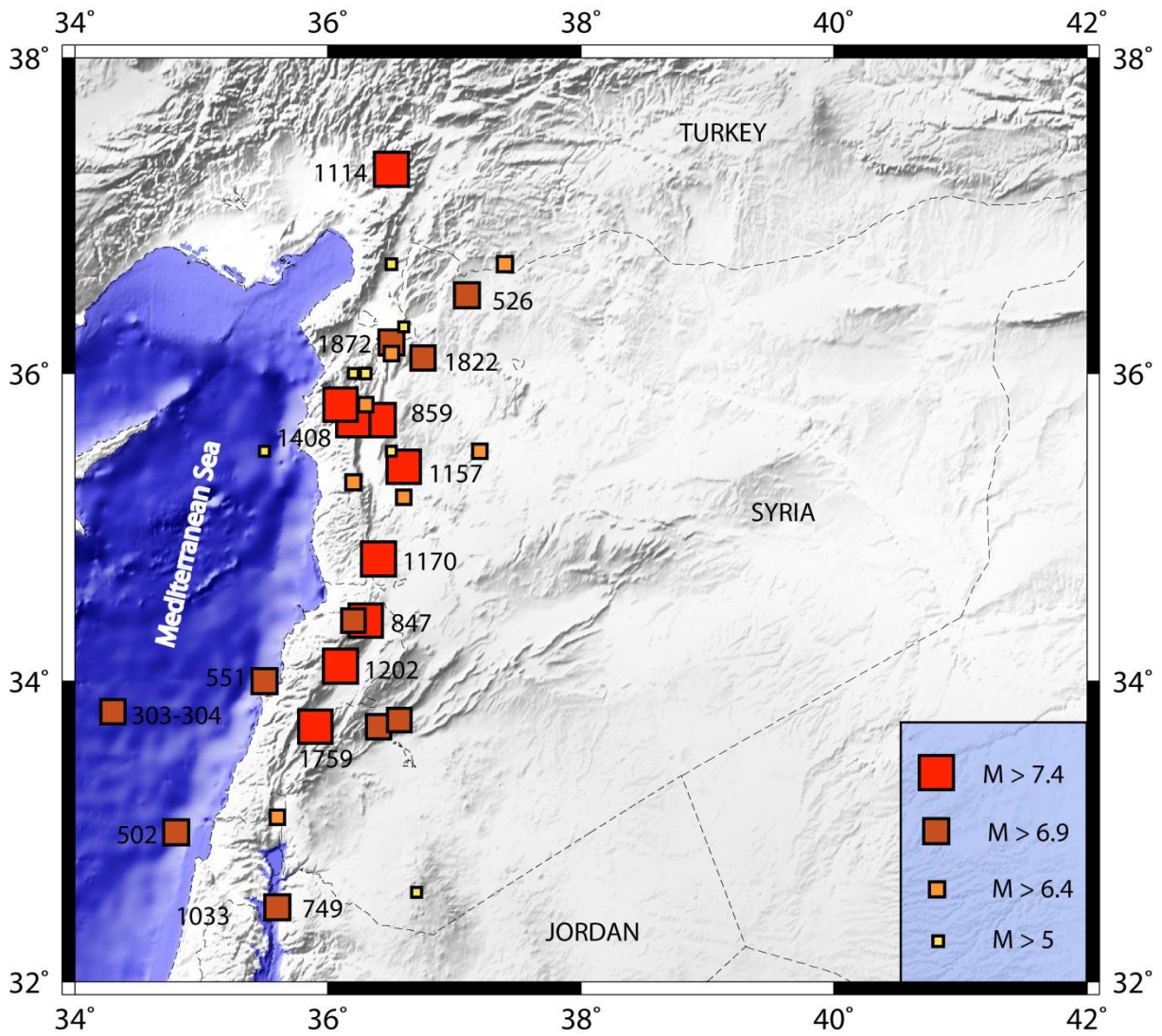
Figure I.3: Map of historical seismicity in Lebanon, Syria and southern Turkey with magnitude greater than 5 from 37 A.D. to 1900 A.D. Data from Table I.1.

I.3.2   *Instrumental seismicity*

The Dead Sea fault shows a relatively moderate instrumental seismicity with most events of a low magnitude, typically ~M=4.5.

The southern parts (Wadi Araba and Jordan Valley) of the Dead Sea Fault system recorded the only two major instrumental earthquakes: The first event occurred in July 11, 1927 (M = 6.2) along the Jordan Valley. The second event, which is the larger instrumental event recorded along the DSF, took place in November 22, 1995 (Mw = 7.3; Figure I.4) in the Gulf of Aqaba. Its magnitude is comparable to the historical earthquakes of the region like the 1068 and 1212 earthquakes (Abou Karaki, 1987; Ambraseys *et al.*, 1994; Zilberman *et al.*, 2005). The earthquake has produced about 2.1 m total displacement of left lateral slip along the 56 km long and trending N20^{o}E fault segment (Klinger *et al.,* 1999). This earthquake was followed by an intense aftershock activity for about 6 months. Despite these two large instrumental events, the Dead Sea Fault instrumental seismicity is lower than the historical seismic activity throughout the last 1000 years or so, which leads us to conclude that the present-day period is a seismic gap.

Figure I.4 shows the instrumental seismicity (M> 3) recorded along the DSF from 1976 to 2011, Earthquakes swarms are located in the Gulf of Aqaba, Lebanon, south of Cyprus and the near to junction with the EAF. Figure I.5 shows the Harvard CMT focal mechanism solutions of earthquakes of magnitude greater than 4.5 between 1976 to January 2011 along the Dead Sea fault zone.
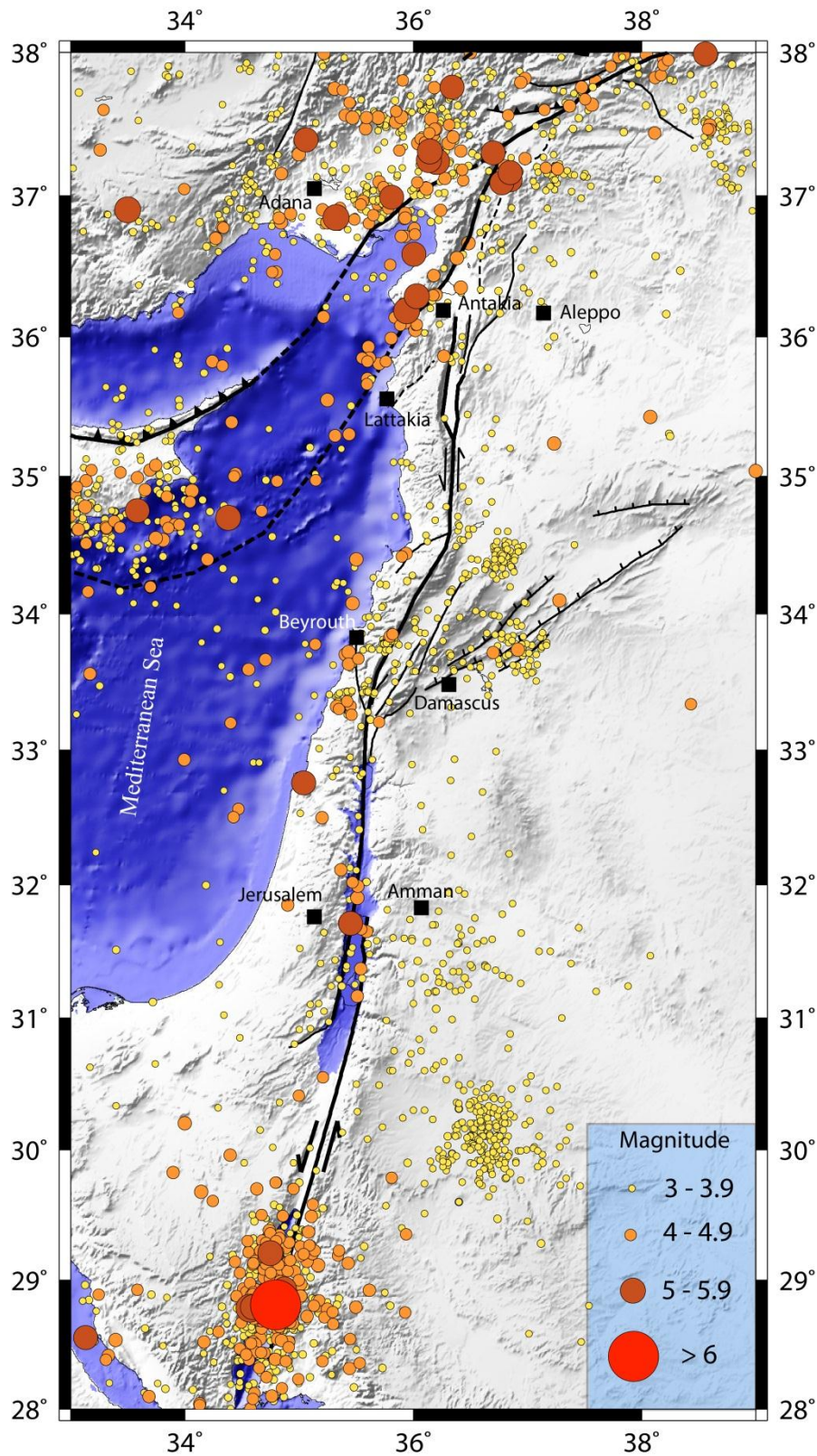
Figure I.4: Instrumental seismicity of the Dead Sea fault between 1964 and 2011, M>3. Data are from: IRIS (Incorporated Research Institutions for Seismology, http://www.iris.edu/hq/), ISC (The International Seismological Center, http://www.isc.ac.uk/) and NEIC (The National Earthquake Information Center, http://earthquake.usgs.gov/regional/neic/). Mapped faults are from Meghraoui et al., (2011) and Ferry et al., (2007).
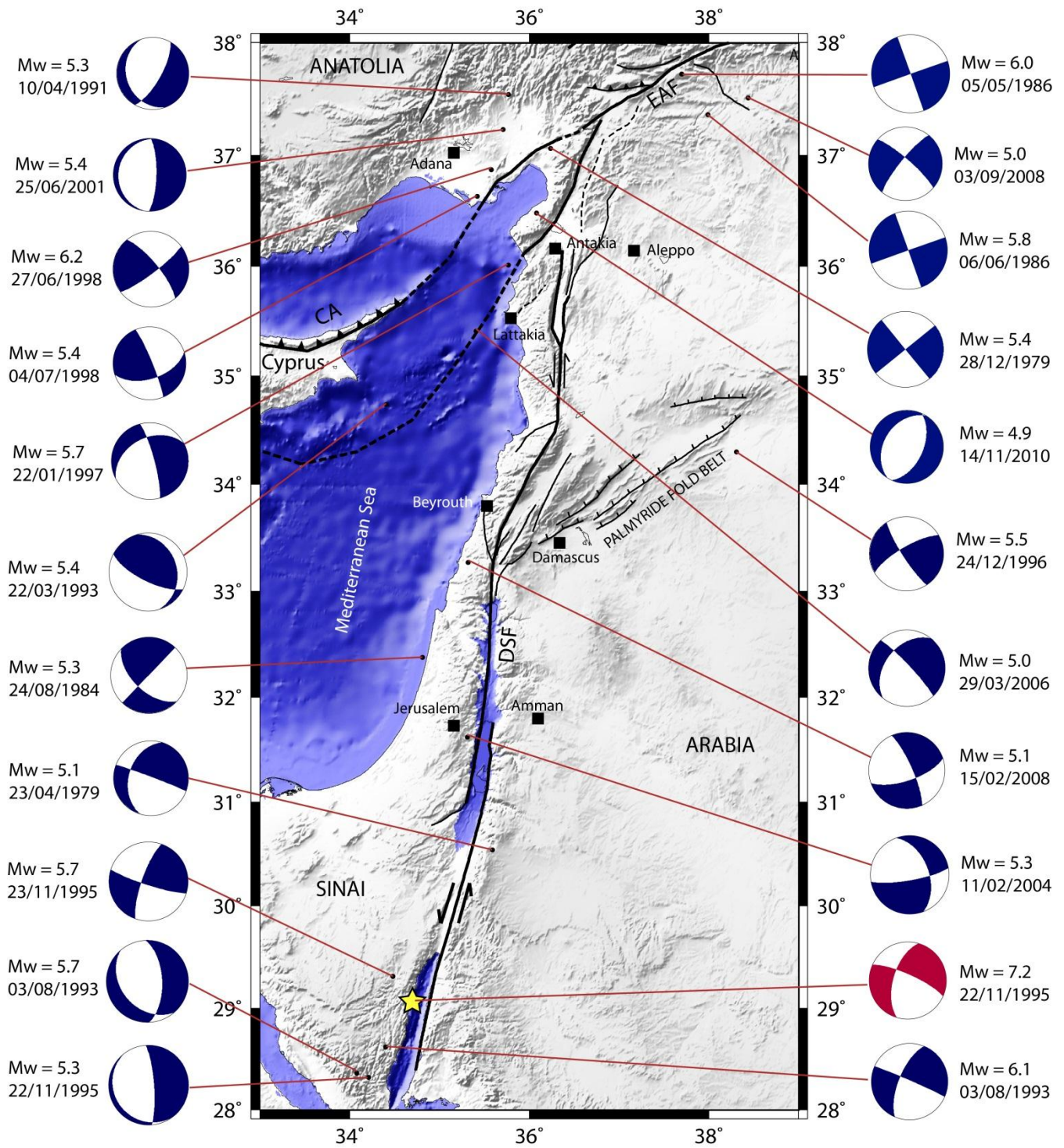
Figure I.5: Focal mechanism of earthquakes between 1976 and 2011 along the Dead Sea Fault, of magnitude greater than 4.5. Data are from catalogues Harvard CMT. Mapped faults are from Meghraoui et al., (2011) and Ferry et al., (2007).

I.4   *Kinematisc of Dead Sea Fault*

I.4.1   *Geodynamic of the Dead Sea Fault*

The slip rate on the Dead Sea fault has been determined by various methods, including geology, geomorphology, seismology, paleoseismology (Table I.2) and geodesy (Table I.3). The slip rate is estimated between 2 and 8 mm/yr depending on the time scale of observations and studied fault segment.

I.4.1.1Long term deformation

Estimates of the slip rate based on the geology is using a total shift along the geological fault during a known period to determine an average rate of displacement associated with this fault. Geological observations of the last 15-20 Myr indicate a slip rate of 2-10 mm/yr (Quennell, 1958; Freund *et al.,* 1968; Freund, 1970; Garfunkel *et al.,* 1981).

The geomorphological estimations of left lateral slip are mainly based on measurements of geomorphic markers such as alluvial fans, terraces, waterways, etc.., across the fault during a specified period, and then dated by isotopic dating. Accordingly, Klinger *et al.,* (2000a, 2000b) suggest along the Wadi Araba segment a slip rate of 2 to 6 mm/yr (for a period of 77 to 140 ka), while Ginat *et al., (1998)* proposes 3 to 7.5 mm/yr (Pleistocene) and Niemi *et al.,* (2001) propose 3.4 to 6 mm/yr (15 kyr). Using offsets of drainage systems surveyed at three sites of the southern segment of DSF, Ferry *et al.,* (2007) propose an average constant slip rate of 4.7-5.1 mm/yr for the last 47.5 Kyr. Galli (1999) gives a value of 10 mm/yr for south of the Dead Sea fault for the last 18 to 70kyr. Zange (1998) noted the offsets of rivers and alluvial fans surfaces of 39 m and 22.5 m, respectively. These offsets have been dated between 8500 and 4700 years and give a slip rate of 4.6 to 4.8 mm/yr for this period. The geomorphological approach was also applied by Garfunkel *et al.,* (1981) on a basalt offset measured at 8 km north of Lebanon. They estimate a slip rate of 5 to 10 mm/yr along the Yammuneh fault during the Pleistocene. This value is in agreement with the study of Daeron *et al.,* (2004a), which correlate the offset of two alluvial fans with distance of 50 km along the Yammuneh fault in Lebanon and estimate a slip rate of 5.1±1.3 mm/yr during the late Pleistocene - Holocene. As mentioned before, Ferry *et al.,* (2011) used paleoseismic data with 28 radiocarbon datings and archaeoseismology at Tell Saydiyeh, supported by a rich historical seismic records, he documented 12 destructive events along the Jordan Valley

segment with a mean interval of ~1160 yr and an average 5 mm/yr slip rate for the last 25 kyr. These results agree with Ferry *et al.,* (2007).

Estimates of the slip rate based on seismicity use the historical and instrumental data to calculate an average return period of major earthquakes and deduce an average slip rate. Garfunkel *et al.,* (1981) estimate a seismic slip-rate between 1.5 and 3.5 mm/yr for the last 1000 to 1500 years on the Dead Sea Fault based on instrumental and historical records. For the segment of Wadi Araba, Klinger *et al.,* (1999) propose a slip rate of 4±2 mm/yr for the last 2000 years, using a maximum 8 m co-seismic displacement for the 1995 earthquake.

Fault segment	Evidence type	Amount of offset	Age of datum	Slip rate mm/yr	Authors
DSF (general)	Geol.	65 km	~4Ma	~ 8.7	Westaway *et al.,* 2001
			7–10 Ma	4–6	Freund *et al.,* 1970
			3.1–3.7 Ma	9–15	Steinitz *et al.,* 1978
			Pliocene-Pleistocene (4–5 Ma)	7–10	Garfunkel *et al.,* 1981
			Last 1,000–1,500 yr	1.5–3.5	Garfunkel *et al.,* 1981
	Offset Miocene rocks	40–45 km	7–12 Ma	3.5–6	Freund *et al.,* 1968
Amik basin	Paleo	7.9 km	Pre-Quaternary	4.94±0.13	Karabacak 2009
	Paleo	42 m	6500 BC	6.07	Altunel *et al.,* 2009
	Paleo	25 m	1500 BC	6.07	Altunel *et al.,* 2009
Missyaf & Al-Ghab	Paleo.	13.6 m	Last 2000 years	6.9±0.1	Meghraoui *et al.,* 2003
	Paleo	13.6 m	3000 years	4.9-6.3	sbeinati *et al.,* 2010
Yammuneh	Offset alluvial fans		25 ka	5.1±1.3b	Daëron *et al.,* 2004
	Offset Homs basalts	8 km	Miocene- Pliocene	5–10	
	Offset Litani river	5 km	1–2 Ma	5–10	Garfunkel *et al.,* 1981
	Offset alluvial fans		~25 kyr	5.1±1.3	Daeron *et al.,* 2004
Roum	Paleo			0.86 – 1.05	Nemer *et al.,* 2006
Serghaya	Offset channels		10 ka	1.4±0.2	Gomez *et al.,* 2003
Hula Basin	Offset of walls	2.1 m	Holocene (817 year)	~ 2.5	Marco *et al.,* 1997
Jordan valley	Geol. offset gullies		the last 47.5 kyr	4.7 to 5.1	Ferry *et al.,* 2007
	Paleo. Offset drainage		Last 25 kyr	5	Ferry *et al.,* 2011
	Paleo		Last 5 kyr	3 – 4	Marco *et al.,* 2005
	Offset channels	100–150 m	post-Lisan	10	Garfunkel *et al.,* 1981
	Paleo		60,000 yr	0.5	Hamiel *et al.,* 2009
Wadi Araba	Offset gullies and fan surfaces on ributaries to Wadi Dahal	54 m	16–11 ka	3.4–4.9	
		39 m	9–6.5 ka	4.3–6.0	
		22.5 m	5.8 ka	3.9	Niemi *et al.,* 2001

Offset of late pleisto. alluvial fan	500 m	77–140 ka	4±2	Klinger *et al.,* 1999
Offsets in drainage basins and alluvial fans	15 km	Late Pliocene or early Pleistocene	3–7.5	Ginat *et al.,* 1998
Slumps in Lisan deposits			6.4	El-Isa *et al.,* 1986
Offset alluvial fans		18-70 kyr	10	Galli 1999
Offset alluvial fans	3 km	0.3–0.6 Ma	5–10	Garfunkel *et al.,* 1981
Offset alluvial fans	150 m	20–23 ka	7.5	Zak and Freund., 1966

Table I-2: Geologic, geomorphologic, seismologic and paleoseismologic estimation of lateral slip rates along the different segments of the Dead Sea transform fault system.

I.4.1.2 Short term deformation (GPS)

Recently, many geodetic studies have been carried out to determine the slip rate on the different segments of the Dead Sea Fault. Table I.3 summarizes the slip rate values for the Dead Sea Fault and its segments as estimated by different studies. Figure I.6 and Figure I.7 present the horizontal GPS velocity field with reference to the Eurasia fixed and Arabia fixed, respectively. The GPS data presented in these figures are from Reilinger *et al.,* 2006, Gomez *et al.,* 2007, Le Béon *et al.,* 2008, Alchalbi *et al.,* 2010 and Al-Tarazi *et al.,* 2011.

A left-lateral slip rate value of the movement along the DSF was given by McClusky et al., (2003). He used continuously recording GPS (CGPS) carried out between 1992 and 2002 and survey-mode GPS (SGPS) observations. He concluded that the motion in the Gulf of Aqaba and on the Dead Sea fault (DSF) grades from pure left lateral strike-slip in the Gulf and on the southern DSF with increasing compression on the central and northern DSF with relative motion from 5.6 to 7.5±1 mm/yr from south to north. Using measurements between 1988 and 2005, Reilinger *et al.,* (2006) proposed a smaller rate for the relative motion of the DSF (4.5-4.8 ±1 mm/yr) with difference of 1-3 mm/yr from McClusky *et al.,* (2003). This difference can be related with the block model or to the number of GPS sites used these studies. McClusky *et al.,* (2003) used an oversimplified plate boundary model (only major plates) to investigate deformation within the plate boundary zones, while Reilinger *et al.,* (2006) used a kinematic block model, including elastic strain accumulation on block bounding faults, where he include beside the major plates other possible micro blocks and especially in the eastern Mediterranean region.

Fault segment	locking depth (km)	Slip rate mm/yr	Authors
DSF (general)		4.5 – 4.8±1	Reilinger *et al.*, 2006
		5.6 – 7.5±1	McClusky *et al.*, 2003
Missyaf & Al-Ghab	5-16 km	1.8-3.3	Alchalbi *et al.*, 2010
	15 km	4.2±0.3	Gomez *et al.*, 2007
		4.8±0.3	Reilinger *et al.*, 2006
	13 km	4.7±0.4	Mahmoud *et al.*, 2005
Yammuneh	15 km	3.9±0.3	Gomez *et al.*, 2007
		3.5±0.4	Reilinger *et al.*, 2006
	13 km	3.4±0.4	Mahmoud *et al.*, 2005
Serghaya		1.7 - 2.8	Wdowinski *et al.*, 2004
South DSF		3.7±0.4	Wdowinski *et al.*, 2004
South DSF		4.5 – 4.7±0.2	ArRajehi *et al.*, 2010
Hula Basin	15 km	3.0±0.3	Gomez *et al.*, 2007
Jordan valley	15 km	4.0±0.3	Gomez *et al.*, 2007
		4.4±0.3	Reilinger *et al.*, 2006
	12 km	3.7±0.4	Wdowinski *et al.*, 2004
	13 km	4.3±0.3	Mahmoud *et al.*, 2005
	8±5 km	4.7±0.4	Al-Tarazi *et al.*, 2011
Wadi Araba	~12 km	4.9±1.4	Le Beon *et al.*, 2008
		4.5±0.3	Reilinger *et al.*, 2006
	13 km	4.4±0.3	Mahmoud *et al.*, 2005
	~15 km	2.6±1.1	Pe'eri *et al.*, 2002
	15±5 km	4.9±0.4	Al-Tarazi *et al.*, 2011
	~ 8.0	~ 4.0	Masson *et al.*, (2012)

Table I-3: Geodetic (GPS) estimates of lateral slip rates along the Dead Sea transform fault system.

Others geodetic studies give a left-lateral slip rate along different segments of the Dead Sea Fault: Le Béon *et al.*, (2008) obtained a velocity of 4.9±1.4 mm/yr with locking depth of ~12 km on the Wadi Araba segment. This value is in agreement with Mahmoud *et al.*, (2005) and Reilinger *et al.*, (2006) and ArRajehi *et al.*, (2010) but contradicts with Pe'eri *et al.*, (2002) who find out 2.6±0.3 mm/yr slip rate of this segment for a ~15 km locking depth using three years of continuous GPS measurements of only 3 sites, two of them are very close the DSF. Recently, Masson *et al.*, 2012 used GPS data from three campaigns over 12 years and he obtained ~4 mm/yr of slip rate and ~8 km of locking depth.

The slip rate for the Jordan Valley is 3.7 to 4.7±0.4 mm/yr left-lateral slip rate with 8.0 – 15 km locking depth (Wdowinski *et al.*, 2004; Mahmoud *et al.*, 2005; Reilinger *et al.*, 2006;

Gomez *et al.*, 2007a; Al-Tarazi *et al.*, 2011). Gomez *et al.,* (2007a) find a 3.9±0.3 mm/yr and 3±0.3 mm/yr for the Yammuneh segment and along the Hula Basin, respectively. Reilinger *et al.,* (2006) propose 3.5 – 3.9 mm/yr for the same segment. Gomez *et al.,* (2007), Mahmoud *et al.,* (2005) and Reilinger *et al.,* (2006) give a slip rate of 4.2-4.8 mm/yr for the Missyaf and Al Ghab segments while Alchalbi *et al.,* (2010) gives a relatively lower value of 1.8-3.3 mm/yr left-lateral slip rate which varies with the suggested locking depth ranging between 5 and 15 km.

In Figures I.6 and I.7, we plot the GPS velocity fields from different studies which were carried out in the eastern Mediterranean (Reilinger *et al.*, 2006; Le Béon *et al.*, 2008; Alchalbi *et al.*, 2010; Al-Tarazi *et al.*, 2011) in Eurasia and Arabian reference frames, respectively. These solutions were combined together by applying a rotational transformation to each of them to have the best fit with the solution of Reilinger at al., (2006).

Following (Savage and Burford, 1973), using 1-D elastic dislocation model of a locked fault and assuming an infinitely long strike-slip fault and expresses the station velocity, b, as a function of the long-term slip rate (V), fault locking depth (D) and distance from the fault (x):

$$b = (V/\pi)\arctan(x/D) \qquad\qquad\qquad (1.1)$$

We plot the GPS velocity parallel to the Dead Sea fault (Figure I.8) in its different parts from north to south using the data shown in the Figure I.7 and along the profiles in the same figure. Velocity is varying from a rate of about 4.5 mm/yr along the southern and central segments to a rate of about 2 mm/yr along the northern segment (north of 35 ° N). Moreover all the profiles across the central or north fault (Figure I.7) do not have a density of points and/or measurement accuracy sufficient to allow unambiguous determination of the locking depth of the fault. A locking depth of 11±9 km is proposed along the southernmost segment (Le Béon *et al.,* 2008) while this looking depth is very difficult to estimate along the northernmost segment (Alchalbi *et al.,* 2010).
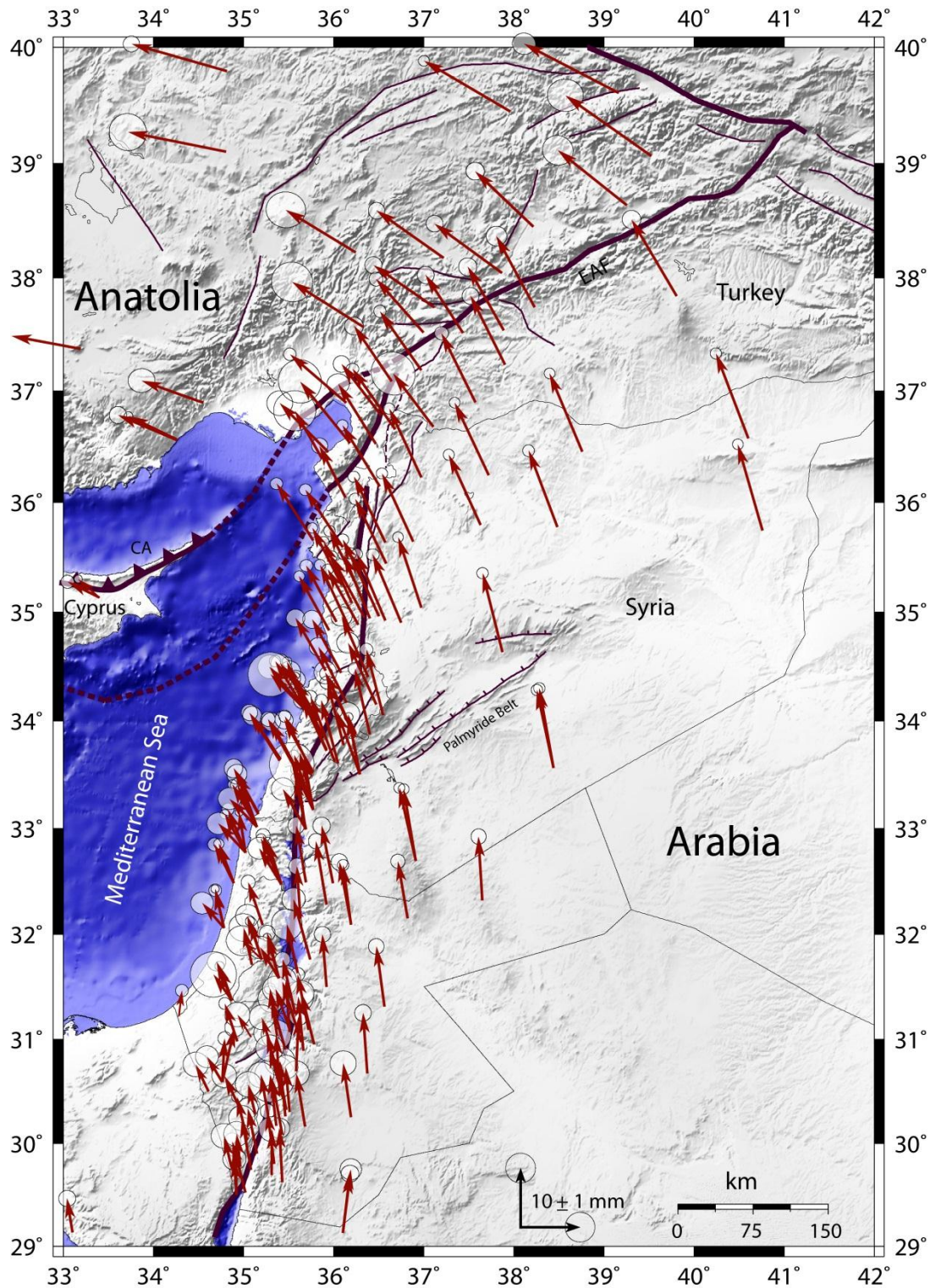
Figure I.6: GPS Horizontal velocity field and the 95% confidence ellipses obtained by previous campaigns in the Eastern Mediterranean region with respect to the Eurasia-fixe reference frame. GPS data are from Reilinger et al., 2006, Gomez et al., 2007 and Le Béon et al., 2008. Mapped faults are from Meghraoui et al., 2011. Also shown in the map are the three major faults in the region, EAF: East Anatolian fault, DSF: Dead Sea fault, CA: Cyprus arc.
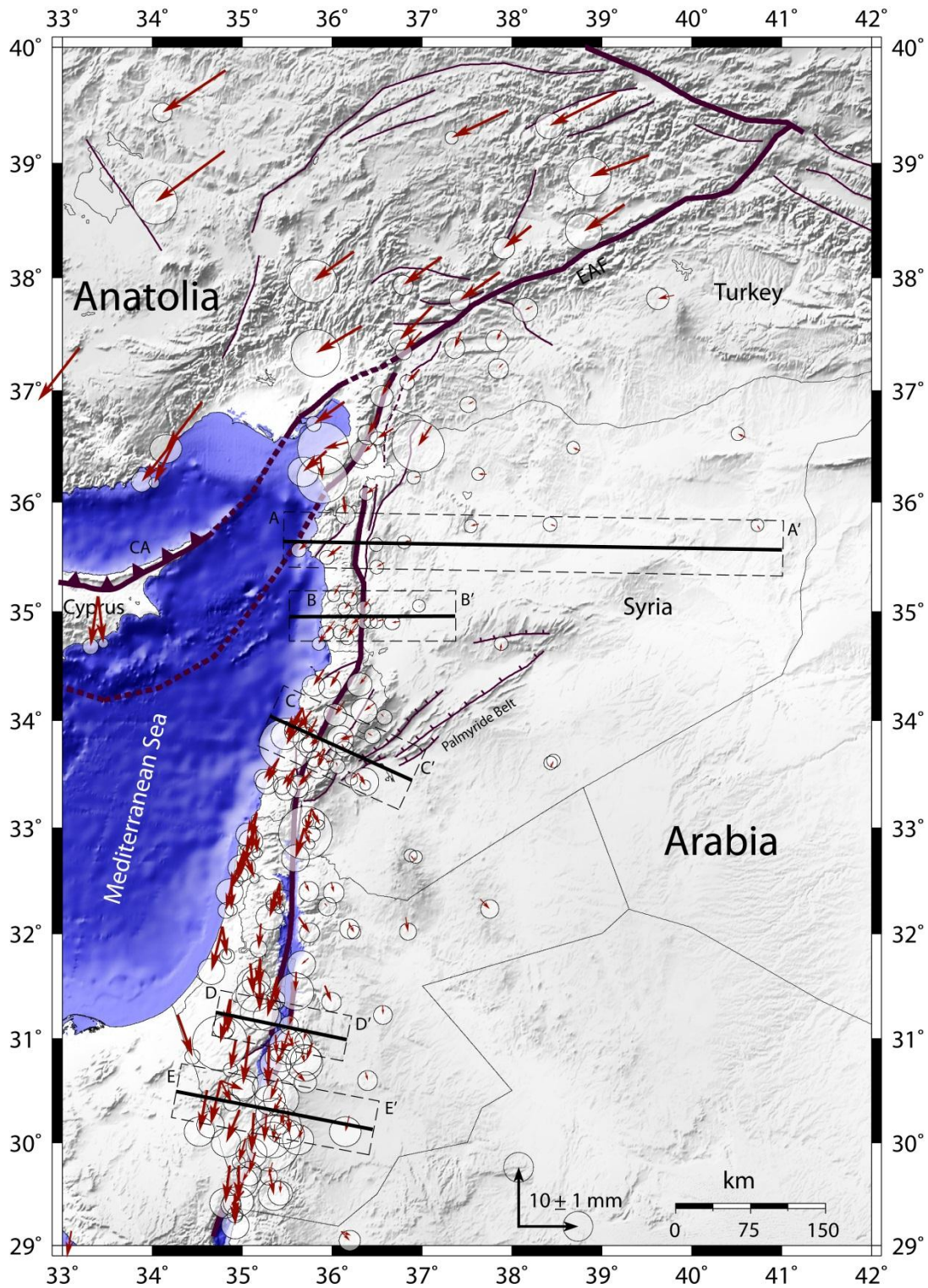
Figure I.7: GPS Horizontal velocity field and the 95% confidence ellipses obtained by previous campaigns in the Eastern Mediterranean region with respect to the Arabia-fixe reference frame. GPS data are from Reilinger et al., 2006, Gomez et al., 2007 and Le Béon et al., 2008., and mapped faults from Meghraoui et al., 2011. Boxes denote the swath encompassed by the profiles shown in Figure I.8. Also shown in the map are the three major faults in the region, EAF: East Anatolian fault, DSF: Dead Sea fault, CA: Cyprus arc.
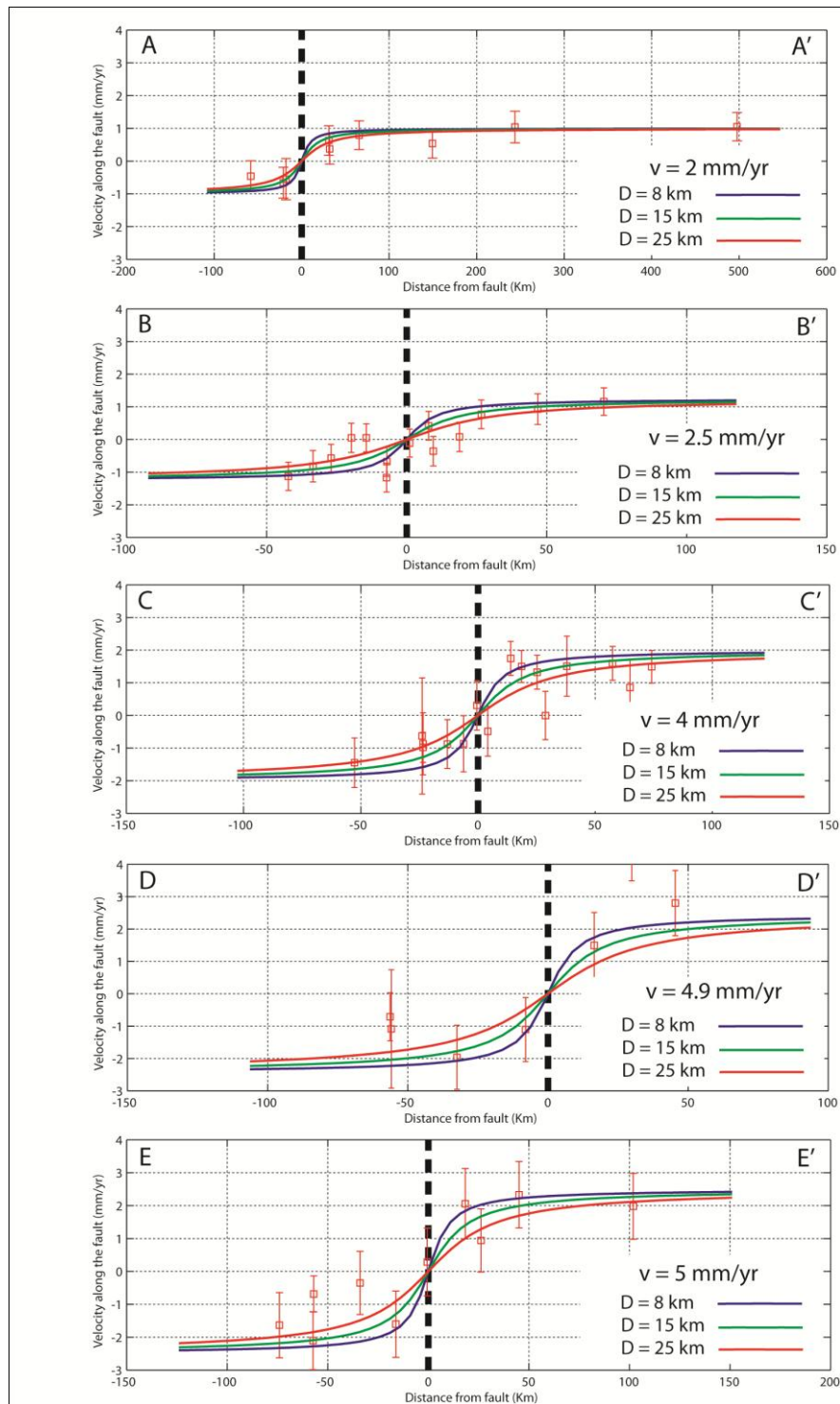
Figure I.8: Plots showing the GPS velocity parallel to the Dead Sea fault in its different parts from north to south. Data are from Reilinger et al., 2006, Gomez et al., 2007 and Le Beon et al., 2008. The position of GPS points is shown relative to the Dead Sea fault which is presented as a dashed line. The plots show the predicted parallel velocities V for different elastic dislocation models (different values of slip rate and locking depth) along the fault and the decreasing of slip rate toward the north. The horizontal axe shows the distance from the fault while the vertical axe shows the velocity parallel to the fault.

I.5   *Conclusion*

In this first chapter we presented the Dead Sea fault system and its geological, seismological and geodetic characteristics. We gave brief tectonic description on the different segments of the fault (Wadi Araba, Jordan Valley, Lebanese restraining bend, Al-Ghab Basin and Karasu Valley) We also show that the DSF can be divided into 2 main sections, north and south, that differ from each other by the geometry, the slip rate, the accumulated total motion and seismic activity. Then we present the seismicity (historical and instrumental) along the Dead Sea Fault, and explain that, nowadays, the DSF is showing a low level seismicity rate in comparison with the historical seismic catalogues, at least on its middle and northern parts. In consequence, and looking to the rich seismicity catalogue and previous seismotectonic studies (Salamon *et al.*, 2003; Sbeinati *et al.*, 2005; Ambraseys, 2009b), we may conclude that the Dead Sea Fault is able to generate a large seismic event with magnitude greater than 7 similar to 859A.D, 1157AD, 1170AD and 1408AD events (Figure I.3). We also present the geodynamics of the Dead Sea Fault in the context of the eastern Mediterranean geodynamic evolution which is constrained by the relative motion between three major Eurasia, Africa and Arabia plates,. The movement of these plates is localized at their boundaries, with the Dead Sea Fault accommodating the relative motion between the Arabia and Africa plate, the Arabia plate moving 20 mm/yr NNW while the African plate moves 10 mm/yr toward Eurasia (Figure I.2).

We review in this chapter the most recent studies held on to determine the slip rate along the Dead Sea Fault, the long term and the short term deformation. We also show that the fault is slipping with different rates along its different segments. The average slip rate deduced from geologic, geomorphologic, seismologic, and paleoseismologic studies is, in general, slightly greater than the geodetic slip rate. A 2-3 mm/yr difference is more important in the northern part where the DSF connects the triple junction area (studied region) and divides into several small branches in NW Syria and SE Turkey. The geodetic slip rate is clearly slower in the north than the southern fault zone (Figure I.8).

The understanding of deformations and strain accumulation in the northern part of the Dead Sea fault and its small segments, beside the determination of slip rate and deformation along the southwestern part of the East Anatolian Fault lead us to constrain the active

tectonics at the junction area between the Arabia, Africa and Eurasia plates, which can be considered as one of the most complicated triple points junctions.

Chapter II

II- The East Anatolian Fault

II.1   Introduction

The neotectonic system of Turkey is largely controlled by the ongoing northward motions of the Africa and Arabia with respect to Eurasia plate. These motions began in the Middle-Late Miocene and resulted in the westward extrusion of the Anatolian block along the North and East Anatolian faults (McKenzie, 1972; Dewey and Sengor, 1979; Sengor and Yilmaz, 1981; Jackson and McKenzie, 1988). The EAF starts at the Karliova triple junction and extends to the southwest for about 600 km (Figure II.1) until it connects another triple junction at the Amik basin, near Antakya (Over *et al.*, 2004).

The North-West movement of the Arabia plate with rate of ~20 mm/yr results in ~10 mm/yr of left lateral strike-slip along the East Anatolian fault (Reilinger *et al.*, 1997b; McClusky *et al.*, 2000; Reilinger *et al.*, 2006). This major fault consists of several local parallel and sub-parallel, left-lateral strike-slip faults with normal and reverse components.

II.2   Tectonic settings of the East Anatolian Fault

II.2.1 General View

The East Anatolian Fault (EAF) is a ~600 km long, and NE-SW trending left-lateral strike-slip fault that forms the northern border of the Arabian plate with the Anatolian plate (Saroglu *et al.*, 1992; Bozkurt, 2001; Westaway, 2003). It contributes to the westward movement of the Anatolian plate which is translated into sinistral strike-slip on the East Anatolian Fault and dextral strike-slip along the North Anatolian Fault (NAF). The EAF extends from Karliova (41°E) where it joins and forms a triple junction with the North Anatolian Fault to Turkoglu in the north of Amik Basin (37°E), where it joins the Dead Sea Fault and form a triple junction (Arpat and Saroglu, 1972; Muehlberger and Gordon, 1987; Perincek and Semen, 1990; Lyberis *et al.*, 1992; Chorowicz *et al.*, 1994; Westaway and Arger, 1996).

The EAF was mapped for the first time by Arpat and Saroglu (1972). Allen, (1969) was the first who described the complex structure of the East Anatolian Fault. The EAF consists of a series of strike-slip fault segments acting as a transform fault, and others segments oblique to movement of the plate (Arpat and Saroglu, 1972; Hempton, 1987; Westaway, 1994; Bozkurt, 2001). Although the sinistral movement governs the entire East

Anatolian Fault, it has significant exceptions of reverse component (Arpat and Saroglu, 1972; Dewey *et al.*, 1986; Muehlberger and Gordon, 1987; Perincek and Semen, 1990; Taymaz *et al.*, 1991b; Lyberis *et al.*, 1992).

In addition, Muehlberger and Gordon (1987) suggests that the EAF does not move as a single sinister unit, but rather as separate segments, each segment slips differently. Therefore, he proposes from deformation point of view that the EAF consists in two principal zones: (1) a zone involved in a NS-oriented compression acting as restraining bend corresponds to the segments 2 and 4 colored in red and (2) a set of quasi-linear strike-slip faults corresponds to the segments 1, 3, and 5 (Figure II.1).
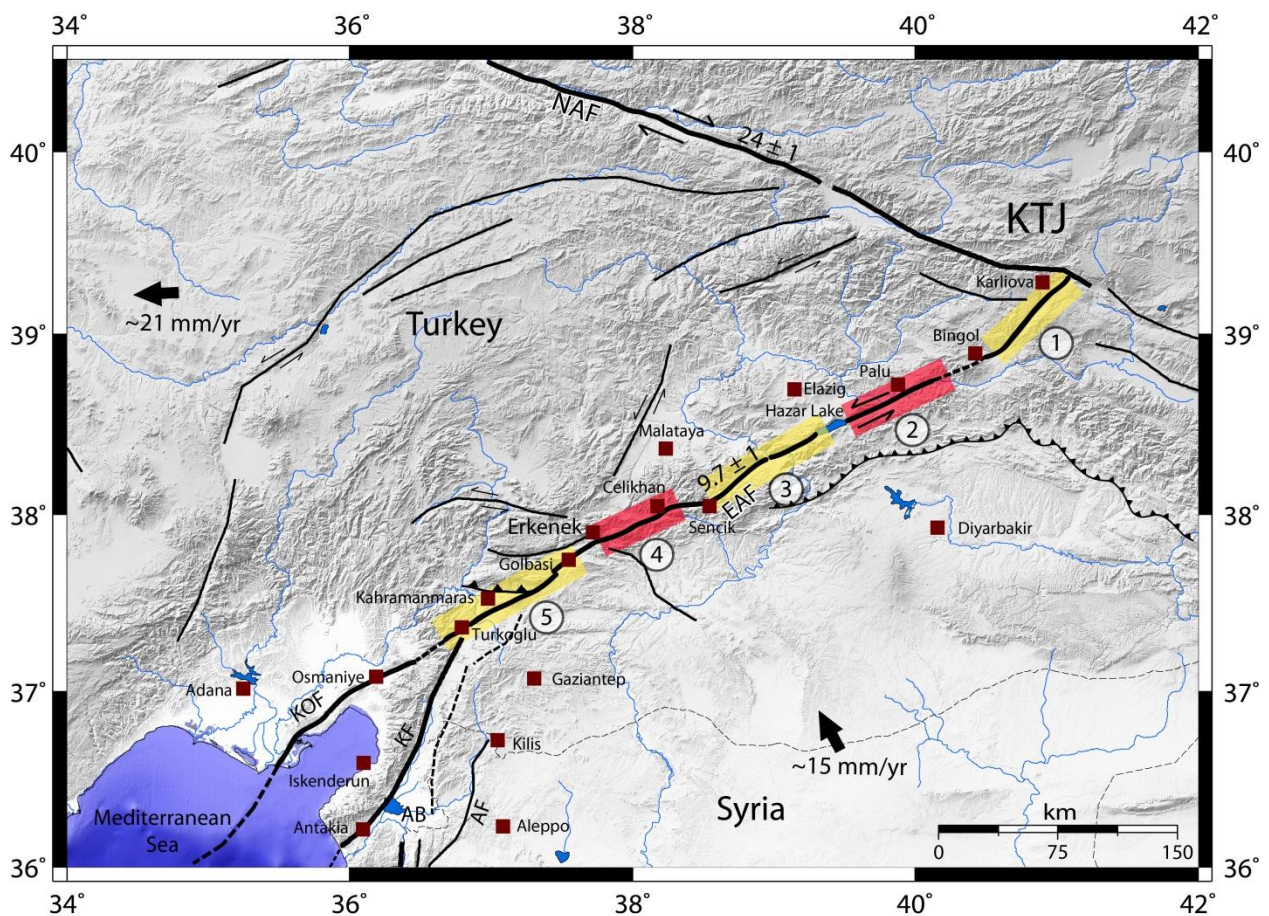
Figure II.1: The East Anatolian fault segments, fault mapping and slip rates from (Westaway, 2003; Meghraoui et al., 2011). Abbreviations for some key tectonic features: AF: Afrin fault, AB: Amik basin, KF: Karasu fault, KOF: Karatas-Osmaniye fault, EAF: East Anatolian fault. Thick black arrows show the plates convergence Directions. Plate movement rates are from McClusky et at., (2003); Reilinger et al., (2006).

In contrast with the Dead Sea Fault which is relatively well known, the age of the East Anatolian fault is still a subject of debate. The EAF initiation was proposed by many studies and can be summarized in 4 main periods.

1- The EAF start to initiate between the late Miocene and early Pliocene (Arpat and Saroglu, 1972; Dewey *et al.*, 1986; Hempton, 1987; Perincek and Semen, 1990; Lyberis *et al.*, 1992), After the opening of Gulf of Suez and when the movement of Arabia relative to Africa began to take place along the Dead Sea Fault (Lyberis, 1988; Steckler *et al.*, 1998).

2- Saroglu *et al.*, (1992) advocates that the EAF started to be active in the late Pliocene, based on maximum offset of 20-25 km of lithological contacts and morphologic features.

3- The third idea is that the EAF started to be formed since ~2 Ma ago (Yurur and Chorowicz, 1998). This suggestion was based on the assumption of a total displacement of 15 km on the fault plane based on structural data (Herece and Akay, 1992) and a slip rate of 7.8 mm/yr.

4- Others propose that the EAF became active about 3 Ma ago when the Malatya-Ovacik fault zone was initiated (Westaway and Arger, 1996; Westaway, 2003).

II.2.2   East Anatolian Fault segments

At a large scale, the East Anatolian Fault consist of five main segments (Saroglu *et al.*, 1992) clearly identified on satellite images or from tectonic morphology (Figure II.1). According to Saroglu *et al.*, (1992), these segments are delimited by pull-apart basins (e.g. Golbasi and Lake Hazar basin), high mountains, or by steps to the left or right, and changes in the fault direction (Hempton, 1985; Hempton, 1987; Westaway and Arger, 1996). Other authors consider the Karatas-Osmaniye Fault (KOF) as a sixth segment of the EAF which is indeed a continuation of it to the west (Hempton, 1987; Perincek and Semen, 1990; Taymaz *et al.*, 1991b; Westaway, 1994; Westaway and Arger, 1996; Arger *et al.*, 2000; Yurtmen *et al.*, 2000; Aksoy *et al.*, 2007). Based on fault geometry and seismic activity, Barka and Kadinsky-Cade (1988) suggested that there may be 14 different segments along the EAF. In the next paragraphs we present the five main segments as identified by Saroglu *et al.*, (1992).

- ***Karliova - Bingol***

This segment begins at the triple junction of Karliova between EAF and NAF at an angle of 50° (Saroglu and Yilmaz, 1990). About 65 km in length with a strike of N50°E, it can be easily traced continuously to the east of Bingol (Figure II.1). The surface morphology is very clear and shows many examples of offsets in rivers and streams. The largest observed shift on this segment is 17 km (Saroglu *et al.*, 1992). This segment is characterized by high seismicity, including the events of May 22, 1971 (MW 6.8) and 1 May 2003 (MW 6.4).

- ***Palu - Lake Hazar***

This segment extends for approximately 50 km and oriented N60°E, from the city of Palu to Lake Hazar which was considered as pull-apart basin by (Hempton *et al.*, 1983). Indeed, the faults in the east and the west of the lake act as left-lateral faults (Aksoy *et al.*, 2007). In this context, it is logical that the fault west of the lake shows movements in normal fault. Sinistral offsets of Pleistocene limestone are observed along this segment. The valley along the River Murat is controlled by the East Anatolian Fault where the Quaternary terraces are deformed and cut by the fault.

- ***Lake Hazar - Sincik***

This segment has 85 km of length and width of 100 m to 2 km, oriented N65°N (Saroglu *et al.*, 1992). This fault segment can be traced easily at its eastern extension along the west and east banks of the Lake Hazar but no data are available for its possible extension under the lake. At many sites, the fault shows typical characteristics of a transform fault, such as mirrors or fault basins. The Euphrates shows about 14 km of offset southwest of the lake.

- ***Celikhan - Erkenek***

This segment has a length of 45 km and trend of N67°E, where the main fault is divided into sub-segments of length between 2 and 17 km and arranged in dextral structures. The Sürgü Fault (SF), a sinister structure also, joins the main fault segment of EAF near to Celikhan with an angle of 30° (Saroglu *et al.*, 1992) where Quaternary deposits are observed. The East Anatolian Fault is defined in this region by two parallel branches of ~17 km of length, separated by 200 to 500 m. The relief shows that the southern branch is younger and it has approximately 600 m of shifting from the northern branch. Many Earthquakes occurred in the 20th century along this segment like the 14 June 1964 earthquake (MS 5.7, epicenter near

Malatya), May 5 and June 6, 1986 (MS 5.9 and 5.6) on the Sürgü fault. The focal mechanism of the earthquake of 1964 shows a normal fault mechanism with a nearly vertical plane (Jackson and McKenzie, 1984). No surface trace was observed after the earthquakes of 1964 and 1986, whose epicenter was quite far from the EAF.

- ***Golbasi - Turkoglu***

This segment extends for 90 km in N55°E direction, from the pull-apart basin of Golbasi to the Turkoglu city located at the intersection between the EAF and the DSF forming the triple junction with the Karatas-Osmaniye Fault (KOF) (Figure II.1). This segment shows an obvious sinistral movement along its entire length. The Goksu River shifting of 13 km is an example of this movement, beside others sinistral offsets of three rivers of 3.5 km to 4 km in the region reported by Saroglu *et al.*, (1992). Despite this evidence of sinistral movement, the authors did not report any destructive earthquakes along this segment. However, based on historical seismicity catalogs, an event can be clearly correlated with this segment of the EAF, the event of November 29, 1114 (MS> 7.8) (Ambraseys and Jackson, 1998; Sbeinati *et al.*, 2005; Ambraseys, 2009a).

II.2.3   The total offset

The total displacement of the East Anatolian Fault stills a subject of discussion among the scientists. The cumulative offset of the Euphrates suggests $3.5 - 13$ km total sinistral displacement while $15 - 27$ km total offset was proposed from offset Early-Pliocene rocks (Arpat and Saroglu, 1972; Hempton, 1985; Hempton, 1987; Saroglu *et al.*, 1992). Bozkurt (2001) notes that the Euphrates river banks are younger than the age of the fault proposed in the literature. Based on similar reasoning, a total shift of 35 - 40 km has been proposed by Westaway and Arger, (1996).

II.3   Seismicity of the East Anatolian Fault

Unlike the North Anatolian fault which has accommodated 11 major earthquakes since 1939, the East Anatolian fault produced relatively unimportant earthquakes during the last century compared to its historical activity. Several seismic events with ($7 \leq M \leq 7.8$) and has therefore accumulated significant strain along its length. Thus, the EAF has been the site of several destructive historical earthquakes (Arpat and Saroglu, 1972; Ambraseys and Jackson, 1998; Sbeinati *et al.*, 2005; Ambraseys, 2009b). The effects and damage of these events were

recorded in many historical documents. The last earthquakes of magnitude more than 6 have occurred in the beginning of 20th century, near to Malatya in 1905 and 1971, 1975 and 2003 near the city of Bingöl (Arpat and Saroglu, 1972; Ambraseys and Barazangi, 1989; Taymaz *et al.*, 1991b).

II.3.1 Historical seismicity

Many destructive earthquakes of magnitude greater than M 7 occurred along the East Anatolian Fault during the historical period (Figure II.2). In the same way as the Dead Sea Fault, major earthquakes have been studied using historical documents and recordings (Ambraseys and Barazangi, 1989; Ambraseys *et al.*, 1994; Westaway, 1994; Ambraseys and White, 1997), which served in the preparation of catalogs of earthquake parameters. The majority of these earthquakes that destroyed many towns and castles is associated with sinistral surface ruptures (Arpat and Saroglu, 1972). According to the catalogs of historical seismicity, the most important event took place on November 29, 1114 (MS> 7.8) near Kahramanmaras and is associated with the Turkoglu − Golbasi segment (Ambraseys and Jackson, 1998; Sbeinati *et al.*, 2005; Ambraseys, 2009a).

The event of August 13, 1822 AD (M 7.4) was the largest earthquake occurred at the junction of the DSF and EAF during the last five centuries. The region between Gaziantep and Antakya in Turkey and Aleppo and Han Sheikhun in northwestern Syria was almost entirely destroyed by this earthquake. It was felt from the coast of Black Sea to Gaza and it was followed by long aftershock sequence. The EAF has produced another destructive earthquake in March 02 1893AD south of Malatya. This event has evidences over an area of 220 km long and 120 km wide and caused a huge loss of lives. The M = 7.1 which took place near the Hazar Lake have destroyed most of the villages around the lake and also caused a lot of life loss. The examples of the high historical seismic activity of the EAF are numerous, like the events of November 22 1685 (M 6.7) and May 12 1866 (M 7.2) in the eastern segment of EAF, the event of 29 May 1789 (7.0<M<7.8) near to Palu, March 27 1875 (M 6.7) southwest of Hazar lake and the 1513 event (M ~7.4) south-east of Turkoglu along the KOF (Ambraseys, 2009b).

In Figure II.2 we show most of the earthquakes with Ms ≥ 6.5 along and near the EAF from Ambraseys (Ambraseys, 2009b) in red squares, the events referred in colored ellipses are from other studies (Arpat and Saroglu, 1972; Barka and Kadinsky-Cade, 1988; Ambraseys

and Barazangi, 1989; Ambraseys and Jackson, 1998; Sbeinati *et al.*, 2005; Ambraseys, 2009a).
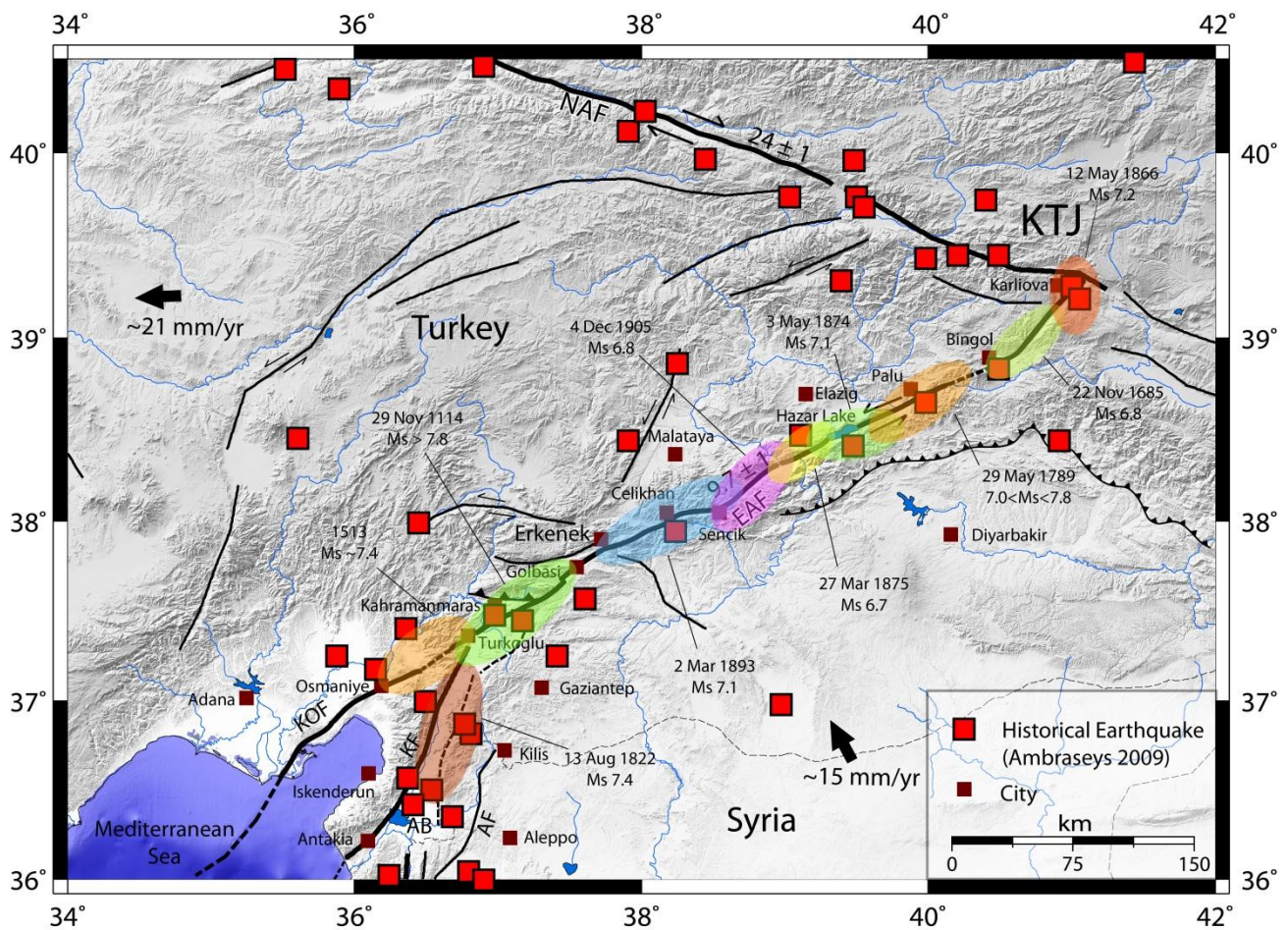

Figure II.2: Distribution of earthquakes along and around the East Anatolian Fault before 1900 for which historical data allowed the assessment of magnitude Ms ≥ 6.5. Mapped faults from Meghraoui et al., (2011). Historical earthquakes from Ambraseys (2009b) are in red squares. Other events referred in colored ellipses are from other studies (Arpat and Saroglu, 1972; Barka and Kadinsky-Cade, 1988; Ambraseys and Barazangi, 1989; Ambraseys and Jackson, 1998; Ambraseys, 2009a). Thick black arrows show the plates convergence Directions.

According to the study of Nalbant et al., (2002), who calculated the evolution of Coulomb stress along the EAF due to seismic and tectonic loads since the 1822 event, which took place on the Karasu Fault, the Turkoglu – Golbasi segment is an area of particularly high seismic hazard, corresponding to an excess of local Coulomb stress of about 20 bars. The second area of hazard they identify is between Lake Hazar and the region of Bingöl (Figure II.1). In addition, the area of seismic gap between Turkoglu and Golbasi is clearly visible on the map of instrumental seismicity in Figure II.3.

II.3.2   *Instrumental Seismicity*

The seismic activity recorded along the East Anatolian Fault is relatively large. Most of the events have magnitudes between 4 and 5 (Figure II.3). During the last decades, this region has produced many major earthquakes, causing loss of life and extensive damage. Some earthquakes of magnitude greater than 6 are identified near the triple junction of Karliova and greater than 5 in the west end of the EAF.
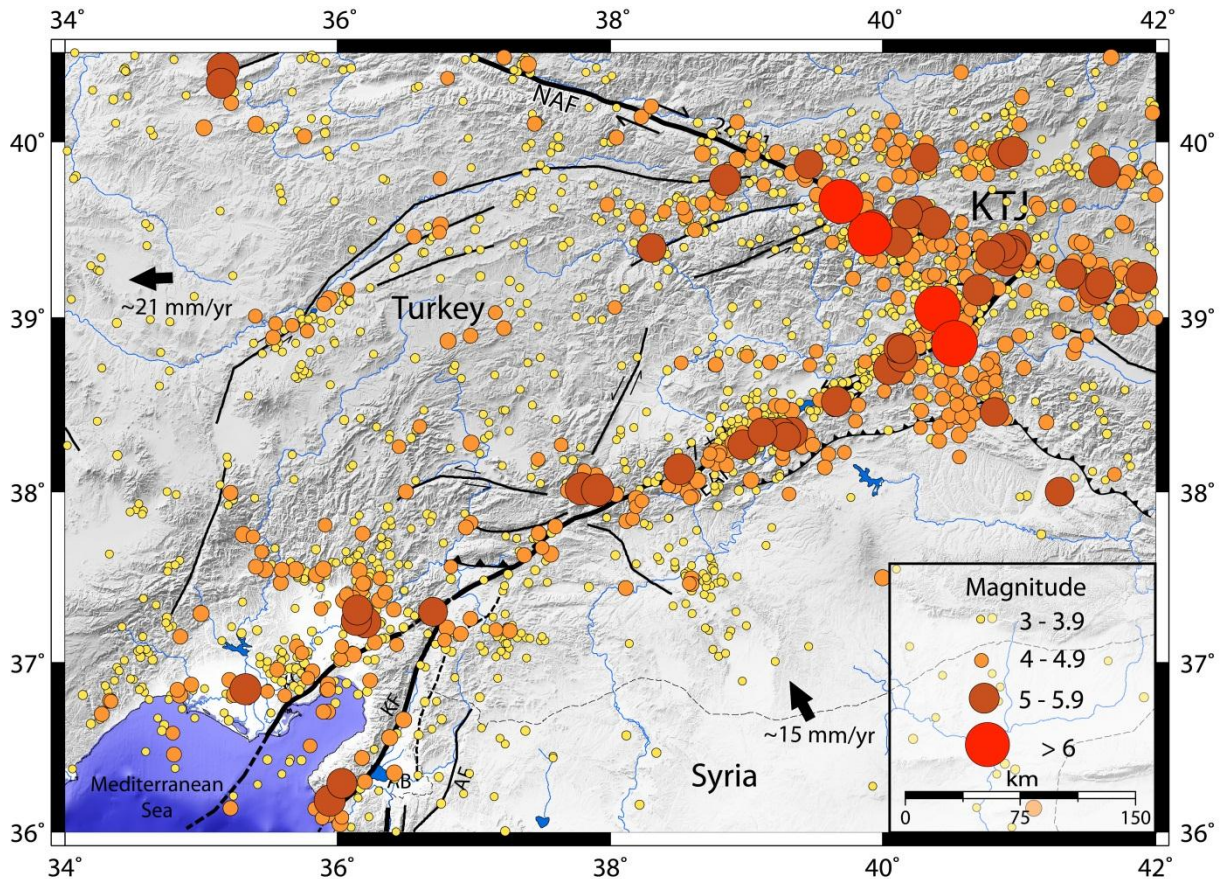
Figure II.3: Instrumental seismicity of the East Anatolian fault between 1964 and 2011, M>3. Data are from: IRIS (Incorporated Research Institutions for Seismology, http://www.iris.edu/hq/), ISC (The International Seismological Center, http://www.isc.ac.uk/) and NEIC (The National Earthquake Information Center, http://earthquake.usgs.gov/regional/neic/). Mapped faults from Meghraoui et al., (2011) and Saroglu et at., (1992). KTJ: Karkiova Triple Junction.

Figure II.3 shows the different instrumental earthquakes (M> 3) recorded along the EAF from 1964 to the present day, with an important seismic activity around Karliova (junction with NAF) and close to the junction with the convergence system of the eastern Mediterranean. Figure II.4 shows the focal mechanisms of earthquakes with magnitude greater than 4.5 occurred from 1964 to the present day along the EAF.

The presence and intersection between two major strike-slip faults, the EAF and the NAF, is the cause of the regular occurrence of destructive earthquakes in the region around Karliova and Bingöl (Figure II.3). Indeed, in this region there are many active faults, working together in dextral and sinistral way, oriented NW-SE and NE-SW respectively. Thus, the two most recent major events that have affected the eastern segment of the EAF took place near its junction with the NAF, particularly near the city of Bingöl (Arpat and Saroglu, 1972; Ambraseys and Barazangi, 1989; Taymaz *et al.*, 1991b). The first took placed on May 22, 1971 (MW 6.8) and the second on 1 May 2003 (MW 6.4) (Figure II.4). Both mechanisms are purely left-lateral strike-slip (Figure II.4). The event of May 22, 1971 with an epicenter located about 10 km south of Bingöl city center was the largest instrumental earthquake recorded on the EAF. The fault responsible for this earthquake is the eastern segment of the EAF. Its epicenter is close to that one of 1 May 2003, which is located about 14 km NNW of Bingöl (Eyidogan *et al.*, 1991; Kalafat *et al.*, 2000). After the earthquake of 1971, surface ruptures of about 60 km oriented NW-SE were observed in southeast of Bingöl. On a map of macroseismic earthquake, the region of maximum damage coincides with the EAF (Seymen and Aydin, 1972). The earthquake of 2003 caused many deformations in the soil, surface ruptures, subsidence and landslides.
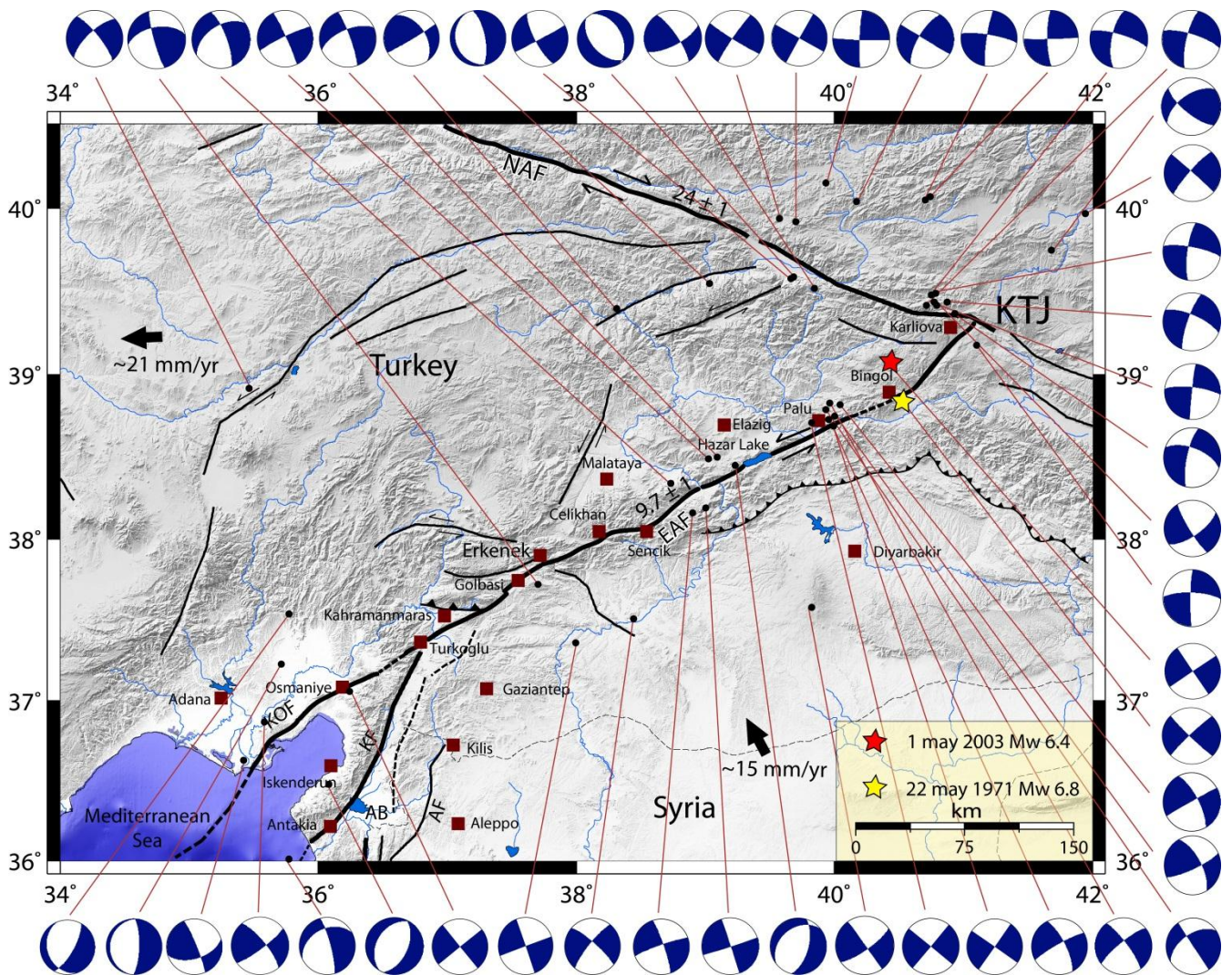
Figure II.4: Focal mechanism of earthquakes between 1976 and 2011 along the East Anatolian Fault, of magnitude greater than 4.5. Data are from catalogues Harvard CMT. Mapped faults from Meghraoui et al., (2011). Red and yellow stars refer to the Mw=6.4 of 1 may 2003 and the Mw=6.8 of 22 may 1971 respectively. The focal mechanism of 22 may 1971(Mw=6.8) is from Taymaz et al., (1991a).

II.4   Kinematic of the East Anatolian Fault

The slip rate of the EAF was determined using several methods, including geodetic, geological, geomorphological, and seismic surveying. The results obtained are summarized in Table II.1. The slip-rate values vary from 4 to 29 mm/yr. These values depend on the time scale of observations and the considered fault segment. The most credible average slip rate value for the EAF is around 10 mm/year, which come from geodetic measurements (Reilinger et al., 2006; McClusky et al., 2000)

II.4.1 Long term deformations

Westaway (2003) estimates a slip-rate of 4 mm/yr over the segment Turkoglu-Golbasi based on an offset of 16 km estimated to be 4 Ma. Westaway and Arger (1996) found that three rivers in southwestern Golbasi are shifted sinisterly by Turkoglu-Golbasi segment for about 3.5 to 4 km in period of 0.86 Ma, which give a slip-rate of 4-4.5 mm/yr along this segment.

Fault segment	Methode	Slip rate mm/yr	Age of datum	Authors
East Anatolian Fault				Arpat et Saroglu, 1972 Dewey *et al.*, 1986
	Geology	6 - 10	4 - 5 Ma	
Golbasi-Turkoglu		~4	4 Ma	Westaway, 2003
Golbasi-Turkoglu		~4.6	0.86 Ma	Westaway et Arger, 1996
East Anatolian Fault		29	35 yrs	Taymaz *et al.*, 1991
East Anatolian Fault	Seismicity	6	207 yrs	Kiratzi, 1993
East Anatolian Fault		9±1	10 yrs	McClusky *et al.*, 2000
East Anatolian Fault		15±3	7 yrs	Reilinger *et al.*, 1997b
East Anatolian Fault		10±1	17 yrs	Reilinger *et al.*, 2006
Karatas-Osmaniye Fault	Geodesy	5.5±1.5	13 yrs	Bertrand *et al.*, 2006
East Anatolian Fault		9.7±0.9	13 yrs	Bertrand *et al.*, 2006
East Anatolian Fault	GPS block model	8.8±0.3	17 yrs	Meghraoui *et al.*, 2011
Karatas-Osmaniye Fault		3.6±0.6	17 yrs	Meghraoui *et al.*, 2011
East Anatolian Fault	Plates reconstruction	19	13 Ma	Lyberis *et al.*, 1992
East Anatolian Fault		7.8 - 9	1.9 Ma	Yürür et Chorowicz, 1998

Table II-1: Estimations of lateral slip rates along the different segments of the East Anatolian fault system from different methods.

The offsets of the Euphrates and the early-Pliocene rocks suggest a total sinistral displacement of 3.5-13 km and 15 to 27 km, respectively (Arpat and Saroglu, 1972; Saroglu *et al.,* 1992). The Euphrates offsets were re-measured in the field by Dewey *et al.*, (1986), the values proposed by them for the offsets were 22 km. The geological slip rate deduced from these offsets was 6 – 10 mm/yr for 4 – 5 Myr.

Studies based on seismicity provide a slip-rate value larger than other methods. Thus, Taymaz *et al.*, (1991a) studied the source parameters of the four largest earthquakes occurred during the last 35 years and obtained a rate about 29 mm/yr with a range of 25-35 mm/yr. Kiratzi, (1993) studied the deformation of the EAF from seismic data covering the period from 1785 to 1992 and he determined an average sinistral slip rate of about 6 mm/yr.

II.4.2 *Short term deformations (GPS)*

Space geodetic studies give a slip rate between 5.5 and 15 mm/yr for the EAF. Reilinger *et al.,* (1997b) propose, from 7 years of observations made between 1988 and 1994, 15±3 mm/yr for the EAF. McClusky *et al.,* (2000) estimations were significantly lower, he estimate 9±1 mm/yr from 10 years of observations made between 1988 and 1997. Finally, Reilinger *et al.,* (2006) estimated the slip rate of EAF at 10±1 mm/yr, using 17 years of measurements between 1988 and 2005. Using the same data, Bertrand (2006) proposed a similar slip rate along the EAF with a value of 9.7±0.9 mm/yr.

A model based on the kinematic plates reconstruction between Arabia, Africa and Anatolia, using the relative motion between the plates and the space geodetic data (movement AF/EU given by DeMets *et al.*, (1990), and movements EU/AN and EU/AR given by Le Pichon *et al.*, (1995), suggests a left lateral slip rate of 7.8 - 9 mm/yr for the EAF (Yurur and Chorowicz, 1998). Similarly, Lyberis *et al.*, (1992) calculated a slip-rate on the EAF using the AN/EU Euler pole given by Jackson and McKenzie (1984), the EU/AF Euler pole given by (Chase, 1978) and the AR/AF Euler pole given by (Le Pichon and Gaulier, 1988), and by considering 80 km of dextral offset along the NAF and 80 km of sinistral movement along the northern section of the Dead Sea Fault and he found a value of 19 mm/yr of sinistral slip rate. Recently, Meghraoui *et al.*, (2011) used the GPS measurements from 1991 to 2004 in Turkey (Reilinger *et al.*, 2006) and 2000 to 2008 in Syria and Lebanon (Alchalbi *et al.*, 2010) for a kinematic modeling of the intersection of the EAF and the DSF and found 8.8±0.3 mm/yr of slip rate along the EAF and 3.6±0.6 mm/yr along Karatas-Osmaniye Fault.

II.5   Conclusions

In this short chapter we highlighted the most important studies about the left-lateral East Anatolian fault in Turkey and discussed its role in the tectonics of the region. The EAF translates the northward movement of Arabian plate toward the Eurasian plate in ~10 mm/yr of pure sinistral slip rate over its length. Sinistral and dextral movements along the EAF and NAF respectively accommodate the deformation resulting from the westward extrusion of the Anatolian plate. The EAF connects between two triple junction areas, the Karliova in the middle east of Turkey where it joins the NAF and the Hatay Triple Junction to the west where it reaches the northern end of the DSF.

We discussed the different theory of the EAF age. Then, we explained its five main segments identified by Saroglu *et al.*, (1992). For each segment we gave brief information about geometry, length, offset and seismicity.

In the other paragraphs we showed the historical and instrumental seismicity along EAF (Figure II.2, Figure II.3). It is very clear that the EAF zone is active on both the historical and instrumental scale. From Figure II.2, we can observe easily the high historical seismicity of the fault. It was the home of many destructive earthquakes during the history over all its segments, especially near to its tow ends where it joins the two triple junctions (e.g. the event of November 29, 1114 (MS> 7.8) near Kahramanmaras which was associated with the segment Turkoglu – Golbasi. The same observation about the high seismicity can be deduced from the Figure II.3 of the recent instrumental event records from 1964 to 2011, during the last five decades, the EAF was able to produce many events relatively large (M>5, e.g., the event of May 2003 Mw = 6.4 near to Bingol) over all its segments except the Golbasi-Turkoglu segment.

Finally, we summarized the slip rate values of EAF determined by different methods. Geological, geomorphological, seismic surveying and geodetic studies were carried on and gave a left lateral slip rate values ranging from 4 to 29 mm/yr. The most credible value is ~10 mm/yr (Reilinger *et al.*, 2006). Comparing with the DSF we notice that the EAF is less studied geologically and geodetically, the raison can be the simple geometry and slip distribution of the EAF where it is more complex for the DSF.

Chapter III

III- GPS network in north-west Syria and south-east Turkey

III.1 Introduction

Global Positioning System (GPS) has become one of the most important tools among the space geodetic techniques during the last 20 years. GPS provides very precise, quick, and accurate estimations of the plate motions and velocities. It was used for the geodynamical studies and active deformations for both the global and the local scales.

The use of GPS measurements is essential in the investigation of active deformation at the Hatay triple junction. The tectonic complexity of the intersection between the three major plates (Arabia, Anatolia, and Africa), and the existence of different geological features including the main and sub faults (DSF, EAF, CA, KF, KOF, AF), require a dense and well distributed GPS network. Most of the previous geodetic measurements in the region were accomplished in the context of GPS studies of the Arabia-Eurasia and Africa-Eurasia convergence, in addition to the large studies of eastern Mediterranean kinematics (McClusky *et al.*, 2000; Reilinger *et al.*, 2006; Alchalbi *et al.*, 2007; ArRajehi *et al.*, 2010). Therefore, these studies were unable to determine in details the active deformation and the strain accumulation along the faults of the Hatay triple junction. The recent short-term estimations of deformation and strain accumulation in this region do not give a definite determination of the slip rates along the faults, which are a matter of debate because of the significant difference between the short-term estimations and the other various time-scale estimations (e.g., geological and geomorphological studies) especially in the northern DSF (Meghraoui *et al.*, 2003).

Therefore, a dense regional GPS network across the Syrian-Turkish border was installed and measured in the context of this study. The main aim of this GPS network is to constrain the active deformation in the Hatay triple junction at a small scale and go into the details of the triple junction kinematics, trying to understand the strain accumulation and distribution along the major and sub faults.

This chapter consists of two main parts. Firstly, we present briefly the GPS system and its advantages in such kinematic studies, and introduce some GPS measurement techniques and basics of the plate kinematics and reference systems, which will be used intensively in the later stages of GPS processing and the interpretation of the results. In the second part we present the GPS network in the Hatay region, north-west Syria and south-east Turkey, and we show the installation, measurements, and processing strategy.

After processing GPS data from our network together with other CGPS sites, we calculate the GPS velocity field around the Hatay triple junction, and then we used them to estimate the Euler poles of plate rotations. The short time span of the GPS measurements causes high uncertainties in the velocity vectors especially in Syria where points are measured during two campaigns only in 2009 and 2010. Nevertheless, these measurements are in general consistent with the previous estimates of slip rate along most of the faults in the region. Details of data processing strategy with "GAMIT/GLOBK" program, error statistics and discussion, GPS velocity field in different reference frames and interpretation in active deformation context are presented in this chapter.

III.2 *Global position system and plate kinematics*

III.2.1 What is GPS

Global positioning system (GPS) is the responsibility of the Joint Program Office (JPO), a component of the Space and Missile Center at El Segundo, California. Early of the 1970th, the US Department of Defense (DOD) ordered to establish, develop, test, acquire, and deploy a space borne positioning system. Since this project was lanced by the US Department of Defense, the primary objectives were military ones, by time it was decided to open this system for a civilian uses. The present navigation system with timing and ranging is the result of this initial directive (Hofmann-Wellenhof *et al.*, 2003).

GPS was designed as a ranging system from known positions of satellites in space to unknown positions on land, at sea, in air, and in space. The main objectives of GPS were the determination of position and velocity instantaneously on continuous basis, and the precise coordination of time.

Every GPS satellite transmits signals centered on two microwaves radio frequencies, L1 and L2. These two waves are produced based on a sine wave with a high accurate frequency $f_0 = 10.23$ MHz grace of a very precise atomic clock. Multiplying this fundamental frequency by integer factors the L1 and L2 carrier waves are generated.

$$f_{L1} = f_0 \times 154 = 1575.42 \ MHz, \text{ with wavelength of } \lambda_{L1} = c/f_{L1} \approx 19 \ cm$$

$$f_{L2} = f_0 \times 120 = 1227.60 \ MHz, \text{ with wavelength of } \lambda_{L2} = c/f_{L2} \approx 24 \ cm$$

Traditional GPS satellites transmit two ranging codes known as coarse acquisition (C/A-code) and precision (P-code). The C/A-code is modulated onto the L1 carrier only, while the P-code is modulated onto both the L1 and the L2 carriers (Hofmann-Wellenhof *et al.*, 1993). The C/A-code resolution (300 m) is 10 times less than the P-code. The determination of range by the military P-code is much more precise than the civilian C/A code (Langley, 1993).

GPS uses pseudoranges derived from the broadcast satellite signal and based on code or carrier phase measurements. In the case of code measurements, the pseudorange is derived from measuring the travel time of the coded signal and multiplying it by its velocity (299,729,458 m/s).

Unfortunately, the clocks of the receiver and the satellite are never perfectly synchronized, a clock error must be taken into account, for this reason, this measurement is referred to as pseudorange rather than range (Langley, 1993). Consequently, each equation of this type contains four unknowns: the three point coordinates contained in the true range and the clock error. Thus, in order to solve for the four unknowns it is necessary to receive signal from four satellites. Indeed, the GPS concept assumes that four or more satellites are in view at any location on earth and in any time in a day for an elevation angle of 15°, the number of available satellites will increase by the decreasing of the elevation angle. Using the carrier phase measurements, the antenna measures only the fractional phase and the integer number (N) of cycles between the antenna of the satellite and the receiver, called ambiguity, still unidentified. Therefore, the ambiguities must be taken into account as additional unknowns. For details of ambiguity resolution see paragraph III.2.5.

III.2.2 GPS segments

III.2.2.1   *Space segment*

The space segment consists of 24 satellites in 6 orbits with an altitude of ~20200 km and a period of approximately 12 hours. The constellation and the satellite number were changed since 1970th for many reasons. In 1986, the number of satellites was 21.The present day constellation is 24 operational satellites and 3 additional active spares, the spare satellites are needed to replace the malfunctioning satellites. The satellites are distributed in 6 orbital planes with an inclination of 55°. Many generations of GPS satellites were lanced in order to modernize the constellation Block IIR-M and Block IIF (Prasad and Ruggieri, 2005). Now, the US Department of Defense is preparing a new generation of GPS satellites called the block III satellites, these satellites are expected to carry GPS into 2030 and beyond (Hofmann-Wellenhof *et al.*, 2008).

III.2.2.2   *Control segment*

The control segment consists of a master control station, monitor stations, and ground antennas. This segment is responsible of the tracking of the satellite for the orbit and clock determination and prediction, time synchronization of satellites, and upload of the navigation data to the satellites. The master control station is located at the consolidated space operations center at Schriever, Colorado Springs, Colorado in US. This station collects the tracking data from the monitor stations and calculates the satellite orbit and clock parameters using Kalman estimator, this data then will be transmitted to the satellite by one of the ground antennas. The

six monitor stations are supplied by a precise atomic time standard and receivers which measure pseudoranges to all available satellites. The measured pseudoranges are smoothed to produce 15 minutes interval data and transmitted to the master control station. The ground antennas are responsible of transmission and receiving data from and to the satellites, this operation is done every 8 hours.

III.2.2.3   User segment

The user segment includes all the military and civilian users equipped with a GPS receiver. The receivers are different according to the observable and the available codes (i.e., C/A-code, P-code). For the majority of GPS applications it is enough to use the C/A-code.

III.2.3 GPS observables

III.2.3.1   The GPS code measurement

The signals emitted by the GPS satellites are modulated by pseudorandom noise (PRN) codes. The PRN codes are random sequences of binary values that give certain identity to every PRN. The codes generated by the GPS satellite are unique, thus, the GPS receiver can easily identify the GPS source of the received signal.

The L1 and L2 carriers are transmitted with navigation message. The navigation message contains important information about the predicted satellites ephemerides, predicted satellite clock correction model coefficients, GPS system status information and the GPS ionospheric model. The pseudorange measurement can be determined by this equation:

$$P_a^1 = \rho_a^1(t, t - \tau_a^1) + I_a^1 + T_a^1 + dm_a^1 + c[dt_a(t) - dt^1(t - \tau_a^1)]$$
$$+ c[d_a(t) + d^1(t - \tau_a^1)] + e_a^1 \qquad\qquad (III.1)$$

ρ_a^1 is the geometric distance between the satellite (1) and the receiver (a).

τ_a^1 is the signal travel time between the satellite (1) and the receiver (a).

I_a^1, T_a^1 are the ionospheric and tropospheric biases along signal bath respectively.

dm_a^1 is the multipath effect.

$dt^1, \ d^1$ are the satellite clock error and the satellite hardware delay.

dt_a, d_a are the receiver click offset and the receiver hardware delay.

e_a^1 is the pseudorange measurement noise.

III.2.3.2   GPS carrier phase measurement

The GPS satellite transmits signals centered on L1 and L2 microwaves radio frequencies. The selection of these high frequencies is based on many reasons. The short wavelength signals are required in order to have a high accuracy positions (~1 cm). A further reason for requiring such high frequencies is to reduce the effect of ionosphere. The ionosphere error on the phase measurements is defined by this equation:

$\delta r_{\text{ion ph}} = \frac{1}{\sin\theta} \times \frac{40.3}{f^2} \times \text{TEC}$ (Kaplan and Hegarty, 2006). Where TEC is the Total Electron Content in the ionosphere layer.

The carrier phase ϕ_a^1 is equal to the difference between the phase ϕ_a of the receiver generated carrier signal at signal reception time, and the phase ϕ^1 of the satellite generated carrier signal at signal transmission time. Only the fractional carrier phase can be measured when the satellite signal is acquired. Therefore, an integer number N of full cycles is still unknown. This value (N) is called the carrier phase ambiguity.

The phase range observable is determined by the equation:

$$\phi_a^1 = \rho_a^1(t, t - \tau_a^1) - I_a^1 + T_a^1 + \delta m_a^1 + c[dt_a(t) - dt^1(t - \tau_a^1)] + c[\delta_a(t) + \delta^1(t - \tau_a^1)]$$
$$+ \lambda N_a^1 + \mathcal{E}_a^1 \qquad\qquad (III.2)$$

ϕ_a^1 is the carrier phase range from the satellite (1) to the receiver (a).

ρ_a^1 is the geometric distance between the satellite (1) and the receiver (a).

τ_a^1 is the signal travel time between the satellite (1) and the receiver (a).

λ is the wavelength in meter.

I_a^1, T_a^1 are the ionospheric and tropospheric biases along signal bath respectively.

δm_a^1 is the multipath effect.

dt^1, δ^1 are the satellite clock error and the satellite hardware delay.

dt_a, δ_a are the receiver click offset and the receiver hardware delay.

$\mathcal{E}_a^1$ is the noise of carrier phase measurement.

N_a^1 is the real ambiguity in cycles.

Some of the physical parameters and errors in the equations III.1 and III.2 like the satellites and receivers clock errors and biases can be easily eliminated by forming linear combinations between the GPS observables.

It is noted that the ionospheric refraction affects positively the pseudorange observable since the signal is delayed when travelling across the ionosphere. In contrast with the negative effect to the phase range observable when the phase is advanced.

III.2.4 GPS linear combinations

III.2.4.1   Single-difference combination

A single difference measurement is the difference between the phase measurements of one satellite signal received simultaneously by two GPS receivers. It is also called the between receiver single differencing (ϕ_{ba}^1). Since the satellites are equipped by very precise atomic clocks, some identical errors can be cancelled as the effect is the same for the two receivers like the satellite clock error (dt^1) and equipment delay δt^1 for the time interval between each of the two receivers (a,b) and the satellite (1). The between receiver single differencing (ϕ_{ba}^1) is expressed by the equation:

$$\phi_{ba}^1 = \phi_a^1(t_a) - \phi_b^1(t_b) = \rho_a^1(t_a, t_a - \tau_a^1) - \rho_b^1(t_b, t_b - \tau_b^1) + cdt_a(t_a) -$$
$$cdt_b(t_b) + c\delta t_a(t_a) - c\delta t_b(t_b) + \lambda N_a^1 - \lambda N_b^1 - I_a^1 + I_b^1 + T_a^1 - T_b^1 +$$
$$\delta m_a^1 - \delta m_b^1 + \mathcal{E}_a^1 - \mathcal{E}_b^1 \qquad\qquad (III.3)$$

Following the same idea we can form the between satellite single difference (ϕ_a^{12}) and the receiver clock errors and bias terms can be eliminated.

$$\phi_a^{12} = \phi_a^1(t_a) - \phi_a^2(t_a) = \rho_a^1(t_a, t_a - \tau_a^1) - \rho_a^2(t_a, t_a - \tau_a^2) + cdt^1(t^1) -$$
$$cdt^2(t^2) + c\delta t^1(t^1) - c\delta t^2(t^2) + \lambda N_a^1 - \lambda N_a^2 - I_a^1 + I_a^2 + T_a^1 - T_a^2 +$$
$$\delta m_a^1 - \delta m_a^2 + \mathcal{E}_a^1 - \mathcal{E}_a^2 \qquad\qquad (II.4)$$

III.2.4.2   Double-difference combination

The double difference measurement (ϕ_{ab}^{12}) is performed by subtracting two between satellites single differences. Using the equation III.4, we can write the equation of double difference for two receivers a and b which receive signals from two satellite 1 and 2:

$$\phi_{ab}^{12} = \phi_a^{12} - \phi_b^{12} = \rho_a^{12} - \rho_b^{12} - I_a^{12} + I_b^{12} - T_a^{12} - T_b^{12} + \delta_a^{12} - \delta m_b^{12}$$
$$+ \lambda N_a^{12} - \lambda N_b^{12} + \mathcal{E}_a^{12} - \mathcal{E}_b^{12} \qquad\qquad (III.5)$$

ϕ_a^{12} and ϕ_b^{12} are the single difference carrier phase measurements between receivers and satellites. In the double difference measurement the receiver and the satellite clock offsets and clock biases are canceled.

III.2.5 Resolution of ambiguity

The carrier phase measurements are affected by the ambiguity term N in the equation III.2, which is unknown number of complete wavelengths between the satellite and the receiver antenna. This initial ambiguity has to be determined with appropriate techniques to achieve the full accuracy possible of the GPS carrier phase measurements. Ambiguity determination is one of the most challenging problems in the geodetic technique of evaluation GPS observations.

The best and simplest possibility for determination the ambiguity would be the use of additional frequencies and signals. Unfortunately, GPS does not provide more than two frequencies. Hence other strategies were developed to solve the ambiguity problem. Among the many different approaches that have been suggested for the carrier phase ambiguity fixing are those documented in Hofmann-Wellenhof and Remondi, (1988), Euler and Goad, (1991), Erickson, (1992), Goad and Yang, (1994), and Hatch and Euler, (1994). These approaches are mainly based on:

1- The geometric method (coordinate domain search).
2- Code and carrier phase combinations (observation domain search).
3- Ambiguity search methods (ambiguity domain search).
4- Combined methods.

Nowadays, the ambiguity search method is considered to be the most effective and powerful method for the ambiguity resolution, especially for the fast solutions, and it is widely discussed in the literature.

The main idea of the ambiguity search method is to search for the optimum ambiguity combination of L1, L2 or derived signals. The search algorithm usually starts with an initial ambiguity float solution and then restricts the solution vector to identify the integer values applying some optimization techniques. In this method, the more satellites that are available, the better is the solution.
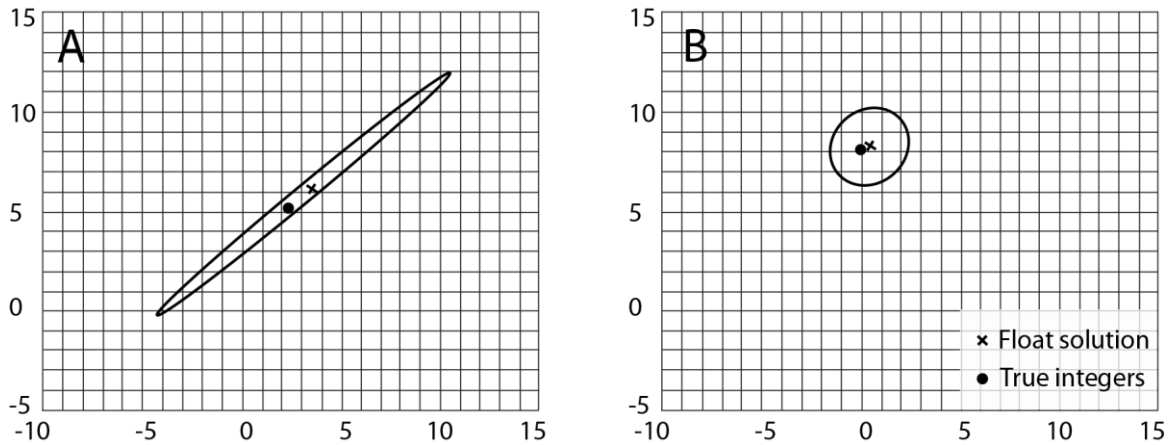
Figure III.1: Lambda method: ambiguity search space before (A) and after (B) decorrelation (adapted from Joosten, Tiberius (2000)).

A very powerful current technique for the ambiguity resolution is the LAMBDA method, which was developed at the Delft University of Technology (Teunissen *et al.*, 1995; Teunissen, 1998; Joosten and Tiberius, 2000). This method (LAMBDA) uses the Least Square Ambiguity Decorrelation Adjustment and is used in GAMIT/GLOBK software. The basic idea is to transform the original real-valued double difference ambiguities, which are highly correlated, into decorrelated real-valued ambiguities. In this case, the number of solution candidates is considerably reduced. By this procedure, the original highly elongated search space is transformed into a sphere-like search space with the same volume (Figure III.1), which allows a much more efficient identification of the integer ambiguities.

III.2.6 Plate kinematics

The movement of the plates on the earth is basically described by the Euler theory formulated by Leonhard Euler in the XVIII centaury (Euler, 1775). This theory suggests that every displacement of a rigid body on a sphere is rotational. Applying this theory to the plate kinematics recommends that the motion of the tectonic plates on the earth surface, which can be approximately considered as a sphere, is rotational. This motion is described as a rotation around a fixed axis passing through the center of the earth (~sphere). The present day plate tectonics are referred as a rotation around a rotation pole called Euler pole, with an angular velocity, which can be represented in spherical and geometric Cartesian coordinate system.

Every plate on the earth surface has two Euler poles which represent the intersection of the axis of rotation with the earth surface (Figure III.2). The plate movement is characterized by a rotation around the Euler pole with an angular velocity (ω). The rotation is

consider positive if it is right handed that means the plate turns about counter clockwise with respect to the rotation axis itself. In this case we have always a positive and negative rotation pole for each plate.
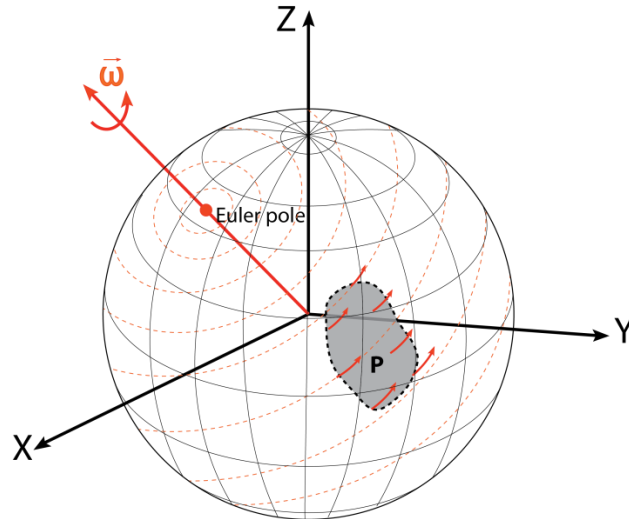
Figure III.2: the plate motion on the earth surface. The plate P rotates around the Euler pole with a rotation velocity ω. The red vectors and circles represent the direction of the trajectories of the rotational motion.

The movement of every point on a plate can be described by linear velocity V, tangent to the earth surface and given by the equation:

$$\vec{V} = \overrightarrow{\omega_p} \times \vec{R}$$

Applying this to a fixed point in plate (p) give:

$$V = \omega_p \times R \times \sin\theta$$

Where ω_p is the plate angular velocity, R is the Earth radius, and θ is the angular distance between the fixed point and the Euler pole of the related plate.

In a similar way, it is possible to explain the relative motion between two plate i and j by the rotation around one axis passing through the center of the earth and have two Euler poles, then the linear velocity of a fixed point in one plate with respect to the other plate is determined by the equation:

$$\vec{V} = \overrightarrow{\omega_{ij}} \times \vec{R}$$

The models of plate motions are estimated essentially in reference frames attached to the lithosphere. Thus, the rotational movement of plates can be estimated with respect to one plate, plate pairs, or with respect to the mean lithosphere. The plate kinematic models referred to the mean lithosphere are called no-net-rotation (NNR). The NNR frame is defined with a constraint that net rotation of all plates on the earth should be zero.

The advance of space geodesy, GPS observations, velocity fields and azimuths and the progressive online availability of these data in different databases center, give the possibility to achieve a new accurate plate kinematic models (e.g., ITRF). These kinematic models based on spatial geodesy techniques show a good agreement with the earlier geological plate kinematics models (Le Pichon, 1968; Morgan, 1968) and other recent geological models as the NUVEL-1 (DeMets *et al.*, 1990) and the NUVEL-1A (Gordon, 1991; DeMets *et al.*, 1994).

NNR-NUVEL1 is an example of geological plate tectonic model describing the angular velocities of the 14 major tectonic plates presented in Table III.1. Comparing the Euler poles and rotation rates from NNR-NUVEL1 (Table III.1) with those of the ITRF2005 (Table III.2 in Paragraph III.2.7), we can notice that a well agreement exists between the geological and geodetic plate models.

Plate	Lat °N	Lon °E	ω °/Myr	rms velocity
Africa	50.60	-74.00	0.30	30
Antarctica	63.00	-115.90	0.25	16
Arabia	45.20	-4.40	0.57	46
Australia	33.80	33.20	0.68	66
Caribbean	25.00	-93.10	0.22	9
Cocos	24.50	-115.80	1.58	77
Eurasia	50.60	-112.40	0.24	25
India	45.50	0.40	0.57	59
Juan de Fuca	-27.40	58.10	0.64	20
Nazca	-2.50	-86.00	0.22	20
North America	47.80	-100.20	0.78	79
Pacific	-63.00	107.40	0.67	67
Philippine Sea	-39.00	-36.70	0.95	42
South America	-25.40	-124.60	0.12	12

Table III-1: NNR-NUVEL1 Euler poles and rotation rates (Gordon, 1991).

The space geodesy offers a new tool to verify that the plate motions are, in general, stable over the past few million years. This conclusion is approved by the high agreement between the motion rates measured using the space geodesy technics for a few years and the predictions of the global geodynamic plate motion models including the last 3 million years. This agreement shows that the space geodesy predictions are a good indicator of the main Cenozoic plate relative motions (Stein, 1993).

III.2.7 The International Terrestrial Reference Frame: ITRF2005

The terrestrial reference frame is achieved through a set of Cartesian station coordinates at specific ultimate epoch, the station coordinates are determined by different space geodetic observations including SLR, VLBI and GPS (Kovalevsky *et al.*, 1989; Boucher, 2000).
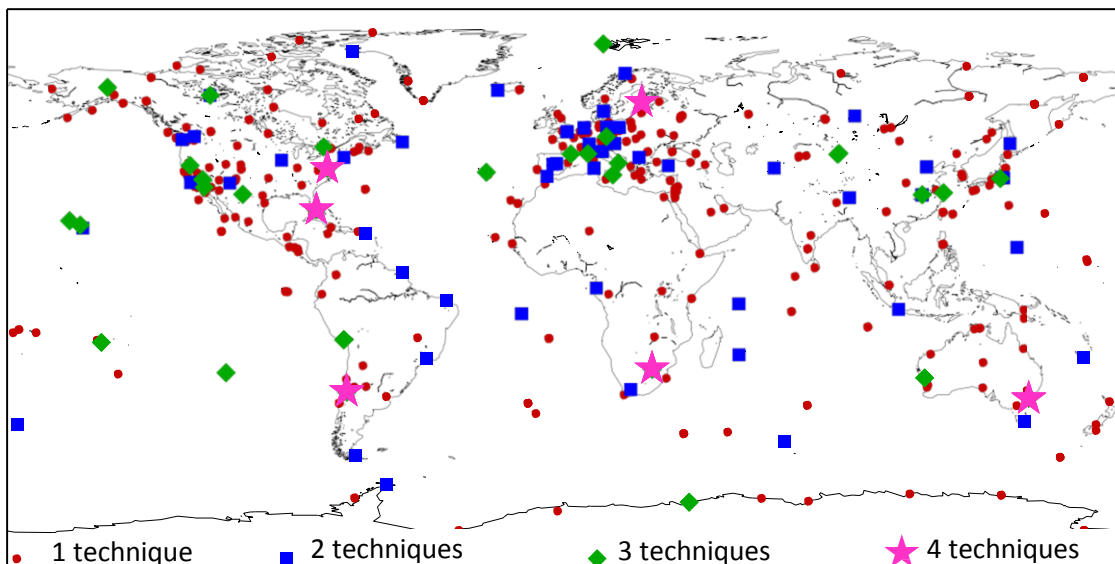
Figure III.3: the ITRF2005 sites with the number of co-located techniques for each site (Altamimi et al., 2007).

The best reference frame currently existing is the International Terrestrial Reference Frame (ITRF). Its origin is the center of mass of whole earth including oceans and atmosphere. Currently, the ITRF is maintained by the International Earth Rotation Service (IERS) through a global network of observing stations. The realization of ITRF is done by using multi geodetic observations including GPS, very long baseline interferometry (VLBI), Lunar Laser Ranging (LLR), Satellite Laser Ranging (SLR), and the Doppler Orbitography

and Radiopositioning Integrated by Satellite (DORIS). The ITRF provide an accurate position of observing station at a centimeter level.

Each version of ITRF is identified by a year code, indicating the year of realization. The last version of ITRF is the ITRF2008 (Altamimi *et al.*, 2011; Altamimi *et al.*, 2012). In this study we used the ITRF2005. The ITRF2005 combination has been performed on one time series (rates and EOPs parameters) of solutions per each space geodesy technique. The time span covered by each series is different: 26 years for VLBI, 13 for SLR, 12 for DORIS and about 10 years for GPS. The ITRF2005 is composed of 608 stations located at 338 sites (Figure III.3) (Altamimi *et al.*, 2007). The unbalance between the northern (268 sites) and the southern (70 sites) hemispheres is a weakness point of the ITRF2005.

ITRF consists of points coordinates (X,Y,Z) in meters and their velocities (Vx,Vy,Vz) in mm/year, with the estimated errors of these values. The coordinates of ITRF2005 refer to the epoch 2000.0, thus, in order to obtain the coordinate in any other time, the velocity can be applied, under the hypothesis of linear motion, to broadcast the desire coordinates. A group of 152 velocities of the ITRF2005 was selected in order to be used in the definition of ITRF2005 plate motion model, which describes the rotation poles and rates of 15 tectonic plates (Table III.2).

Plate	Lat	Lon	ω	rms
	°N	°E	°/Myr	°/Myr
AF	50.00	-82.50	0.269	0.003
AN	58.81	-125.32	0.223	0.007
AR	49.64	5.06	0.579	0.019
AU	32.41	37.37	0.628	0.003
CA	39.32	-104.28	0.241	0.145
EU	56.33	-95.98	0.261	0.003
IN	49.82	21.84	0.614	0.108
NA	-4.29	-87.39	0.192	0.002
NU	49.95	-82.50	0.269	0.003
NZ	45.10	-101.44	0.642	0.015
OK	-32.04	-132.91	0.083	0.006
PA	-62.57	112.87	0.682	0.004
SA	-16.80	-129.63	0.121	0.003
SO	53.66	-89.54	0.309	0.019
YA	59.43	-109.74	0.310	0.021

Table III-2: ITRF 2005 Euler poles and rotation rates (Altamimi et al., 2007).

III.3 GPS network in the Hatay Triple Junction

III.3.1 GPS network installation

The GPS network in the Hatay region was designed to better characterize the kinematic of the tectonic plates and blocks of the region. It consists of 57 campaign GPS sites covering the North-West of Syria and the South-East of Turkey (Figure III.4). The geometry of our GPS network and the consistency with the previous field investigations was taken into account during the installation, so that the 24 sites in Turkey and 33 sites in Syria form all together 4 main profiles. These profiles cross most of the main active faults and sub-faults and related tectonic blocks in the region.

- **Profile I**: This profile crosses the Al-Ghab basin and related north-south border faults including the northern Dead Sea Fault and the NE-SW trending Lattakia fault (LF) and extends for ~160 km in E-W direction.

- **Profile II**: It crosses the easternmost fault system of the northern Al-Ghab Basin that includes the Idleb and Afrin faults and extends for 120 km with E-W trending.

- **Profile III**: It crosses the Karatas-Osmaniye fault (KOF), the northern Ghab Basin and related Idleb and the Afamia fault system; it extends for 240 km in NW-SE direction.

- **Profile IV**: It crosses the Karasu Valley and the south-western East Anatolian fault, extending for 220 km with a NW-SE trend.

The 4 GPS profiles across the Hatay region (Figure III.4) illustrate a network configuration that may contribute to an accurate estimate of the tectonic activity and fault slip rate variation. The points' alignment and the continuity of the profiles from Syria to Turkey are taken into account for a better assessment of the velocity field and physical parameters of fault branches along the major fault systems. The campaign GPS network is supported by some permanent GPS sites belonging to regional GPS networks in Syria and Turkey. 8 CGPS stations in Turkey (MRST, DZCT, ANDT, CKVT, CRMT, ELZT, GAZT, and MLYT) and 6 CGPS stations in Syria (HALB, TUAB, BUSF, RAQA, PALM, UDMC). The Figure III.4 shows all the campaign sites and a part of the regional permanent sites.

Most of our campaign GPS sites were chosen to be installed in bedrock, except 2 sites installed on a pillar and on a big stable building in Turkey and Syria respectively. We used two different types of monumentation and antenna setup for the site in Turkey and Syria.

Those in Turkey consist of a stainless steel pin of 1.5 cm in diameter and 15 cm in length that was cemented into a drilled hole in solid bedrock, at the upper end it allows another rod of 1.20 m to be installed with a tripod leveling system on which the antenna can be fixed by screwing (Figure III.5). This type needs time to install and can have some errors due to the leveling system and the experience of the person who installs it. Its advantage is that the antenna height can be adjusted and its height from the ground decreases the error of reflected GPS signals. The monuments in Syria consist of a stainless steel pin of 1.5 cm in diameter and 15 cm long that was cemented into a drilled hole in solid bedrock, in its upper end we can screw another pin of 25 cm long, and then the antenna will be fixed on the other end (Figure III.6). This type is easy and fast to install but the small height of the antenna can disturb the received GPS signal.
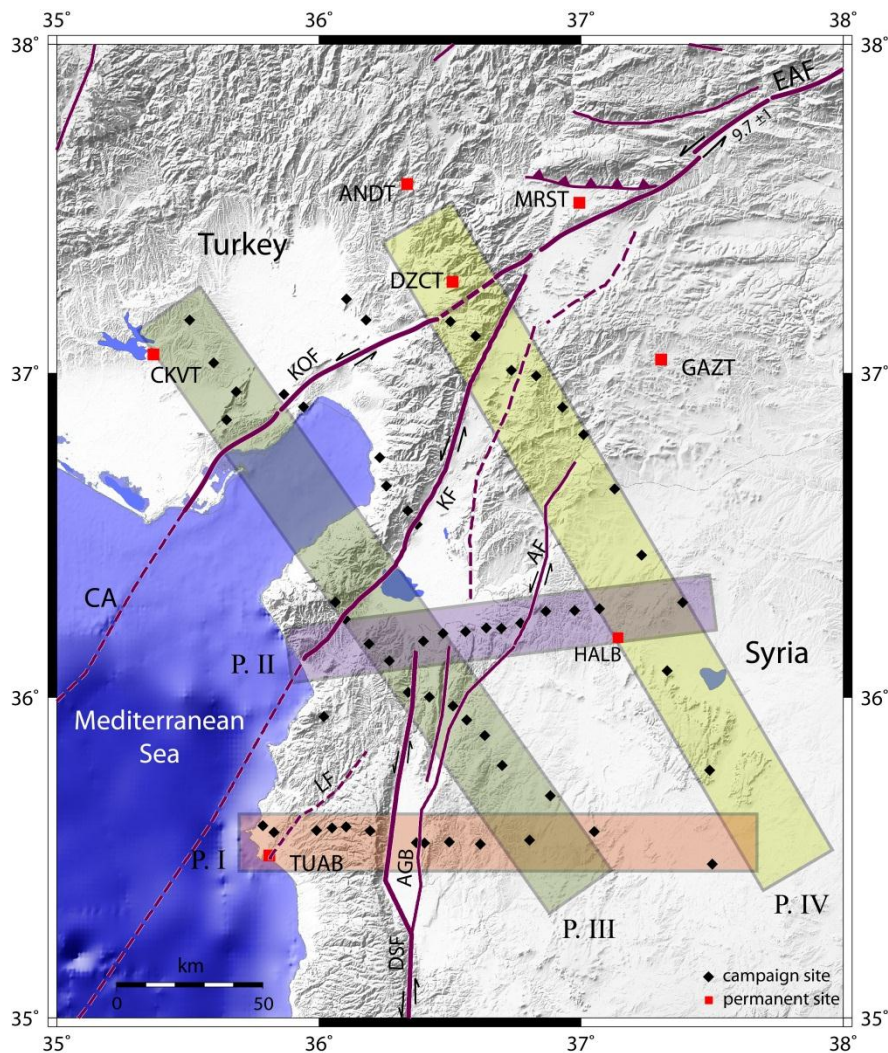
Figure III.4: Map illustrate the campaign GPS sites (black diamonds) in North-West Syria and South-East Turkey and a part of the regional CGPS sites (red squares) used in this study. The colored rectangles refer to the 4 GPS profiles mentioned previously. Abbreviations for some

key tectonic features: AGF: Al-Ghab fault, AF: Afrin fault, CA: Cyprus Arc, KF: Karasu fault, KOF: Karatas-Osmaniye fault, LF: Lattakia fault, DSF: Dead Sea fault, EAF: East Anatolian fault, MF: Missyaf fault, SF: Serghaya fault, RF: Roum fault, YF: Yammuneh fault.

III.3.2 GPS campaigns in Syria and Turkey

A long part of my work during my PhD was to install and measure the campaign GPS network in Syria and Turkey. I participated in all the GPS campaigns held to install and measure the 57 GPS sites. In the next stage I did the data check quality and processing. In order to have these data, 5 GPS campaigns were launched in 2009, 2010 and 2011 in the two countries.

III.3.2.1   Campaigns of 2009

In September 2009, I participated in GPS campaign organized by the Institut de Physique du Globe of Strasbourg (IPGS) in order to install and measure the GPS points in Hatay region in South-East Turkey. 24 GPS points were installed and measured between 5 September and 7 October of 2009. This campaign was done in collaboration with Ziyadin Cakir and Hakan Yavasoglu from Istanbul Technical University (ITU) and Onder Yonlu from Eskisehir Osmangazi University in Turkey. We also received a very important contribution from Marmara Research Center (TUBITAK). They provide the GPS devices and other equipment.

Figure III.5: Example of GPS monument used in Turkey with Thales Z Max receivers and Thales Z Max Ashtech antenna

The GPS sites were all observed for 24 hours over two sessions of 12 hours in two different days using Thales Z Max receivers with Thales Z Max Ashtech antenna (Figure III.5) provided by TUBITAK. The GPS data were logged with a 30s sampling rate and the antennas were fixed on monuments using antenna masts in order to minimize antenna setup errors. The GPS data were checked regularly and the points were re-measured when poor data was founded.

Figure III.6 : Example of GPS monument used in Syria Thales DSNP 6502MK receivers and Leica AT504 Choke Ring Antenna

In November of the same year, IPGS organized another GPS campaign in Syria in collaboration with Tishreen University in Lattakia and the National Earthquake Center in Damascus (NEC). From 3 to 22 November we installed 33 GPS sites in North-West Syria, and measured the majority of them during this period. Some of the points were measured in the beginning of 2010 (see Table III.4). The GPS devices and other equipment for this campaign were provided by the NEC of Damascus. Abdulmutaleb Alchalbi and the GPS group from NEC had a big contribution to this campaign in Syria. The 33 sites were observed for one session of 24 hours belonging to 2 different GPS days using Thales DSNP 6502MK receivers and Leica AT504 Choke Ring Antenna (Figure III.6). The antenna setup was completed using the monuments explained above. Pre-processing problems were solved by the use of "TEQC" program. Data quality check was performed after each session in order to verify our measurements records and detect the possible errors like missing epochs or short time of measurement. In few cases we had to re-measure the site because of device problem or bad measurement quality.

III.3.2.2   *Campaigns of 2010*

In 2010, I participated in two other campaigns in Syria and Turkey. The 24 GPS points in Turkey were measured between 24 August and 5 September using the same instruments of the first campaign beside ASHTECH UZ-12 receiver with Ashtech antenna with ground plane. The GPS campaign was supported with the participation of the same group of the 2009 campaign with the participation of Sheldon Warden from IPG of Strasbourg. The observation for every point was done in the same method of first campaign with 24 hours over two sessions of 12 hours. The GPS data were also logged at a 30 second sampling rate.

Between 23 November and 9 December 2010, I participated also in a field work mission in order to help the GPS group of NEC in Syria to observe the 33 GPS site in North-West Syria. For this campaign we used also the same GPS devices and equipment with the participating of the same group of the campaign of 2009 in Syria. The GPS data were logged at a 30 second of sampling rate and all sites were observed for one session of 24 hours.

We always made a check of data during the campaign to identify all the bad-quality data and try to compensate the deficiency. For this, few GPS points were re-measured several times in the same campaign.

III.3.2.3   *Campaign of 2011*

The last campaign in Hatay region in Turkey was achieved in September 2011. In collaboration with ITU and TUBITAK as all our GPS campaign in the region, we observed all the GPS sites for the third time in three years. We followed the same strategy of measuring and data analysis. Between 6 and 17 September I collaborated with our colleagues from Turkey and Jacque Durant from IPG of Strasbourg. One GPS site was lost in this campaign because of electrical line construction (PT30, Table III.3).

Unfortunately, it was not possible to measure the GPS sites in the Syrian side for the third campaign of 2011 as it was planned for the GPS project in North-West Syria and South-East Turkey.

The GPS Data of all these campaigns have been processed together with other permanent GPS data of 8 CGPS sites in Turkey. These data are provided by TUBITAK. Also, data of 6 CGPS in Syria are involved in the processing provided by NEC in Damascus.

Site name	Lon °	Lat °	2009 Sep - OCT GPS (doy)	2010 Aug - Sep GPS (doy)	2011 Sep GPS (doy)
PT01	35.685	36.943	262 , 263	236 , 237	249 , 250
PT02	35.648	36.857	262 , 263	236 , 237	249 , 250
PT04	35.866	36.935	264 , 265	238 , 239	251 , 252
PT05	35.941	36.896	264 , 265	238 , 239	251 , 252
PT07	36.269	36.114	272 , 274	242 , 243	257 , 258
PT08	36.191	36.166	272 , 274	242 , 243	257 , 258
PT09	36.341	36.017	273 , 275	242 , 243	257 , 258
PT12	36.019	35.941	273 , 275	242 , 243	257 , 258
PT24	36.063	36.296	270 , 271	240 , 248	259 , 260
PT26	36.101	36.243	270 , 271	241 , 248	259 , 260
PT30	36.232	36.741	268 , 269	238 , 248	point lost
PT31	36.257	36.654	268 , 269	239 , 240	251 , 252
PT33	36.339	36.577	266 , 267	240 , 241	259 , 260
PT34	36.374	36.535	266 , 267	240 , 241	259 , 260
PT35	37.009	36.812	279 , 280	244 , 245	255 , 256
PT36	36.929	36.895	279 , 280	244 , 245	255 , 256
PT37	36.829	36.992	278 , 279	244 , 245	255 , 256
PT38	36.734	37.009	276 , 278	244 , 245	255 , 256
PT39	36.598	37.114	276 , 277	246 , 247	253 , 254
PT40	36.502	37.158	276 , 277	246 , 247	253 , 254
PT42	36.105	37.227	258 , 259	246 , 247	253 , 254
PT43	36.179	37.162	258 , 259	246 , 247	253 , 254
PT46	35.506	37.162	260 , 261	236 , 237	249 , 250
PT47	35.599	37.031	260 , 261	236 , 237	249 , 250

Table III-3: The GPS campaign sites in South-East Turkey and their geographic coordinates. The last three columns show the GPS day of year (doy) for the measurements of campaigns in 2009, 2010 and 2011.

Site name	Lon °	Lat °	2009 Nov GPS (doy)	2010 Nov - Dec GPS (doy)
AA01	37.501	35.482	-	13 , 14 , 342 , 343
AA02	37.051	35.583	308 , 309	341 , 342
AA03	36.616	35.544	-	11 , 12 , 333 , 334
AA04	36.497	35.551	-	12 , 13 , 335 , 336
AA05	36.403	35.547	-	13 , 14 , 335 , 336
AA06	36.371	35.549	-	11 , 12 , 334 , 335
AA08	36.195	35.585	342 , 343	329 , 330
AA09**	36.104	35.598	343 , 344	329 , 330
AA10	36.050	35.595	341 , 342	328 , 329
AA11	35.991	35.587	308 , 309	327 , 328

AA12	35.828	35.581	307 , 308	328 , 329
AA13	35.786	35.602	306 , 307	327 , 328
AA14	36.803	35.557	-	75 , 76 , 334 , 335
BB02	36.883	35.695	308 , 309	341 , 342
BB03	36.699	35.789	307 , 308	335 , 336
BB04	36.633	35.882	306 , 307	326 , 327
BB05	36.564	35.931	306 , 307	326 , 327
BB06	36.511	35.974	307 , 308	334 , 335
BB08	36.421	36.002	313 , 314	333 , 334
CC01	37.128	36.645	349 , 350	341 , 342
CC02	37.231	36.441	343 , 344	340 , 341
CC03	37.329	36.083	342 , 343	340 , 341
CC04	37.490	35.774	341 , 342	342 , 343
DD01	36.398	36.175	314 , 315	327 , 328
DD02	36.473	36.198	314 , 315	328 , 329
DD03	36.559	36.204	315 , 316	329 , 330
DD04	36.638	36.216	315 , 316	328 , 329
DD05	36.696	36.215	348 , 349	329 , 330
DD06	36.770	36.230	348 , 349	333 , 334
DD07	36.866	36.267	349 , 350	335 , 336
DD08	36.976	36.270	350 , 351	342 , 343
DD09	37.070	36.275	344 , 345	341 , 342
DD10	37.388	36.294	343 , 344	340 , 341

Table III-4: The GPS campaign sites in North-West Syria and their geographic coordinates. The last three columns show the campaigns in 2009 and 2010. (**) The point (AA09) is the same point named DOHA used by Alchalbi et al., (2010). In our processing we will introduce the data of this point from the years 2000, 2007 and 2008.

III.3.3 GPS measurement strategy

The GPS measurements were logged to 30s of sampling interval which is the ideal for best control of the uncertainties obtained for the daily solutions and by consequences for the coordinates and velocities. We fixed the elevation angle of the visible satellites to 15°. This angle determination is to control the signals received by the antenna to be registered. The aim behind this regulation is to increase the quality of our measurements. A smaller elevation angle gives larger errors of the multipath trajectory. It also increases the errors caused by the atmospheric delay since the signals transmitted by a low satellite cross a long distance in a dispersive space. We used ground plane antennas In order to reduce the reception of near-field reflected signals which is an important error source in GPS measurement.

III.4 GPS Data processing with GAMIIT

III.4.1 GPS processing method in GAMIT

We used GAMIT software to process our GPS campaigns data collected from the 57 sites in our region of study with other permanent International GNSS Service (IGS) data for 71 sites (see paragraph III.4.2). Using GAMIT, we produce daily solutions of the GPS measurements. For each day, we use a weighted least squares algorithm to estimate the relative positions of a set of stations, orbital and earth-rotation parameters, zenith delays for each station with interval of 2 hours, and phase ambiguities by fitting to doubly differenced of phase observations of the GPS signals. Indeed, GAMIT produces two solutions, the first is to have estimates of coordinates with uncertainty of few decimeters, and the second solution is to obtain the final coordinates estimates and an associated covariance matrix called quasi observations of station positions and orbital and earth rotation parameters to be used after as input to GLOBK to estimate precise positions and velocities (Feigl *et al.*, 1993b; Dong *et al.*, 1998). A linear combination (LC) of L1 and L2 is used in GAMIT in order to cancel the ionosphere effect which can introduce tens of meters to the signal path; the LC combination is effective for baselines of length more than a few kilometers.

For the GPS processing in GAMIT, we use the Earth orientation parameters (EOP) given by the International Earth Rotation Service (IERS) and the orbits distributed by the International GNSS Service (IGS). We also introduce lunar and solar ephemerides (luntab. and soltab.), antenna phase-center models (antmod.dat), satellite parameters table (svnav.dat) and ocean tidal loading (otl.grid). In addition, we use a priori station coordinates (L-file), geodetic datums (gdetic.dat), characteristics of receiver and antenna names (rcvant.dat), atmospheric mapping function coefficients and hydrostatic zenith daleys based on the numerical weather model (VMF1).

III.4.2 Stabilization: Permanent IGS sites

Although the GPS satellites provide a natural dynamic frame for ground-based geodesy, the doubly differenced phase observations do not fix a ground station to the orbital group with accuracy of millimeter level which is required for scientific studies, especially for detecting the active deformation of low rate such the slip rate expected in our region of study of the triple junction (a few millimeter per year). Rather, we define and realize a precise

terrestrial frame by applying constraints to one or more sites in our network. These sites should be carefully chosen according to their accuracy, stability, and continuity of measurements in order to construct the best stabilization frame to connect our network with the international terrestrial reference frame.

The simplest and most strong approach to frame realization is to incorporate into our solution a number of sites whose coordinates and velocities are precisely known in a reference frame. For this aim we include into our GAMIT processing a set of the IGS stations which are well defined in the no-net-rotation (NNR) of the International Terrestrial Reference Frame 2005 (ITRF05) (Figure III.7).
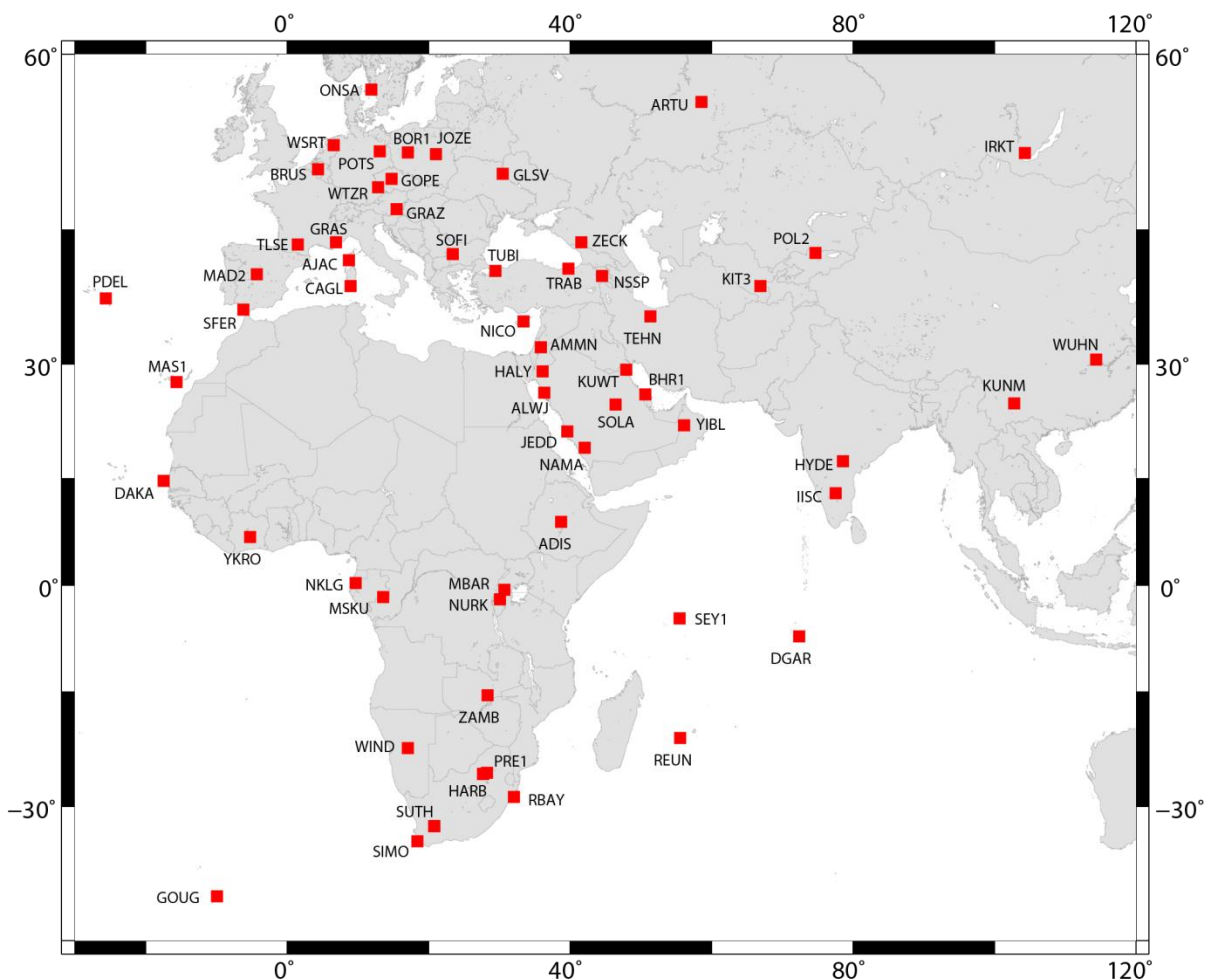
Figure III.7: Permanent IGS GPS points introduced to the processing of our locale GPS points to perform the stabilization frame.

We choose the permanent IGS site according to some conditions:

- All the sites have continues measurements for at least 7 years (most of sites have measurements since 1998 till 2012).

- The sites are distributed on major tectonic plates, Africa, Eurasia, and Arabia. This help to have a good reference frame for stabilization (good network geometry).

- Their coordinates and velocities are well known in the ITRF05.

In Figure III.7, we show the 71 IGS sites used in this study during the GPS processing with GAMIT/GLOBK.

III.4.3 Time series, errors, RMS

After using "GAMIT" program to process the GPS raw data and produce daily solution for all station, the program "GLOBK" was used to produce time series of day-to-day repeatability for the station coordinates, which can then be plotted and examined for outliers and the appropriate scaling to obtain reasonable uncertainties. This first step in GPS post processing allows us to check and clean the measurements of our GPS stations from strange values. The presence of large values indicates unwelcome outliers that will lead to an underestimate of the velocity uncertainties for these stations. For each site, the outlier epochs are identified separately in each coordinate direction and then applied to all three coordinate directions. Once we obtained a clean data set, we repeat the processing to have new daily solutions for the station positions. Examples for different time series from our processing are presented in the Figures III.9, III.10, III.11. Figure III.9 shows time series examples of a permanent IGS stations (TEHN, BHR1, ALWJ, TLSE) which are included into the processing in order to help in the definition of different reference frames. Time series examples of GPS campaign sites from our network in Syria (AA01, BB08, CC03, DD06) and Turkey (PT04, PT26, PT35, PT46) are shown in Figure III.10 and Figure III.11 respectively.

Time series of station position tend to show significant quasi-annual and other long-period components (e.g., station TEHN in Figure III.9) whose origins are mainly due to the site effects. In order to take into account the site effects and other components of random walk in the time series, we applied a random walk of 2 mm/√yr in horizontal positions of the stations.
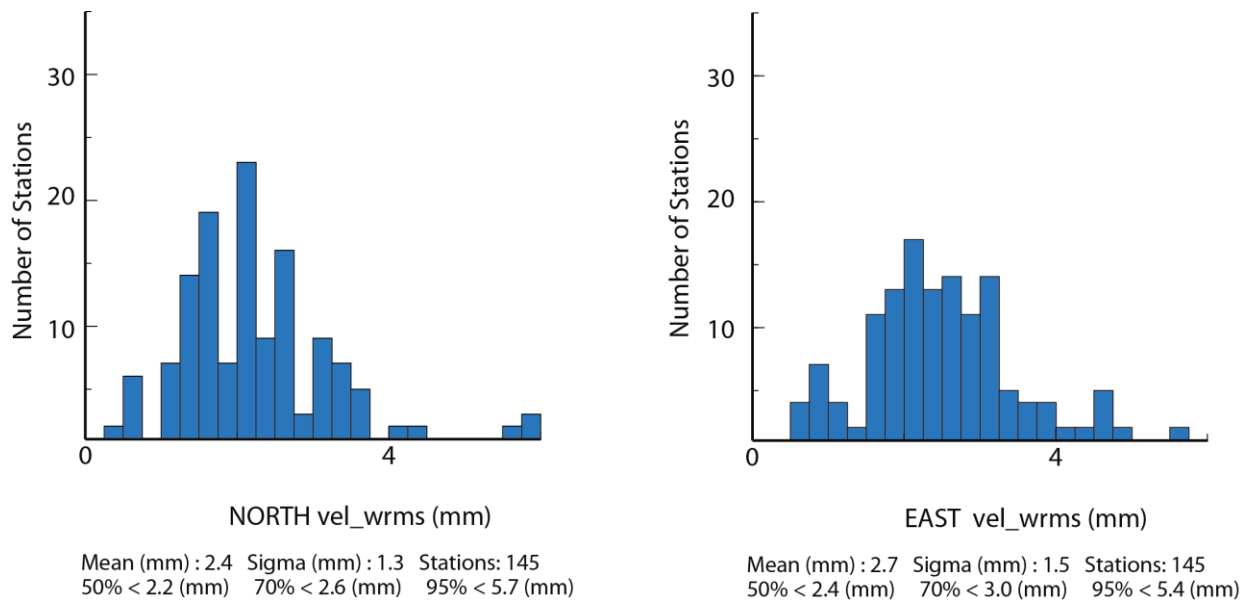
Figure III.8: the weighted root mean square of the north and east component of GPS velocity vectors.

Figure III.8 shows histograms of the weighted root mean square (wrms) of east and north directions for all the time series in our processing. We notice that for the east and the north velocity components, 70% of the wrms values are less than 3 mm and 95% are less than 5.7 mm. The wrms histogram seems normal and the values are well distributed around a mean value of 2.3 mm.
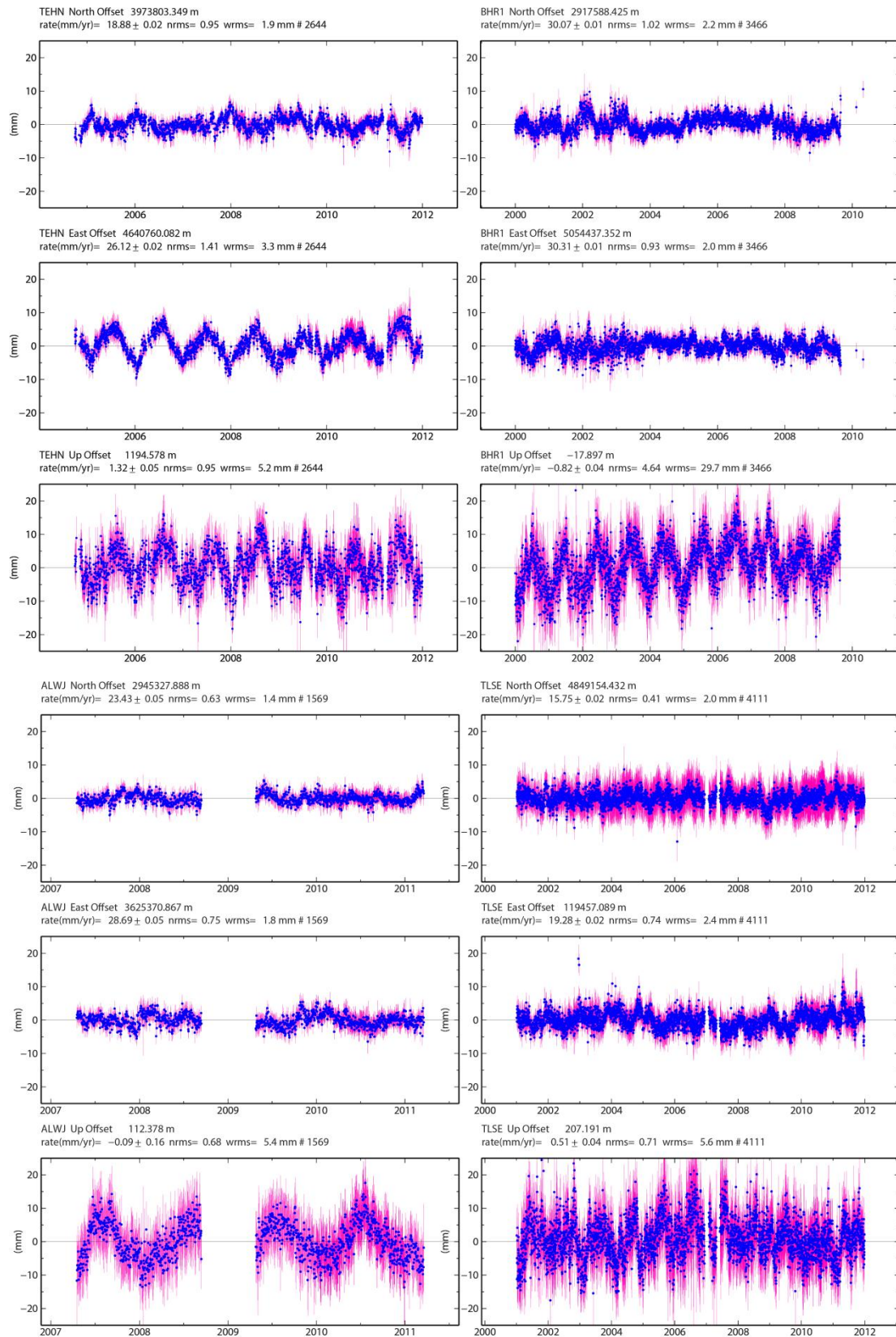
Figure III.9: Time series of four permanent IGS stations (TEHN, BHR1, ALWJ, TLSE), velocity rate, number of measurements, and their weighted and normalized RMS over the east, north, and up components.
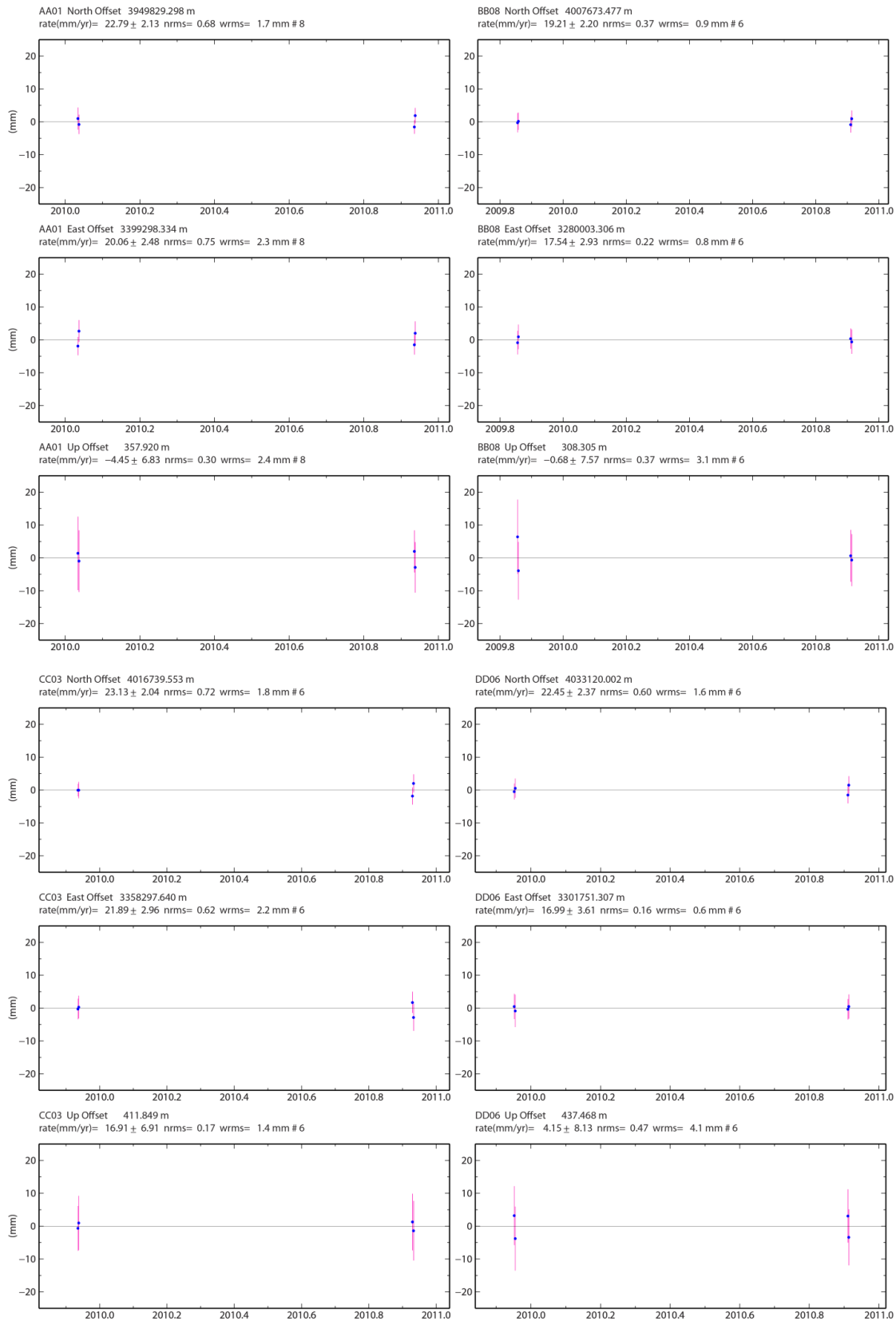
Figure III.10: Time series of four campaign GPS sites in Syria (AA01, BB08, CC03, DD06), velocity rate, number of measurements, and their weighted and normalized RMS over the east, north, and up components.
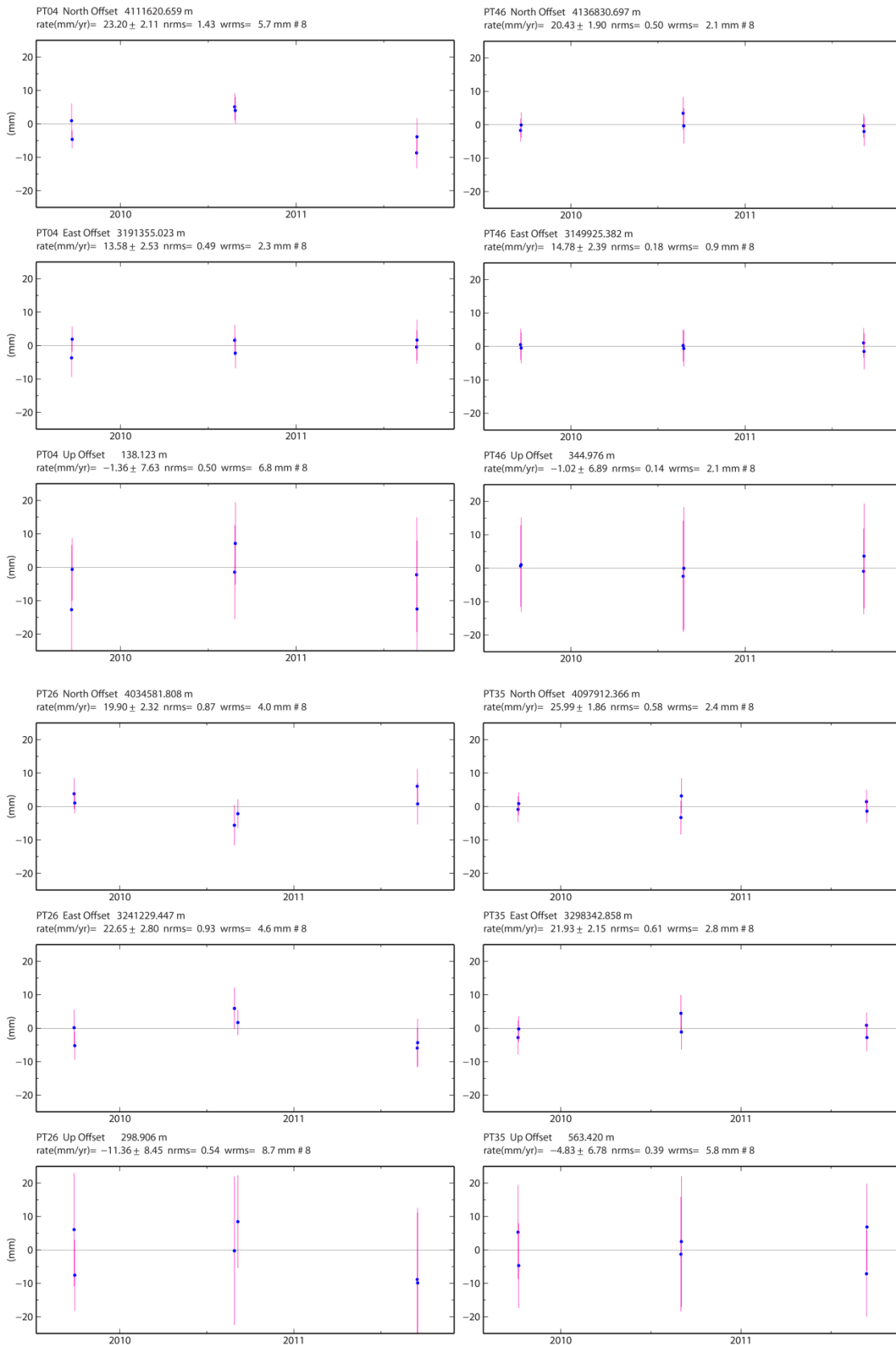
Figure III.11: Time series of four campaign GPS sites in Turkey (PT04, PT26, PT35, PT46), velocity rate, number of measurements, and their weighted and normalized RMS over the east, north, and up components.

III.5 **Results**

The first result deduced from the GPS processing is the velocity field. We determine the velocity (direction, and rate) of each site. A group of sites can be used later to determine the plate (block) motion relative to a specific reference frame.

III.5.1 GPS velocity field in ITRF2005 reference frame

After clean up the data from outliers and errors, we used "GLOBK" program to produce a velocity field, all our GPS sites were processed together with the international GNSS service (IGS) sites for all the period between 1998 and 2011. We used ITRF2005 (Altamimi *et al.*, 2007) as reference frame for our processing of time series and velocity field. The use of ITRF2005 as a reference was performed by including the permanent IGS points into the processing with their coordinates and velocities which are well known in this reference frame. The long time span for the IGS points (1998-2011), the continuity of the measurements for most of these stations (Figure III.7), and their distribution over the major tectonic plates around our region of study, gives the possibility to have a very constrained reference frame in ITRF2005. Though some of sites in the Figure III.12 do not have continuous measurements or a long time span, they were used in this study for their necessity and importance (poor GPS covering for a region) to define a reference frame (e.g. the case of Arabian plate).

Scaling the velocity uncertainties by the square root of the chi-square per degree of freedom from our solution would be applicable if the error spectrum were white and spatially homogeneous, which is not the case. The analyses of continuous GPS data conducted by Zhang *et al.,* (1997) and Mao *et al.,* (1999) show that the noise in GPS time series might be characterized by colored noise with a spectral index which varies from about 0.5 (fractal white noise) to 1.5 (fractal random walk) liable on the difference between stations and the applied method of analysis. In order to represent the uncertainties of GPS stations more realistically and also to account for a possible random walk component due to the monument instability (Langbein and Johnson, 1997), we applied a random walk of 2 mm/√yr in horizontal positions of the stations as McClusky *et al.*, (2000). This value of random walk was chosen in order to have more realistic uncertainties for the long time measured CGPS sites as well as for the CGPS sites which are measured for a short time.

In Figure III.12 is presented the velocity field realized for all the continuous GPS sites in this study and their 95% confidence ellipses, in the ITRF2005 reference frame. Sites in our region of study are excluded from this figure because of invisibility, the velocity field of our GPS network around the Hatay triple junction and some other regional permanent sites in Syria and Turkey are shown in Figure III.13, in the same reference frame of ITRF05.
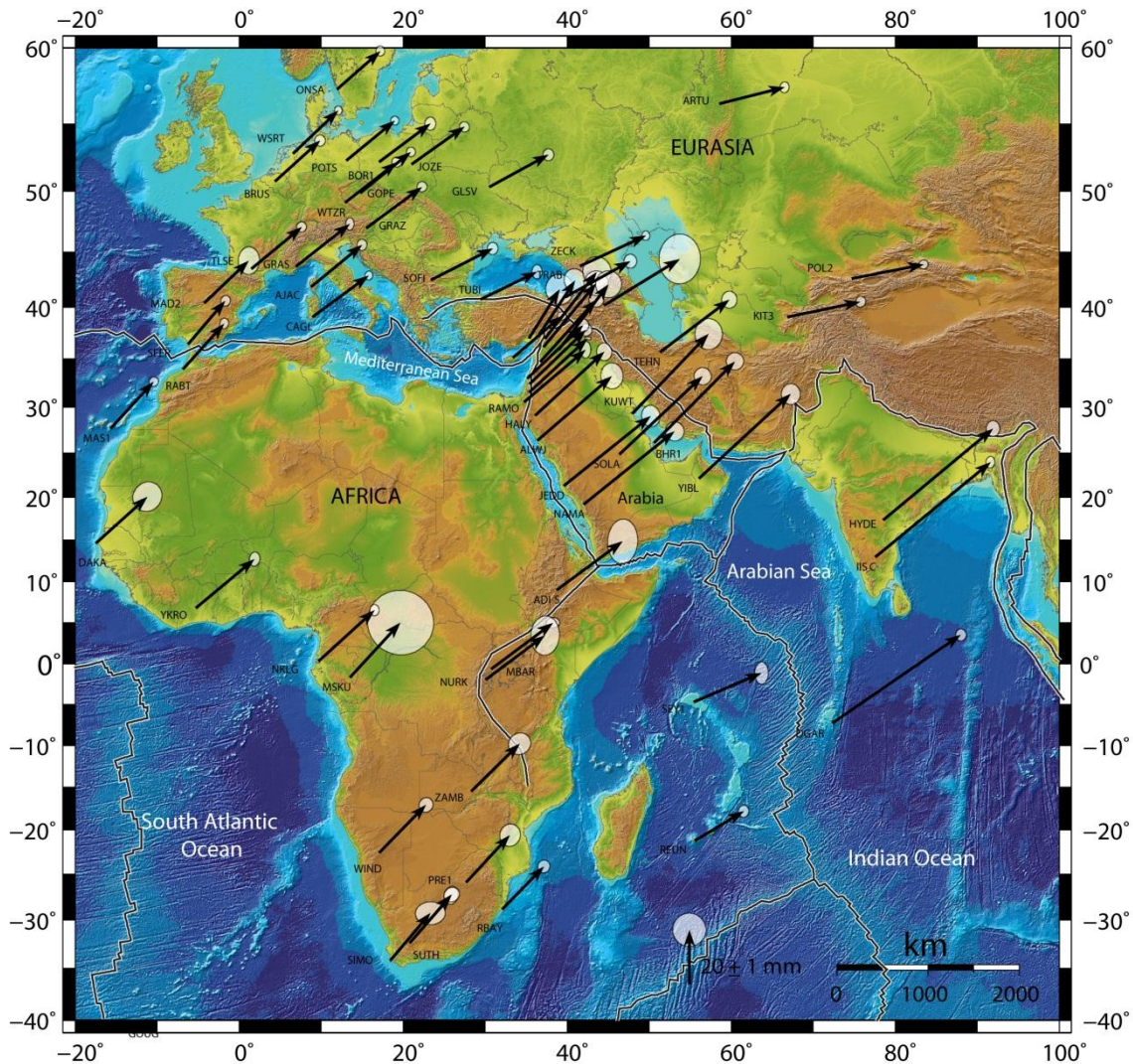
Figure III.12: GPS velocity field of the IGS permanent stations used in this study to constrain our observations to the global GPS network and their 95% confidence ellipses shown in the ITRF05 reference. Data are from January 1998 to December 2011.

The relatively large error ellipses for some IGS sites (e.g. ADIS, MSKU) are probably caused by a lack of data (discontinuous measurements) or other problems of instability of the site. In general, we can observe that our GPS velocity field is well defined in the ITRF05 reference frame and the vectors show reasonable uncertainties for the continuous sites (Red

vectors in Figure III.13). In addition, we can observe also that the velocity field of the regional GPS network shown in Figure III.13 is consistent with the global solution of the international sites, the error ellipses are clearly larger for our GPS points in Syria and Turkey than others CGPS points which can be considered as normal for such number of measurements and time span (2 measurements in Syria and 3 in Turkey). But we can observe that the regional continuous sites have the same uncertainties level (< 1 mm/yr) as the IGS points.
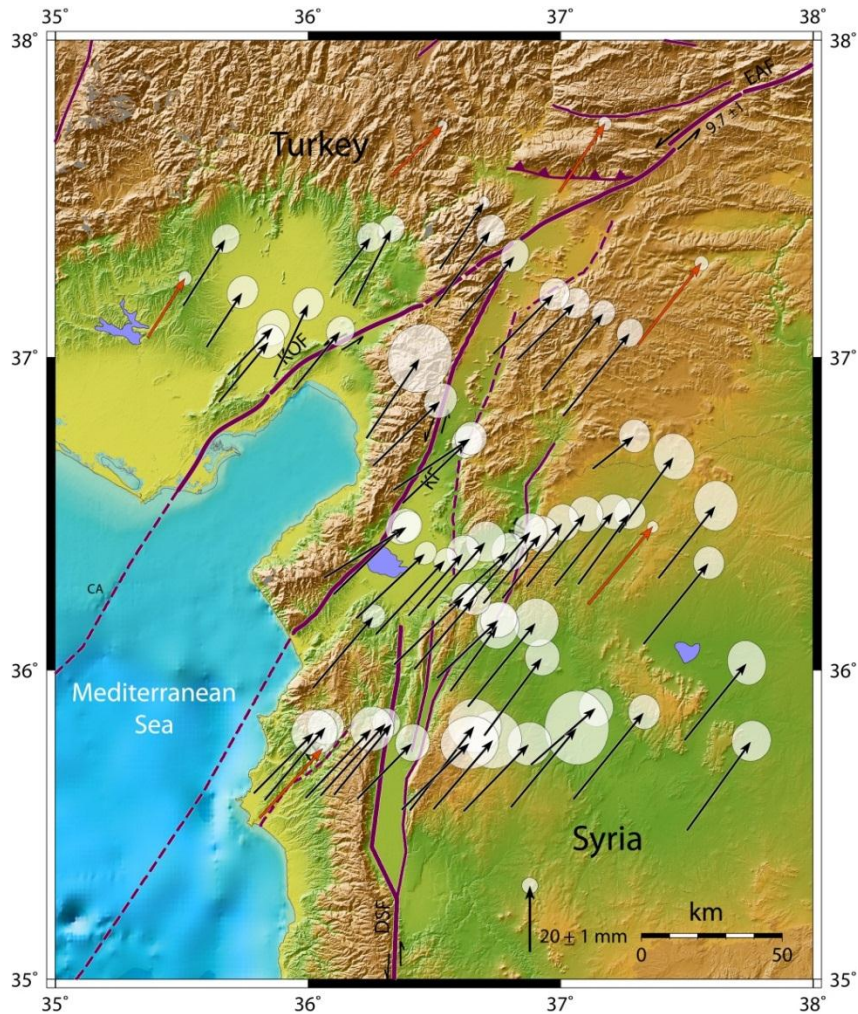
Figure III.13: GPS velocity field of the Hatay GPS network and regional permanent stations in Syria and Turkey and their 95% confidence ellipses shown in the ITRF05 reference. Red vectors are for CGPS.

The sufficient number of GPS sites in the Arabian and Eurasian plates will help in the realization of reference frames and the relative Euler poles for these plates, which will be used to determine the relative motion and rotation received by their limited faults. Figure III.12 shows clearly the difference in velocity rate between the Arabian and African plates and

attests for the continuously opening of the Red Sea (McKenzie and Davies, 1970; Cochran, 1983).

The rotation pole and Euler vectors of the related major plates need to be calculated in order to define new reference frames of our GPS velocity field. We used a set of sites belonging to specific plate and use their velocity vectors to define the Euler pole of this plate. These sites were chosen regarding to the measurement quality, the uncertainty level, and their spatial distribution and geometry. In paragraphs III.5.2 and III.5.3 we show the CGPS sites used to define the Euler pole of Eurasia and Arabia plates, respectively.

III.5.2 GPS velocity field in Eurasia reference frame

The good spatial distribution of the IGS permanent sites included in the processing of this study over the main plates (Eurasia, Africa, and Arabia, see Figure III.7) and their long time span of measurement (11 year of continuous data for the majority of sites), enable us to calculate the Euler poles for the major plates with good level of uncertainty compared to other previous estimations. The use of our new Euler poles to represent the velocity field in different reference frames is important for the interpretation of the velocity field. For example, in order to define the Arabian reference frame with minimum of residuals for the sites in Arabia plate it is crucial to use the Euler pole calculated from these sites velocity. Our Euler poles estimations especially for the Arabia plate were done based on good number of sites and considerable time of measurement which give them the preference compare to previous estimations.

Many tests were performed to realize the Eurasia rotational pole by minimizing the velocity components of different sites, the residuals were calculated for different sites group until we determined the sites which give the minimum of residuals.

We used 13 sites distributed in Eurasia plate to realize a reference frame in Eurasia fixed. All these sites have continuous measurements and very good level of uncertainty, less than 0.33 mm/yr and 0.4 mm/yr for the east and north components respectively. Table III.5 shows the velocities of 13 GPS sites used in the determination of the Eurasian reference frame in ITRF2005 and the residuals (velocities in Eurasian reference frame) of the solution. This solution gives WRMS total = 0.42 mm/yr. The Euler pole of Eurasia plate calculated from these sites is defined at 57.351±0.7 °N, -93.045±0.8 °E with a rotation rate of 0.255±0.004 °/Myr.

Figure III.14 shows the GPS velocity field of permanent sites in Arabia and Anatolia plates and the surrounding sites in Eurasian reference frame. The realization of this velocity field was done by subtracting the rotation of Eurasia plate from the ITRF05 velocity field. The vectors of our GPS network are not shown in this figure for a problem of visibility and they are shown in Figure III.15.

Longitude	Latitude	ITRF 2005		Eurasia		Sig. E	Sig. N	Corr	Site
		Ve	Vn	Ve	Vn				
17.073	52.277	18.79	14.06	-0.07	-0.19	0.33	0.40	-0.002	BOR1
4.359	50.798	16.56	15.01	-0.15	-0.15	0.32	0.34	0.004	BRUS
30.497	50.364	21.69	11.85	-0.09	-0.69	0.33	0.36	0.006	GLSV
14.786	49.914	18.56	14.99	-0.47	0.52	0.27	0.29	-0.005	GOPE
6.921	43.755	19.77	15.59	0.69	0.55	0.25	0.38	0.022	GRAS
15.493	47.067	20.50	15.09	0.64	0.68	0.30	0.31	0.010	GRAZ
21.032	52.097	19.41	13.79	-0.27	-0.03	0.30	0.31	-0.035	JOZE
11.926	57.395	15.90	14.00	-0.45	-0.71	0.27	0.30	-0.015	ONSA
13.066	52.379	17.83	14.66	-0.21	0.04	0.25	0.27	-0.009	POTS
1.481	43.561	18.44	15.30	0.30	0.03	0.30	0.31	0.023	TLSE
6.605	52.915	16.51	15.74	-0.04	0.69	0.23	0.27	0.005	WSRT
12.879	49.144	19.09	14.83	0.23	0.20	0.30	0.30	0.001	WTZR
41.565	43.788	24.13	11.18	-0.48	0.58	0.24	0.29	0.016	ZECK

Table III-5: the IGS sites used to determine the Eurasian reference frame and Euler pole of rotation, and their horizontal velocity components in ITRF05 and Eurasia reference frame and the uncertainties for East and North directions.
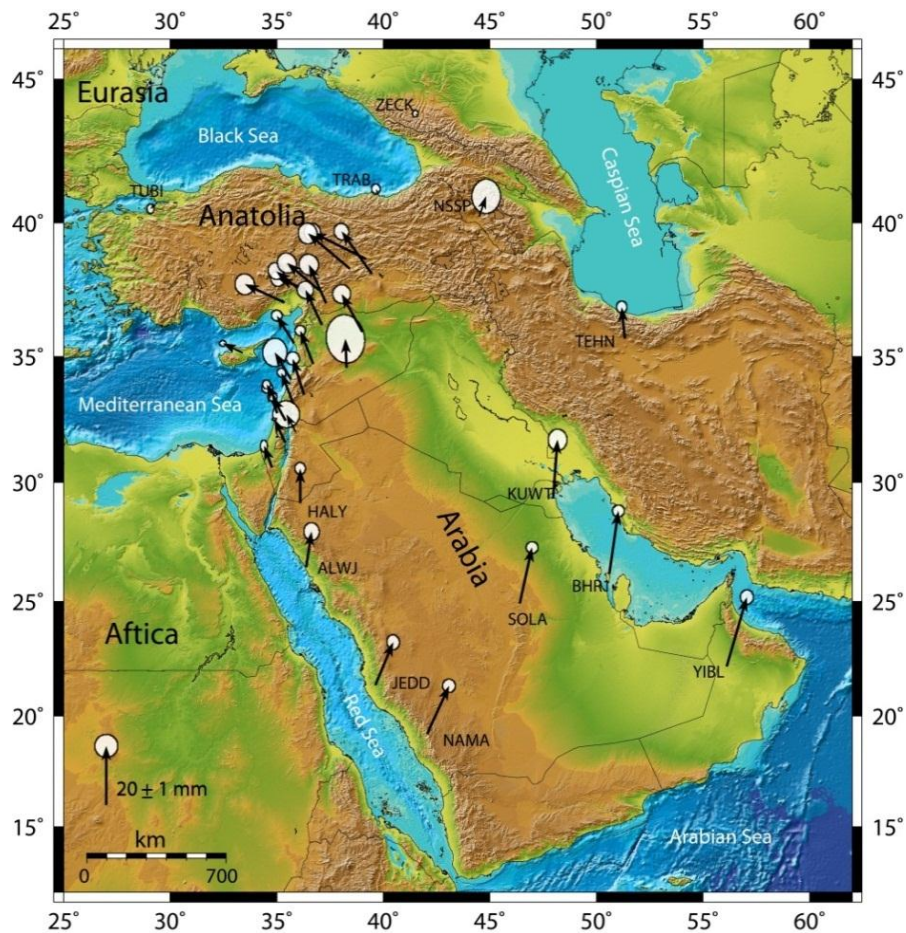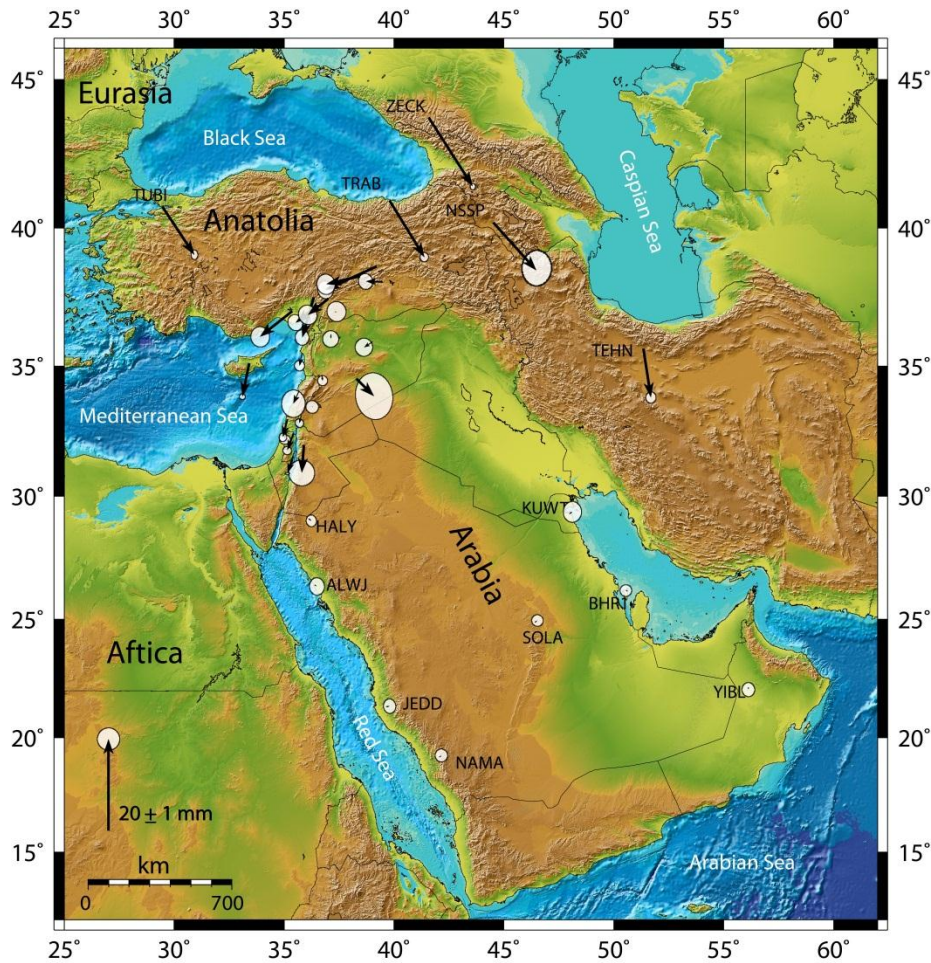
Figure III.14: GPS velocity field of the permanent GPS sites in Arabian plate and its vicinity and with their 95% confidence ellipses shown in the Eurasia reference frame realized in this study.

The velocity field of Arabian plate in Eurasian reference frame (Figure III.14) shows the rotational movement relative to Eurasia plate around an Euler pole located at 27.533±0.6 °N, 17.715±0.8°E with an angular velocity rate of 0.393±0.005 °/Myr. This estimation of Euler pole is compatible with recent geodetic study of ArRajehi *et al.*, (2010) who found an Euler pole at 27.5±0.1 °N, 17.6±0.3 °E, 0.404±0.004 °/Myr (Table III.6). The clear relative difference in the movement rate between the sites related to Arabia plate (e.g., YIBL, SOLA, NAMA) and those located in the Eurasia plate appear in Figure III.14 (TUBI, TRAB, and ZECK) with a very small rate (~2 mm/yr), express the northward motion of Arabia toward the Eurasia with a rate of ~ 20 mm/yr estimated in previous Geodetic studies (e.g., Reilinger *et al., 2011).*
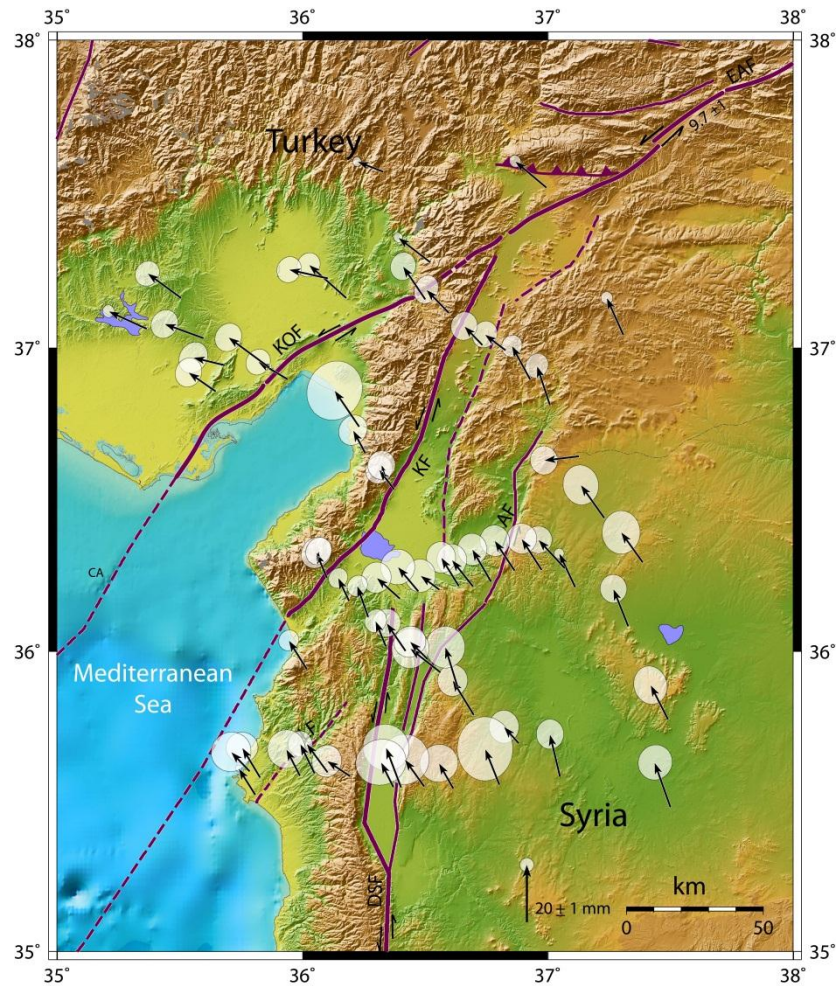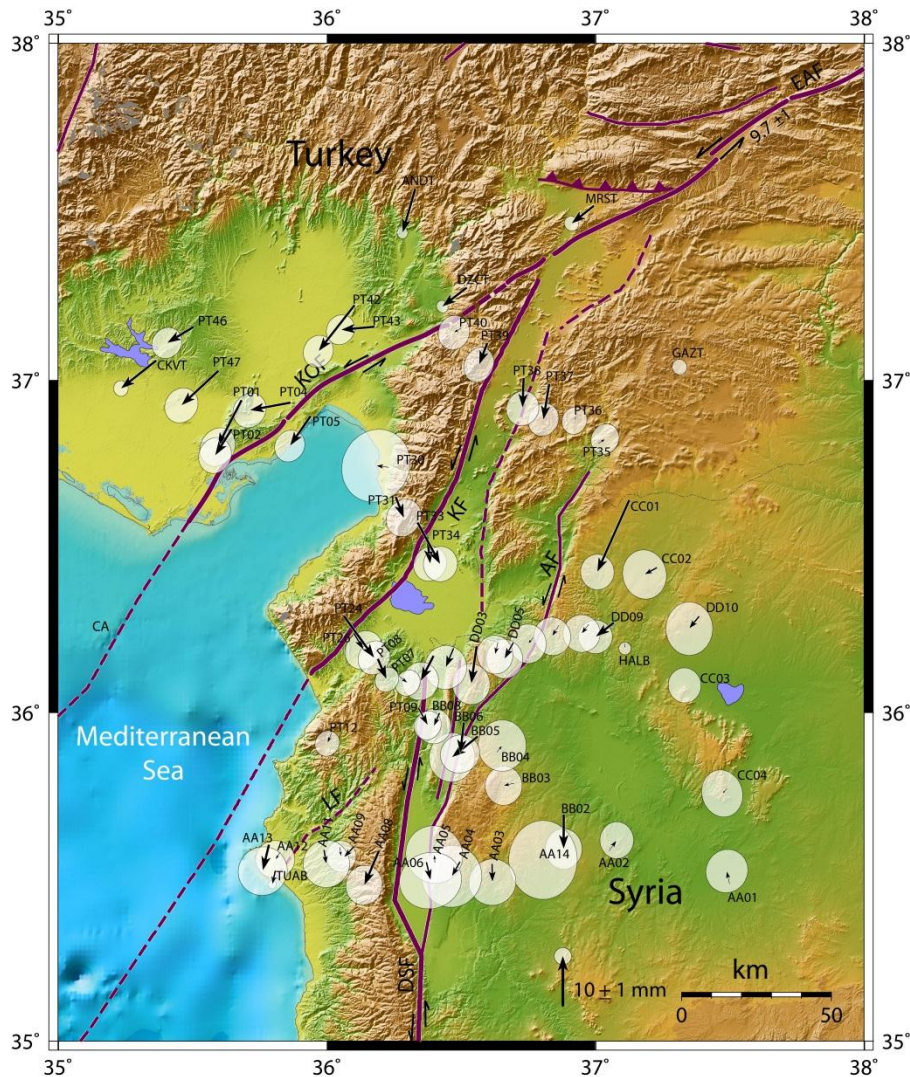
Figure III.15: GPS velocity field of the Hatay GPS network and regional permanent stations in Syria and Turkey and their 95% confidence ellipses shown in the Eurasia reference frame realized in this study.

The northward motion of Arabia plate creates a region with intense deformation in the north and northeastern boundaries of the Arabian plate (Reilinger *et al.*, 1997b; McClusky *et al.*, 2000; McClusky *et al.*, 2003; Tatar *et al.*, 2004). This fact is demonstrated in our velocity field in Figure III.14 by the clear difference between the NNE velocity vectors in Arabia plate with a rate of ~25 mm/yr (e.g., KUWT, YIBL, and BHR1) and the other GPS vectors to the north-northeast of Arabia plate. The extrusion of Anatolia plate is also easily pointed in Figure III.14 by the westward direction of some GPS vectors.

Euler pole	Lat. °N	Lon. °E	Rotation rate °/Myr	Reference
EU	57.35±0.73	-93.04±0.85	0.255±0.004	This study
EU	56.33±0.54	-95.97±0.96	0.261±0.003	Altamimi et al., (2007)
EU	55.851	-97.378	0.263±0.001	SOPAC solution
AR	50.64±0.51	-5.66±1.24	0.507±0.014	This study

AR	49.64±0.58	5.06±2.27	0.579±0.019	Altamimi et al., (2007)
AR	50.209	4.162	0.567±0.011	SOPAC solution
AF	49.66±0.67	-83.81±1.58	0.251 ±0.004	This study
AF	49.95±0.48	-82.50±1.25	0.269±0.003	Altamimi et al., (2007)
AF	48.997	-80.424	0.275±0.003	SOPAC solution
AR-EU	27.53±0.6	17.71±0.8	0.393± 0.005	This study
AR-EU	27.5±0.1	17.6±0.3	0.404±0.004	ArRajehi et al., (2010)
AR-EU	28.4±0.9	18.4±1.0	0.428±0.009	Reilinger et al., (2006)
AR-EU	27.4±1.0	18.4±2.2	0.40±0.04	McClusky et al., (2003)
AR-EU	26.22±1.2	22.87±2.1	0.427±0.029	Sella et al., (2002)
AR-EU	27.9±0.5	19.5±1.4	0.41±0.1	Vernant et al., (2004)
AR-EU	24.6±2.3	13.7±5.0	0.5±0.05	NUVEL1-A (DeMets et al., 1994)
AR-AF	31.55±0.8	23.16±1.1	0.385±0.006	This study
AR-AF	31.7±0.2	24.6±0.3	0.369±0.005	ArRajehi et al., (2010)
AR-AF	31.5±0.6	25.2±0.7	0.393±0.005	Reilinger et al., (2006)
AR-AF	30.5±1.0	25.7±2.3	0.37±0.04	McClusky et al., (2003)
AR-AF	31.64±2.5	20.29±1.1	0.38±0.018	Vigny et al., (2006)
AR-AF	31.26±1.3	29.55±1.8	0.400±0.030	Sella et al., (2002)
AR-AF	31.5±1.2	23.0±2.7	0.40±0.05	Chu and Gordon (2002)
AR-AF	32.2	24	0.376	Joffe and Garfunkel (1987)
AR-AF	32.59	23.7	0.418	Jestin et al., (2007)

Table III-6 :   Euler vectors for Arabia (AR), Africa (AF), and Eurasia (EU) and the relative Euler poles of AR-EU and AR-AF this study and other previous studies. Our Euler poles are calculated from GPS vectors of this study. SOPAC solution (http://sopac.ucsd.edu/cgi-bin/poleRotationValues.cgi).

The Figure III.15 shows the velocity field in Eurasia reference frame for the campaign sites of our study in Syria and Turkey. The deformation and the relative plate movement cannot be visibly identified using this velocity field in such small region, therefore a velocity field in Arabian reference frame is needed in order to demonstrate the deformation along the plate boundaries and others faults which contribute to the kinematic of the junction.

III.5.3 GPS velocity field in Arabia reference frame

The definition of the Arabian reference frame was performed by the use of permanent sites well distributed in Arabia plate and far from the boundaries, where the deformation affects the velocity vector and by consequence the determination of the Arabian Euler vector. The 8 sites shown in Table III.7 were only used to define the rigid core of Arabia plate and all of them have uncertainty below 1 mm/yr. The permanent sites in the northeast of the plate where excluded because of the possible internal deformation. The velocities of these sites

were minimized in the ITRF05 reference and an Euler pole of Arabian plate was calculated at 50.645±0.51 °N, -5.662±1.24 °E with an angular velocity of 0.507±0.014 °/Myr. The Arabia GPS Euler vector provides a very good fit to well constrained velocities at GPS sites distributed in the Arabia plate (Figure III.14) and it give a WRMS = 0.62 mm/yr.

Longitude	Latitude	ITRF 2005		Arabia		Sig. E	Sig. N	Corr	Site
		Ve	*Vn*	*Ve*	*Vn*				
36.378	26.458	27.33	23.65	0.50	-0.34	0.67	0.78	-0.025	ALWJ
50.608	26.209	29.64	29.80	-0.34	0.09	0.52	0.52	0.001	BHR1
36.100	29.139	25.35	23.38	0.60	-0.49	0.46	0.53	-0.033	HALY
39.631	21.369	31.78	25.54	0.76	0.10	0.55	0.65	-0.041	JEDD
47.972	29.325	27.91	29.23	0.62	0.45	0.82	0.93	0.001	KUWT
42.045	19.211	33.29	26.79	0.47	0.32	0.56	0.58	-0.009	NAMA
46.401	24.911	30.44	28.61	0.54	0.42	0.52	0.52	-0.016	SOLA
56.112	22.186	33.58	30.96	0.00	-0.48	0.57	0.63	-0.013	YIBL

Table III-7: the permanent GPS sites used to determine the Arabian reference frame and Eular pole of rotation, and their horizontal velocity components in ITRF05 and Arabia reference frames and the uncertainties for East and North directions.

The GPS velocity field in Arabian reference frame (Figure III.16) indicates no significant internal deformation (WRMS of residuals motions for Arabia equals to 0.62 mm/yr) in agreement with other geodetic studies in the region (ArRajehi *et al.*, 2010; Reilinger and McClusky, 2011). Most GPS sites in the Arabian plate have a velocity rate less than the GPS uncertainties (~1 mm/yr) except in the northwest near to the triple junction where the deformation become more complex and many geological structures contribute to the active deformation pattern at the plate boundaries, like the Palmyride fold belt where previous studies suggest shortening rate of ~1 mm/yr (Chaimov *et al.*, 1990; Alchalbi *et al.*, 2010).

Figure III.16: GPS velocity field of the permanent GPS sites in Arabian plate and around and their 95% confidence ellipses shown in the Arabia reference frame realized in this study.

The northern boundary of the Arabia plate shows a significant left lateral slip rate at the EAF, the same observation can be also made for the DSF. The sites distributed in the Anatolia and Sinai plates have a significant sinistral movement relative to the sites belong to Arabia plate.

The velocity field obtained from our GPS network sites (Figure III.17) suffers a high rate of uncertainty, especially sites in Syria. As it was mentioned before, our GPS sites in Syria were measured twice, during the campaigns of 2009 and 2010, while sites in Turkey have additional measurements during the campaign of 2011 that explains the better uncertainties of sites in Turkey compared with those in Syria. In general, the GPS velocity vectors have uncertainty of 2.42 mm/yr in Syria and 1.92 mm/yr in Turkey. The CGPS sites in Turkey and Syria have better uncertainties with less than 1 mm/yr (e.g., HALB, TUAB in Figure III.17). We notice also that vectors in Syria have abnormal values or directions (Figure

III.17) which are unexpected in the Arabian reference frame and can be clarified by the insufficient measurements (2 measurements with 1 year of time difference).

Figure III.17: GPS velocity field of the Hatay GPS network and regional permanent stations in Syria and Turkey and their 95% confidence ellipses shown in the Arabia reference frame realized in this study.

Despite the high uncertainty of our GPS velocity field, it offers a good tool to describe the active deformation pattern in the Hatay triple junction and have an assessment of the strain accumulation along major faults in the region as illustrated in Figure III.18. The velocity vectors shown in Figure III.17 and III.16 do not disagree with other velocity rates from other studies (1–2 mm/yr across DSF, 2–3.5 mm/yr across KOF, 3–5 mm/yr across KF and 2–3 mm/yr across the AF, (Gomez *et al.*, 2007b; Meghraoui *et al.*, 2011). A quick and simple interpretation of the GPS velocity field (Figure III.17) and the GPS velocities parallel and perpendicular to major faults in the region (Figure III.19) demonstrate that GPS points located

in the west of DSF (e.g., AA13, TUAB) have an insignificant southward movement relative to those in the other side of fault. This observation can be carried out after excluding some sites which do not necessarily represent appropriately the plate motion and have a significant error ellipsis (e.g., BB02 in Figure III.17). This leads us to suggest that the DSF does not show significant slip rate along its northern segment and a maximum value can be deduced from the GPS vectors is 1.0-2.0 mm/yr (Figure III.18) which is in agreement with Alchalbi *et al.,* (2010). Comparing the vectors in the east and west of Afrin fault (e.g., DD03, DD05, HALP, DD08 in Figure III.18) and their velocities parallel to the fault in profile 2 (Figure III.19), we can propose a left lateral slip rate value of ~3.0 mm/yr, however it is not totally in agreement with the 4.7±0.7 mm/yr proposed velocity by Meghraoui *et al.,* (2011).

The south-westward motion of Anatolian plate relative to Arabia can be deduced from the vectors of CKVT, PT47, PT01, and ANDT in Figure III.17, which have a maximum velocity of ~10 mm/yr (Figure III.17). Points, like PT05, PT39, and PT31 show a movement rate of 2.0-6.0 mm/yr (Figure III.17) which is half of those of Anatolian plate and the slip rate of EAF. This leads us to conclude that these pointes do not belong to the Anatolian plate. The KOF in this case appears as a plate boundary of Anatolia with a slip rate of ~4.8 mm/yr (profiles 3 and 4 in Figure III.19). The difference in slip rate between KOF and EAF which has ~10.0 mm/yr (McClusky *et al.*, 2000; ArRajehi *et al.*, 2010) leads us to conclude that the KOF in not a segment of EAF.
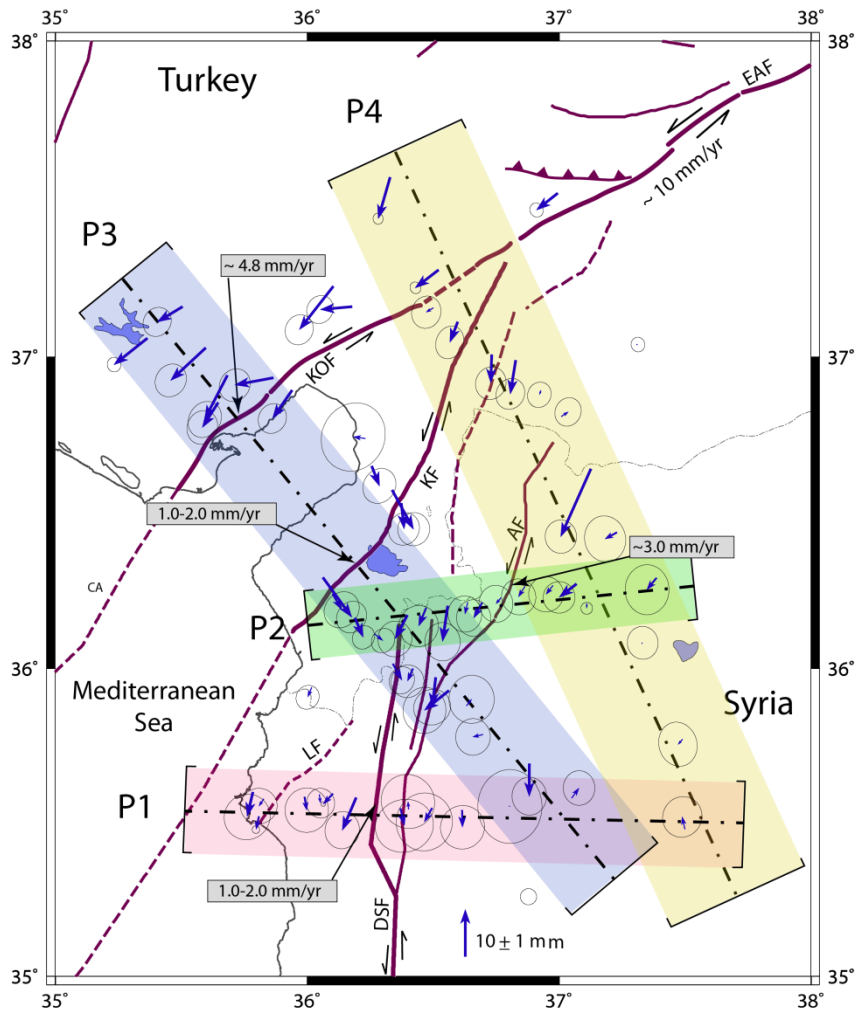
Figure III.18 : Illustration of the faults strike-slip rates resulting from our GPS velocity field of the Hatay GPS in Syria and Turkey. GPS vectors and their 95% confidence ellipses are shown in the Arabia reference frame realized in this study. Profiles P1, P2, P3, and P4 are shown in Figure III.19.

Furthermore, an equivalent observation is possible for the velocity vector of points east and west of the Karasu Fault, the points around the KF show similar south-east direction with a significant difference between points in the west of KF (PT24, PT33) and those in the east (PT26,PT34) (Figure III.17), the relative difference suggests a small component of left-lateral strike-slip with a compressional component of 2.0-5.0 mm/yr (See Figure III.19, Profile 3), this assumption contradicts with previous studies suggesting extensional behavior (e.g., Reilinger *et al.,* 2006).
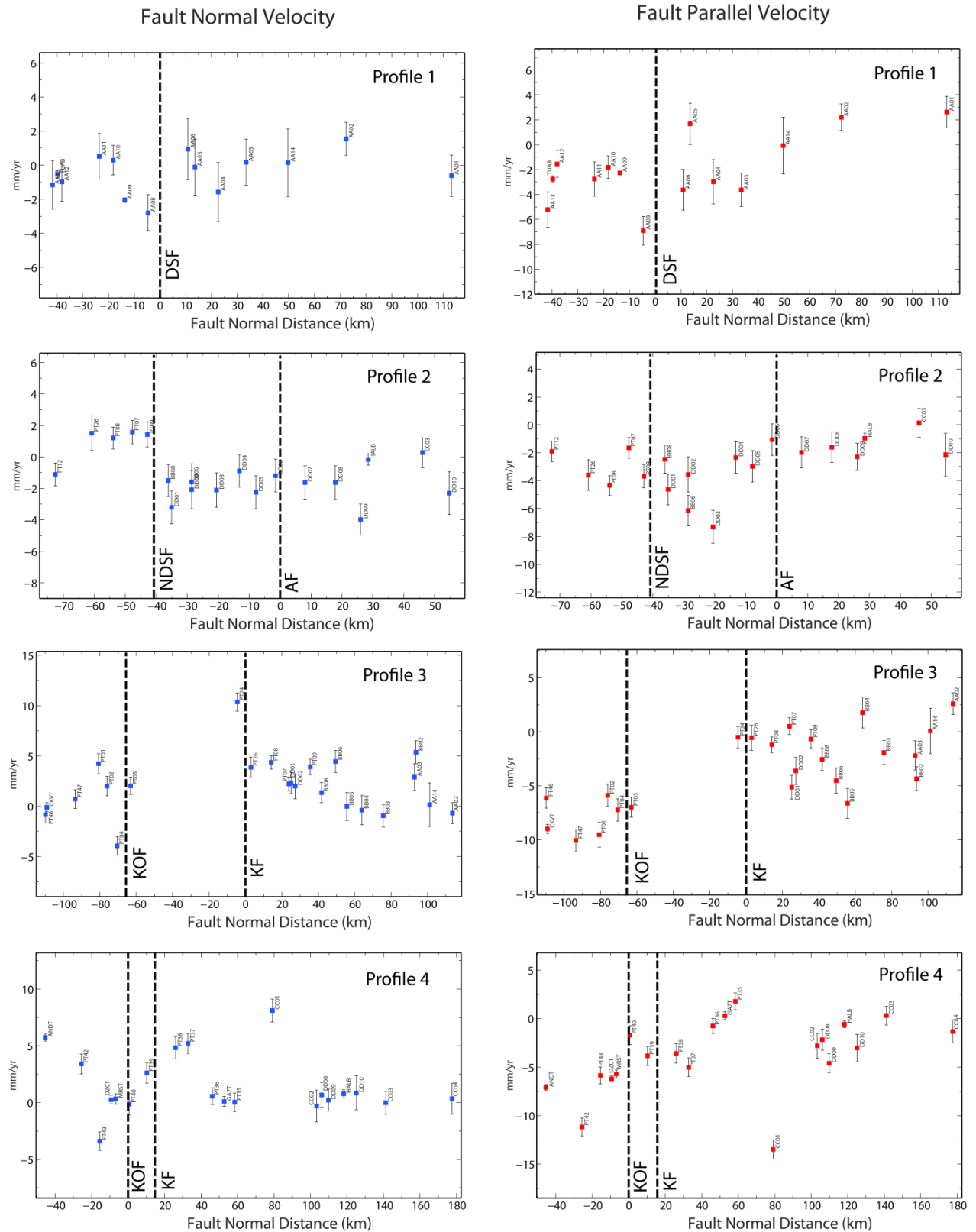
Figure III.19 : Plots showing the GPS velocities parallel (Right) and perpendicular (left) to the main faults in the Hatay triple junction region. The location of the profiles is shown in Figure III.18.

III.6 Conclusions

The new GPS network in Hatay triple junction provides a new geodetic tool to characterize the deformation in a complex area from tectonic point of view. The 57 GPS sites in north-west Syria and south-east Turkey installed in 2009 and repeatedly measured in 2010 and 2011 have several advantages for the present-day and the future research in the region. During the design and installation of our GPS network we took into account the previous GPS network existing in the region (Reilinger *et al.*, 2006; Alchalbi *et al.*, 2010). Previous GPS sites were used in the big scale studies to describe the motion of the major plates Anatolia, Africa, and Arabia, and the deformation along their boundaries. The GPS network in Hatay region is a regional network, the density of sites and their alignment in profiles perpendicular to most geological features give the ability to better study the small fault segments as well as the major faults.

The Hatay GPS network was supported by 71 IGS sites distributed on the different plates around the triple junction. These sites helped in the adjustment of our measurements to the global GPS network. Other continuous GPS sites from Syrian and Turkish GPS network which are near to the study area were also introduced to our network. The GPS sites in Syria were measured only in the campaigns of 2009 and 2010 which affected negatively the GPS velocity field. The GPS vectors suffer from high uncertainties because of the short time span (1 year). In general, the examination of time series and histograms of wrms and nrms showed that our solution is in the acceptable level of uncertainty and can be used in the kinematic interpretation of the Hatay triple junction.

The estimation of Euler vector of Arabia relative to Eurasia plate was performed by different continuous GPS sites well distributed and far from any high rate deformation zone which give our estimation a high reliability. Arabian Euler pole in this study is similar to other estimations (e.g., ArRajehi et al., 2010). In our study we define an Euler pole for the relative rotation of Arabia with Eurasia at 27.533±0.6°N, 17.715±0.8 °E and an angular velocity of 0.393±0.005 °/Myr. The Euler pole of Arabia in ITRF05 reference frame is 50.645±0.51°N, -5.662±1.24 °E, 0.507±0.014 °/Myr. No significant internal deformation in Arabia plate is detected since the velocity rate of GPS sites are less than the GPS uncertainties (~1 mm/yr), Eurasia plate is moving around a pole located at 57.351±0.7 °N, -93.045±0.8°E with angular rate of 0.256±0.004 °/Myr.

Although the vectors of our regional GPS sites have relative high uncertainties, a simple interpretation of the parallel and perpendicular velocities of the four main profiles in our GPS network (Figure III.18), enable us to propose slip rate of different faults. We found a slip rate along the north DSF of 1.0-2.0 mm/yr, ~3.0 mm/yr along the AF, and 4.8 mm/yr along the KOF. These estimations agree with most of previous studies e.g., (McClusky *et al.*, 2000; Alchalbi *et al.*, 2010; ArRajehi *et al.*, 2010; Meghraoui *et al.*, 2011).

The GPS velocity vectors obtained in this study will be partially used in the block modeling presented in Chapter IV. The GPS vectors in Syria will be excluded because of the insufficient quality and uncertainty. It will be compensated by the existence of GPS sites from other studies. We think that extra measurements on this GPS network will increase significantly the quality of velocity field, and then will help more in the understanding of kinematic of the triple junction.

Chapter IV

IV- Block modeling with GPS measurements

IV.1 Introduction

The active deformation patterns and the kinematic configuration in the Hatay triple junction cannot be directly explained by the GPS velocity field as shown in chapter III. Using simple models to solve the deformations like the 2-D elastic dislocation model of Savage and Burford (1973), we can assess the strain accumulation, slip rate, and locking depth of the fault segments at the Hatay triple junction, thanks to the density of our regional GPS network and the distribution of our GPS sites along profiles perpendicular to most of faults with sites near and far from most of faults. However, the complexity of the region resulting from the existence of small fault segments and other tectonic features, and its contribution to the kinematics of the region, makes this models unable to provide a complete image of the deformations in such complex area, since they mostly assume an infinite fault length which is not the case in the triple junction. This chapter shows that the active deformation at the Hatay triple junction and its nearby region can be explained by a finite number of rotating elastic spherical blocks limited by faults. In this case, a large amount of deformation caused by the relative movements of blocks accommodated along the bounding faults.

We used *"DEFNODE"* program (McCaffrey, 1995; McCaffrey, 2002) that performs a 3D elastic dislocation model. The tectonic plates in this model are represented as closed spherical polygons on the earth surface. The faults are considered as the limits between two blocks and can be represented in 3 dimensions by along-strike nodes coincide with the blocks boundaries on the earth surface and down- dip nodes defining the fault direction, width, and dip angle.

Block rotation and fault locking parameters are inverted using the GPS velocities and applying dislocations in an elastic and homogeneous half-space (Okada, 1985). In this inversion, we minimize the data misfit defined by the reduced chi-square statistic, by applying simulated annealing to perform downhill simplex minimization described by Press *et al.,* (1986).

The GPS velocity field of our network in northwest Syria and south East Turkey was used partially in this modeling for the insufficient uncertainty of some GPS vectors. A combination of other GPS velocity fields (Reilinger *et al.*, 2006; Le Béon *et al.*, 2008; Alchalbi *et al.*, 2010; Al-Tarazi *et al.*, 2011) will be used also in this study. The data and the combination method are explained in Chapter IV.2.2.

We have tested several plate configurations to model the active deformation at the intersection between the three major tectonic plates of Arabia, Africa, Eurasia and their bounding major faults EAF, DSF, and CA. We also show the models tested with other micro blocks and faults in order to fit the GPS measurements. We present in this chapter the four main models. We started with the simplest model in which we calculate the active deformation along the three main faults and the rotation parameters of three major plates. The other models contain more tectonic structures such as the Karasu, Karatas-Osmaniye faults and the Amanous and Iskenderun blocks (Figure IV.4). Modeling results show that the simple model cannot explain adequately the GPS velocity field and thus a more complex model is required to have a good assessment of the strain accumulation along the plate boundary faults.

This chapter presents in detail the results of inversion results and the analysis of different profiles crossing the mapped faults (DSF, EAF, KOF, KF, and CA) represented in the model D (Figure IV.4). Parameters of slip deficit and locking depths on faults were deduced from model D, we also estimate the parameter ϕ (the ratio of locked to total slip along the fault surface, that is, the coupling fraction) and its variation on the fault plane. Detailed information about slip rates along the faults will be presented beside the adjusted block motions parameters and rotational Euler poles of the blocks.

IV.2 Data and analysis

IV.2.1 Data selection and rejection

In order to model the active deformation around the Hatay Triple Junction and deduce the physical parameters of major faults in the study region, we use our GPS velocity field together with previous GPS measurements around the Hatay Triple Junction. The GPS data sets and the way they are combined and used in modeling are described in the section below.

IV.2.1.1   GPS data obtain in this study

To model tectonic blocks around the Hatay Triple Junction, we used the velocity vectors from our regional network solution in Syria and Turkey presented in detail in the Chapter III. As explained in the chapter III, the GPS points in Turkey have been measured during 3 times between 2009 and 2011 whereas those in Syria were measured during only 2 campaigns in 2009 and in 2010. Therefore, in our modeling, we exclude the GPS sites in Syria because the velocity vectors have in general very high uncertainties in comparison with

those in Turkish side. This is also because we think that good and reliable velocities cannot be determined from only two campaigns. The exclusion of these points in Syria was compensated by the existence of numerous GPS vectors provided by Gomez *et al.*, (2007) in Syria. We keep the 6 permanent sites from the permanent Syrian GPS network.

IV.2.1.2   *GPS data from previous studies*
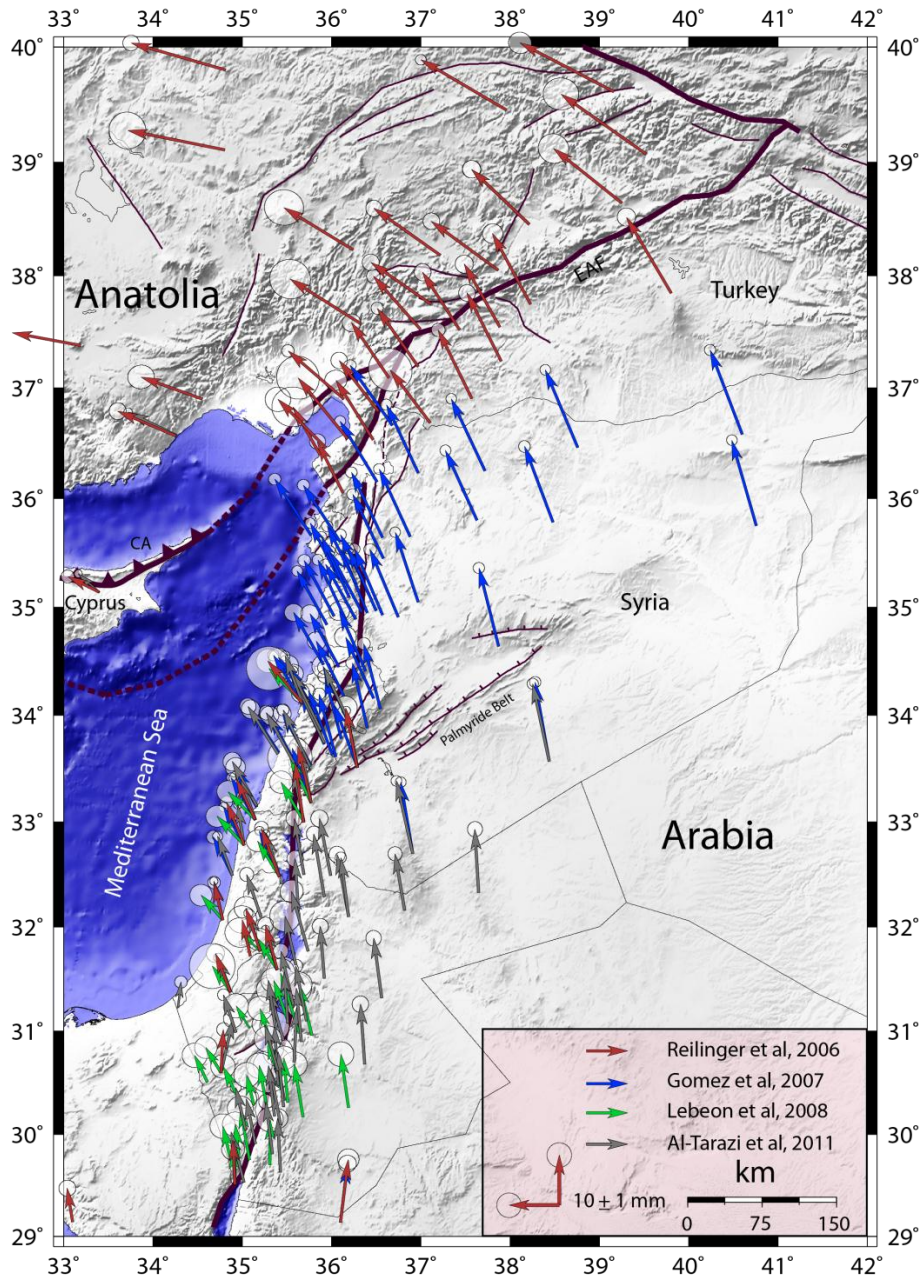
Figure IV.1: GPS horizontal velocity field and the 95% confidence ellipses obtained by previous campaigns in the Eastern Mediterranean region with respect to the Eurasia-fixed reference frame. GPS data are from Reilinger et al., (2006), Gomez et al., (2007), Le Béon et al., (2008)

and Al-Tarazi et al., (2011), and mapped faults from Meghraoui et al., (2011). Also, shown in the map are the three major faults in the region, EAF: East Anatolian fault, DSF: Dead Sea fault, CA: Cyprus arc.

In addition to the GPS solutions we obtained in this project, in our modeling we also use the GPS measurements of Reilinger *et al.,* (2006) for the period between 1988 and 2005, the solution of Le Béon *et al.,* (2008) over 6 years, the solution of Alchalbi *et al.,* (2010) with measurements between 2000 and 2008 over Syria and Lebanon, and the solution of Al-Tarazi *et al.,* (2011) with measurements between 2005 and 2010 in the southern part of the Dead Sea Fault.

In the modeling, only the GPS vectors that are located in our model domain were used in the parameters assessment (Figure IV.5). Many of them were also rejected due to the following reasons: (1) those that have a velocity value clearly different from other nearby velocities which can be related to site effects and not related to tectonic effect specially the sites far from faults, (2) those vectors with uncertainty greater than 3 mm/yr. The exclusion does not affect the inversion significantly because most of the rejected vectors (4 points) are common points in the different solutions.

IV.2.2 Combination of different GPS velocity solutions

In addition to our GPS solution in Turkey and the 6 continuous GPS station in Syria, we use the solutions of (Reilinger *et al.*, 2006; Le Béon *et al.*, 2008; Alchalbi *et al.*, 2010; Al-Tarazi *et al.*, 2011). These different solutions must be appropriately combined in order to be used in the block modeling. They are individually combined using GAMIT that applies rotational transformations minimizing the residual misfit of GPS velocities for the sites that are common to Reilinger *et al.,* (2006). Hence, to apply the rotational transformation, we use 12 common sites from Le Béon *et al.,* (2008), 12 common sites from Alchalbi *et al.,* (2010), 16 common sites from Al-Tarazi *et al.,* (2011), and 10 common sites from our study, with RMS misfit of 0.48, 0.66, 0.14 and 0.36 mm/yr, respectively. Part of the combined data is shown in Figure IV.1 in Eurasian fixed reference frame.

All the common points are permanent sites. The distribution of these points in the study region and far in Arabian, Eurasia and African plate give the rotational transformations with high reliability and well fit to each other. The choice of Reilinger *et al.,* (2006) solution for the transformation is due to its longer time span of measurements (~17 years), the number

and distribution of the sites, and the small uncertainties of the velocity vectors. In all these criteria, GPS velocity field of Reilinger *et al.,* 2006 gives the best solution.

GPS solution	Time span	Common sites	RMS mm/yr	NRMS
Reilinger *et al.*, 2006	17 years	---	---	---
Le Béon *et al.*, 2008	6 years	12	0.48	24.21
Alchalbi *et al.*, 2010	8 years	12	0.66	17.84
Al-Tarazi *et al.*, 2011	5 years	16	0.14	32.11
This study	3 years	10	0.36	7.2

Table IV-1: The different GPS solutions used in the inversion and their time span, the number of common sites, the RMSs fit, the NRMSs of the transformations between Reilinger et al., 2006 and all other solutions.

IV.3 Inversion approach (Method)

In this method the tectonic blocks (plates) are assumed to be closed spherical polygons on the earth surface with faults coinciding with the block boundaries. Each point within a block is estimated to rotate with the same angular velocity (rigid blocks). At the edge of the model domain, the block boundaries are considered as fully creeping faults. Therefore, the model is not affected by the boundary conditions. The relative angular velocities between blocks, the creep distribution along the faults, and GPS velocity field rotations are estimated by least squares fit to GPS vectors.

Therefore, inversion procedure should realizes a simultaneous estimation of the angular velocities of elastic blocks on a sphere and creep fractions on block-bounding faults (e.g. coupling fraction). This is done by using the DEFNODE program provided by McCaffrey (1995; 2002; 2005) that uses simulated annealing to downhill simplex minimization (Press *et al.*, 1986). DEFNODE minimizes data misfit, defined by the reduced chi-square statistic: $\chi_n^2 = (\sum r^2/s^2) / DOF$, where **r** is the residual, **s** is the standard deviation and DOF is the degrees of freedom which is the number of data minus the number of free parameters.

IV.4 Faults

The faults in this models are represented in 3D dimensions within a spherical earth; each fault was formed by a series of node points on the surface and in depth (McCaffrey, 1995; McCaffrey, 2002) (Figure IV.2). The position of nodes in depth defines dip and curvature of the fault. Our faults are almost vertical with 89°.
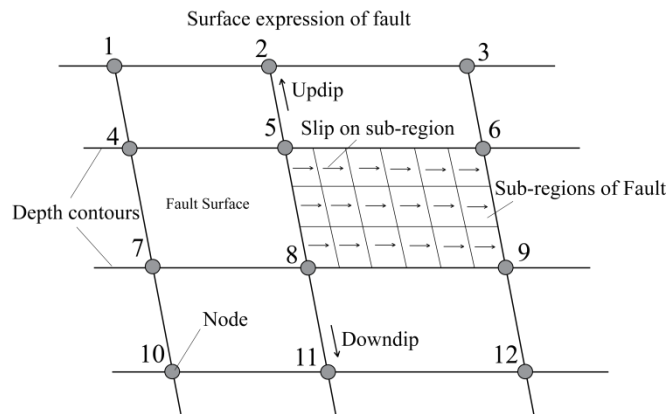
Figure IV.2: Fault surface specified by nodes in 3 dimensions, shows the numbering system for the nodes.

All faults in our models extend down to 30 km depth, below which faults are considered to be creeping at same rate of the relative velocity of related plates. The fault surface is approximated by tiles of quadrilateral (squares) patches of 2x2 km in size along the strike and dip direction. The patches are chosen to be very small in order to reduce the deviations from rectangles since the formulation of Okada (1985) used assumes displacement on rectangle patches. The effect of using squares can be neglected because only the centroid, orientation, and area of the fault patch are important (McCaffrey, 2005).

Since the faults are locked during the interseismic period, the short-term slip (creep) rate across the fault is too small and unimportant in compared to the long-term slip rate deduced from the relative motion of the two adjacent plates.

In this work we use McCaffrey (2005) approach, hence we use a purely kinematic quantity represented as ϕ.

$$\phi = 1 - V_c/V$$

Where:

-   V_c is the short-term creep vector (the steady displacement rate across the fault surface over a short time, presumably parallel to V).

-   *V* is the long-term slip vector on the fault (over many earthquake cycles) (i.e., plate velocity).

When $\phi = 0$, the creep occurs at the full relative motion between two blocks and if $\phi = 1$ there is no creep on the fault in the interseismic period which mean the fault is totally locked. When $0.0 < \phi < 1.0$, the fault is partially locked, in most cases, ϕ is neither 0 nor 1, which is interpreted as a spatial average of creeping and locked patches on the fault surface (McCaffrey *et al.*, 2000; Scholz, 2002; Lay and Schwartz, 2004).

The relative motion of the blocks adjacent to the fault and their Euler vectors determine the motion on the fault. The slip rate deficit vector on the fault is the scalar coupling value ϕ multiplied by the relative motion vector *V* between the two blocks at a given fault. Interseismic back-slip approach (- $\phi*V$) is applied along the faults that separate blocks, following the elastic dislocation modeling (Savage, 1983) and the elastic half-space formulations of Okada (1985; 1992) to determine the elastic contribution to the velocity field from the fault slip rate deficit.

The fault behaviour is estimated by using the common approach of locking depth. The fault is assumed to be locked from the surface down to the locking depth Z1, below which it creeps partially till the depth of Z2 where it starts freely creeping at a full rate. In our study, we prevent the faults from creeping at the near surface by applying $\phi=1$ for $0 \leq Z \leq 7$ km. We then estimate values of the free parameter ϕ for the depth from 7 km to Z2 (which is also estimated in the inversion). ϕ decreases from 1 to 0 between the depths of Z1 and Z2 (down to 30 km). Therefore, while the fault is partially locked ($0.0 \leq \phi \leq 1.0$) at depths between Z1 (min 7 km) and Z2, it creeps freely at a full rate ($\phi = 0$) below Z2. As illustrated in Figure IV.3, the transition from fully locked ($\phi = 1$) to fully creeping ($\phi = 0$) state between Z1 and Z2 can be assumed to be either linear (blue line) or obey an exponential function (green line) proposed by Wang *et al.,* (2003). In this study, we use the approximation of Wang *et al.,* (2003) in all the models. Nodes are placed on the surface and down-dip till to the depth of 30 km. The choice of the value 7 km for Z1 (where fault is prevented to creep by the $\phi = 1$ constraint) was taken into account studies of locking depth estimates along continental strike-

slip faults elsewhere in the world that suggest locking depths mostly below 7 km (Genrich *et al.*, 2000; Le Béon *et al.*, 2008; Walters *et al.*, 2011).
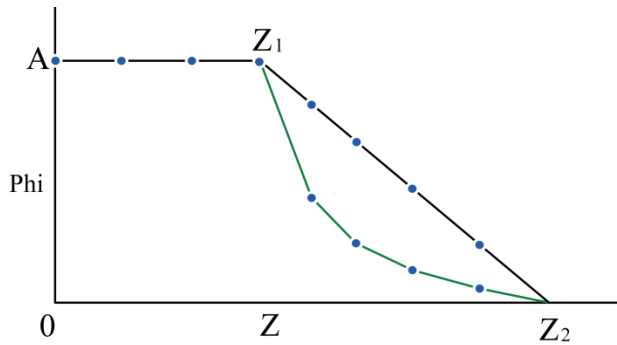
Figure IV.3: The distribution of ϕ (phi) along depth (green curve) between Z1 and Z2 following Wang et al., (2003). $\phi = 1$ at A.

According to Wang *et al.,* (2003)

Phi (z) = 1.0   for $Z \leq Z_1$

Phi (z) = {exp [– (Z'/G')] – exp [– (1.0/G')]} / {1.0 – exp [– (1.0/G')]} for $Z_1 < Z < Z_2$:

Phi (z) = 0.0   for $Z \geq Z_2$

Where: G' = G $(0.0 \leq G \leq 10)$

G' = 20 – G $(10 < G \leq 20)$

Z' = (Z – Z1) / (Z2 – Z1)

IV.5 Block model

Different block solutions have been tested to explain the GPS data presented above. Figure IV.4 shows the 4 different block models accounting the intersection between major Arabian, Anatolian, and African plates in the Hatay Triple Junction and the main faults forming their boundaries, along which interseismic strain is being accumulated to be released by the next big earthquake.

In the first stage of modeling (model A), we test the block model proposed by Reilinger *et al.,* (2006) which contains the Arabian, Anatolian, and African (Sinai) plates separated by the Dead Sea Fault, the East Anatolian Fault, and the Cyprus Arc (Figure IV.4A), this model fit to our data with RMS = 1.95. In the later stages of modeling (model B, C, and D), this simple model was made more complicated by adding other small blocks to better explain the GPS data and kinematics of the faults in the region (Figure IV.4). Addition

of minor blocks was done on the basis of field studies in which they were identified and mapped (Meghraoui *et al.*, 2011). In model B, a small block called here as the Iskenderun block is placed between the Sinai and Anatolian plates. Limited by the subduction Cyprus arc zone to the south, the Karatas-Osmaniye fault to the north, and the Karasu fault to the east, this block is not well constraint by GPS vectors because significant portion of it is located offshore in the Mediterranean, though, the RMS of this model is reduced to 1.74.
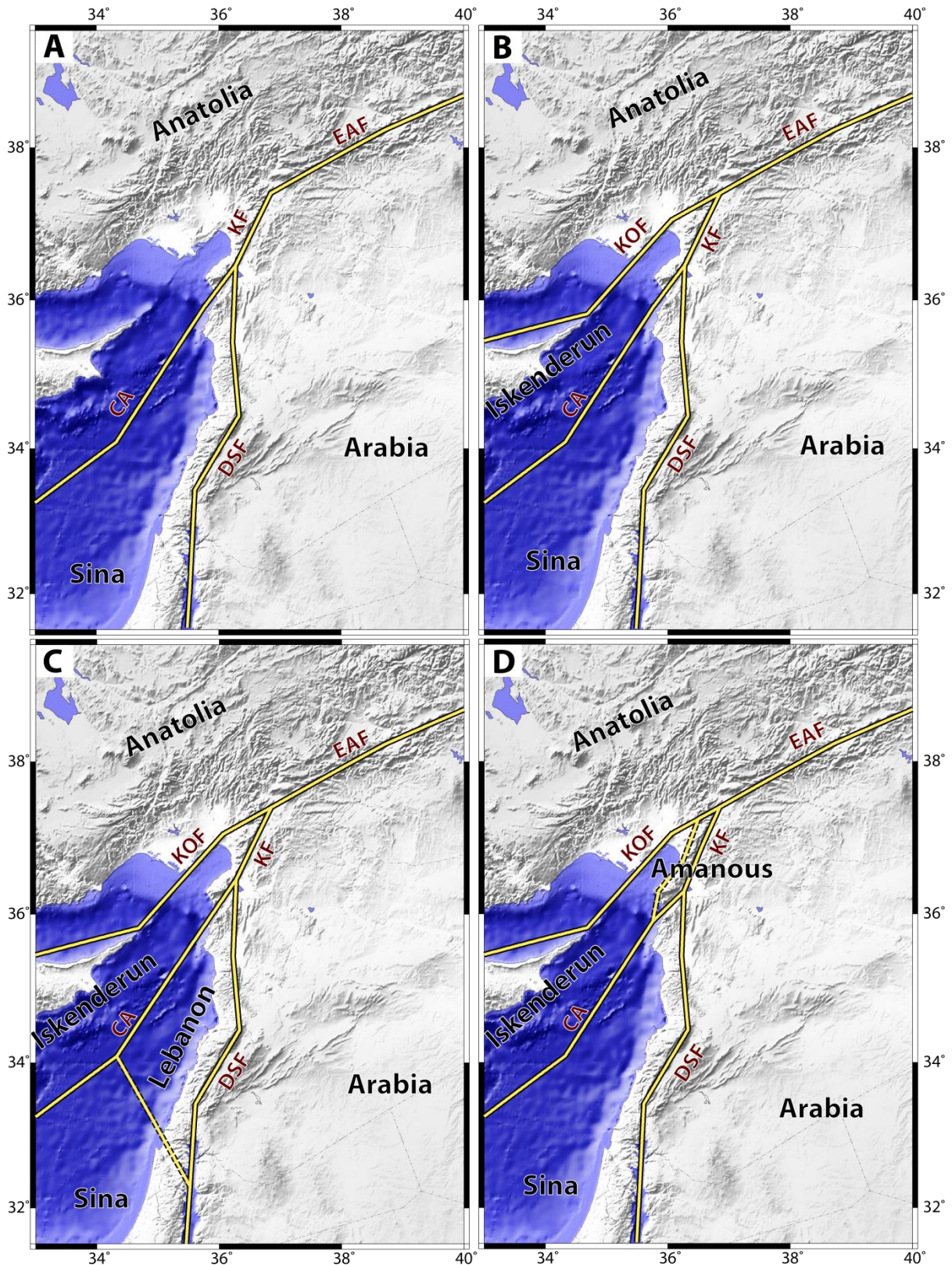
Figure IV.4: Block models tested for the study area with different plate configurations: (A) Model with three blocks; Arabia, Anatolia, and Sinai separated by three main faults, the Dead Sea Fault (DSF), the East Anatolian Fault (EAF), and the Cyprus Arc (CA). (B) Model with the additional Iskenderun block separated from Anatolian plate by the Karatas-Osmaniye Fault

(KOF) and from Africa (Sinai) by the CA. (C) model with additional Iskenderun and Lebanon blocks to the NW of the DSF. (D) Model with the additional Iskenderun and Amanous blocks. Dashed line represent the block limits considered as non-locked faults and introduced to the model for their necessity of block definition.

In model C (Figure IV.4C), we add another block called the Lebanon block limited by the CA and the DSF. This model allows individual rotation for Lebanon and north-western Syria, and provides a better fit to the GPS data than the model A but similar to model B with RMS = 1.74. In the last model D, with RMS = 1.59, we use the Amanous micro block to better explain the GPS vectors that deviate from the general SW trend to the S-SE direction in the Amanous Mountains. In all the models, the faults coincide with the blocks boundaries except the western boundary of the Amanous block whereas the outer limit of the block is considered as non-locked (free slipping), and thus no elastic strain is produced across it. Detailed discussion about these models and their results is in chapter V.

IV.6 Modeling results

The combined GPS data were inverted to estimate the parameters of block rotations and slip rate along fault using various block configurations. Here, only the four main models shown in Figure IV.5 are discussed. The model A that contains the three main plates (Anatolia, Sina, and Arabia) separated with the three major faults (EAF, DSF, CA) has a reduced chi-square (χ_n^2) misfit of 3.63 mm. The model has 253 degree of freedom (DOF), 272 observations and 19 free parameters. The free parameters are computed for the model by the equation:

$$Fp = 3 \times Nb + Ns + Vf$$

Where *Nb* is the number of blocks (3 angular velocity for each block in the inversion), *Ns* is related to faults segmentations; *Vf* is the number of velocity fields. In figure IV.6.A, we can observe clearly that our data do not satisfy the configurations of model A around the HTJ. Misfits between observed and calculated GPS vectors in this model are localized around the Hatay region and obviously large compare to the residuals far from this region. For this raison, we will add more features to this model trying to reduce this misfit in other models.

Model B with four blocks has a better fit to the GPS data as χ_n^2 is reduced to 3.26 mm although the additional block gives rise to 7 extra free parameters in the model. Adding the Lebanon or Amanous block as the fifth block further improves the kinematic models with

$\chi_n^2 = 3.10$ and $\chi_n^2 = 3.13$ in models C and D respectively. We prefer the model D with the Amanous block that has the lowest weighted or Normalized Root Mean Square (WRMS/NRMS) misfit (Table IV.2).

Model #	WRMS mm/yr	NRMS	Red chi**2	DOF	Data	Free parameter	Total ch**2
A	1.16	1.83	3.63	253	272	19	918.08
B	1.09	1.70	3.26	246	272	26	801.44
C	1.07	1.66	3.10	259	288	29	803.06
D	1.04	1.64	3.13	235	270	35	735.83

Table IV-2: Statistics of observations fit to the different models.
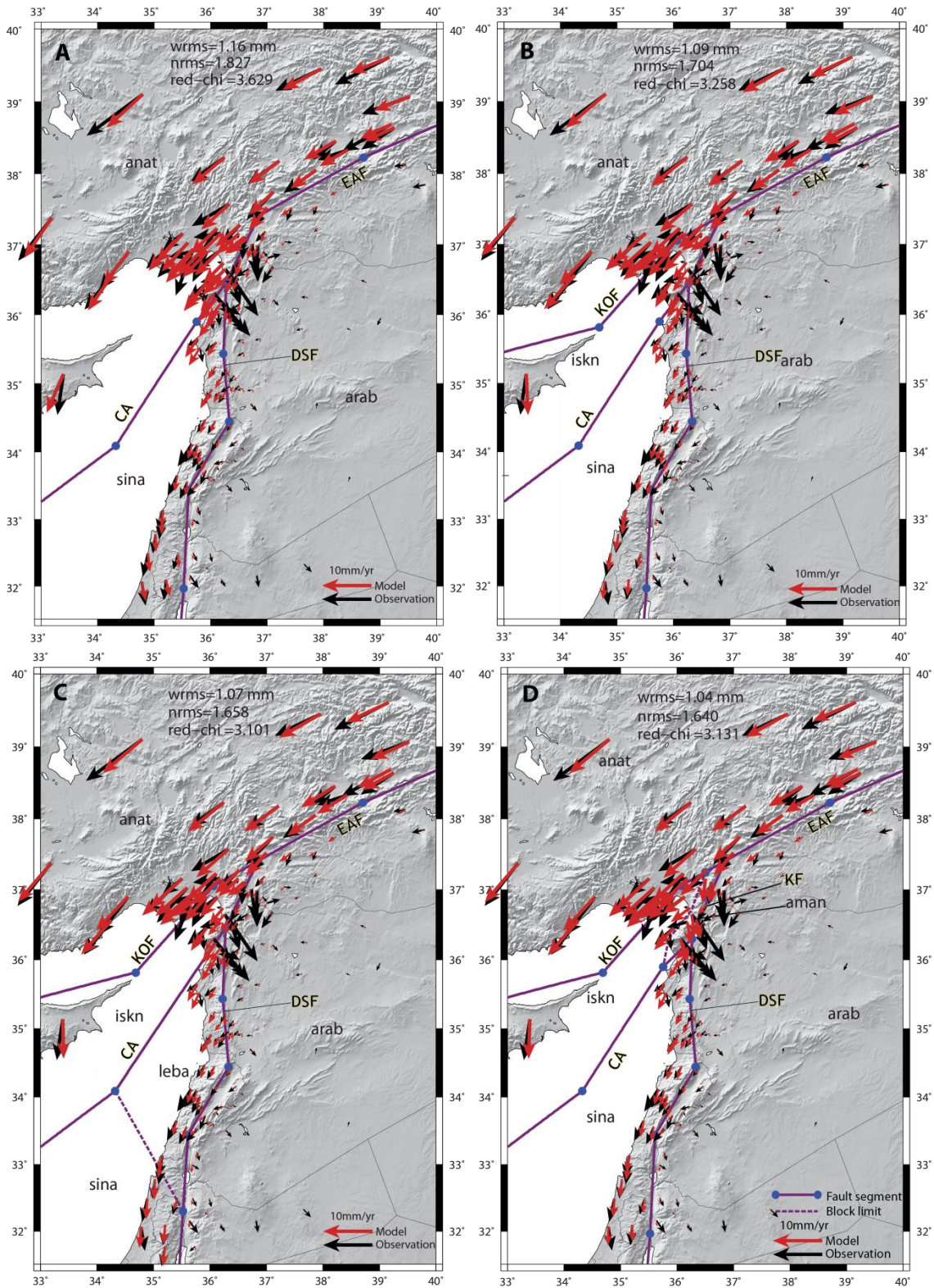
Figure IV.5: Block modeling of the GPS velocities in the study area using various plate configurations. Red and black vectors are the modeled and observed velocities. Fitting parameters (wrms = weighted root mean square; nrms = normalized root mean square; red-chi = reduced χ2) are given on the top of each model.
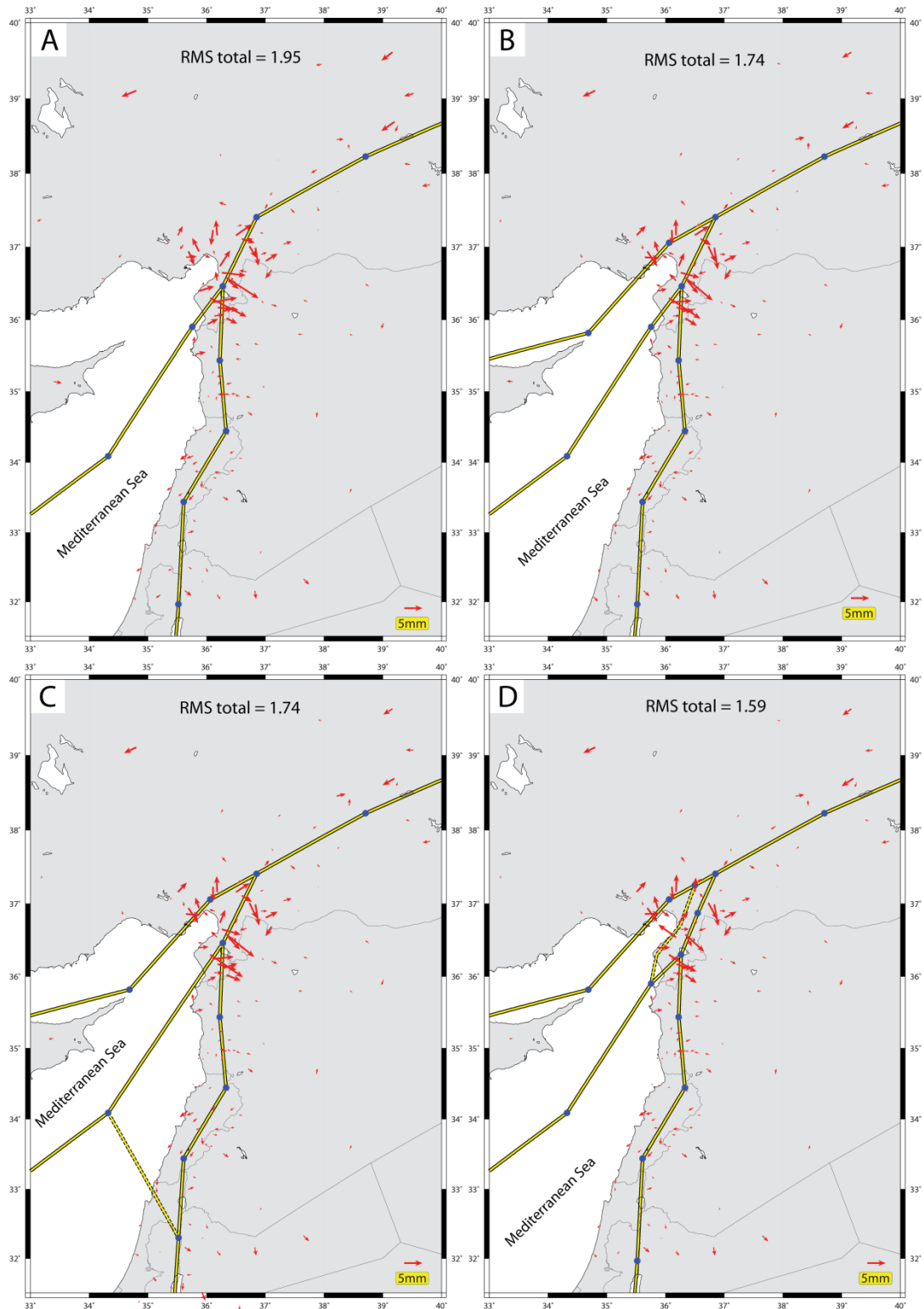
Figure IV.6: Residuals of model vectors and observed GPS vectors for the different models used in this study. RMSs are calculated for all the data used and shown in the figure.

Misfits were calculated for all the models in order to identify the best fit to data and to ensure that our model is consistent with the kinematic characteristic of the study region (Table IV.3). Misfit between the model and the GPS data in four different plate configurations is

within the expected levels of uncertainty (Table IV.2). The 272 GPS velocity components fit at NRMS = 1.83 mm/y and WRMS = 1.16 mm/yr for the model A, NRMS = 1.70 mm/y and WRMS=1.09 mm/yr for the model B, NRMS = 1.66 and WRMS = 1.07 mm/yr for the model C, and NRMS = 1.64 and WRMS = 1.04 mm/yr for the model D. Therefore, model fit improves with increasing number of blocks as expected. However, adding blocks that are not consistent with the field observations should be avoid in modeling. RMS misfits vary from 1.95 to 1.59 mm, with the model D providing the best fit. In order to evaluate the misfit of our network measurements around the Hatay region and to detect its impact to models, we calculate the RMS misfit for the region between 35.35°E and 37°E and 35.5°N and 37.3°N where we have large misfits between the modeled and observed GPS vectors, especially near to Amanous Mountains. Despite of the high RMS values in this region, the check shows that model D gives also the best fit among the other proposed models. Residuals vectors plotted in Figure IV.7 are pointing in random directions, suggesting that a systematic error is not present in the models.

	Overall Model				Around HTJ		
Model #	RMS E	RMS N	RMS Total		RMS E	RMS N	RMS Total
A	2.26	1.59	1.95		3.47	2.32	2.95
B	1.87	1.59	1.74		4.24	3.18	3.75
C	1.88	1.61	1.74		4.46	2.89	3.76
D	1.67	1.51	1.59		2.40	2.34	2.37

Table IV-3: The RMS misfits for the four tested models. We show the RMS for east and north components and the total RMS. RMS were calculated for the data overall the model domain, and also for the data near to the Hatay Triple Junction (HTJ), in the range 35.35° /37° /35.5° /37.3°, where we have more vectors from our GPS network.
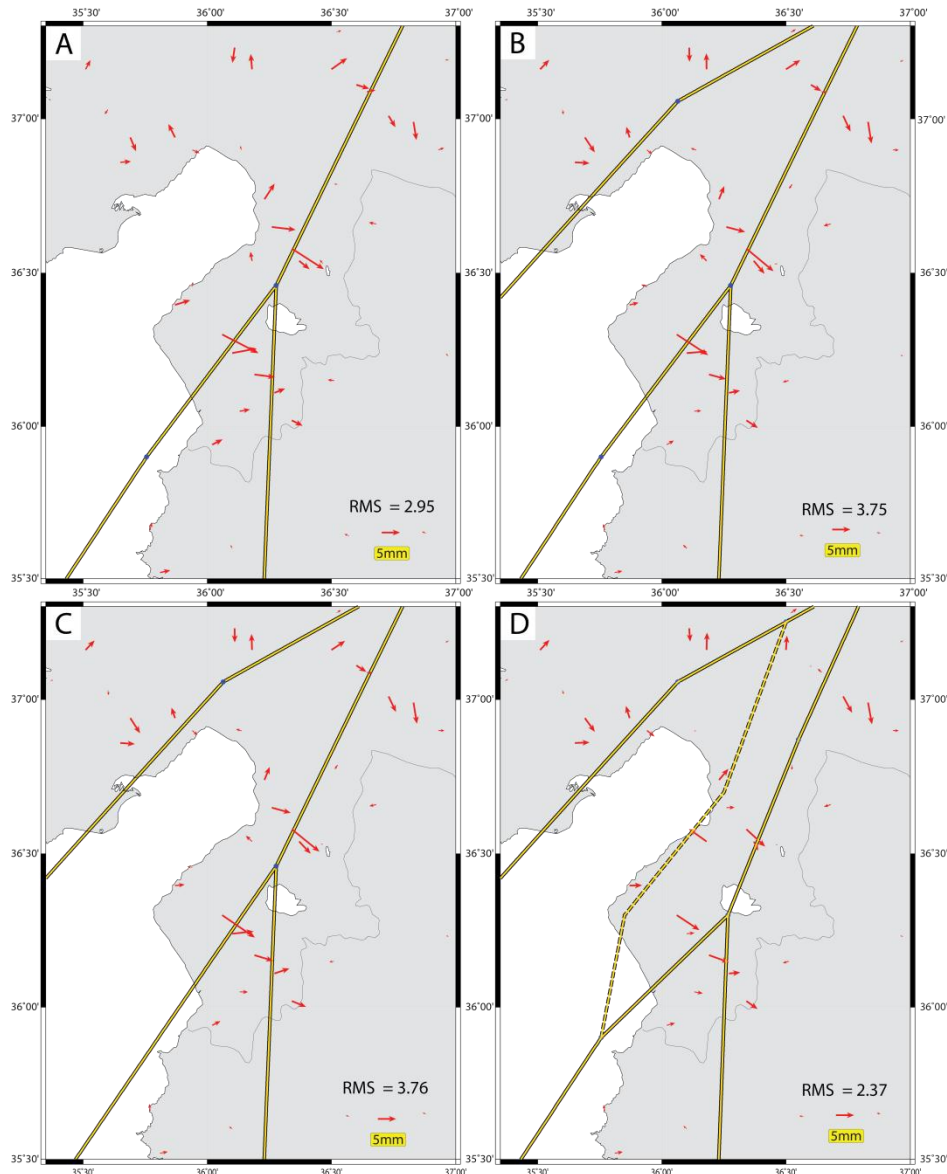
Figure IV.7: Residuals GPS for the four different models used in this study. RMS are calculated for the data around the Hatay triple junction, in the range 35.35°/37°/35.5°/37.3°, where our GPS network points are dense.

IV.6.1 Profiles across major faults

We calculated the GPS velocity components across and along different profiles from the observed and resulting GPS velocities (Figure IV.9). Profiles crossing the main faults in model D show that the kinematic model with 5 blocks can explain well most of the GPS observations over a large region.
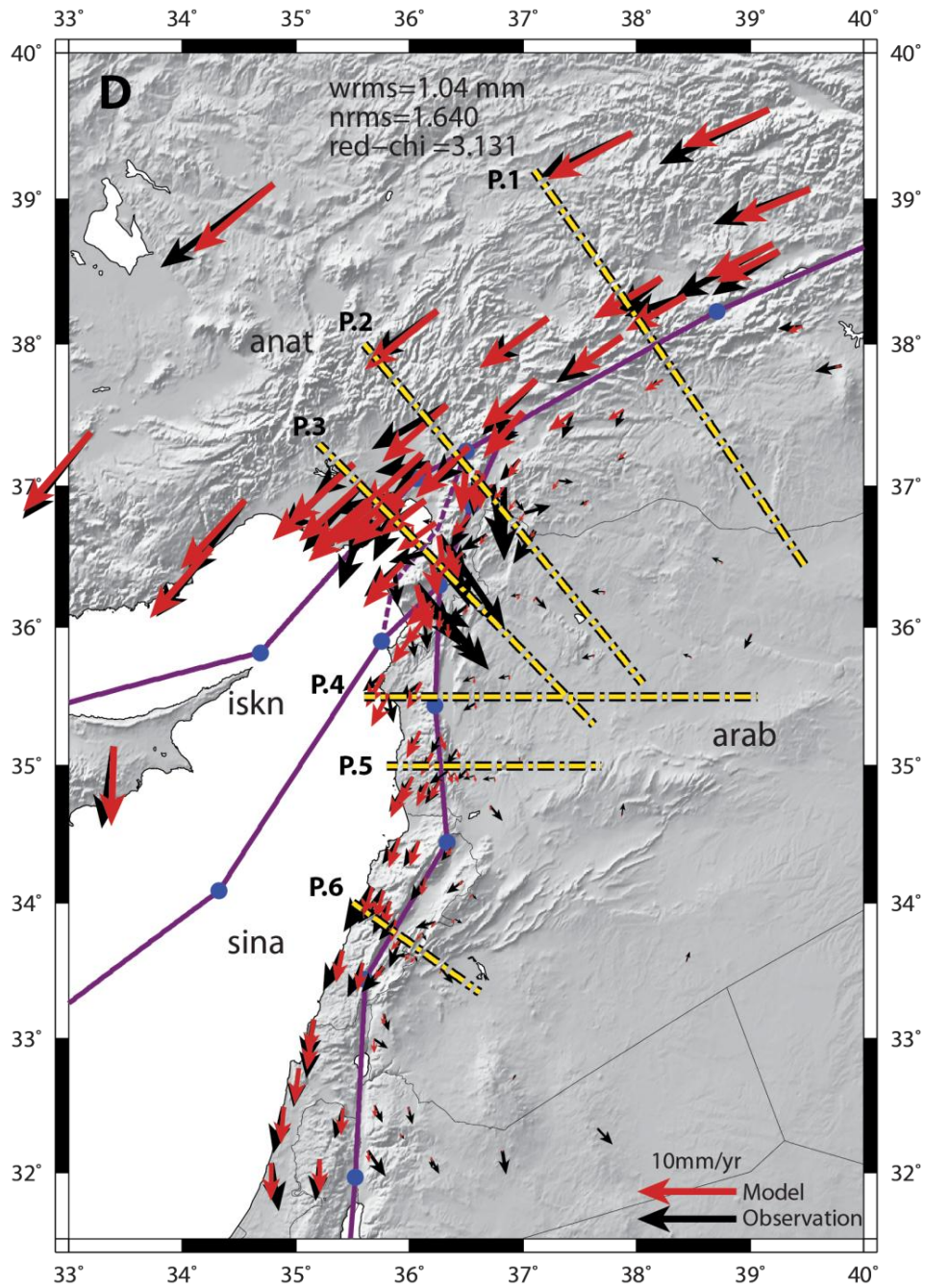
Figure IV.8: Model D with observed and calculated GPS vectors in black and red, respectively. The yellow lines encountered in black represent the 6 profiles perpendicular to crossing faults. The profiles are shown in figure IV.9.
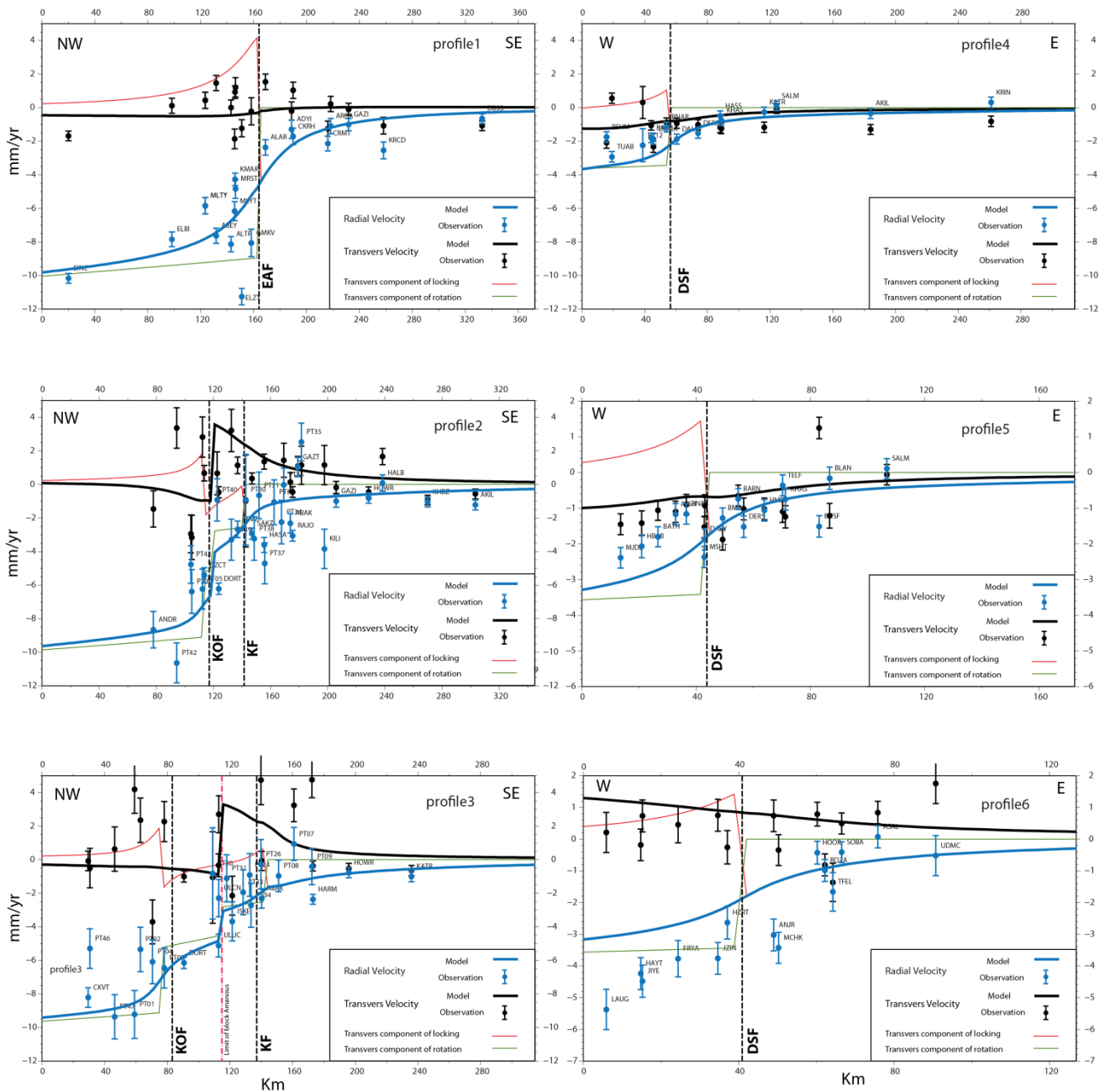
Figure IV.9: The Observed and calculated GPS velocities along profile lines 1 through 6 shown in figure IV.8. Blue lines and symbols show component of velocity normal to profile line (i.e. the fault parallel component). Black lines and symbols show velocity component parallel to profile line (i.e., fault normal component). Symbols are the observed GPS velocities with standard deviation error bars scaled by 0.75. Red and green lines represent the parallel components of the locking and rotation respectively.

Some parameters of the velocity field are readily clearly visible in the profiles. Profiles show the relative motion of various blocks with respect to the Arabian plate. Green lines show fault parallel component of rotation in counter clockwise sense (negative values) to Arabia. The red line shows surface displacement due to the back slip applied in order to fit the

near field GPS data along the fault. The differences of blocks rotation component appear clearly in profiles 2 and 3 as vertical steps for each block. Profiles 1 to 4 cross the most blocks of our model (Arabia, Amanous, Iskenderun, and Anatolia) and show that the predicted velocity field and blocks rotation are in good agreement with the observed GPS data. However this is not the case for the profiles 5 and 6 where a soft difference between observed and calculated velocity field can be easily estimated for the normal and parallel components across the Lebanese restraining bend and part of the northern DSF.

The positive slop in profiles 2 and 3 for the fault perpendicular component of velocity field (black lines) between 120 km and 200 km from the end of profiles indicates significant contraction on the Karasu fault. Profile 1, which is perpendicular to the EAF, shows that the fault is nearly purely left lateral strike-slip with a slip rate of 9.0 mm/yr between the Arabian and Anatolian plates and very small component of along profile velocity (~0.5 mm/y). The same amount of relative velocity between these two blocks can be deduced directly from profiles 2 and 3. The small amount of the fault perpendicular velocity component in the profile 4 and 5 attests for the 1.6 mm/yr of extension along the northern DSF (see figure IV.13 for the values).

In Profile 6, the model does not fit well to the GPS observations. We observe that the GPS data shown in this profile, which are mainly the data of Gomez *et al.,* (2007), can fit better to the kinematic model with a velocity rate of 4.5 mm/yr as proposed by Gomez *et al.,* 2007, while the value predicted from our model is 3.5 mm/yr for the Lebanese restraining bend with a lake of about 1 mm/yr.

IV.6.2 *Slip deficit, locking depth and variation of ϕ*

In this section, we present the scalar parameter ϕ (phi) and the locking depth predicted by model D only (Figure IV.10). ϕ variation and locking depth predicted by the other models are presented in the auxiliary materials.

In the inversion, we applied along strike smoothing by limiting the along strike gradient in ϕ (in unites of ϕ per degree of distance) by use of penalty function, so the change of ϕ value stays less than factor λ. After doing a test of smoothing factor λ for different values (λ=0, 0.2, 0.4, 0.6, 0.8), we found that $\lambda = 0.2$ gives the best fit in our model. As described before, the scalar ϕ is the ratio of locked to total slip along the fault surface and it can be expressed by the equation: $\phi = 1 - V_c/V$. The value of ϕ parameter is directly involved to the

slip rate deficit distribution along the fault plan ($\phi*V$). For the model D, we use a smooth factor $\lambda = 0.2$ and with Z_1 fixed at 7 km of depth. This is the depth from surface where ϕ is not allowed to change with depth. In this case we make sure that the inversion will take into account full coupling of fault on the surface which is thought to be the case in the region. The average of formal uncertainties for the values estimates of ϕ in this inversion is 0.2 with 95% of the uncertainties less than 0.35.
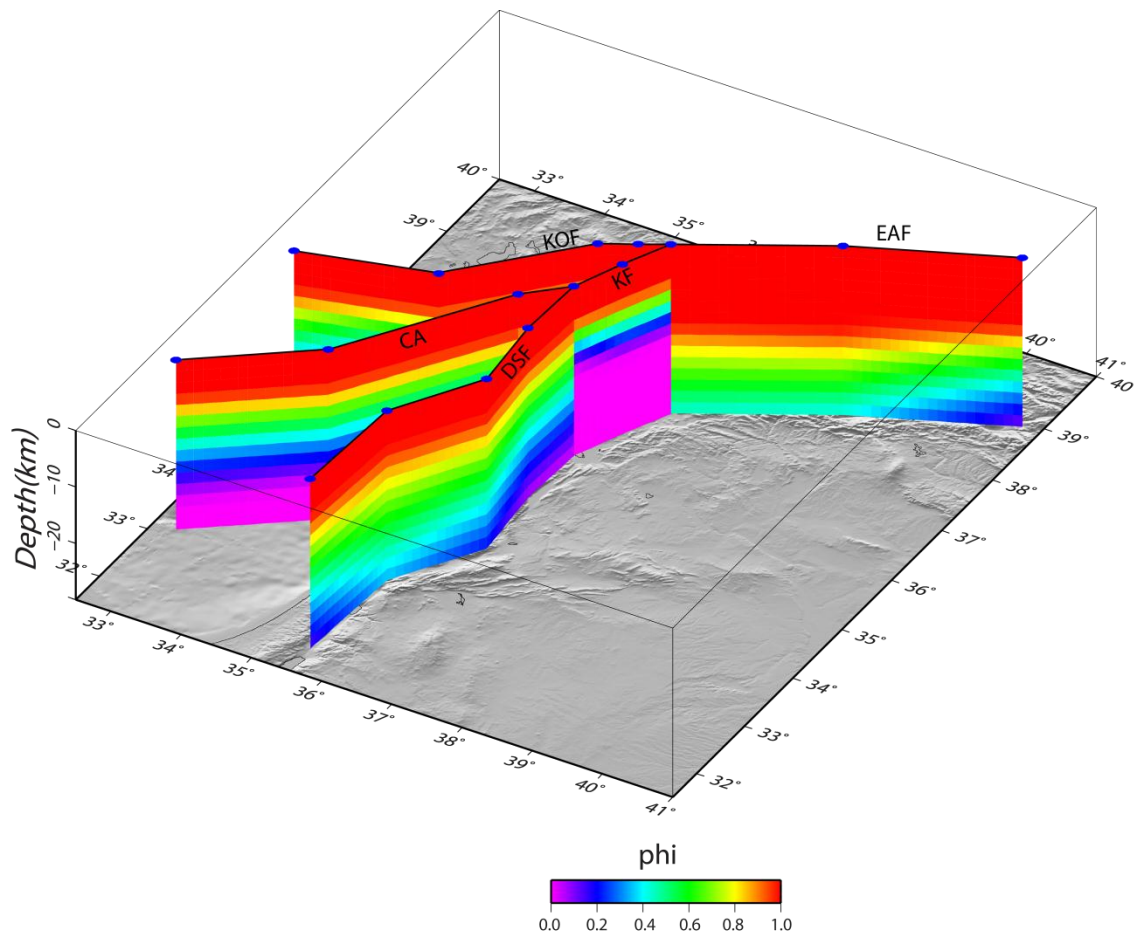
Figure IV.10: Variation of phi (ϕ) parameter along the different faults (DSF, EAF, CF, CA and KOF) from the inversion of model D in Figure IV.5.

Figure IV.10 illustrates that the EAF is fully locked ($\phi = 1$) from surface to the depth of ~15 km. The fault creeps only partially down to the depths of 30 km as indicated by the value of ϕ being greater than 0.2. The depth of the coupling along the DSF is relatively shallow and occurs to the depth of ~11 km. Full creep occurs at depths of about 25 km along the northern section of the DSF where as full creep occurs at much deeper depths along the southern section of the DSF. The Karasu fault shows a shallow locking depth of 8 km from surface. The fault is totally creeping after $Z_2 = 15$ km of depth with a very small transition

zone between full locked and full creeping. The Cyprus arc shows the same full locking depth as KF and almost the same way of ϕ value changes which can make the assumption that they are connected and acting as an uniform fault, except that the CA is totally creeping after 20 km with a larger transition zone than KF.
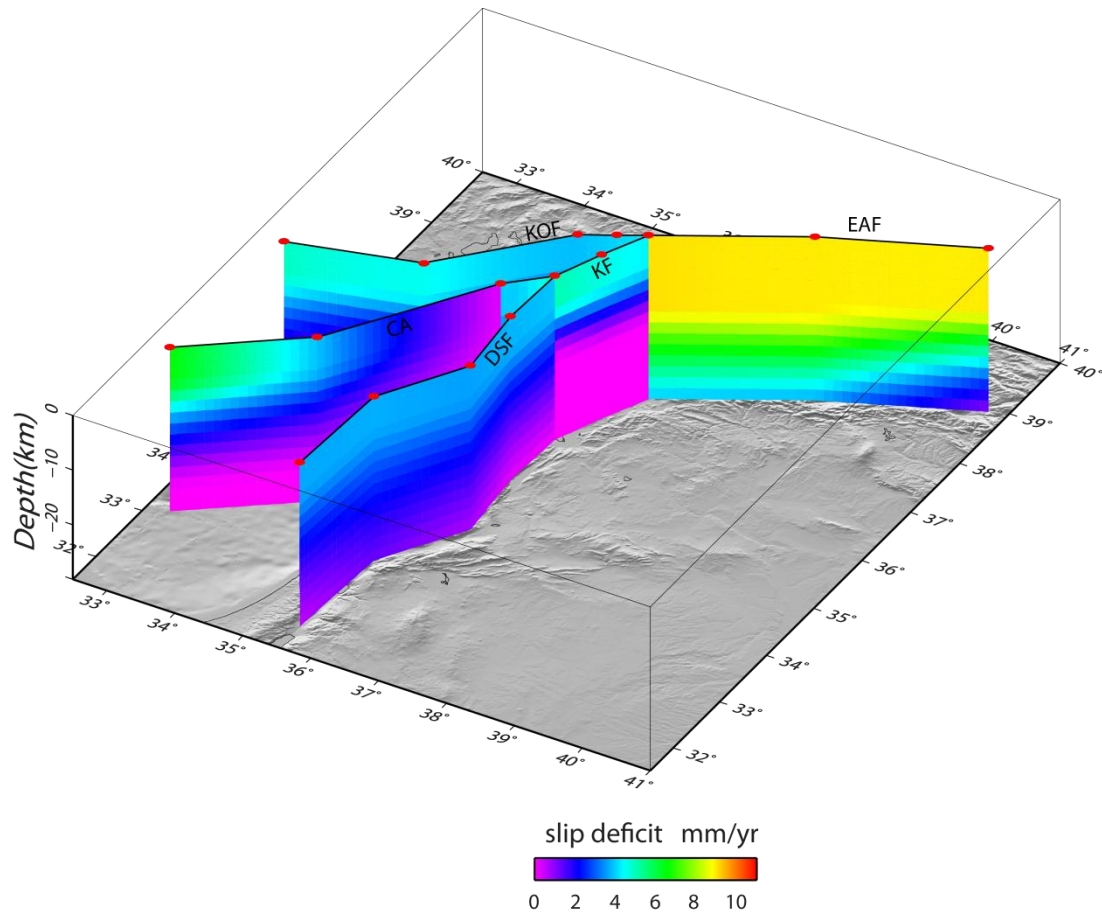
Figure IV.11: Slip rate deficit calculated based on ϕ values and V the relative velocity between the blocks adjacent the faults (DSF, EAF, CF, CA, and KOF). Values of ϕ and V were taken from the inversion of model D in Figure IV.5.

The slip rate deficit, $\phi*V$ is calculated along the faults from surface to 30 km of depth where V is the slip vector on the faults surface (Figure IV.11). V is varying along the faults due to the rotational component of the relative blocks motions, which results in change of slip deficit over the related faults. On the surface and during the interseismic period, the slip rate deficit represents the lack of slip on the fault surface necessary to satisfy the total relative motion of adjacent blocks. The maximum values of slip rate deficit will be on the surface, and it changes down dip along the transition zone of the fault surface where the faults are partially locked only ($0 < \phi < 1$). The value of slip rate deficit can be used to deduce a moment rate on the fault and then expect the magnitude of the next earthquake along this fault in some

conditions (steady build-up of the moment rate over time and one big earthquake to release this moment). A slip deficit of 9.0±0.3 mm/yr is predicted along the EAF from our model (Figure IV.11), 4.5±1.0 mm/yr along the CF, 3.5±0.3 mm/yr along the DSF. The KOF has a slip deficit of 3.5-4.2±0.7 mm/yr. The value is varying along the CA toward NE from 6.0±1.0 mm/yr to 1.2±0.8 mm/yr.

IV.6.3 Fault slip rates

The fault slip rates were predicted through the four different models we proposed for the kinematics of the Hatay triple junction and its surrounding (Figure IV.12). The different plate configurations of the region give different velocity slip rate on the faults with moderate difference for some fault segments.

IV.6.3.1   The Dead Sea fault:

The Dead Sea Fault has almost a uniform slip rate along its strike for all the segments proposed in this inversion of model D (Figure IV.12). A value of 3.3±0.3 mm/yr to 3.6±0.3 mm/yr along the north segments (Missyaf fault, Al-Ghab fault) was predicted, which is in consistence within the error range with estimates of Alchalbi *et al.,* (2010) who proposed 1.8-3.3 mm/yr for the same segment. But our estimate is about 1 mm/yr lower than those estimated by (Mahmoud *et al.*, 2005; Reilinger *et al.*, 2006; Gomez *et al.*, 2007a). The Jordan Valley and the Lebanese restraining bend have a slip rate of 3.5±0.3 mm/yr, a value very similar to that inferred by Wdowinski *et al.,* (2004) and ArRajehi *et al.,* (2010), but slightly smaller than that estimated by (Mahmoud *et al.*, 2005; Reilinger *et al.*, 2006; Al-Tarazi *et al.*, 2011). An extension of 1.6±0.3 mm/yr was obtained for northern DSF while 1.0±0.2 mm/yr of contraction was observed crossing the middle segment of the DSF (Lebanese restraining bend) consistent with geological observations.

Similar values of slip rates were found from inversions of model A and B for these segments. In the model C, when Lebanon block was added and allowed to rotate with another rotation pole, the predicted slip rates values are larger and more consistent with other geological and paleoseismological studies (Figure IV.12) (Freund *et al.*, 1968; Ferry *et al.*, 2007b; Sbeinati *et al.*, 2010).
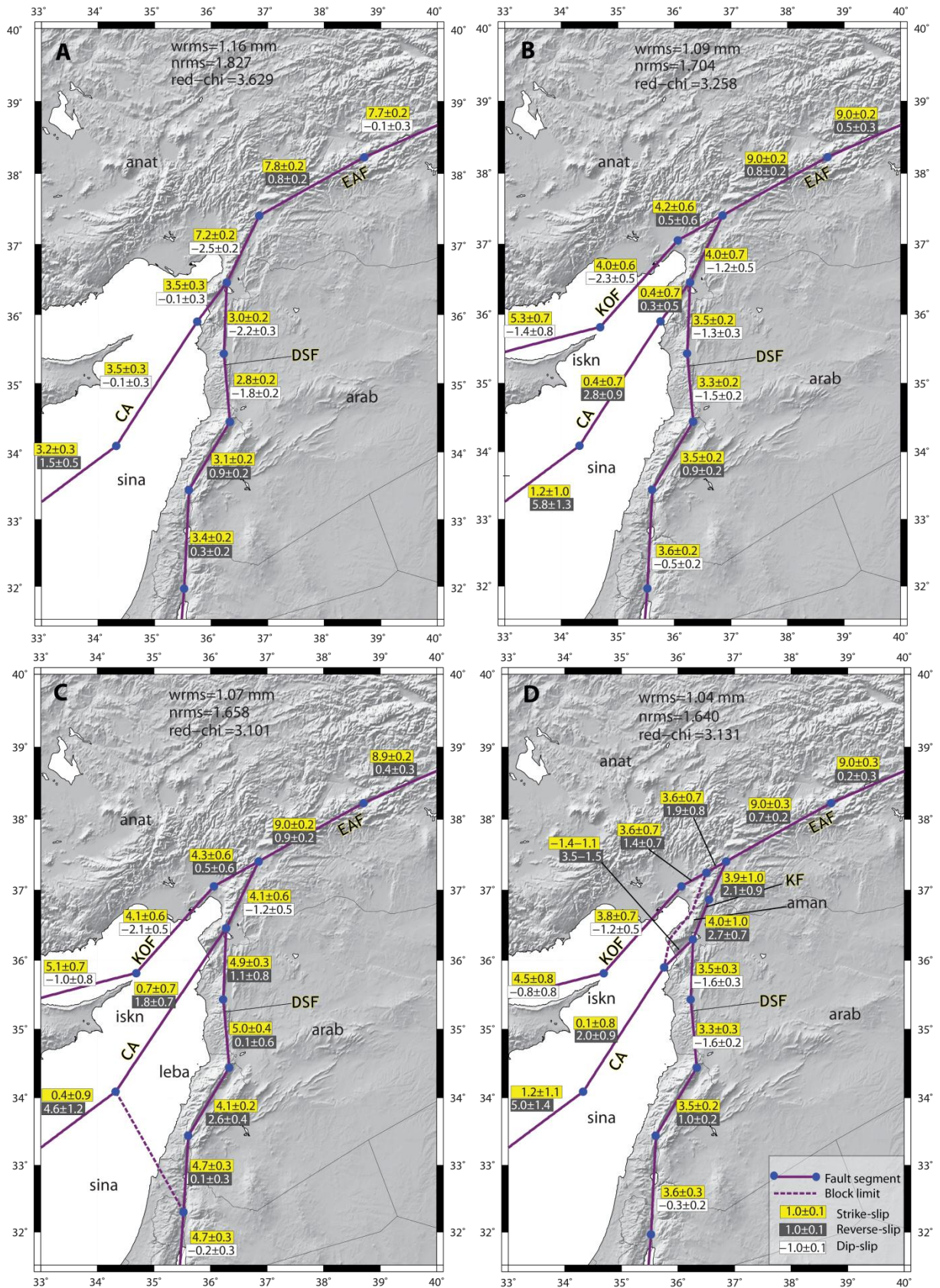
Figure IV.12: Fault slips rates predicted by the four models with different plate configurations. Weighted and normal root mean square and reduced chi square are presented to illustrate model fit. Numbers encountered in yellow rectangles are left-lateral strike-slip rate (mm/yr).

Numbers encountered in white (negative) and grey (positive) rectangles are extension and shortening rates, respectively.

IV.6.3.2   The East Anatolian fault:

Except the model A (Figure IV.12), all the models predict similar slip rates for the East Anatolian Fault and is ~9.0±0.2 mm/yr, comparable to previous estimates based on geodetic measurements (McClusky *et al.*, 2000; Bertrand, 2006; Reilinger *et al.*, 2006) and long term geological estimates (Arpat and Saroglu, 1972; Dewey *et al.*, 1986; Yurur and Chorowicz, 1998; Meghraoui *et al.*, 2011). Modeling shows that the EAF does not experience any significant (> 1 mm) convergence or extension. It is worth to note that the model A with only three main plates gives a non-negligible difference (1.2±0.2 mm/yr) in the slip rate of EAF.

IV.6.3.3   The Karatas-Osmaniye fault:

The slip rate on the KOF varies between 3.6 mm/yr to 5.3 mm/yr depending on the block model used in the inversion (Figure IV.12). The model D gives 3.6±0.7 mm/yr on the segment connecting to the EAF and KF in the triple junction. This value increases on its submarine segment towards the SW and reaches 4.5±0.8 mm/yr. Block modeling using GPS data, Meghraoui *et al.,* (2011) propose 3.6±0.6 mm/yr slip rate for this fault, similar to our model value for the NE segment of KOF. Another geodetic study by Bertrand (2006) proposes 5.5±1.5 mm/yr of slip rate along the KOF. The models containing KOF predict contraction of 1.6±0.8 mm/yr on the onshore segment and an extension of 1.2±0.6 mm/yr on the offshore segment, which results from the change in fault strike to the west.

IV.6.3.4   The Karasu fault

The Karasu fault in the models A, B and C is defined as an onshore continuation of the Cyprus Arc. In the model D it is an independent fault forming the eastern limit of the Amanous block, whereas the western limit of this block is considered as free slipping fault. In all models, except the model A, the KF shows almost the same velocity slip rate of 4.0±1.0 mm/yr, which is in agreement within the uncertainty with the geologically estimated slip rate of Karabacak (2010) who derive a slip rate of 4.94±0.13 mm/yr from 7.9 km of offset. However, the slip rate predicted by the model A is about %80 higher (7.2±0.2 mm/yr) (See Figure IV.12), suggesting that the simple model with three plates only does not provide reliable estimates for fault slip rates. The sum of the slip rates along the KF and KOF is almost equal to that of the EAF, implying that slip on the EAF is partitioned westward by the

KF and KOF. The KF shows a 2.4±0.9 mm/yr of contraction in model D, whereas in the other models it shows 1.2±0.5 to 2.5±0.2 mm/yr of extension component. This big difference is due to the presence of the Amanous block and its ability to rotate around different Euler pole of the Iskenderun block.

IV.6.3.5   The Cyprus Arc

The dominant nature of the Cyprus Arc is the subduction nature with a convergence rate of 2.0±0.9 mm/yr to 5.0±1.4 mm/yr and negligible along strike-slip rate. This is not the case in the model A that gives more strike-slip deformations than down-dip deformations.

IV.6.4 Block motions and rotation Euler poles

The angular velocities of blocks relative to the Arabian plate indicate counter clockwise rotation around their poles located to the east and southeast in the Arabian plate (Figure IV.14). The Anatolian block moves in the southwest direction relative to Arabia around a pole located at 45.127±2.45 °E, 27.61±0.98 °N, (see Table IV.4), with angular velocity of 0.391±0.056 °/Myr. The velocity of Anatolia relative to Arabia (9.34 mm/yr) reproduces almost the same amount of slip rate on the EAF with negligible fault perpendicular motion. This is most probably due to the fact that the motion of the Anatolian block is parallel to the general trend of the EAF. At the same time, this motion yields a smaller slip rate on the KOF varying between 3.6 mm/yr and 4.5 mm/yr.

Fixd	Movg	Long.	Lat.	Omega	SigOme	Emax	Emin	Azi	Wx	Wy	Wz
arab	anat	45.127	27.610	0.391	0.056	2.64	0.32	121.33	0.245	0.246	0.181
arab	iskn	37.946	35.070	1.099	0.243	0.99	0.31	140.84	0.709	0.553	0.631
arab	sina	46.494	31.012	0.202	0.067	4.69	0.66	162.12	0.119	0.126	0.104
arab	aman	41.220	37.313	0.638	0.927	8.00	0.86	6.06	0.382	0.335	0.387

Table IV-4: The Euler vectors relative to Arabia and 1 sigma uncertainties for the block model D in our study.

Moving nearly in the same direction (SSE), the Sinai and Iskenderun blocks have an angular rotation rate of 3.929±0.36 °/Myr and 5.389±0.94 °/Myr, respectively. 1.09±0.24 °/Myr angular velocity of Iskenderun block is five times greater than that of the Sinai block (i.e., 0.20±0.06 °/Myr) due to the difference of Euler poles locations. The rotation pole the Iskenderun block is located at 37.946±0.5 °E, 35.07±0.85 °N, near to the block. The Sinai

block on the other hand rotates around a pole located at 46.494±4.44 °E, 31.012±1.51 °N. The 2.0-5.0 mm/yr of reverse slip on the Cyprus Arc in our model (Figure IV.13) attests for the rotation velocity difference of two adjacent blocks.
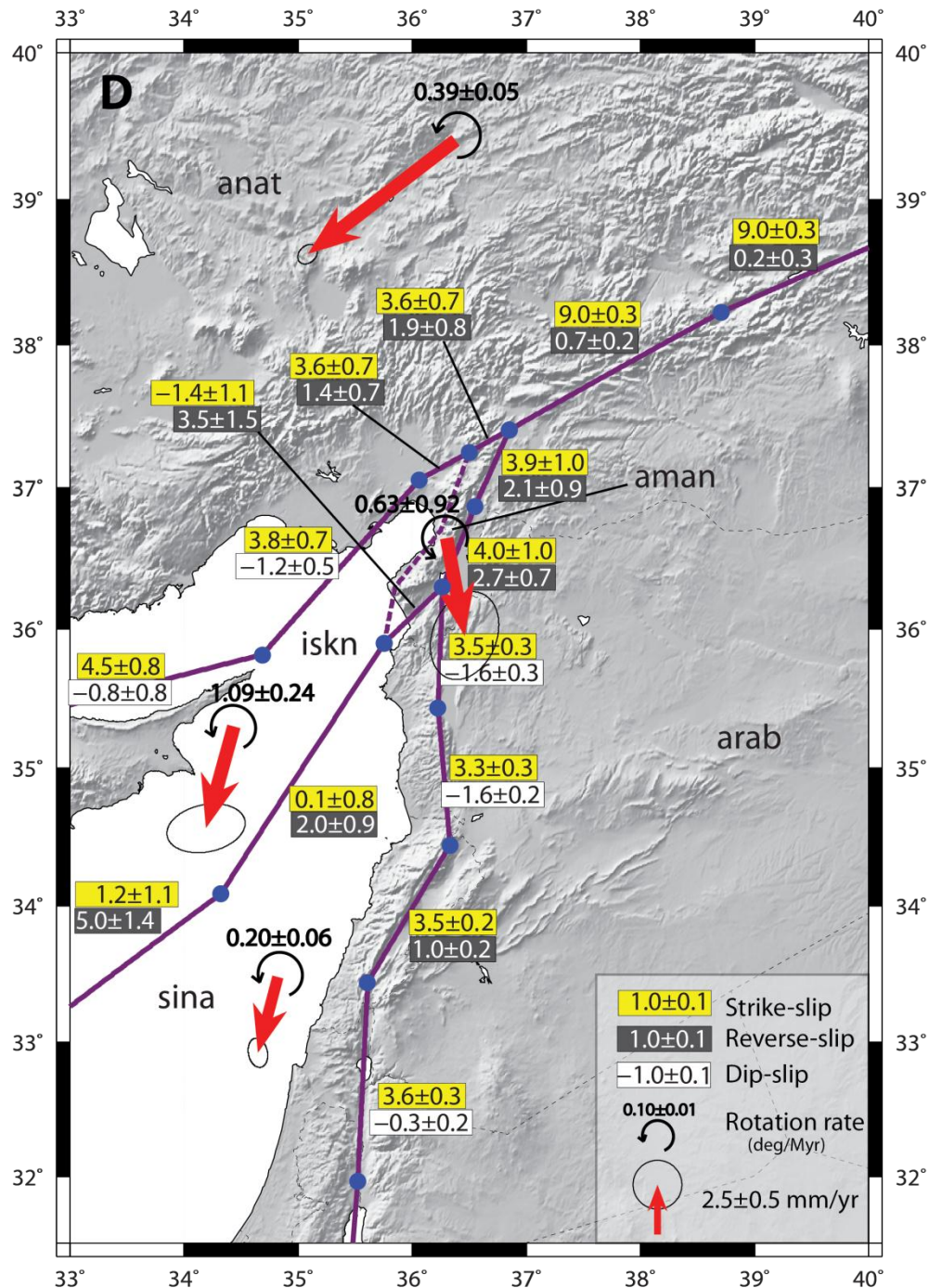
Figure IV.13: Relative slip rates on fault of block model D. Red arrows represent GPS-derived block velocity relative to Arabia, black curve arrows and numbers show the directions and the values of blocks angular velocities relative to Arabia respectively.

The Amanous block rotates relatively to Arabia with a rate of 0.63±0.92 °/Myr around an Euler pole located at 41.222±1.77 °E, 37.313±7.8 °N. The rotation appears in southward motion of the block relative to Arabia (4.982±1.14 mm/yr) and creates an important component of reverse slip on the Karasu fault of ~2.4±0.9 mm/yr.
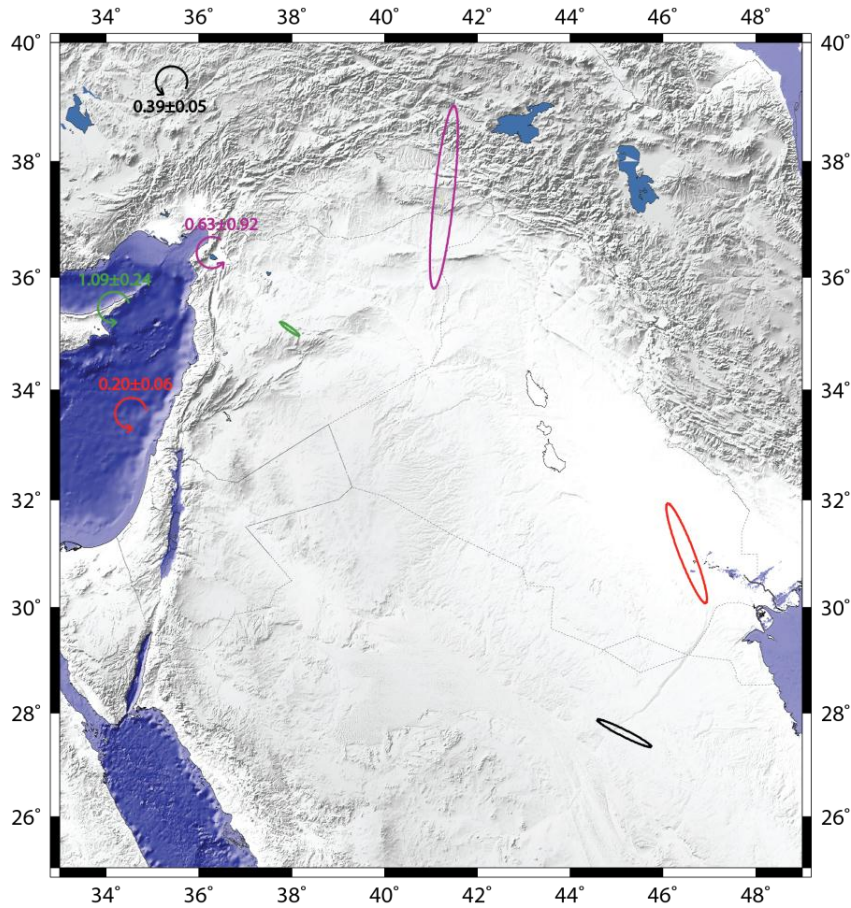
Figure IV.14: The rotational Euler poles positions and the rate of rotation in °/Myr from model D (Table IV.4) for the blocks: Anatolia (black), Iskenderun (green), Amanous (purple), and Sinai (red) in relative to Arabian plate.

IV.7 Conclusions

Geodetic data are inverted for angular velocities and fault parameters within a finite number of lithospheric blocks representing the junction between three major plates, Arabia, Eurasia, and Africa. Existence of micro blocks and minor faults in the region give more complexity to the triple junction of Hatay. Therefore, a simple 2D elastic dislocation model cannot solve the problem. Consequently a 3D elastic dislocation model is used to perform the inversion of the GPS data and assessment of blocks rotations and faults parameters.

Only GPS data were used in this modeling. In the inversion, we used the vectors from our sites that were measured at least three or more times. We therefore exclude most of the sites in Syria that were occupied only twice. Including the points in Syria in the modeling decreases the quality of the parameter estimations, especially in northwest Syria. In addition to our GPS data, other GPS solutions in the region were used in the modeling; these different GPS velocity fields were combined together by applying a rotational transformation.

In this study, four different block models were tested trying to explain the GPS vectors around the HTJ. The first one is a simple model (A) consisting of three major blocks (Arabia, Sinai, and Anatolia) and three principal faults (DSF, EAF, and CA). Models with other tectonic features were tested; models B, C, and D contain other micro blocks named Iskenderun, Lebanon, and Amanous, and some known faults such as KOF and KF. The results of inversions with these different blocks show that a 3-plate model fails to explain the GPS velocity field adequately. Thus, GPS data require a more complex model for depicting the kinematics of the region. A new block, named the Iskenderun block, is needed to better explain the GPS data in the Turkish side (Figure IV.5 B). In this model, the KOF and the KF are connecting to the EAF, forming the Maras triple junction. Another new block is required to explain the south-southeast pointing GPS vectors in the Amanous Mountains (Figure IV.5 D). This new micro block is called the Amanous block in this study. The model D (Figure IV.5) with Anatolia, Arabia, Sinai, Iskenderun, Amanous blocks and the DSF, EAF, CA, KOF and KF gives the best fit to GPS data used in this study. This model is also compatible with tectonic and kinematics of the region.

The estimated relative slip rates on faults are similar to other published estimations with some exceptions. The Karasu Fault shows a sinistral slip rate of 4.0±1.0 mm/yr and a compressional behavior with a revers slip rate of 2.1-2.7 mm/yr, which contradicts with the

extensional nature proposed by previous studies (e.g., Reilinger *et al.,* 2006). The Dead Sea fault experiences a relative slip rate of ~3.5±0.3 mm/yr along all its segments with an extension rate of 1.6±0.3 mm/yr on the northern segment and a shortening rate of 1.0±0.2 mm/yr on the Lebanese restraining bend which is slightly smaller than the value proposed by Gomez *et al.,* (2007) (1.6±0.4 mm/yr) and three times smaller than the value predicted by the regional block model of Reilinger *et al.,* (2006) (3.1±0.4 mm/yr). We can also conclude that the EAF experience no significant extension or compression (0.2±0.3 mm/yr of compression), which is consistent with the dominant strike-slip behavior of EAF attested also by the focal mechanism along the fault. This conclusion disagrees with extension value of (2.9–5.1)±0.3 mm/yr proposed by Reilinger *et al.,* (2006). The slip rate predicted by our models for the CA disagree with the estimations from other regional models; a maximum left lateral slip rate 1.2±1.1 mm/yr and 5.0±1.4 mm/yr of reverse slip rate were estimated in this study while Reilinger *et al.,* (2006) proposes a left lateral strike-slip rate of 7.0±0.4 mm/yr and an extensional component of 3.5±0.4 mm/yr.

A new Euler pole for the relative angular velocity of Anatolia-Arabia was determined at 27.61±0.98 °N, 45.127±2.45 °E, with a rotation of 0.391± 0.056 °/Myr. The Sinai block moves relative to Arabian block around an Euler pole located at 31.012±1.51 °N, 46.464±4.44 °E in angular velocity of 0.202±0.067 °/Myr. The Amanous and Iskenderun micro blocks move relatively with Arabia around poles located at 37.31±7.8 °N, 41.22±1.77 °E and 35.07±0.75 °N, 37.94±0.5 °E with angular velocities of 0.63±0.92 °/Myr and 1.09±0.24 °/Myr, respectively.

A locking depth of 15 km is estimated for the EAF, 4-5 km deeper than that of the Dead Sea Fault. The East Anatolian Fault is however partially locked down to the depths of 30 km with no significant extension or compression. In general, slip rates and kinematics of faults are consistent with the geological observations in the region.

Chapter V

V- General discussion and conclusions: Implications to the regional seismic hazard

V.1   Introduction

In the previous chapters we gave an overview and description of the Dead Sea fault and the East Anatolian Fault. Then we described and explained the characteristics of the GPS network installed within the context of this study. We tried to understand the deformation pattern in the region of Hatay, where a triple point junction formed by the intersection of three major fault zones which are the East Anatolian fault, the Dead Sea fault, and the Cyprus Arc zone. This region is tectonically complex mainly due to the existence of several active sub-segments on which the slip rates remain poorly constraint.

The main aim of the GPS network installed in the region was to better constrain the active deformation along the different fault segments at the triple junction of Hatay, and to determine in more precisely way the physical parameters of these faults which will lead us in later stage to understand the kinematics of the Hatay triple junction. This understanding gives us the ability to determine the active deformations distribution and transferring between the major and sub-faults and the contribution of each tectonic feature to the kinematics of the region. The 57 GPS sites of our network were installed in September 2009 and re-measured in 2010 and 2011 as described in chapter III. The GPS data processing was performed using GAMIT/GLOBK program in three-step approach as described by Dong *et al.,*(1998) and Feigl *et al.,* (1993a). A set of permanent GPS sites from regional and international (IGS) network were introduced to the processing in order to calibrate our regional observations to the global GPS network. This IGS stations cover a large domain including Africa, Eurasia and Middle East and provide daily solutions computed not only during our campaigns period but also (from January 1999 to December 2011) in order to constrain the reference frame definition. The horizontal velocity components were estimated according to the International Terrestrial Reference Frame (ITRF05, Altamimi *et al.,* 2007) using a set of 12 IGS sites as a stabilization frame (GRAS, GRAZ, JOZE, POTS, WZTR, RABT, MAS1, PDEL, BOR1, TLSE, WTZR, WSRT). Furthermore, we defined an Arabia fixed reference frame minimizing the observed velocities on 8 CGPS sites in Arabia plate. Using the same method, we defined also Eurasian and African reference frames. In Table V.1, we show the Euler Poles and the angular velocities calculated in this study for Eurasia, Africa and Arabia plate and compare it with other studies.

Euler pole	Lat. °N	Lon. °E	Rotation rate °/Myr	Reference
EU	57.35 ± 0.73	-93.04 ± 0.85	0.255 ± 0.004	This study
EU	56.33 ± 0.54	-95.97 ± 0.96	0.261 ± 0.003	Altamimi et al., (2007)
EU	55.851	-97.378	0.263 ± 0.001	SOPAC solution
AR	50.64 ± 0.51	-5.66 ± 1.24	0.507 ± 0.014	This study
AR	49.64 ± 0.58	5.06 ± 2.27	0.579 ± 0.019	Altamimi et al., (2007)
AR	50.209	4.162	0.567 ± 0.011	SOPAC solution
AF	49.66 ± 0.67	-83.81 ± 1.58	0.251 ±0.004	This study
AF	49.95 ± 0.48	-82.50 ± 1.25	0.269 ± 0.003	Altamimi et al., (2007)
AF	48.997	-80.424	0.275 ± 0.003	SOPAC solution
AR-EU	27.53 ± 0.6	17.71 ± 0.8	0.393± 0.005	This study
AR-EU	27.5 ± 0.1	17.6 ± 0.3	0.404 ± 0.004	ArRajehi et al., (2010)
AR-EU	28.4 ± 0.9	18.4 ± 1.0	0.428 ± 0.009	Reilinger et al., (2006)
AR-EU	27.4 ± 1.0	18.4 ± 2.2	0.40 ± 0.04	McClusky et al., (2003)
AR-EU	26.22 ± 1.2	22.87 ± 2.1	0.427 ± 0.029	Sella et al., (2002)
AR-EU	27.9 ± 0.5	19.5 ± 1.4	0.41 ± 0.1	Vernant et al., (2004)
AR-EU	24.6 ± 2.3	13.7 ± 5.0	0.5 ± 0.05	NUVEL1-A (DeMets et al., 1994)
AR-AF	31.55 ± 0.8	23.16 ± 1.1	0.385 ± 0.006	This study
AR-AF	31.7 ± 0.2	24.6 ± 0.3	0.369 ± 0.005	ArRajehi et al., (2010)
AR-AF	31.5 ± 0.6	25.2 ± 0.7	0.393 ± 0.005	Reilinger et al., (2006)
AR-AF	30.5 ± 1.0	25.7 ± 2.3	0.37 ± 0.04	McClusky et al., (2003)
AR-AF	31.64 ± 2.5	20.29 ± 1.1	0.38 ± 0.018	Vigny et al., (2006)
AR-AF	31.26 ± 1.3	29.55 ± 1.8	0.400 ± 0.030	Sella et al., (2002)
AR-AF	31.5 ± 1.2	23.0 ± 2.7	0.40 ± 0.05	Chu and Gordon (2002)
AR-AF	32.2	24	0.376	Joffe and Garfunkel (1987)
AR-AF	32.59	23.7	0.418	Jestin et al., (2007)

Table V.1: The rotation pole and angular velocity for the Eurasia, Africa and Arabia plates and relative Euler poles of Arabia-Eurasia (AR-EU) and Arabia-Africa (AR-AF), calculated from GPS vectors of this study. SOPAC pole rotation tables (http://sopac.ucsd.edu/cgi-bin/poleRotationValues.cgi).

The calculated velocity field in Arabian reference frame is used in later steps for the interpretation of active deformation in the HTJ and in the block modeling. We consider that the determination of Arabian reference frame in our study has a strong stability, thanks to the good number of continuous GPS sites (Tables V.2) and the long time span of the measurements. The velocity vectors of these sites have in average 0.63 mm on the east and west components and do not exceed the level of 1 mm. Besides the 8 sites are well distributed and can represent properly the movement of the Arabian plate. The Euler pole of Arabia plate was estimated in our study at (50.645±0.51 °N, -5.661±1.24 °E, 0.507±0.014 °/Myr) and has a significant difference with the SOPAC solution and Altamimi *et al.,* (2007) (Table V.1). Our

estimations of Euler poles of Eurasia and Africa are comparable to those of the same studies. The Euler poles proposed in our study for the relative motion of Eurasia-Arabia and Arabia-Africa (Table V.1) are compatible with the other geodetic studies and especially with ArRajehi *et al.,* (2010) and Reilinger at al., (2006).

Longitude	Latitude	Ve	Vn	Sig. E	Sig. N	Corr	Site
36.378	26.458	27.33	23.65	0.67	0.78	-0.025	ALWJ
50.608	26.209	29.64	29.80	0.52	0.52	0.001	BHR1
36.100	29.139	25.35	23.38	0.46	0.53	-0.033	HALY
39.631	21.369	31.78	25.54	0.55	0.65	-0.041	JEDD
47.972	29.325	27.91	29.23	0.82	0.93	0.001	KUWT
42.045	19.211	33.29	26.79	0.56	0.58	-0.009	NAMA
46.401	24.911	30.44	28.61	0.52	0.52	-0.016	SOLA
56.112	22.186	33.58	30.96	0.57	0.63	-0.013	YIBL

Table V-2 : GPS sites in Arabian plate used in the determination of the Arabian reference frame. The velocities are defined in the ITRF05 reference frame.

V.2   GPS velocity field and block model results in the HTJ

The GPS velocity field deduced from 2009, 2010 and 2011 campaigns for the 57 campaign sites and 14 permanent sites in the regions provides new tools to describe the deformations in the HTJ and understand the small scale tectonics. However, the campaigns are not sufficient to obtain an accurate velocity rate for some of the faults.

The velocity vectors suffer from a relative inaccuracy due to the short time span measurements (1 or 2 years). In general our campaign GPS vectors uncertainties are ~2.4 mm/yr for the sites in Syria and~1.9 mm/yr for the other sites in Turkey. This difference in uncertainties between sites in Turkey and Syria can be explained by the number of campaigns and the time span which are both greater in Turkey than in Syria. The CGPS sites in Turkey and Syria have better uncertainties with less than 1 mm/yr (Figure V.1). Some points in the Syrian side have anomalous values or direction which can be justified by the insufficient measurements (2 measurements with 1 year of time difference), (e.g., points CC01, BB02, and AA08 in Figure V.1).

Despite the large uncertainties in our GPS results, we think that our velocity field has sufficient accuracy, especially in Turkish side, to be used for active deformation interpretation around the HTJ. If we compare the velocity vectors from our solution with those from other solutions of Reilinger *et al.,* (2006) and Alchalbi *et al.,* (2010) (Figures V.1 and V.2) we can conclude that in general our velocity field is in agreement with the other solution. Point AA09 from our solution attests for this agreement since it is a common point with Alchalbi *et al.,* (2010) under other name (DOHA). The big uncertainties and the random directions of vectors are the result of the lack of measurements and not related to the measurement quality.
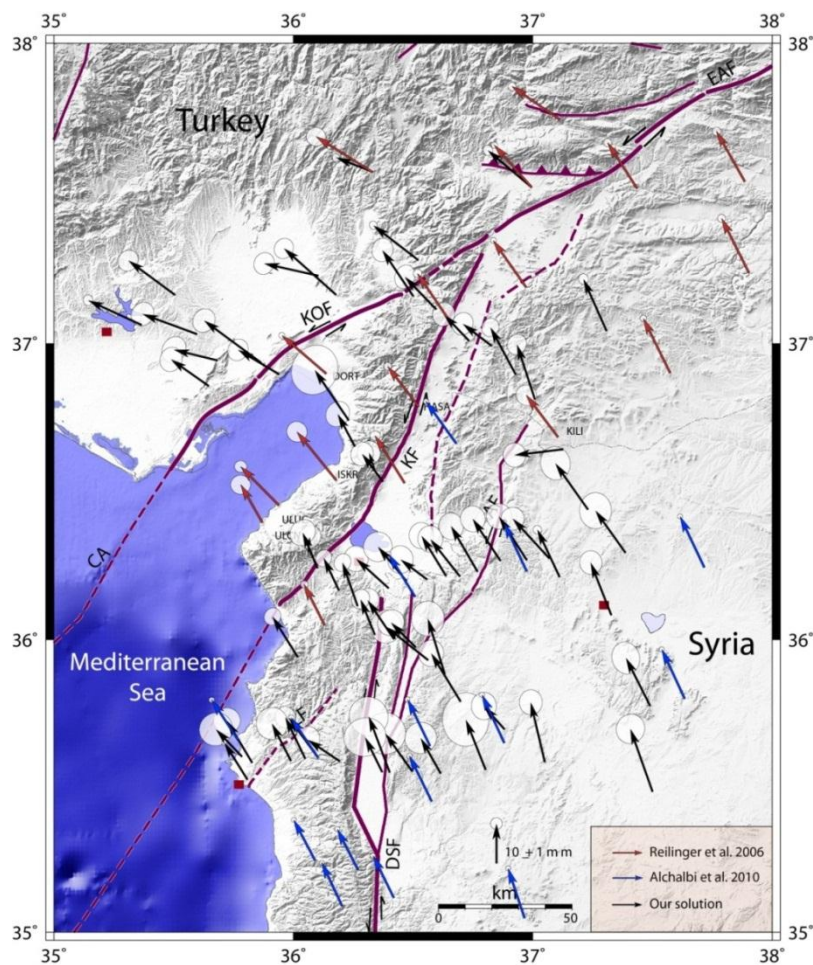
Figure V.1: The GPS velocity field and 95% confidence ellipses representing our solution for the 2009, 2010 and 2011 measurements in the Eurasia fixed reference frame. Black arrows are from this study. Solutions from Reilinger et al., (2006) and Alchalbi et al., (2010) are plotted in red and blue, respectively.

A block model was necessary to explain the GPS data in such a complex region from tectonic point of view. We tried to define the model which gives the best fit to the available data in the region.
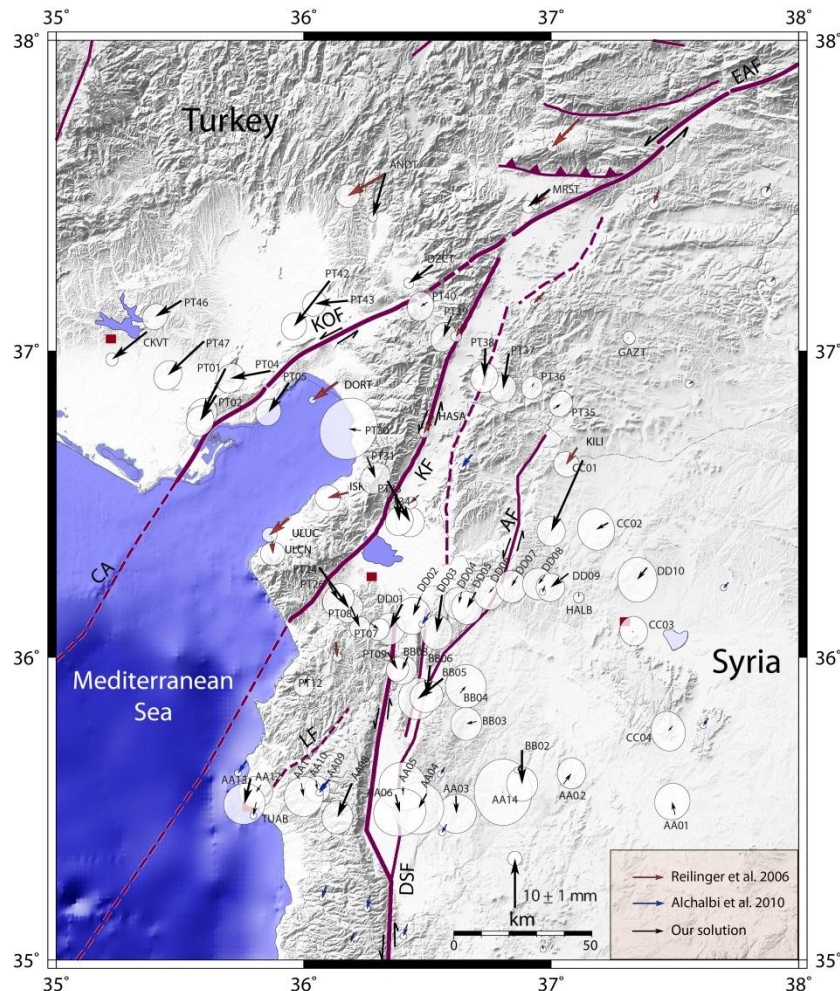
Figure V.2: The GPS velocity field and 95% confidence ellipses representing our solution for the 2009, 2010 and 2011 measurements in the Arabia fixed reference frame. Black arrows are from this study. Solutions from Reilinger et al., (2006) and Alchalbi et al., (2010) are plotted in red and blue, respectively. Fault mapping and slip rates from Meghraoui et al., (2011).

The model D (Figure V.3) is the model used for the interpretation of our results (as explained in chapter 4). This model is developed from the basic simple model used in the previous studies (3 plates and 3 main faults, e.g., Reilinger *et al.,* 2006). In addition to Arabia, Anatolia, and Sinai blocks which are limited by EAF, CA, and DSF, we added an Iskenderun block bounded by the Cyprus subduction zone and the Karatas-Osmaniye fault from south and north respectively, and the Amanous block which is located at the core of the triple junction. The Amanous block was proposed to explain the SE direction of some GPS vectors in the Amanous Mountains. It is limited by Karasu fault from the east, and its limit from the

west was proposed to be free from any elastic deformation. There is no mapped fault to the west of Amanous Mountains but we think that Amanous block exists and its western limits can be different from what we proposed in Figure V.3. With further investigations and geological studies, these limits can be defined more clearly and it can be offshore or inland fault. This fault can be connected to KOF near to Ceyhan, which explains the change from reverse-slip to dip-slip nature of the fault around the city.

Figure V.3: Illustration of different blocks and relative slip rates on faults in block model D. Red arrows represent GPS-derived block velocity relative to Arabia, and black curve arrows and numbers show the directions and the values of blocks angular velocities relative to Arabia respectively.

The Block model D gives a slip rate of 3.5±0.3 mm/yr along the northern segment of the DSF. This amount of slip rate overestimates the GPS vectors in Figure V.2 where the vectors from our study and previous studies do not show any significant relative movement

along the northern DSF between the two adjacent plates. By examining the profiles 5 and 6 in figure IV.19, we can conclude that block model fails to fit the GPS data along the DSF, while the fit between the model and the GPS measurements is better along the other faults and especially on the triple junction. This misfit between the model and measurement along the DSF can be related to the poor constraint on the Sinai plate east to the DSF, or to the unsatisfactory representing of blocks around the DSF. In such model, the DSF shows almost constant velocity rate along all its segments, where many studies suggest a clear difference in slip rate between segments in the south and the north (Gomez *et al.*, 2007a; Le Béon *et al.*, 2008; Alchalbi *et al.*, 2010; Al-Tarazi *et al.*, 2011). In order to have better assessment of slip rate along the DSF it is recommended to introduce one block or more in the model which allow for the internal deformation in the north-west of Arabia plate and the north-east of Sinai plate. The most important part of our model is the triple junction where our model has a good fit to the GPS data and allows for a good interpretation in the term of active deformation and seismic hazard.

V.3   *Slip rate and seismic hazard in the Triple junction*

The direct results of our study are the estimated faults slip rates and locking depth of the mapped faults in the northwest of Syria and southeast of Turkey, beside the parameters of blocks angular velocities, which includes the three main faults forming the triple junction of Hatay (EAF, DSF, CA) and other smaller faults as the Karasu fault and the Karatas-Osmaniye fault. The results obtained in this study are very useful to the prediction of future earthquake size on mapped faults, it can be used together with other seismologic, geologic, and paleoseismologic studies for the seismic hazard analysis.

Numerous studies were realized in order to use historical and instrumental data to develop regressions between earthquake size and earthquake rupture length, area, fault displacement, and fault slip rate (Utsu and Seki, 1954; Tocher, 1958; Kanamori and Anderson, 1975; Bonilla *et al.*, 1984; Ambraseys and Melville, 1988; Wells and Coppersmith, 1994; Anderson *et al.*, 1996; Wang and Ou, 1998; Papazachos *et al.*, 2004). However, some other researchers find that there is dependency of earthquake size on earthquake return time and tectonic environment in which earthquake occur, (e.g., Kanamori and Allen (1986) and Scholz *et al.,* (1986)). The slip rate of fault on which an earthquake occurs is a good indicator for the seismic hazard analysis as explained by Wesnousky (1986), who sorted the faults into high and low slip rate categories. Anderson et al., (1996) used observations of earthquakes that occurred on faults for which slip rate are reported, and developed a regression for moment magnitude M_w (Hanks and Kanamori, 1979). He found this relationship between the moment magnitude, the length of rupture and the slip rate of the fault:

$$Mw = 5.12 + 1.16 * \log L - 0.20 \log S \qquad (V.1)$$

Where L is the length of fault rupture in km and S is the fault slip rate in mm/yr.

Another regression between the moment magnitude of earthquake and the average displacement in km was defined by Wells and Coppersmith (1994) as the following:

$$M = 6.93 + 0.82 * \log (AD) \qquad (V.2)$$

Using these regressions and taking into account the results of our study and the historical seismicity in the region, we can predict the magnitude of the next credible big earthquake along the different faults in the HTJ.

V.3.1   The Dead Sea Fault

In our velocity field (Figure V.2), the DSF does not show significant relative slip rate in the northern part. A maximum value of 1-2 mm/yr can be proposed from the profile 1 in Figure (III.19). We believe that the value of 3.5±0.3 mm/yr resulting from our block model in chapter IV is overestimated and does not represent the actual slip rate on this segment of the DSF. Therefore, we will use the value estimated by the profile 1 to interpret this segment for the seismic hazard.

Meghraoui et al., (2003) assumes 830 years of seismic quiescence, since the Mw= 7.3-7.5 of AD 1170, along the Missyaf segment of the northern DSF of length of 70 km. Considering the 1-2 mm/yr of slip rate we can calculate the total strain accumulation caused by the relative plates motions which give a value of ~1.66 m. Assuming that this segment will be ruptured and the accumulated strain will be released in a big earthquake, we can use the equation (V.2) of Wells and Coppersmith (1994) to predict the potential magnitude of this earthquake which will be ~7.1. Using the equation (V.1) of Anderson et al., (1996) for the same fault segment and considering a whole segment rupture, we can use directly the predicted slip rate and we find a value of Mw ~ 7.2. This magnitude value is comparable to the value predicted by Meghraoui et al., (2003) and mentioned previously.

V.3.2   The East Anatolian Fault

Velocity vectors from our solution and previous solutions around the EAF (Figure V.2) indicate the pure left lateral nature of this fault. In the Arabian reference frame, points in the Anatolian plate have significant southwest movement in comparing with those to the south of EAF in the Arabian plate and relative slip rate of ~8.5 mm/yr can be calculated from these points along the EAF. A similar value was deduced from our block model D, The EAF shows a uniform slip rate of 9.0±0.3 mm/yr and experiences no significant reverse or normal slip rate.

Using the 9.0±0.3 mm/yr value for the different segments of the fault we can also predict the maximum magnitude value of the possible earthquake, with keeping in mind the destructive historical earthquakes which occurred on the EAF (e.g., M 7.8 in 1114 AD, M 7.2 in1866 AD). If we consider the 90 km length segment of Golbasi-Turkoglu in the south-east of EAF not far from the triple junction, where the earthquake of 1114 (M 7.8) occurred, we can assume that a total strain accumulation of ~8m can be released in the next large

earthquake with a possible magnitude of 7.5 – 7.7. The same reasoning will lead us to a similar prediction over all the other segments of EAF and magnitude values between 6.8 and 7.3 should be expected, considering the earthquakes (Ms=7.1, 1893), (Ms=6.8, 1905), (Ms=7.1, 1874). These predicted magnitudes over the different segments of the EAF are very close to the historical earthquakes magnitudes along the related segments.

V.3.3   The Karatas-Osmaniye Fault

Although stations located on the Arabian plate show negligible movements, Anatolia exhibits a south-westward movement with a maximum velocity of 10.2±1.6 mm/yr at ANDR station (Figure V.2). To the southwest, the reduced GPS velocities (4.5–5.8 mm/yr) at DORT, ISKE, ULUC, PT05 and ULCN which are about half of those of the Anatolian plate and left-lateral slip of the EAF, imply a significant fault slip and related seismic activity along the Karatas-Osmaniye Fault (KOF). This is confirmed by the prominent fault scarp morphology and related active features and by the occurrence of the Mw 6.2 Adana earthquake of 1998 (Aktar et al., 2000).

In our block model, the Karatas-Osmaniye fault experiences extensional component between 0.8±0.8 mm/yr and 1.2±0.5 mm/yr. This extensional nature changes to be compressional along the NE segment where it connects to the EAF. The KOF is receiving the deformation caused by the relative motion of Anatolian and Iskenderun blocks with a left lateral strike-slip rate of 3.6±0.7-4.5±0.8 mm/yr (Figure V.3).

Considering the M ~7.4 1513 event (Ambraseys, 2009a) which occurred probably along KOF, and taking into account the slip rate deduced from our block model, we can give 1.8-2.25 m of total accumulated strain. Following the regression of Wells and Coppersmith (1994) we can predict a magnitude of (7.1-7.2) for the next Earthquake on this fault. A similar value can be predicted using the equation (V.1) and assuming a rupture on a fault segment of 75 km. These predictions allow us to conclude that the ongoing strain accumulation rate on the KOF can be released in a future earthquake and generate a destructive earthquake similar to the M ~7.4 1513 event.

V.3.4   The Karasu Fault

Examining the velocity field in Arabian reference frame (Figure V.2) and the GPS profiles in Figure III.19, we can notice that points PT24 and PT33 to the west of KF, show

southeast direction similar to the direction of PT26 and PT34 in the east of the fault, with a clear difference in velocity rate. This relative difference suggests insignificant left-lateral slip rate with compressional component of 2.0 - 4.0 mm/yr which contradict with previous studies suggesting extensional behavior (e.g., Reilinger *et al.,* 2006).

The Karasu fault in our block model has a left lateral strike-slip of 4.0±10 mm/yr in addition to a reverse component change from 2.1±0.9 mm/yr to 2.7±0.7 mm/yr. This compressive nature of the KF agrees with previous studies and analysis (Capan et al., 1987; Yurur and Chorowicz, 1998; Adiyaman and Chorowicz, 2002).

The latest large earthquake on the Karasu fault was the Ms 7.4 of 1822, calculating the average displacement accumulating since that time as a result of the left lateral movement we find 0.75 m. Applying this value to the equation V.2, a maximum value of moment magnitude of a possible earthquake in the near future is M = 6.8. Considering a segment length of 50 km, a magnitude M = 6.95 can be predicted from equation V.1, which is significantly lower than the last historical earthquake.

V.4   Conclusions

In this thesis we provided new GPS velocity field in the eastern Mediterranean around the Hatay triple junction in NW Syria and SE Turkey. Our GPS velocity field serves in the understanding of the active deformations in the region and to identify the tectonic structures role in the kinematics of the junction between Arabia, Sinai, and Anatolia. We provided also new estimations of the slip rate and the locking depth of the most mapped faults related to the junction. We have proposed also a new block model for the triple junction, more complex than previous models (McClusky et al., 2003; Reilinger et al., 2006). The most important features in this model is the Amanous micro block; this block was integrated to our model because of the necessity to explain the GPS vectors in the Amanous range. The statistical parameters calculated show that a complex model with 5 blocks gives the best fit to GPS data used in this study. New estimates of Euler poles and relative angular velocity of different blocks were given.

The perspectives that can be proposed to improve our understanding of the active deformation in the HTJ are summarized here below:

- Repeated GPS measurements on our dense network are needed in the next coming years to improve the uncertainty of GPS velocity field, especially in Syrian side where the sites were measured only in 2 campaigns, and therefore we did not include them to the inversion of our block model.
- The block model inversions can be improved by including different types of data such as geologic faults slip rates, and/or earthquake-derived fault slip vector azimuths. Using such kind of data to models would provide a better assessment of block rotation parameters and then, a more precise assessment of the faults slip rates.
- Further geophysical and geological investigations are fundamental to map the fault of Iskenderun. More information and a better comprehension about this fault will help to constrain the Amanous and Iskenderun blocks which were proposed in the chapter 4.
- The major faults in the Hatay Triple Junction studied in this thesis show a high potential to generate large earthquakes (M > 7). Therefore, detailed studies and more investigations are needed to better constrain the deformations pattern along the different fault segments (e.g., Afrin fault, Idleb fault, and Lattakia fault) in order to

define the seismic hazard related to each segment individually, and update the related seismic hazard and risk maps of the Hatay region.

Auxiliary materials

ARTICLE IN PRESS

Contents lists available at SciVerse ScienceDirect

Journal of Geodynamics

journal homepage: http://www.elsevier.com/locate/jog

Kinematic study at the junction of the East Anatolian fault and the Dead Sea fault from GPS measurements

Yasser Mahmoud[a,*], Frederic Masson[a], Mustapha Meghraoui[a], Ziyadin Cakir[b], Abdulmutaleb Alchalbi[c], Hakan Yavasoglu[d], Onder Yönlü[e], Mohamed Daoud[c], Semih Ergintav[f], Sedat Inan[f]

[a] IPGS, CNRS/University of Strasbourg, France
[b] Department of Geology, Istanbul Technical University, Turkey
[c] NEC-Syrian National Earthquake Center, Damascus, Syria
[d] Department of Geomatics, Istanbul Technical University, Turkey
[e] Department of Geology, Eskisehir Osmangazi University, Turkey
[f] TUBITAK, Marmara Research Center, Gebze, Turkey

ARTICLE INFO

ABSTRACT

The Hatay Triple Junction (HTJ) is a tectonically complex area located at the intersection between the left-lateral East Anatolian fault (EAF), the Cyprus subduction arc and the left-lateral Dead Sea fault (DSF) which is a transform boundary between the Arabian and Sinai plates as they converge toward Eurasia. Previous GPS studies indicate a left-lateral strike-slip rate across the DSF varying from 5 mm/yr (along the southern part) to 2 mm/yr (along the northern part) (Alchalbi et al., 2010; Gomez et al., 2007; Le Béon et al., 2008; Mahmoud et al., 2005; Al-Tarazi et al., 2011). In contrast, the EAF has a roughly constant velocity along strike estimated at 9.7 ± 0.9 mm/yr (Reilinger et al., 2006). The HTJ contains several well-identified active fault segments (DSF, EAF, Osmaniye fault, Karasu fault, Latakia fault, Jisr-al-shuggur fault, Idleb fault and Afrin fault) (Meghraoui et al., 2011), the fault-slip rates for which are poorly constrained.

In order to constrain better the slip rate on faults, we established a network of 57 GPS sites in NW Syria and in SE Turkey. The first campaign was carried out in September 2009; a second took place in September and November 2010 and a third (only in Turkey) in September 2011. Although the velocity field vectors computed from the 2009, 2010 and 2011 measurements appear consistent with other local studies, the results are hampered by large uncertainties due to the short observation period. However, preliminary interpretations are consistent with decreasing velocity along the DSF from south to north reported previously.

© 2012 Elsevier Ltd. All rights reserved.

1. Introduction

The intersection between the Dead Sea fault (DSF), East Anatolian fault (EAF) and Cyprus arc corresponds to the Hatay Triple Junction (HTJ) in south-eastern Turkey and north-western Syria (Fig. 1) forming the plate boundaries between Arabia, Africa and Anatolia (Jackson and McKenzie, 1988). The Hatay tectonic zone is among the few Fault-Fault-Trench (FFT) triple junctions. Other comparable FFT triple junctions are the Mendocino (North America-Pacific-Juan de Fuca plates) and the Kamchatka-Aleutian (Eurasia-Okhotsk-North America plates) that are mainly in oceanic domains (Furlong, 1984; Kozhurin, 2007; McKenzie and Morgan,

1969). The HTJ has the unique advantage to be partly intra-continental and offers a visible and accessible intersection between the EAF, the DSF and the Cyprus subduction zone. Recently, GPS studies provide 18 ± 2 mm/yr for the north-westward motion of Arabia toward Eurasia and 6 ± 2 mm/yr for the northward motion of Africa toward Eurasia in the eastern Mediterranean (Reilinger et al., 2006). At a large scale, the junction is at the intersection between the EAF, DSF and the Cyprus arc with its inland continuation, the Karasu Valley Fault (KVF) in southern Turkey and northern Syria (Meghraoui et al., 2011). The active deformation and related block tectonics in the vicinity of the TJ are, however, poorly constrained and a better assessment of fault strain accumulation rate and interseismic behavior are needed in the HTJ.

The junction appears nowadays as a zone of diffuse and low-level seismicity but the presence of major active strike-slip faults and cumulative offsets (Altunel et al., 2009; Karabacak et al., 2010; Meghraoui et al., 2011) suggests the occurrence of large

* Corresponding author.
E-mail addresses: yasser.mahmoud@eost.u-strasbg.fr, yasser@unistra.fr
(Y. Mahmoud).

ARTICLE IN PRESS
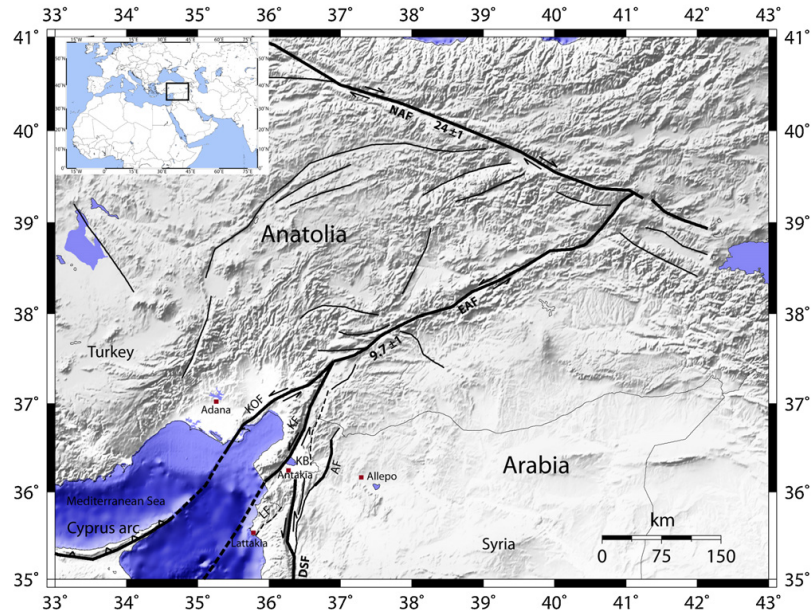
Fig. 1. Map showing the Hatay triple junction area and the principal faults in the region (Meghraoui et al., 2011). The key tectonic features: AGF: Al Ghab fault, AF: Afrin fault, CA: Cyprus Arc, DSF: Dead sea fault, KB: Karasu basin, KF: Karasu fault, KOF: Karatas-Osmaniye fault, LF: Lattakia fault, MF: Missyaf fault, NAF: north Anatolian fault, EAF: East Anatolian fault.

earthquakes with coseismic rupture displacements. Indeed, the HTJ has been the site of numerous historical earthquakes, where in particular the largest seismic event occurred on 19 November 1114 (M 7.8) along the EAF, 29 December 1408 (M 7.4) along the DSF and 13 August 1822 (M 7.3) along the Karasu Fault (Ambraseys and Jackson, 1998; Sbeinati et al., 2005; Sbeinati, 2010). The M_w 6.2 Adana earthquake of 1998 near the EAF (Aktar et al., 2000) and the M_w 6.8 Cyprus subduction zone earthquake of 1996 (Papazachos and Papaioannou, 1999) also attest to the occurrence of large earthquakes more recently. The junction "sensu stricto" was relatively quiescent during the last century, but its late Quaternary tectonics, historical seismic activity and geodetic studies indicate the possibility of a significant seismic strain release (Altunel et al., 2009; Ambraseys and Jackson, 1998; Meghraoui et al., 2003; Salamon et al., 2003; Sbeinati et al., 2005).

In this paper, we present a kinematic synthesis of the active tectonics of the HTJ and compare with the previous geodetic rates, reported along faults comprising this complex junction. A new GPS network that consists in four profiles across the DSF, the EAF and Karasu Valley Fault has been installed and measured and is expected to provide better constraints of the active deformation at the HTJ. After data processing and analysis, we present new results and discuss their consistency with previous tectonic and geodetic studies of the region.

2. Kinematic synthesis of the DSF

Recent studies have characterized the first order geodetic velocity field around the DSF (Alchalbi et al., 2010; Gomez et al., 2007; Le Béon et al., 2008; Reilinger et al., 2006; Al-Tarazi et al., 2011). These separate velocity fields have been individually combined applying rotational transformations, which minimize the residual misfit of GPS velocities for the sites that are common to Reilinger et al.

(2006), in order to apply the rotational transformation we used (12) common sites from Alchalbi et al. (2010) and Gomez et al. (2007), (12) common sites from Le Béon et al. (2008) and (16) common sites from Al-Tarazi et al. (2011), the RMSs fit for these transformations are 0.66 mm/yr, 0.48 mm/yr and 0.2 mm/yr, respectively. Part of the combined data is shown in Fig. 2a in an Arabia fixed reference frame. Following (Savage and Burford, 1973), using 1-D elastic dislocation model of a locked fault assumes an infinitely long strike-slip fault and expresses the station velocity, b, as a function of the long-term slip rate (V), fault locking depth (D) and distance from the fault (x):

$$b = \left(\frac{V}{\pi}\right) \arctan\left(\frac{x}{D}\right) \tag{1}$$

From this relationship, it is possible to estimate the relative movement of the Africa-Sinai block compared to Arabia using a simple block model. Assuming a single fault with uniform slip along strike, this results in a rate of strain accumulation for the DSF of ~4.5 ± 0.3 mm/yr (Reilinger et al., 2006).

However, more detailed information of the velocity field confirms that the velocity is varying along strike. From a rate of about 4.5 mm/yr along the southern and central segments (Mahmoud et al., 2005) to a rate of about 2 mm/yr along the northern segment (north of 35°; Alchalbi et al., 2010). Moreover all the profiles across the fault (Fig. 2b), central or north do not have a density of points and/or measurement accuracy sufficient to allow unambiguous determination of the locking depth of the fault. A locking depth of 11 ± 9 km is proposed along the southernmost segment (Le Béon et al., 2008) while this looking depth is very difficult to estimate along the northernmost segment (Alchalbi et al., 2010).

The slip rate of ~4.5 mm/yr proposed along the southern and central parts of the DSF is consistent with 1000–1300 yr mean return periods for strike-slip earthquakes within the Lebanese

ARTICLE IN PRESS

restraining bend (Daeron et al., 2007; Gomez et al., 2003; Nemer et al., 2008) and along the southern DSF segment (Ferry et al., 2007; Klinger et al., 2000a). They are also consistent with paleoseimological and geomorphological studies (Ambraseys et al., 1994; Freund, 1970; Ginat et al., 1998; Guidoboni et al., 1994; Klinger et al., 2000a, 2000b; Niemi et al., 2001; Zilberman et al., 2005; Ferry et al., 2011). Conversely, the very low velocity observed along the northern segment is not consistent with long-term rates (Meghraoui et al., 2003; Sbeinati et al., 2010) and is not easily integrated into a regional kinematic model of the HTJ.

3. Geodetic data around the HTJ

GPS campaigns using Trimble 4000SSI, 4000SSE, 4700, 5700 and Ashtech UZ12 were initiated in Hatay province in 1991 and

observed again in 1994, 1996, 1998, 2002 and 2004. Fig. 5 shows the location of the 22 GPS sites and the velocities from Reilinger et al. (2006) computed for an Arabia fixed reference frame. The GPS stations were re-measured in 2004 in conjunction with the Massachusetts Institute of Technology, with Strasbourg participation supported in the frame of the EC-Funded project APAME (Meghraoui et al., 2011).

Although stations located on the Arabian plate show negligible movements, Anatolia exhibits a south-westward movement with a maximum velocity of 10.2 ± 1.6 mm/yr at ANDR station (Fig. 5). To the southwest, GPS velocities at DORT, ISKE, ULUC and ULCN show similar directions with stations north of the EAF and they seem to belong to the Anatolian plate. However, their reduced velocities (4.5–5.8 mm/yr) which are about half of those of the Anatolian plate and left-lateral slip of the EAF, imply a significant fault slip and
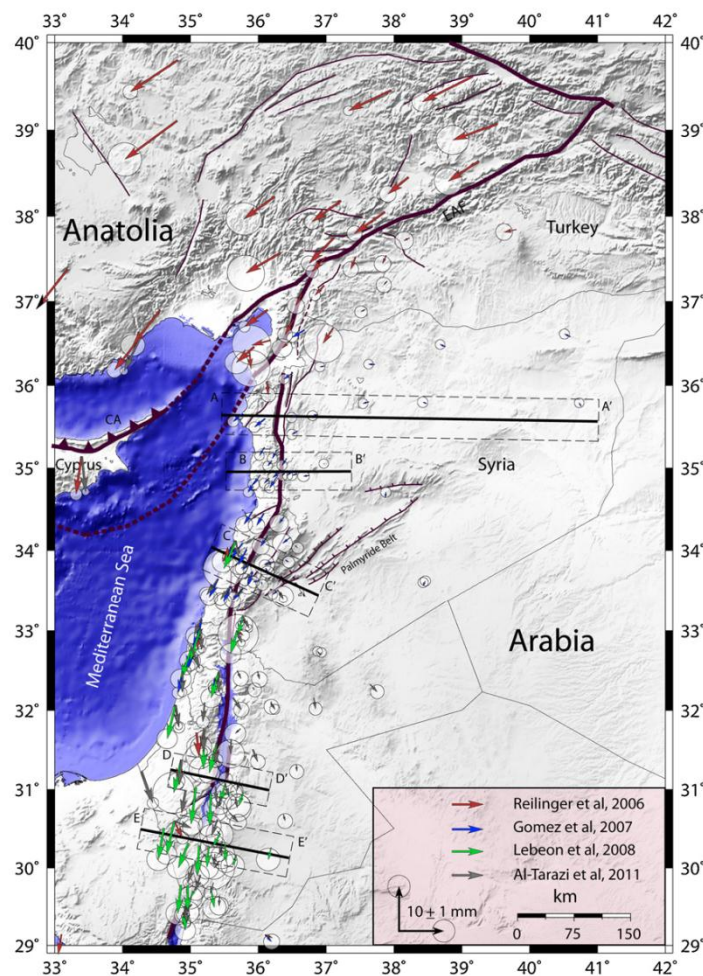
Fig. 2. (a) GPS Horizontal velocity field and the 95% confidence ellipses obtained by previous campaigns in the Eastern Mediterranean region with respect to the Arabia-fixed reference frame. GPS data are from Reilinger et al. (2006), Gomez et al. (2007) and Le Béon et al. (2008) and Al-Tarazi et al. (2011), and mapped faults from Meghraoui et al. (2011). Boxes denote the swath encompassed by the profiles shown in (b). Also shown in the map are the three major faults in the region, EAF: East Anatolian fault, DSF: Dead Sea fault, CA: Cyprus arc. (b) Plots showing the GPS velocity parallel to the Dead Sea fault in its different parts from north to south. Data are from Reilinger et al. (2006), Gomez et al. (2007) and Le Béon et al. (2008). The position of GPS points is shown relative to the Dead Sea fault which is presented as a dashed line. The plots show the predicted parallel velocities V for different elastic dislocation models (different values of slip rate and locking depth) along the fault and the decreasing of slip rate toward the north. The horizontal axe shows the distance from the fault while the vertical axe shows the velocity parallel to the fault.

Auxiliary materials

Fig. 2. (Continued).

ARTICLE IN PRESS

related seismic activity along the Karatas-Osmaniye Fault (KOF). This is confirmed by the prominent fault scarp morphology and related active features and by the occurrence of the M_w 6.2 Adana earthquake of 1998 (Aktar et al., 2000). Furthermore, an equivalent observation can be made from the velocity vector distribution east and west of the Karasu Fault that suggests left-lateral slip with extensional component of 0.4–2.0 mm/yr along the fault. One may also observe the southward motion of SENK station located south of the Amik Basin and west of the DSF, suggesting a position on the African plate.

Unfortunately, the number of stations relative to the complex HTJ tectonics does not allow a precise determination of the individual velocity for each fault. Previous GPS studies in the eastern Mediterranean were designed for large scale tectonic issues that include the collision between the Arabian plate with Eurasia and the westward extrusion of Anatolia (Masson et al., 2007; Reilinger et al., 2006). The local tectonic complexities at the Hatay junction and the intersection between EAF, DSF and Cyprus subduction zone need a dense GPS network and detailed investigations of fault kinematics. Therefore, we developed a new GPS campaign network to densify the existing one. Moreover, the network had to be transnational in order to characterize faults which are distributed across the boundary between Turkey and Syria.

4. The new GPS network

To better characterize of the kinematic field, new GPS field campaigns were launched in southern Turkey and northern Syria. Taking into account the previous field investigations and GPS network, a new network of 4 GPS profiles across active faults and related tectonic blocks was installed and measured in 2009. The 4 GPS profiles across the Hatay region (Fig. 3) illustrate a network configuration that may contribute to an accurate estimate of the distributed tectonic activity and fault slip rate. This network contains 24 sites in Turkey and 33 sites in Syria.

The point's alignment and the continuity of the profiles from Syria to Turkey are taken into account for a better assessment of the velocity field and physical parameters of fault branches along the major fault systems. Profile 1 (E-W) crosses the Ghab basin and related north-south border faults and the NE-SW trending Lattakia
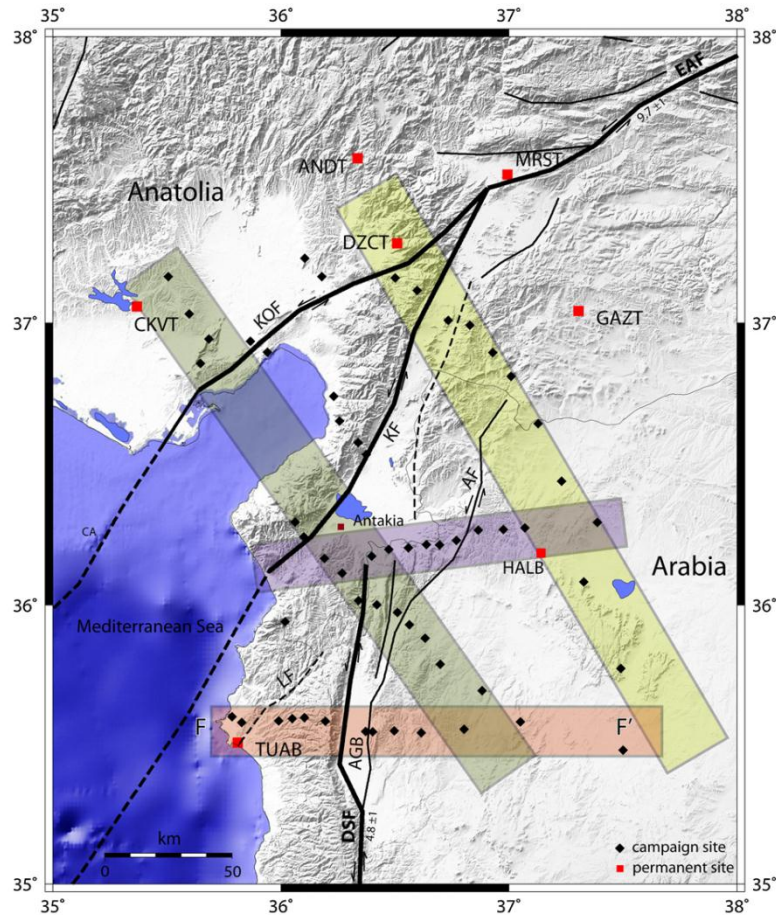
Fig. 3. New GPS network in NW Syria and SE Turkey. Black points are the campaign sites. The sites are distributed along 4 main profiles (33 points) in Syria with an extension of 2 profiles (24 points) in Turkey. The geometry of our GPS network is taken into account for a better assessment of velocity field and physical parameters of fault branches along the three major fault systems. The red points are permanent GPS stations near to the study area in Syria and Turkey. (For interpretation of the references to color in this figure legend, the reader is referred to the web version of the article.)

Please cite this article in press as: Mahmoud, Y., et al., Kinematic study at the junction of the East Anatolian fault and the Dead Sea fault from GPS measurements. J. Geodyn. (2012), http://dx.doi.org/10.1016/j.jog.2012.05.006

ARTICLE IN PRESS

fault. Profile 2 crosses the easternmost fault system of the northern Ghab Basin that includes the Idleb and Afrin faults. Profile 3 (NW-SE) crosses KOF, the northern Ghab Basin and related Idleb and Afamia fault system. The Profile 4 crosses the Karasu Valley and East Anatolian fault.

As partly indicated in Fig. 3, the network is sustained by several CGPS stations in Turkey (MRST, DZCT, ANDT, CKVT, CRMT, ELZT, GAZT, MLYT) and Syria (HALB, TUAB, BUSF, RAQA, PALM, UDMC).

5. Data processing and preliminary results

The first campaign was carried out in September 2009 with the measurements of 24 points in Turkey, all sites observed for 24 h over two sessions of 12 h using Thales Z Max receivers with Thales Z Max Ashtech antenna. The 33 points in Syria were measured in October and November 2009 where each site was observed for one session of 24 h using Thales DSNP 6502MK receivers with Leica AT504 Choke Ring Antenna. The GPS data were logged with a 15 s and 30 s sampling rate in Turkey and in Syria, respectively, and antennas were fixed on monuments using antenna masts in order to minimize antenna setup errors. A second campaign took place in September and November 2010 where all the sites were measured with the same instruments and method used for the 2009 campaign. A third campaign took place in September 2011. Unfortunately, it was not possible to measure the Syrian sites and only the Turkish side of the network has been measured three times.

The GPS data were processed together with previously collected data from a set of 8 permanent sites in Turkey and 6 others in Syria using the GAMIT/GLOBK program (Dong et al., 1998; Herring et al., 1997; King and Bock, 2000). We analyze the data in a three-step approach as described by Feigl et al. (1993) and Dong et al. (1998). In the first step, we use double difference GPS phase observations to estimate (1) the zenith delay of atmosphere at each site every 2 h, (2) the orbital and Earth orientation parameters (EOP), and (3) station coordinates for each day. We have integrated the dataset of about 50 IGS (International GPS Service) permanent stations in order to calibrate our regional observations to the global GPS network. The IGS stations cover a large domain including Africa, Eurasia and Middle East (Fig. 4) and provide daily solutions computed not only during our campaign periods but also (from January 1999 to December 2011) in order to constrain the reference frame definition. In the second step, we combine the loosely constrained parameters and their covariance in a Kalman filter to estimate a consistent set of positions and velocities. At the third step, we define the reference frame for coordinates and velocities. The horizontal velocity components have been estimated according to the International Terrestrial Reference Frame (ITRF05, Altamimi et al., 2007) using a set of 12 IGS sites as a stabilization frame (GRAS, GRAZ, JOZE, POTS, WZTR, RABT, MAS1, PDEL, BOR1, TLSE, WTZR, WSRT). Furthermore, we define an Arabia fixed reference frame minimizing the observed velocities and the velocity computed from the Arabian rotation. In Table 1 we show the Euler Pole and the angular velocities calculated in this study for Eurasia, Africa and Arabia plate and compare it with other studies (Fig. 6a,b).

In Fig. 6a and b, the preliminary velocity field obtained from the data measured in 2009, 2010 and 2011 is shown in an Eurasia and an Arabia fixed reference frame (Table 2). Our new velocity
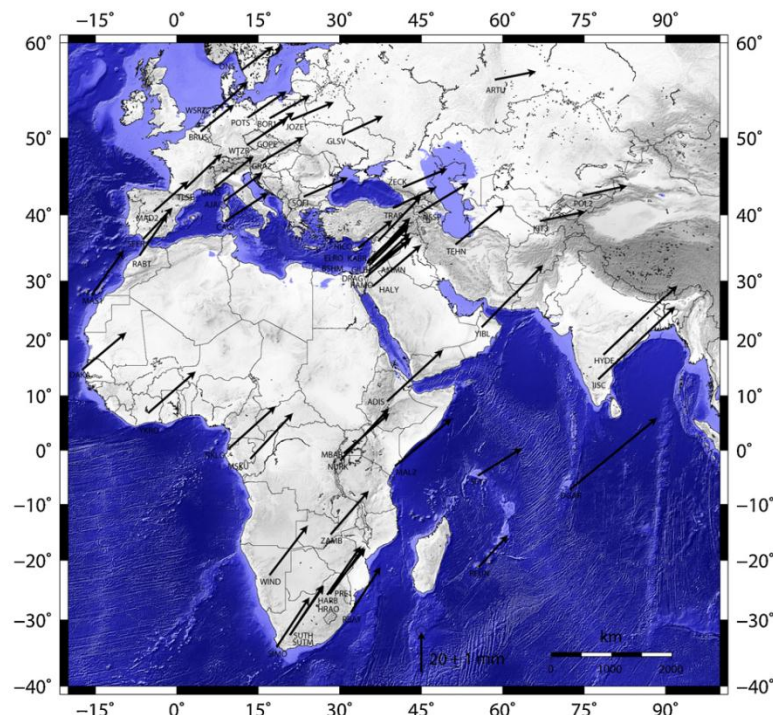
Fig. 4. GPS velocity field of the 50 IGS permanent stations used in this study to constrain our observations to the global GPS network and their 95% confidence ellipses shown in the ITRF05 reference. Data are from January 1999 to December 2010.

ARTICLE IN PRESS

Table 1

The rotation pole and angular velocity for the Eurasia, Africa and Arabia plate from this study and Altamimi et al. (2007) and from the SOPAC pole rotation tables (http://sopac.ucsd.edu/cgi-bin/poleRotationValues.cgi). Solutions for Altamimi et al. (2007) and this study are relative to ITRF2005, the SOPAC solution is relative to ITRF2000.

	Lat. °N	Lon. °E	Rotation rate °/Ma
Eurasia			
This study	58.647	−100.781	0.230
Altamimi et al. (2007)	56.330	−95.979	0.261
SOPAC solution	55.851	−97.378	0.263
Africa			
This study	44.439	−79.292	0.287
Altamimi et al. (2007)	49.955	−82.501	0.269
SOPAC solution	48.997	−80.424	0.275
Arabia			
This study	49.087	6.043	0.561
Altamimi et al. (2007)	49.642	5.061	0.579
SOPAC solution	50.209	4.162	0.567

field has been also combined following the method described above, in order to be directly comparable to the previously published geodetic data of Reilinger et al. (2006) and Alchalbi et al. (2010). Due to the small time interval between the two campaigns (~1 yr), the velocities suffer a high uncertainties. Fig. 6c shows a profile across the DSF corresponding to profile F–F′ of Fig. 3. In our point of view, only one very important conclusion can be underlined. It concerns the decreasing of the velocity of the DSF going northward and it appears that our data are consistent with 1–2 mm/yr velocity rate along the northern part of the DSF. In fact, we observe that most of the sites located west of the DSF and within the Ghab basin have velocities very small relatively to the Arabian plate. It questions the rigidity of the Sinai block in its northern end and the relationships with the Cyprus subduction zone. Effectively, the triangle located between the DSF and the Cyprus arc belonging to the Sinai block does not show significant movement relatively to Arabia. In contrast, south of Syria the Sinai block shows a significant movement relatively to the Arabia block, and hence the differential movement within the Sinai block indicate a major variation in its rigidity (Alchalbi et al., 2010).
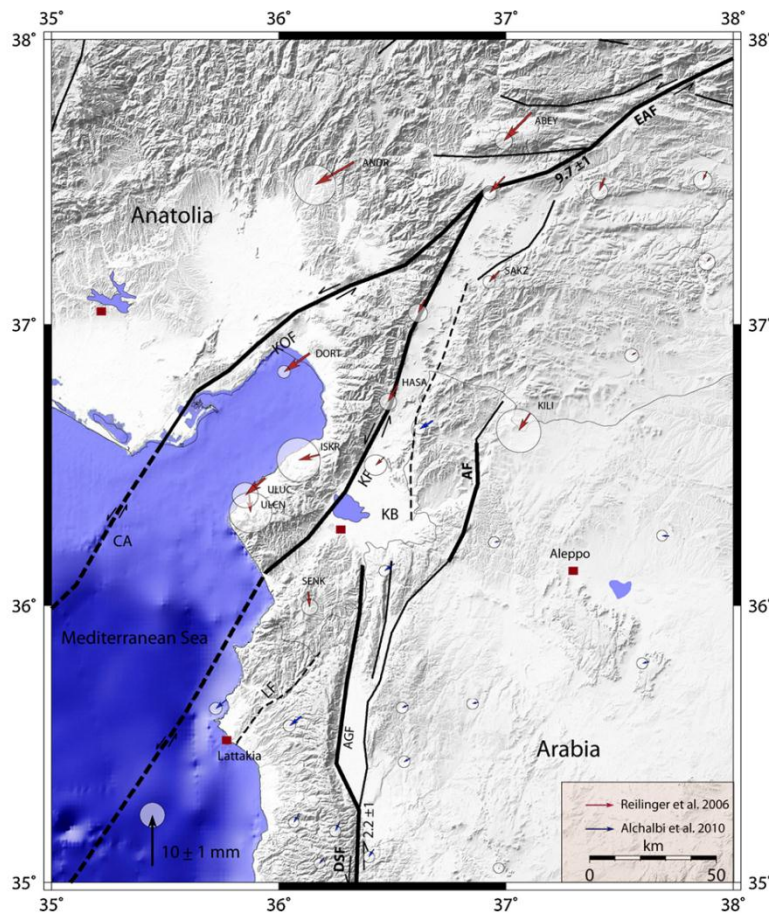
Fig. 5. GPS velocity field in the triple junction area from Reilinger et al. (2006) and Alchalbi et al. (2010) in an Arabia fixed reference frame.

ARTICLE IN PRESS

8   *Y. Mahmoud et al. / Journal of Geodynamics xxx (2012) xxx–xxx*

Table 2
Velocities of GPS sites shown in Fig. 6b.

Site	Longitude	Latitude	Eurasia-fixed		Arabia-fixed		Sig. E	Sig. N	Corr
			Ve	Vn	Ve	Vn			
Campaign sites in Syria									
AA01	37.501	35.482	−3.32	15.43	4.61	5.79	2.33	2.51	0.035
AA02	37.051	35.583	−3.84	12.82	4.23	3.53	1.98	2.15	0.006
AA03	36.616	35.544	−4.53	7.09	3.54	−1.85	2.70	2.68	0.013
AA04	36.497	35.551	−6.80	10.79	1.29	1.95	3.48	3.61	−0.001
AA05	36.403	35.547	−4.80	16.06	3.30	7.30	3.29	3.35	−0.048
AA06	36.371	35.549	−3.76	7.65	4.34	−1.09	3.59	3.29	0.055
AA08	36.195	35.585	−7.05	3.14	1.10	−5.46	2.18	2.34	0.029
AA09	36.104	35.598	−5.30	8.72	2.87	0.20	2.54	2.73	0.054
AA10	36.050	35.595	−5.32	8.03	2.85	−0.45	1.73	1.83	−0.014
AA11	35.991	35.587	−6.35	10.84	1.81	2.41	2.72	2.78	0.011
AA12	35.828	35.581	−7.56	10.96	0.61	2.66	2.28	2.21	0.001
AA13	35.786	35.602	−9.60	7.58	−1.40	−0.69	2.83	2.82	0.033
AA14	36.803	35.557	−2.39	7.82	5.67	−1.26	3.98	4.64	−0.012
BB02	36.883	35.695	−5.65	3.33	2.53	−5.82	2.17	2.37	−0.007
BB03	36.699	35.789	−5.05	12.70	3.23	3.70	2.23	2.30	0.012
BB04	36.633	35.882	−0.23	14.48	8.14	5.53	3.52	3.45	0.051
BB05	36.564	35.931	−7.06	9.36	1.36	0.46	3.21	3.11	0.063
BB06	36.511	35.974	−3.38	5.01	5.08	−3.85	2.30	2.24	0.045
BB08	36.421	36.002	−5.40	7.33	3.10	−1.45	1.99	2.04	0.020
CC01	37.128	36.645	−14.20	−3.86	−5.20	−13.20	1.94	2.06	−0.006
CC02	37.231	36.441	−7.08	8.26	1.73	−1.17	2.52	2.84	−0.051
CC03	37.329	36.083	−5.65	9.86	2.83	0.35	1.83	2.02	0.002
CC04	37.490	35.774	−7.13	7.33	1.07	−2.30	2.38	2.74	−0.074
DD01	36.398	36.175	−5.81	8.16	2.85	−0.60	2.12	2.22	0.030
DD02	36.473	36.198	−6.51	7.95	2.16	−0.87	2.44	2.54	0.005
DD03	36.559	36.204	−2.73	4.09	5.94	−4.79	2.29	2.46	−0.010
DD04	36.638	36.216	−2.47	11.17	6.19	2.22	2.03	2.22	−0.026
DD05	36.696	36.215	−7.60	7.28	1.06	−1.72	2.06	2.27	−0.014
DD06	36.770	36.230	−5.36	7.56	3.31	−1.49	2.07	2.33	−0.014
DD07	36.866	36.267	−9.39	9.84	−0.69	0.71	2.06	2.21	−0.027
DD08	36.976	36.270	−7.31	10.30	1.37	1.08	2.07	2.14	0.019
DD09	37.070	36.275	−6.84	6.38	1.84	−2.92	2.04	2.00	−0.001
DD10	37.388	36.294	−7.08	6.61	1.59	−2.94	2.69	3.09	0.003
Campaign sites in Turkey									
PT01	35.685	36.943	−13.63	3.76	−4.24	−4.43	2.03	2.21	0.164
PT02	35.648	36.857	−12.38	7.59	−3.05	−0.56	1.87	2.07	0.086
PT04	35.866	36.935	−17.68	9.30	−8.30	0.97	1.97	2.09	0.120
PT05	35.941	36.896	−13.95	5.15	−4.62	−3.24	1.78	1.89	0.118
PT07	36.269	36.114	−5.42	9.86	3.19	1.20	1.44	1.51	0.128
PT08	36.191	36.166	−5.30	7.26	3.36	−1.33	1.37	1.45	0.120
PT09	36.341	36.017	−5.26	7.44	3.26	−1.27	1.55	1.68	0.095
PT12	36.019	35.941	−7.96	9.07	0.52	0.62	1.43	1.48	0.096
PT24	36.063	36.296	−5.48	1.97	3.32	−6.52	1.82	1.95	0.105
PT26	36.101	36.243	−7.95	7.83	0.79	−0.69	2.07	2.14	0.097
PT30	36.232	36.741	−11.98	9.70	−2.81	1.08	3.94	4.20	0.095
PT31	36.257	36.654	−10.69	7.66	−1.60	−0.99	2.10	2.19	0.113
PT33	36.339	36.577	−4.54	1.48	4.47	−7.23	1.93	2.02	0.001
PT34	36.374	36.535	−8.57	4.56	0.40	−4.18	1.90	2.01	0.065
PT35	37.009	36.812	−6.87	13.04	2.29	3.79	1.65	1.78	0.084
PT36	36.929	36.895	−8.31	10.91	0.93	1.73	1.48	1.57	0.091
PT37	36.829	36.992	−9.38	5.09	−0.04	−4.02	1.90	1.99	0.136
PT38	36.734	37.009	−9.52	6.54	−0.16	−2.49	1.89	2.01	0.055
PT39	36.598	37.114	−10.41	7.13	−0.94	−1.79	1.76	2.03	0.149
PT40	36.502	37.158	−10.05	10.39	−0.54	1.55	1.82	2.01	0.068
PT42	36.105	37.227	−16.72	2.72	−7.11	−5.81	1.76	1.87	0.094
PT43	36.179	37.162	−16.56	10.95	−7.02	2.37	1.66	1.74	0.100
PT46	35.506	37.162	−15.36	9.40	−5.75	1.36	1.74	1.80	0.118
PT47	35.599	37.031	−17.19	5.55	−7.71	−2.56	1.93	2.03	0.132
Other CGPS sites (data obtained from SOPAC and UNAVCO archives)									
AMMN	35.880	32.029	−6.34	3.22	−1.34	−5.13	0.09	0.08	−0.019
BSHM	35.023	32.779	−5.85	7.02	−0.12	−0.63	0.07	0.07	−0.054
DRAG	35.392	31.593	−5.82	6.67	−1.18	−1.28	0.01	0.01	−0.118
GILB	35.416	32.479	−6.67	6.96	−1.23	−1.01	0.07	0.07	−0.057
HALY	36.100	29.139	−2.61	8.28	−0.22	−0.24	0.08	0.07	−0.027
KABR	35.145	33.023	−6.84	6.24	−0.89	−1.51	0.08	0.08	0.021
NICO	33.396	35.141	−8.85	1.23	−0.88	−5.10	0.01	0.01	−0.133
TEHN	51.334	35.697	−3.38	10.85	2.63	−9.49	0.02	0.02	−0.073
YIBL	56.112	22.186	2.59	23.53	−3.43	−0.27	0.03	0.02	−0.079

ARTICLE IN PRESS
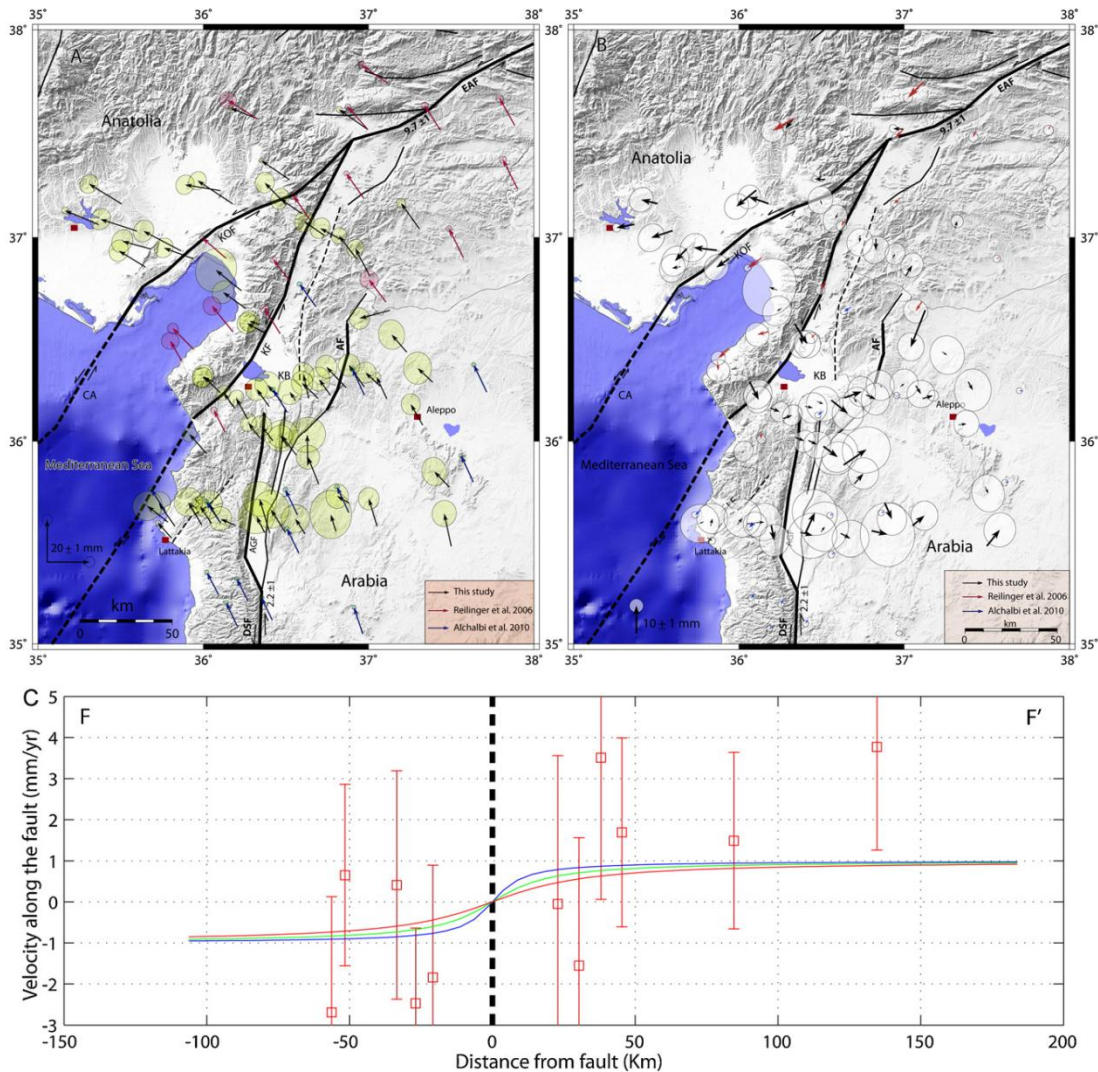
Fig. 6. (a) The GPS velocity field representing our solution for the 2009, 2010 and 2011 measurements in the Eurasia fixed reference frame. Black arrows are from this study, solutions from Reilinger et al. (2006) and Alchalbi et al. (2010) are plotted in red and blue, respectively. Fault mapping and slip rates from Meghraoui et al. (2011). Abbreviations for some key tectonic features: AGF: Al Ghab fault; AF: Afrin fault; CA: Cyprus Arc; KB: Karasu basin; KF: Karasu fault; KOF: Karatas-Osmaniye fault; LF: Lattakia fault; DSF: Dead Sea fault; EAF: East Anatolian fault. (b) The same as (a) but in the Arabia fixed reference frame. (c) The 1-D elastic dislocation models with different values of slip rate and locking depth corresponding to the profile F–F′ in Fig. 3 and the GPS velocity parallel to the fault. The plotted values are determined from the 2009 and 2010 measurements in Syria. The DSF is presented as a dashed line, the horizontal axe shows the distance from the fault while the vertical axe shows the velocity parallel to the fault. (For interpretation of the references to color in this figure legend, the reader is referred to the web version of the article.)

6. Conclusion and discussion

The GPS velocity field deduced from 2009, 2010 and 2011 campaigns for the 57 campaign sites and 14 permanent sites in the regions provides new data to describe the deformations in the HTJ and understand the tectonics of small faults. However, the campaigns are not sufficient to obtain an accurate velocity rate for most of the principal faults. Fig. 6b, does not contradict velocity rates proposed in previous studies (1–2 mm/yr across DSF, 2–3.5 mm/yr across KOF, 3–5 mm/yr across KF and 2–3 mm/yr across the AF, Gomez et al., 2007; Meghraoui et al., 2011).

The velocity vectors suffer a relative inaccuracy due to the short span time of the measurements (1 or 2 years). In general our campaign GPS velocity field vectors uncertainties are about 2.5 mm/yr for the sites in the Syrian side and about 1.5 mm/yr for the other sites in Turkey. This difference in uncertainties between sites in Turkey and Syria can be explained by the number of campaigns and the time span which are both greater in Turkey than in Syria. The CGPS sites in Turkey and Syria have better uncertainties with less than 1 mm/yr.

Despite the large uncertainties in our GPS results, we think that with further measurements, the accuracy can be improved and the

profile network may help in a better understanding of the major and small fault segments tectonics and kinematics. The GPS station density and distribution in profiles perpendicular to most of fault segments in HTJ, and a longer time span of measurements will reduce the uncertainties of site velocity estimates and slip rates along faults.

References

Aktar, M., Ergin, M., Zalaybey, S., Tapirdamaz, C., Yrük, A., Biçmen, F., 2000. A lower crustal event in the northeastern Mediterranean: the 1998 Adana earthquake ($M_w = 6.2$) and its aftershocks. Geophysical Research Letters 27, 2361–2364.

Al-Tarazi, E., Rajab, J.A., Gomez, F., Cochran, W., Jaafar, R., Ferry, M., 2011. GPS measurements of near-field deformation along the southern Dead Sea Fault System. Geochemistry, Geophysics, Geosystems 12, Q12021.

Alchalbi, A., Daoud, M., Gomez, F., McClusky, S., Reilinger, R., Romeyeh, M.A., Alsouod, A., Yassminh, R., Ballani, B., Darawcheh, R., 2010. Crustal deformation in northwestern Arabia from GPS measurements in Syria: slow slip rate along the northern Dead Sea Fault. Geophysical Journal International 180, 125–135.

Altamimi, Z., Collilieux, X., Legrand, J., Garayt, B., Boucher, C., 2007. ITRF2005: a new release of the International Terrestrial Reference Frame based on time series of station positions and Earth Orientation Parameters. Journal of Geophysical Research 112, B09401.

Altunel, E., Meghraoui, M., Karabacak, V., Akyüz, S.H., Ferry, M., Yalçiner, C., Munschy, M., 2009. Archaeological sites (Tell and Road) offset by the Dead Sea Fault in the Amik Basin, Southern Turkey. Geophysical Journal International 179, 1313–1329.

Ambraseys, N.N., Jackson, J.A., 1998. Faulting associated with historical and recent earthquakes in the Eastern Mediterranean region. Geophysical Journal International 133, 390–406.

Ambraseys, N.N., Melville, C.P., Adams, R.D., 1994. The Seismicity of Egypt, Arabia, and the Red Sea: A Historical Review. Cambridge Univ Pr.

Daeron, M., Klinger, Y., Tapponnier, P., Elias, A., Jacques, E., Sursock, A., 2007. 12,000-year-long record of 10 to 13 paleoearthquakes on the Yammouneh Fault, Levant fault system, Lebanon. Bulletin of the Seismological Society of America 97 (3), 749–771.

Dong, D., Herring, T.A., King, R.W., 1998. Estimating regional deformation from a combination of space and terrestrial geodetic data. Journal of Geodesy 72, 200–214.

Feigl, K.L., Agnew, D.C., Bock, Y., Dong, D.N., Donnellan, A., Hager, B.H., Herring, T.A., Jackson, D.D., King, R.W., Larsen, S.K., 1993. Measurement of the velocity field in central and southern California. Journal of Geophysical Research 98, 21,677–21,712.

Ferry, M., Meghraoui, M., Abou Karaki, N., Al-Taj, M., Khalil, L., 2011. Episodic behavior of the Jordan Valley section of the Dead Sea fault inferred from a 14-ka-long integrated catalog of large earthquakes. Bulletin of the Seismological Society of America 101, 39.

Ferry, M., Meghraoui, M., Karaki, N.A., Al-Taj, M., Amoush, H., Al-Dhaisat, S., Barjous, M., 2007. A 48-kyr-long slip rate history for the Jordan Valley segment of the Dead Sea Fault. Earth and Planetary Science Letters 260, 394–406.

Freund, R., 1970. The geometry of faulting in the Galilee. Israel Journal of Earth Sciences 19, 117–140.

Furlong, K.P., 1984. Lithospheric behavior with triple junction migration: an example based on the Mendocino triple junction. Physics of the Earth and Planetary Interiors 36, 213–223.

Ginat, H., Enzel, Y., Avni, Y., 1998. Translocated Plio-Pleistocene drainage systems along the Arava fault of the Dead Sea transform. Tectonophysics 284, 151–160.

Gomez, F., Karam, G., Khawlie, M., McClusky, S., Vernant, P., Reilinger, R., Jaafar, R., Tabet, C., Khair, K., Barazangi, M., 2007. Global Positioning System measurements of strain accumulation and slip transfer through the restraining bend along the Dead Sea fault system in Lebanon. Geophysical Journal International 168, 1021–1028.

Gomez, F., Meghraoui, M., Darkal, A.N., Hijazi, F., Mouty, M., Suleiman, Y., Sbeinati, R., Darawcheh, R., Al Ghazzi, R., Barazangi, M., 2003. Holocene faulting and earthquake recurrence along the Serghaya branch of the Dead Sea fault system in Syria and Lebanon. Geophysical Journal International 153, 658–674.

Guidoboni, E., Comastri, A., Traina, G., Phillips, B., Istituto nazionale di geofisica, 1994. Catalogue of Ancient Earthquakes in the Mediterranean Area up to the 10th Century. Istituto nazionale di geofisica, Rome.

Herring, T.A., King, R.W., McClusky, S.C., 1997. Geodetic constraints on interseismic, coseismic, and postseismic deformation in southern California. Annual Report to SCEC.

Jackson, J., McKenzie, D., 1988. The relationship between plate motions and seismic moment tensors, and the rates of active deformation in the Mediterranean and Middle East. Geophysical Journal 93, 45–73.

Karabacak, V., Altunel, E., Megraoui, M., Akyuz, h.s., 2010. Field evidences from northern Dead Sea Fault zone (South Turkey): new findings for the initiation age and slip rate. Tectonophysics 480, 172–182.

King, R.W., Bock, Y., 2000. Documentation for the MIT GPS Analysis Software: GAMIT. Massachusetts Institute of Technology, Cambridge.

Klinger, Y., Avouac, J.P., Abou Karaki, N., Dorbath, L., Bourles, D., Reyss, J.L., 2000a. Slip rate on the Dead Sea transform fault in northern Araba valley (Jordan). Geophysical Journal International 142, 755–768.

Klinger, Y., Avouac, J.P., Dorbath, L., Karaki, N.A., Tisnerat, N., 2000b. Seismic behaviour of the Dead Sea fault along Araba valley, Jordan. Geophysical Journal International 142, 769–782.

Kozhurin, A., 2007. Active faulting in the Kamchatsky Peninsula, Kamchatka-Aleutian Junction. Geophysical Monograph 172, 107–116.

Le Béon, M., Klinger, Y., Amrat, A.Q., Agnon, A., Dorbath, L., Baer, G., Ruegg, J.C., Charade, O., Mayyas, O., 2008. Slip rate and locking depth from GPS profiles across the southern Dead Sea Transform,. Journal of Geophysical Research 113, 1–19.

Mahmoud, S., Reilinger, R., McClusky, S., Vernant, P., Tealeb, A., 2005. GPS evidence for northward motion of the Sinai Block: implications for E. Mediterranean tectonics. Earth and Planetary Science Letters 238, 217–224.

Masson, F., Anvari, M., Djamour, Y., Walpersdorf, A., Tavakoli, F., Daignieres, M., Nankali, H., Van Gorp, S., 2007. Large scale velocity field and strain tensor in Iran inferred from GPS measurements: new insight for the present day deformation pattern within NE Iran. Geophysical Journal International 170, 436–440.

McKenzie, D.P., Morgan, W.J., 1969. Evolution of Triple Junctions.

Meghraoui, M., Cakir, Z., Masson, F., Mahmoud, Y., Ergintav, S., Alchalbi, A., Inan, S., Daoud, M., Yonlu, O., Altunel, E., 2011. Kinematic modelling at the triple junction between the Anatolian, Arabian, African plates (NW Syria and in SE Turkey). Geophysical Research Abstracts, vol. 13, EGU2011-12599, EGU General Assembly, Vienna 2011.

Meghraoui, M., Gomez, F., Sbeinati, R., Van der Woerd, J., Mounty, M., Darkal, A.N., Radwan, Y., Layyous, I., Al-Najjar, H., Darawcheh, R., Hijazi, F., Al-Ghazzi, R., Barazangi, M., 2003. Evidence for 830 years of seismic quiescence from palaeoseismology, archaeoseismology, and historical seismicity along the Dead Sea Fault in Syria. Earth and Planetary Science Letters 210, 35–52.

Nemer, T., Gomez, F., Al Haddad, S., Tabet, C., 2008. Coseismic growth of sedimentary basins along the Yammouneh strike slip fault (Lebanon). Geophysical Journal International 175, 1023–1039.

Niemi, T.M., Zhang, H., Atallah, M., Harrison, J.B.J., 2001. Late Pleistocene and Holocene slip rate of the northern Wadi Araba fault, Dead Sea transform, Jordan. Journal of Seismology 5, 449–474.

Papazachos, B.C., Papaioannou, C.A., 1999. Lithospheric boundaries and plate motions in the Cyprus area. Tectonophysics 308, 193–204.

Reilinger, R., McClusky, S., Vernant, P., Lawrence, S., Ergintav, S., Cakmak, R., Ozener, H., Kadirov, F., Guliev, I., Stepanyan, R., 2006. GPS constraints on continental deformation in the Africa–Arabia–Eurasia continental collision zone and implications for the dynamics of plate interactions. Journal of Geophysical Research 111.

Salamon, A., Hofstetter, A., Garfunkel, Z., Ron, H., 2003. Seismotectonics of the Sinai subplate – the eastern Mediterranean region. Geophysical Journal International 155, 149–173.

Savage, J.C., Burford, R.O., 1973. Geodetic determination of relative plate motion in central California. Journal of Geophysical Research 78, 832–845.

Sbeinati, M.R., 2010. Historical seismology, paleo-Archeoseismology and seismic hazard along the dead sea fault in Syria. Ph.D. Thesis. Strasbourg University, 332 pp.

Sbeinati, M.R., Darawcheh, R., Mouty, M., 2005. The historical earthquakes of Syria: an analysis of large and moderate earthquakes from 1365 BC to 1900 AD. Annals of Geophysics 48, 3.

Sbeinati, M.R., Meghraoui, M., Suleyman, G., Gomez, F., Grootes, P., Nadeau, M.J., Al Najjar, H., Al-Ghazzi, R., 2010. Timing of earthquake ruptures at theAl Harif Roman aqueduct (Dead Sea fault, Syria) from archaeoseismology and paleoseismology. In: Sintubin, M., Stewart, I.S., Niemi, T.M., Altunel, E. (Eds.), Special Volume Archaeoseismology and Paleoseismology. Ancient Earthquakes: Geological Society of America Special Paper 471., http://dx.doi.org/10.1130/2010.2471(20).

Zilberman, E., Amit, R., Porat, N., Enzel, Y., Avner, U., 2005. Surface ruptures induced by the devastating 1068 AD earthquake in the southern Arava valley, Dead Sea Rift, Israel. Tectonophysics 408, 79–99.
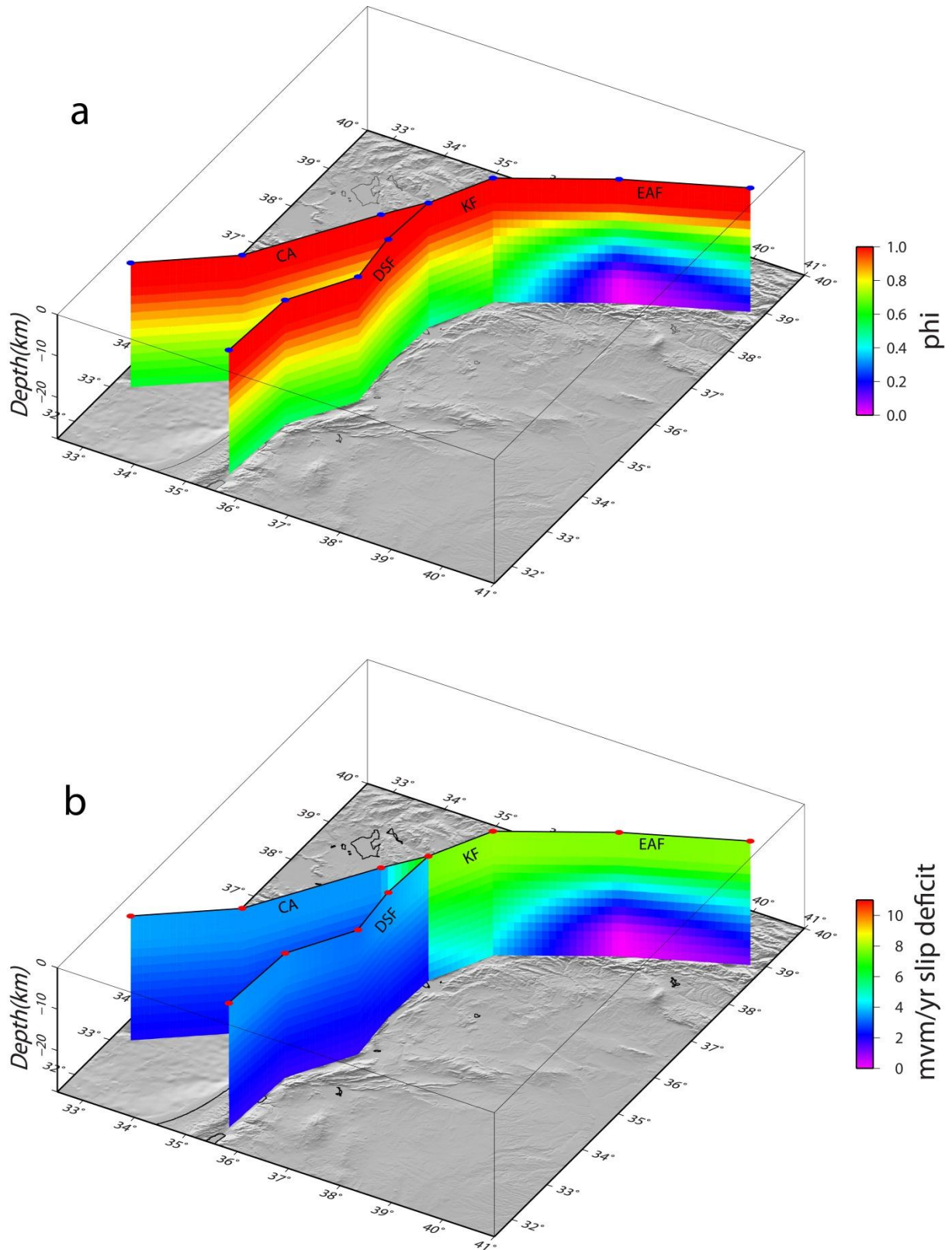
Figure a.1: (a) Scalar of phi (ϕ) parameter from the inversion of model A in Figure IV.5. (b) Scalar of slip rate deficit calculated based on ϕ values and the relative velocity V. Values of ϕ and V were taken from the inversion of model A in figure IV.5.
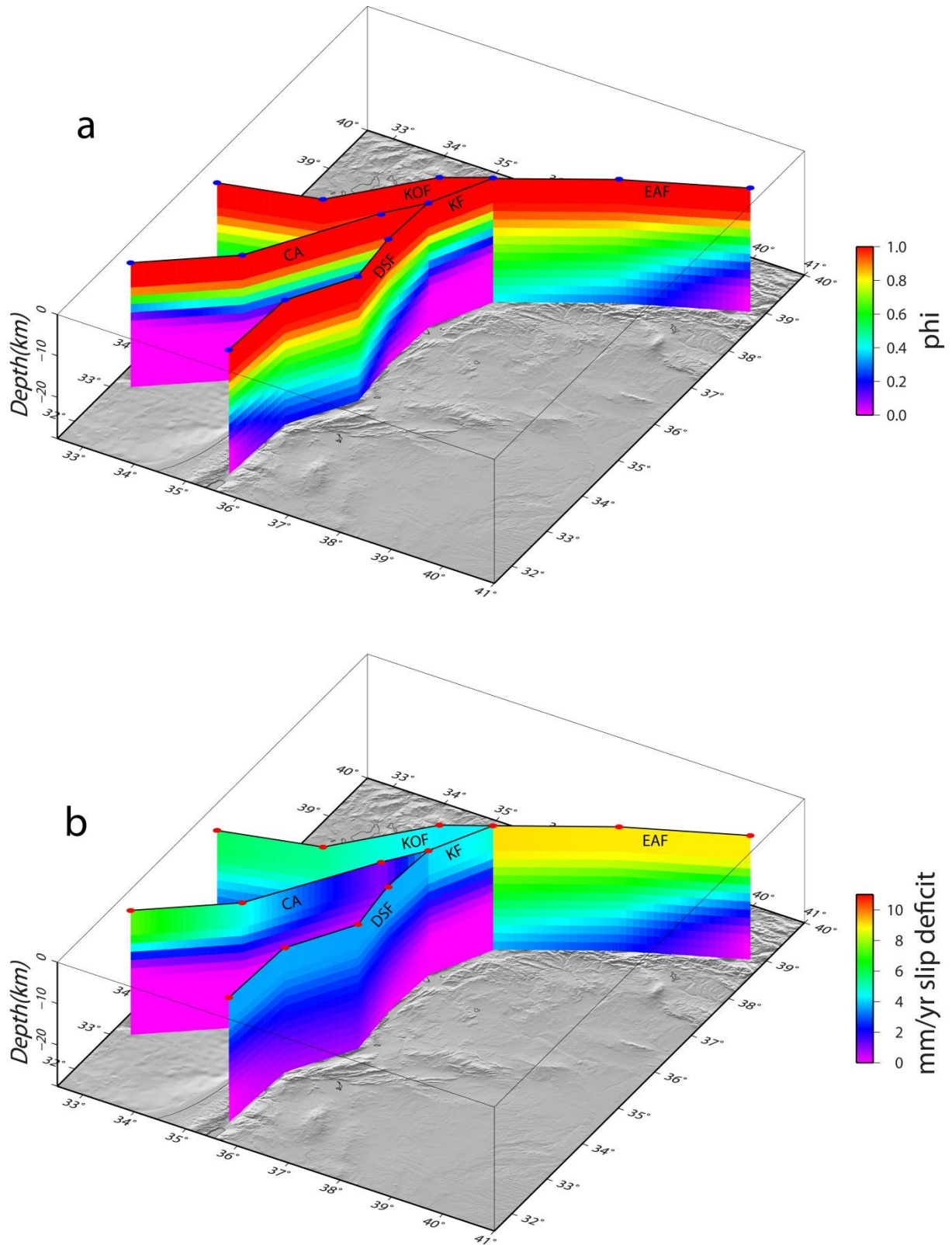
Figure a.2: (a) Scalar of phi (ϕ) parameter from the inversion of model B in Figure IV.5. (b) Scalar of slip rate deficit calculated based on ϕ values and the relative velocity V. Values of ϕ and V were taken from the inversion of model B in figure IV.5.
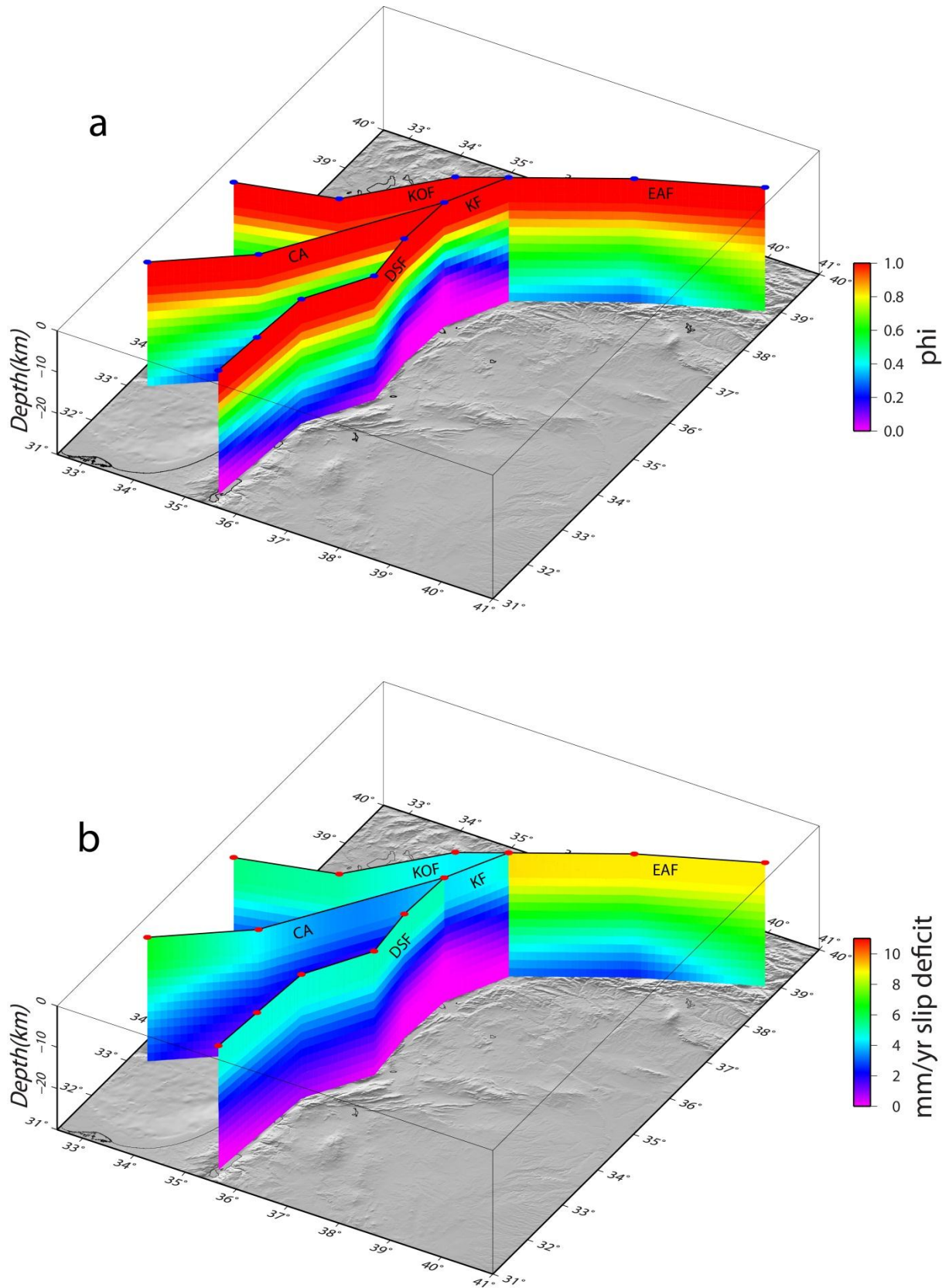
Figure a.3: (a) Scalar of phi (ϕ) parameter from the inversion of model C in Figure IV.5. (b) Scalar of slip rate deficit calculated based on ϕ values and the relative velocity V. Values of ϕ and V were taken from the inversion of model C in figure IV.5.
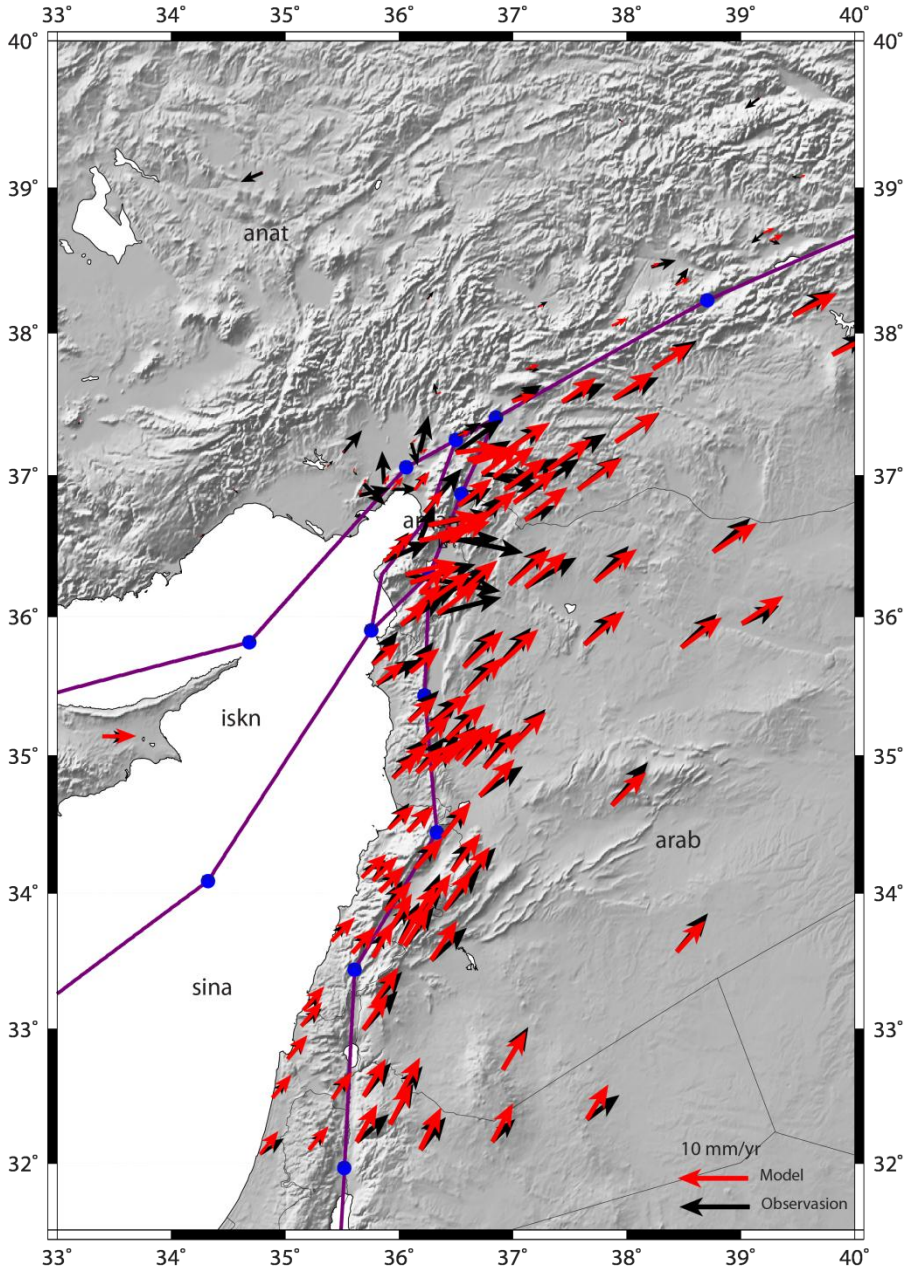
Figure a.4: GPS velocity field of GPS data used in the block model from different solutions with respect to Anatolian reference frame. Black vectors are GPS measurements, red vectors are the model velocities. GPS data is the same as in Figure IV.5.

List of Figures

List of Tables

References

Abou Karaki, N., 1987. Synthese et carte sismotectonique des pays de la bordure orientale de la Méditerranée: sismicité du systeme de failles du Jourdain—Mer Morte, *Université Louis Pasteur de Strasbourg*.

Adiyaman, Ö. & Chorowicz, J., 2002. Late Cenozoic tectonics and volcanism in the northwestern corner of the Arabian plate: a consequence of the strike-slip Dead Sea fault zone and the lateral escape of Anatolia, *Journal of Volcanology and geothermal Research,* 117**,** 327-345.

Aksoy, E., Inceoz, M. & Kocyigit, A., 2007. Lake Hazar basin: A negative flower structure on the east anatolian fault system (EAFS), SE Turkey, *Turkish J. Earth Sci,* 16**,** 319-338.

Akyuz, H.S., Altunel, E., Karabacak, V. & Yalciner, C.C., 2006. Historical earthquake activity of the northern part of the Dead Sea Fault Zone, southern Turkey, *Tectonophysics,* 426**,** 281-293.

Al-Tarazi, E., Rajab, J.A., Gomez, F., Cochran, W., Jaafar, R. & Ferry, M., 2011. GPS measurements of near-field deformation along the southern Dead Sea Fault System, *Geochemistry Geophysics Geosystems,* 12**,** Q12021.

Alchalbi, A., Daoud, M., Gomez, F., McClusky, S., Reilinger, R., Abu Romeyeh, M., Alsouod, A., Yassminh, R., Ballani, B. & Darawcheh, R., 2007. New GPS observations on fault slip rate and locking depth for the northern Dead Sea Fault System in western Syria: Implications for tectonics and earthquake hazards, pp. 03.

Alchalbi, A., Daoud, M., Gomez, F., McClusky, S., Reilinger, R., Romeyeh, M.A., Alsouod, A., Yassminh, R., Ballani, B. & Darawcheh, R., 2010. Crustal deformation in northwestern Arabia from GPS measurements in Syria: Slow slip rate along the northern Dead Sea Fault, *Geophysical Journal International,* 180**,** 125-135.

Allen, C.R., 1969. Faulting in northern Turkey, *Div. Geol. Sciences***,** pp.32.

Altamimi, Z., Collilieux, X., Legrand, J., Garayt, B. & Boucher, C., 2007. ITRF2005: A new release of the International Terrestrial Reference Frame based on time series of station positions and Earth Orientation Parameters, *Journal of Geophysical Research,* 112**,** B09401.

Altamimi, Z., Collilieux, X. & Métivier, L., 2011. ITRF2008: an improved solution of the international terrestrial reference frame, *Journal of Geodesy,* 85**,** 457-473.

Altamimi, Z., Métivier, L. & Collilieux, X., 2012. ITRF2008 plate motion model, *Journal of Geophysical Research,* 117**,** B07402.

Ambraseys, N.N., 2009a. The 12th century seismic paroxysmin the Middle East: a historical perspective, *Annals of Geophysics,* 47.

Ambraseys, N.N., 2009b. *Earthquakes in the Mediterranean and Middle East: a multidisciplinary study of seismicity up to 1900,* edn, Vol., pp. Pages, Cambridge University Press.

Ambraseys, N.N. & Barazangi, M., 1989. The 1759 earthquake in the Bekaa Valley: implications for earthquake hazard assessment in the Eastern Mediterranean region, *Journal of Geophysical Research,* 94**,** 4007-4013.

Ambraseys, N.N. & Jackson, J.A., 1998. Faulting associated with historical and recent earthquakes in the Eastern Mediterranean region, *Geophysical Journal International,* 133**,** 390-406.

Ambraseys, N.N. & Melville, C.P., 1988. An analysis of the eastern Mediterranean earthquake of 20 May 1202, *Historical seismograms and earthquakes of the world***,** 181-200.

Ambraseys, N.N., Melville, C.P. & Adams, R.D., 1994. *The seismicity of Egypt, Arabia, and the Red Sea: a historical review,* edn, Vol., pp. Pages, Cambridge Univ Pr.

Ambraseys, N.N. & White, D., 1997. The seismicity of the eastern Mediterranean region during the first millennium of our era, *J. Earthq. Eng.***,** 603-632.

Amit, R., Zilberman, E., Enzel, Y. & Porat, N., 2002. Paleoseismic evidence for time dependency of seismic response on a fault system in the southern Arava Valley, Dead Sea rift, *Geological Society of America Bulletin,* 114**,** 192.

References

Anderson, J.G., Wesnousky, S.G. & Stirling, M.W., 1996. Earthquake size as a function of fault slip rate, *Bulletin of the Seismological Society of America,* 86**,** 683-690.

Arger, J., Mitchell, J. & Westaway, R.W.C., 2000. Neogene and Quaternary volcanism of southeastern Turkey, *Geological Society, London, Special Publications,* 173**,** 459-487.

Arpat, E. & Saroglu, F., 1972. The East Anatolian fault system: thoughts on its development, *Bull. Miner. Res. Explor. Inst. Turk,* 78**,** 33-39.

ArRajehi, A., McClusky, S., Reilinger, R., Daoud, M., Alchalbi, A., Ergintav, S., Gomez, F., Sholan, J., Bou-Rabee, F. & Ogubazghi, G., 2010. Geodetic constraints on present-day motion of the Arabian Plate: Implications for Red Sea and Gulf of Aden rifting, *Tectonics,* 29**,** TC3011.

Barka, A., Itu, M.F., Ayazaga, I. & Reilinger, R., 1997. Active tectonics of the Eastern Mediterranean region: deduced from GPS, neotectonic and seismicity data.

Barka, A.A. & Kadinsky-Cade, K., 1988. Strike-slip fault geometry in Turkey and its influence on earthquake activity, *Tectonics,* 7**,** 663-684.

Begin, Z.B., Steinberg, D.M., Ichinose, G.A. & Marco, S., 2005. A 40,000 year unchanging seismic regime in the Dead Sea rift, *Geology,* 33**,** 257.

Bertrand, S., 2006. Present-day crustal motions at the triple junction between the Dead Sea Fault, the East Anatolian Fault and the Cyprus Arc (SE Turkey), pp. 10004.

Beydoun, Z.R., 1997. Earthquakes in Lebanon: an overview', *Lebanese Science Bulletin,* 10**,** 109-129.

Bonilla, M.G., Mark, R.K. & Lienkaemper, J.J., 1984. Statistical relations among earthquake magnitude, surface rupture length, and surface fault displacement, *Bulletin of the Seismological Society of America,* 74**,** 2379-2411.

Boucher, C., 2000. Terrestrial coordinate systems and frames, *Encyclopedia of Astronomy and Astrophysics,* 1**,** 1906.

Bozkurt, E., 2001. Neotectonics of Turkey-a synthesis, *Geodinamica Acta,* 14**,** 3-30.

Brew, G., Lupa, J., Barazangi, M., Sawaf, T., Al-Imam, A. & Zaza, T., 2001. Structure and tectonic development of the Ghab basin and the Dead Sea fault system, Syria, *Journal of the Geological Society,* 158**,** 665.

Butler, R.W.H. & Spencer, S., 1999. Landscape evolution and the preservation of tectonic landforms along the northern Yammouneh Fault, Lebanon, *Geological Society, London, Special Publications,* 162**,** 143-156.

Butler, R.W.H., Spencer, S. & Griffiths, H.M., 1998. The structural response to evolving plate kinematics during transpression: evolution of the Lebanese restraining bend of the Dead Sea Transform, *Geological Society, London, Special Publications,* 135**,** 81-106.

Capan, U.Z., Vidal, P. & Cantagrel, J.M., 1987. K-Ar, Nd, Sr and Pb isotopic study of Quaternary volcanism in Karasu Valley (Hatay), N end of Dead Sea rift zone in SE Turkey, *Yerbilimleri,* 14**,** 165-178.

Chaimov, T., Barazangi, M., Al-Saad, D., Sawaf, T. & Gebran, A., 1990. Crustal shortening in the Palmyride fold belt, Syria, and implications for movement along the Dead Sea fault system, *Tectonics,* 9**,** 1369-1386.

Chase, C.G., 1978. Plate kinematics: the Americas, East Africa, and the rest of the world, *Earth and Planetary Science Letters,* 37**,** 355-368.

Chorowicz, J., Luxey, P., Lyberis, N., Carvalho, J., Parrot, J.F., Yururr, T. & Gundogdu, N., 1994. The Maras Triple Junction (Southern Turkey) based on digital elevation model and satellite imagery interpretation, *Journal of Geophysical Research,* 99**,** 20225-20220,20242.

Chu, D. & Gordon, R.G., 2002. Current plate motions across the Red Sea, *Geophysical Journal International,* 135**,** 313-328.

Cochran, J.R., 1983. A model for the development of the Red Sea, *Am. Assoc. Petrol. Geol,* 67**,** 41-69.

Daeron, M., Benedetti, L., Tapponnier, P., Sursock, A. & Finkel, R.C., 2004a. Constraints on the post not, vert, similar 25-ka slip rate of the Yammouneh Fault (Lebanon) using in situ cosmogenic 36 Cl dating of offset limestone-clast fans, *Earth Planet. Sci. Lett,* 227**,** 105-119.

References

Daeron, M., Elias, A., Klinger, Y., Tapponnier, P., Jacques, E. & Sursock, A., 2004. Sources of the AD 551, 1202 and 1759 earthquakes (Lebanon and Syria), pp. 1294.

DeMets, C., Gordon, R.G., Argus, D.F. & Stein, S., 1990. Current plate motions, *Geophysical Journal International,* 101**,** 425-478.

DeMets, C., Gordon, R.G., Argus, D.F. & Stein, S., 1994. Effect of recent revisions to the geomagnetic reversal timescale on estimates of current plate motions, *Geophys. Res. Lett,* 21**,** 2191-2194.

Dewey, J.F., Hempton, M.R., Kidd, W.S.F., Saroglu, F. & Sengor, A.M.C., 1986. Shortening of continental lithosphere: the neotectonics of Eastern Anatolia-a young collision zone, *Geological Society, London, Special Publications,* 19**,** 1-36.

Dewey, J.F. & Sengor, A.M.C., 1979. aegean and surrounding regions: complex multi-plate and continuum tectonics in a convergent zone, *Geological Society of America Bulletin,* 90**,** 84-92.

Dilek, Y., 2006. Collision tectonics of the Mediterranean region: causes and consequences, *SPECIAL PAPERS-GEOLOGICAL SOCIETY OF AMERICA,* 409**,** 1.

Dilek, Y., 2010. Eastern Mediterranean geodynamics, *International Geology Review,* 52**,** 111-116.

Doglioni, C., Agostini, S., Crespi, M., Innocenti, F., Manetti, P., Riguzzi, F. & Savascin, Y., 2002. On the extension in western Anatolia and the Aegean Sea, *Journal of the Virtual Explorer,* 8**,** 169-183.

Dong, D., Herring, T.A. & King, R.W., 1998. Estimating regional deformation from a combination of space and terrestrial geodetic data, *Journal of Geodesy,* 72**,** 200-214.

Erickson, C., 1992. *Investigations of C/A code and carrier measurements and techniques for rapid static GPS surveys,* edn, Vol., pp. Pages, Citeseer.

Eueler, H.J. & Goad, C.C., 1991. On optimal filtering of GPS dual frequency observations without using orbit information, *Journal of Geodesy,* 65**,** 130-143.

Euler, L., 1775. Formulae generales pro translatione quacunque corporum rigidorum, *Novi Acad. Sci. Petrop,* 20**,** 189-207.

Eyidogan, H., Guclu, U., Utku, Z. & Degirmenci, E., 1991. Turkiye Buyuk Depremleri Makro¬Sismik Rehberi (1900-1988), *ITU MF Jeofizik Muhendisligi BOlama Yayinlari.*

Faccenna, C., Jolivet, L., Piromallo, C. & Morelli, A., 2003. Subduction and the depth of convection in the Mediterranean mantle, *J. geophys. Res,* 108**,** 2099.

Feigl, K.L., Agnew, D.C., Bock, Y., Dong, D., Donnellan, A., Hager, B.H., Herring, T.A., Jackson, D.D., Jordan, T.H. & King, R.W., 1993a. Space geodetic measurement of crustal deformation in central and southern California, 1984-1992, *Journal of Geophysical Research,* 982**,** 21677-21712.

Feigl, K.L., Agnew, D.C., Bock, Y., Dong, D.N., Donnellan, A., Hager, B.H., Herring, T.A., Jackson, D.D., King, R.W. & Larsen, S.K., 1993b. Measurement of the velocity field in central and southern California, *J. Geophys. Res,* 98**,** 21,677-621,712.

Ferry, M., Meghraoui, M., Abou Karaki, N., Al-Taj, M. & Amoush, H., 2007a. Episodic behavior of the Dead Sea fault from slip rate variations and integrated seismicity, pp. 1095.

Ferry, M., Meghraoui, M., Abou Karaki, N., Al-Taj, M. & Khalil, L., 2011. Episodic behavior of the Jordan Valley section of the Dead Sea fault inferred from a 14-ka-long integrated catalog of large earthquakes, *Bulletin of the Seismological Society of America,* 101**,** 39.

Ferry, M., Meghraoui, M., Karaki, N.A., Al-Taj, M., Amoush, H., Al-Dhaisat, S. & Barjous, M., 2007b. A 48-kyr-long slip rate history for the Jordan Valley segment of the Dead Sea Fault, *Earth and Planetary Science Letters,* 260**,** 394-406.

Freund, R., 1970. The geometry of faulting in the Galilee, *Israel Journal of Earth Sciences,* 19**,** 117–140.

Freund, R., Zak, I. & Garfunkel, Z., 1968. Age and rate of the sinistral movement along the Dead Sea Rift.

Galli, P., 1999. Active tectonics along the Wadi Araba-Jordan Valley transform fault, *Journal of Geophysical Research,* 104**,** 2777-2796.

171

References

Garfunkel, Z., 1981. Internal structure of the Dead Sea leaky transform (rift) in relation to plate kinematics, *Tectonophysics, 80,* 81-108.

Garfunkel, Z., Zak, I. & Freund, R., 1981. Active faulting in the Dead Sea rift, *Tectonophysics, 80,* 1-26.

Genrich, J.F., Bock, Y., McCaffrey, R., Prawirodirdjo, L., Stevens, C.W., Puntodewo, S.S.O., Subarya, C. & Wdowinski, S., 2000. Distribution of slip at the northern Sumatran fault system, *Journal of Geophysical Research,* 105**,** 28.

Ginat, H., Enzel, Y. & Avni, Y., 1998. Translocated Plio-Pleistocene drainage systems along the Arava fault of the Dead Sea transform, *Tectonophysics, 284,* 151-160.

Goad, C.C. & Yang, M., 1994. On automatic precision airborne GPS positioning, *Proc KIS94. Banff, August***,** 131-138.

Gomez, F., Karam, G., Khawlie, M., McClusky, S., Vernant, P., Reilinger, R., Jaafar, R., Tabet, C., Khair, K. & Barazangi, M., 2007a. Global Positioning System measurements of strain accumulation and slip transfer through the restraining bend along the Dead Sea fault system in Lebanon, *Geophysical Journal International,* 168**,** 1021-1028.

Gomez, F., Khawlie, M., Tabet, C., Khair, K., Darkal, A.N. & Barazangi, M., 2006. Neotectonics of the northern Dead Sea fault system in Lebanon and Syria based on SAR imagery and high resolution DEM data, *Earth and Planetary Science Letters*.

Gomez, F., Meghraoui, M., Darkal, A.N., Hijazi, F., Mouty, M., Suleiman, Y., Sbeinati, R., Darawcheh, R., Al Ghazzi, R. & Barazangi, M., 2003. Holocene faulting and earthquake recurrence along the Serghaya branch of the Dead Sea fault system in Syria and Lebanon, *Geophysical Journal International,* 153**,** 658-674.

Gomez, F., Nemer, T., Tabet, C., Khawlie, M., Meghraoui, M. & Barazangi, M., 2007b. Strain partitioning of active transpression within the Lebanese restraining bend of the Dead Sea Fault (Lebanon and SW Syria), *Geological Society, London, Special Publications, 290,* 285.

Gordon, R.G., 1991. No-net-rotation model of current plate velocities incorporating plate motion model NUVEL-1, *Geophysical research letters, 18,* 2039-2042.

Griffiths, H.M., Clark, R.A., Thorp, K.M. & Spencer, S., 2000. Strain accommodation at the lateral margin of an active transpressive zone: geological and seismological evidence from the Lebanese restraining bend, *Journal of the Geological Society,* 157**,** 289.

Guidoboni, E., Comastri, A., Traina, G., Phillips, B. & Istituto nazionale di, g., 1994. *Catalogue of Ancient Earthquakes in the Mediterranean Area up to the 10th Century,* edn, Vol., pp. Pages, Istituto nazionale di geofisica Rome.

Hamiel, Y., Amit, R., Begin, Z.B., Marco, S., Katz, O., Salamon, A., Zilberman, E. & Porat, N., 2009. The seismicity along the Dead Sea Fault during the last 60,000 years, *Bulletin of the Seismological Society of America,* 99**,** 2020.

Hanks, T.C. & Kanamori, H., 1979. A moment magnitude scale, *J. geophys. Res,* 84**,** 2348-2350.

Hatch, R. & Euler, H.J., 1994. Comparison of several AROF kinematic techniques, pp. 363-370.

Heimann, A., 2001. Stages in the development of the northern Dead Sea Transform., *Fourth International Turkish Geology Symposium, September 2001,,* Abstract, ,Cukurova University, Adana, Turkey**,** 181.

Hempton, M.R., 1985. Structure and deformation history of the Bitlis suture near Lake Hazar, southeastern Turkey, *Bulletin of the Geological Society of America,* 96**,** 233.

Hempton, M.R., 1987. Constraints on Arabian plate motion and extensional history of the Red Sea, *Tectonics,* 6**,** 687-705.

Hempton, M.R., Dunne, L.A. & Dewey, J.F., 1983. Sedimentation in an active strike-slip basin, southeastern Turkey, *The Journal of Geology***,** 401-412.

Herece, E. & Akay, E., 1992. East Anatolian Fault between Karliova and Celikhan, *Proc. gh Petroleum Congress, Chamber of Pet. Eng. And Turk. Assoc. of Pet. Geol.***,** 361-372.

Hofmann-Wellenhof, B., Legat, K. & Wieser, M., 2003. *Navigation: principles of positioning and guidance,* edn, Vol., pp. Pages, Springer Verlag.

References

Hofmann-Wellenhof, B., Lichtenegger, H. & Collins, J., 1993. Global positioning System. Theory and Practice, *Global Positioning System. Theory and practice., by Hofmann-Wellenhof, B.; Lichtenegger, H.; Collins, J.. Springer, Wien (Austria), 1993, 347 p., ISBN 3-211-82477-4, Price DM 79.00. ISBN 0-387-82477-4 (USA).* 1.

Hofmann-Wellenhof, B., Lichtenegger, H. & Wasle, E., 2008. *GNSS--global navigation satellite systems: GPS, GLONASS, Galileo, and more,* edn, Vol., pp. Pages, Springer Verlag Wien.

Hofmann-Wellenhof, B. & Remondi, B., 1988. The antenna exchange: One aspect of high-precision GPS kinematic survey, *GPS-Techniques Applied to Geodesy and Surveying*, 259-277.

Jackson, J. & McKenzie, D., 1984. Active tectonics of the Alpine Himalayan Belt between western Turkey and Pakistan, *Geophysical Journal of the Royal Astronomical Society,* 77, 185-264.

Jackson, J. & McKenzie, D., 1988. The relationship between plate motions and seismic moment tensors, and the rates of active deformation in the Mediterranean and Middle East, *Geophysical Journal,* 93, 45-73.

Jestin, F., Huchon, P. & Gaulier, J.M., 2007. The Somalia plate and the East African rift system: Present-day kinematics, *Geophysical Journal International,* 116, 637-654.

Joffe, S. & Garfunkel, Z., 1987. Plate kinematics of the circum Red Sea, a re-evaluation, *Tectonophysics,* 141, 5-22.

Jolivet, L. & Brun, J.P., 2010. Cenozoic geodynamic evolution of the Aegean, *International Journal of Earth Sciences,* 99, 109-138.

Jolivet, L. & Faccenna, C., 2000. Mediterranean extension and the Africa-Eurasia collision, *Tectonics,* 19, 1095-1106.

Joosten, P. & Tiberius, C., 2000. Fixing the Ambiguity: Are you sure they're right?, *GPS World,* 11 (5), 46-51.

Kalafat, D., Oz, G., Kara, M., Oguto, Z., Kil/c, K., Pinar, A. & Yilmazer, M., 2000. 1981-1997 Turkiye ve Dolaylari Deprem Katalogu (M>4.0), *Bebek, Istanbul (in Turkish).*

Kanamori, H. & Allen, C.R., 1986. Earthquake repeat time and average stress drop, *Earthquake Source Mechanics,* 37, 227-236.

Kanamori, H. & Anderson, D.L., 1975. Theoretical basis of some empirical relations in seismology, *Bulletin of the Seismological Society of America,* 65, 1073-1095.

Kaplan, E.D. & Hegarty, C.J., 2006. *Understanding GPS: principles and applications,* edn, Vol., pp. Pages, Artech House Publishers.

Karabacak, V., Altunel, E., Megraoui, M. & Akyuz, h.s., 2010. Field evidences from northern Dead Sea Fault zone (South Turkey): New findings for the initiation age and slip rate, *Tectonophysics,* 480, 172–182.

Khair, K., Karakaisis, G.F. & Papadimitriou, E.E., 2000. Seismic zonation of the Dead Sea transform fault area, *Annals of Geophysics,* 43.

Khair, K., Tsokas, G.N. & Sawaf, T., 1997. Crustal structure of the northern Levant region: multiple source Werner deconvolution estimates for Bouguer gravity anomalies, *Geophysical Journal International,* 128, 605-616.

Kiratzi, A.A., 1993. A study on the active crustal deformation of the North and East Anatolian Fault Zones, *Tectonophysics,* 225, 191-203.

Klinger, Y., Avouac, J.P., Dorbath, L., Karaki, N.A. & Tisnerat, N., 2000b. Seismic behaviour of the Dead Sea fault along Araba valley, Jordan, *Geophysical Journal International,* 142, 769-782.

Klinger, Y., Rivera, L., Haessler, H. & Maurin, J.C., 1999. Active faulting in the Gulf of Aqaba: New knowledge from the MW 7.3 earthquake of 22 November 1995, *Bulletin of the Seismological Society of America,* 89, 1025.

Kovalevsky, J., Mueller, I.I. & Kolaczek, B., 1989. Reference frames in astronomy and geophysics.

Langbein, J. & Johnson, H., 1997. Correlated errors in geodetic time series: Implications for time-dependent deformation, *Journal of Geophysical Research,* 102, 591-603.

Langley, R.B., 1993. The GPS observables, *GPS World,* 4, 52-59.

References

Lay, T. & Schwartz, S.Y., 2004. Comment on Coupling semantics and science in earthquake research, *Eos, Transactions American Geophysical Union,* 85**,** 339.

Le Béon, M., Klinger, Y., Amrat, A.Q., Agnon, A., Dorbath, L., Baer, G., Ruegg, J.C., Charade, O. & Mayyas, O., 2008. Slip rate and locking depth from GPS profiles across the southern Dead Sea Transform, *J. Geophys. Res,* 113**,** 1–19.

Le Pichon, X., 1968. Sea-floor spreading and continental drift, *Journal of Geophysical Research,* 73**,** 3661-3697.

Le Pichon, X., Chamot-Rooke, N., Lallemant, S., Noomen, R. & Veis, G., 1995. Geodetic determination of the kinematics of central Greece with respect to Europe: Implications for eastern Mediterranean tectonics, *Journal of Geophysical Research,* 100**,** 12675-12612,12690.

Le Pichon, X. & Gaulier, J.M., 1988. The rotation of Arabia and the Levant fault system, *Tectonophysics,* 153**,** 271-294.

Lyberis, N., 1988. Tectonic evolution of the Gulf of Suez and the Gulf of Aqaba, *Tectonophysics,* 153**,** 209-220.

Lyberis, N., Yurur, T., Chorowicz, J., Kasapoglu, E. & Gundogdu, N., 1992. The East Anatolian Fault: an oblique collisional belt, *Tectonophysics,* 204**,** 1-15.

Mahmoud, S., Reilinger, R., McClusky, S., Vernant, P. & Tealeb, A., 2005. GPS evidence for northward motion of the Sinai Block: implications for E. Mediterranean tectonics, *Earth and Planetary Science Letters,* 238**,** 217-224.

Mao, A., Harrison, C.G.A. & Dixon, T.H., 1999. Noise in GPS coordinate time series, *Journal of Geophysical Research,* 104**,** 2797-2816.

Marco, S., Agnon, A., Ellenblum, R., Eidelman, A., Basson, U. & Boas, A., 1997. 817-Year-old walls offset sinistrally 2.1 m by the Dead Sea transform, *Journal of Geodynamics,* 24**,** 11-20.

Marco, S., Hartal, M., Hazan, N., Lev, L. & Stein, M., 2003. Archaeology, history, and geology of the AD 749 earthquake, Dead Sea transform, *Geology,* 31**,** 665.

Marco, S., Stein, M., Agnon, A. & Ron, H., 1996. Long-term earthquake clustering: A 50,000-year paleoseismic record in the Dead Sea Graben, *J. geophys. Res,* 101**,** 6179-6191.

Masson, F., Hamiel, Y., Al-Qaryouti, M., Deprez, A., Klinger, Y. & Agnon, A., 2012. Slip rate and locking depth of the southern Dead Sea fault revisited from new GPS measurements, *Wegener 2012,* Volume of Abstracts**,** P 69.

McCaffrey, R., 1995. DEFNODE users' guide, *Rensselaer Polytechnic Institute, Troy,* 2004.

McCaffrey, R., 2002. Crustal block rotations and plate coupling, *Plate Boundary Zones, Geodyn. Ser,* 30**,** 101-122.

McCaffrey, R., 2005. Block kinematics of the Pacific-North America plate boundary in the southwestern United States from inversion of GPS, seismological, and geologic data, *J. geophys. Res,* 110.

McCaffrey, R., Long, M.D., Goldfinger, C., Zwick, P.C., Nabelek, J.L., Johnson, C.K. & Smith, C., 2000. Rotation and plate locking at the southern Cascadia subduction zone, *Geophys. Res. Lett,* 27**,** 3117-3120.

McClusky, S., Balassanian, S., Barka, A., Demir, C., Ergintav, S., Georgiev, I., Gurkan, O., Hamburger, M., Hurst, K. & Kahle, H., 2000. Global Positioning System constraints on plate kinematics and dynamics in the eastern Mediterranean and Caucasus, *Journal of Geophysical Research,* 105**,** 5695-5719.

McClusky, S., Reilinger, R., Mahmoud, S., Ben Sari, D. & Tealeb, A., 2003. GPS constraints on Africa (Nubia) and Arabia plate motions, *Geophysical Journal International,* 155**,** 126-138.

McKenzie, D., 1972. Active tectonics of the Mediterranean region, *Geophysical Journal of the Royal Astronomical Society,* 30**,** 109-185.

McKenzie, D., 1976. The East Anatolian Fault: a major structure in eastern Turkey, *Earth and Planetary Science Letters,* 29**,** 189-193.

McKenzie, D.P. & Davies, D., 1970. Plate tectonics of the Red Sea and east Africa, *Nature,* 226**,** 243-248.

References

Meghraoui, M., Cakir, Z., Masson, F., Mahmoud, Y., Ergintav, S., Alchalbi, A., Inan, S., Daoud, M., Yonlu, O. & Altunel, E., 2011. Kinematic modelling at the triple junction between the Anatolian, Arabian, African plates (NW Syria and in SE Turkey), *Geophysical Research Abstracts, Vol. 13, EGU2011-12599, EGU General Assembly, Vienna 2011.*

Meghraoui, M., Gomez, F., Sbeinati, R., Van der Woerd, J., Mounty, M., Darkal, A.N., Radwan, Y., Layyous, I., Al-Najjar, H., Darawcheh, R., Hijazi, F., Al-Ghazzi, R. & Barazangi, M., 2003. Evidence for 830 years of seismic quiescence from palaeoseismology, archaeoseismology, and historical seismicity along the Dead Sea Fault in Syria, *Earth & Planetary Science Letters,* 210**,** 35-52.

Migowski, C., Agnon, A., Bookman, R., Negendank, J.F.W. & Stein, M., 2004. Recurrence pattern of Holocene earthquakes along the Dead Sea transform revealed by varve-counting and radiocarbon dating of lacustrine sediments, *Earth and Planetary Science Letters,* 222**,** 301-314.

Morgan, W.J., 1968. *Rises, trenches, great faults, and crustal blocks,* edn, Vol., pp. Pages, Woods Hole Oceanographic Institution.

Muehlberger, W.R. & Gordon, M.B., 1987. Observations on the complexity of the East Anatolian Fault, Turkey, *Journal of Structural Geology,* 9**,** 899-903.

Nalbant, S.S., McCloskey, J., Steacy, S. & Barka, A.A., 2002. Stress accumulation and increased seismic risk in eastern Turkey, *Earth and Planetary Science Letters,* 195**,** 291-298.

Nemer, T. & Meghraoui, M., 2006. Evidence of coseismic ruptures along the Roum fault (Lebanon): a possible source for the AD 1837 earthquake, *Journal of Structural Geology,* 28**,** 1483-1495.

Niemi, T.M., Zhang, H., Atallah, M. & Harrison, J.B.J., 2001. Late Pleistocene and Holocene slip rate of the northern Wadi Araba fault, Dead Sea transform, Jordan, *Journal of seismology,* 5**,** 449-474.

Okada, Y., 1985. Surface deformation due to shear and tensile faults in a half-space, *Bulletin of the Seismological Society of America,* 75**,** 1135-1154.

Okada, Y., 1992. Internal deformation due to shear and tensile faults in a half-space, *Bulletin of the Seismological Society of America,* 82**,** 1018-1040.

Over, S., Kavak, K., Bellier, O. & Ozden, S., 2004. Is the Amik Basin (SE Turkey) a triple-junction area? Analyses of SPOT XS imagery and seismicity, *International Journal of Remote Sensing,* 25**,** 3857-3872.

Papazachos, B.C., Scordilis, E.M., Panagiotopoulos, D.G., Papazachos, C.B. & Karakaisis, G.F., 2004. Global relations between seismic fault parameters and moment magnitude of earthquakes, *Bull. Geol. Soc. Greece,* 36**,** 1482-1489.

Pe'eri, S., Wdowinski, S., Shtibelman, A., Bechor, N., Bock, Y., Nikolaidis, R. & van Domselaar, M., 2002. Current plate motion across the Dead Sea Fault from three years of continuous GPS monitoring, *Geophysical research letters,* 29**,** 42-41.

Perincek, D. & Semen, I., 1990. The structural relationship between the East Anatolian and Dead Sea fault zones in southeastern Turkey, *Tectonophysics,* 172**,** 331-340.

Piromallo, C. & Morelli, A., 2003. P wave tomography of the mantle under the Alpine-Mediterranean area, *J. geophys. Res,* 108.

Prasad, R. & Ruggieri, M., 2005. *Applied satellite navigation-using GPS, GALILEO and augmentation systems,* edn, Vol., pp. Pages.

Press, W.H., Flannery, B.P., Teukolsky, S.A. & Vetterling, W.T., 1986. *Numerical recipes,* edn, Vol. 547, pp. Pages, Cambridge Univ Press.

Quennell, A., 1958. The structural and geomorphic evolution of the Dead Sea rift, *Quarterly Journal of the Geological Society,* 114**,** 1.

Reilinger, R. & McClusky, S., 2011. Nubia-Arabia-Eurasia plate motions and the dynamics of Mediterranean and Middle East tectonics, *Geophysical Journal International.*

Reilinger, R., McClusky, S., Vernant, P., Lawrence, S., Ergintav, S., Cakmak, R., Ozener, H., Kadirov, F., Guliev, I. & Stepanyan, R., 2006. GPS constraints on continental deformation in the Africa-

Arabia-Eurasia continental collision zone and implications for the dynamics of plate interactions, *J. Geophys. Res,* 111.

Reilinger, R.E., McClusky, S.C., Oral, M.B., King, R.W., Toksoz, M.N., Barka, A.A., Kinik, I., Lenk, O. & Sanli, I., 1997b. Global Positioning System measurements of present-day crustal movements in the Arabia-Africa-Eurasia plate collision zone, *Journal of Geophysical Research,* 102**,** 9983-9999.

Salamon, A., Hofstetter, A., Garfunkel, Z. & Ron, H., 2003. Seismotectonics of the Sinai subplate-The eastern Mediterranean region, *Geophysical Journal International,* 155**,** 149-173.

Saroglu, F., Emre, Ö. & Kusçu, I., 1992. The East Anatolian fault zone of Turkey, *Annales Tectonicae,* 6**,** 99-125.

Saroglu, F. & Yilmaz, Y., 1990. Tectonics of the Karliova triple junction, *Bulletin of the Technical University of Istanbul,* 44**,** 475-493.

Savage, J.C., 1983. A dislocation model of strain accumulation and release at a subduction zone, *J. geophys. Res,* 88**,** 4984-4996.

Savage, J.C. & Burford, R.O., 1973. Geodetic determination of relative plate motion in central California, *Journal of Geophysical Research,* 78**,** 832-845.

Sbeinati, M.R., 2010. Historical seismology, paleo-Archeoseismology and seismic hazard along the dead sea fault in Syria, *PhD Thesis, Strasbourg University*.

Sbeinati, M.R., Darawcheh, R. & Mouty, M., 2005. The historical earthquakes of Syria: an analysis of large and moderate earthquakes from 1365 BC to 1900 AD, *Annals of Geophysics,* 48**,** 3.

Sbeinati, M.R., Meghraoui, M., Suleyman, G., Gomez, F., Grootes, P., Nadeau, M.J. & Al Najjar, H., 2010. Timing of earthquake ruptures at theAl Harif Roman aqueduct (Dead Sea fault, Syria) from archaeoseismology and paleoseismology, *Ancient Earthquakes***,** 243.

Scholz, C.H., 2002. *The mechanics of earthquakes and faulting,* edn, Vol., pp. Pages, Cambridge Univ Pr.

Scholz, C.H., Aviles, C.A. & Wesnousky, S.G., 1986. Scaling differences between large interplate and intraplate earthquakes, *Bulletin of the Seismological Society of America,* 76**,** 65-70.

Sengor, A.M. & Yilmaz, Y., 1981. Tethyan evolution of Turkey: a plate tectonic approach, *Tectonophysics,* 75**,** 181-190, 193-199, 203-241.

Sengor, A.M.C., 1979. The North Anatolian transform fault: its age, offset and tectonic significance, *Journal of the Geological Society,* 136**,** 269.

Sengor, A.M.C., Gorur, N. & Saroglu, F., 1985. Strike-slip faulting and related basin formation in zones of tectonic escape: Turkey as a case study, *Strike-slip faulting and Basin formation,* 37**,** 227-264.

Seymen, I. & Aydin, A., 1972. Bingol deprem fayi ve bunun Kuzey Anadolu Fayi ile ili~kisi, MTA Bull.**,** 79.

Spakman, W., Wortel, M.J.R. & Vlaar, N.J., 1988. The Hellenic subduction zone: a tomographic image and its geodynamic implications, *Geophysical research letters,* 15**,** 60-63.

Steckler, M.S., Feinstein, S., Kohn, B.P., Lavier, L.L. & Eyal, M., 1998. Pattern of mantle thinning from subsidence and heat flow measurements in the Gulf of Suez: Evidence for the rotation of Sinai and along-strike flow from the Red Sea, *Tectonics,* 17**,** 903-920.

Stein, S., 1993. Space geodesy and plate motions, *Contributions of Space Geodesy to Geodynamics: Crustal Dynamics, Geodyn. Ser,* 23**,** 5-20.

Straub, C. & Kahle, H.G., 1994. Global Positioning System (GPS) estimates of crustal deformation in the Marmara Sea region, Northwestern Anatolia, *Earth and Planetary Science Letters,* 121**,** 495-502.

Straub, C. & Kahle, H.G., 1995. Active crustal deformation in the Marmara Sea region, NW Anatolia, inferred from GPS measurements, *Geophysical research letters,* 22**,** 2533-2536.

Tatar, O., Piper, J.D.A., Gursoy, H., Heimann, A. & Koçbulut, F., 2004. Neotectonic deformation in the transition zone between the Dead Sea Transform and the East Anatolian Fault Zone,

Southern Turkey: a palaeomagnetic study of the Karasu Rift Volcanism, *Tectonophysics,* 385**,** 17-43.

Taymaz, T., Eyidogan, H. & Jackson, J., 1991a. Source parameters of large earthquakes in the East Anatolian Fault Zone (Turkey), *Geophysical Journal International,* 106**,** 537-550.

Taymaz, T., Jackson, J. & McKenzie, D., 1991b. Active tectonics of the north and central Aegean Sea, *Geophysical Journal International,* 106**,** 433-490.

Teunissen, P.J.G., 1998. GPS carrier phase ambiguity fixing concepts, *TEUNISSEN, PJG; KLEUSBERG, A. GPS for Geodesy,* 2**,** 319-388.

Teunissen, P.J.G., Jonge, P.J. & Tiberius, C., 1995. A NEW WAY TO FIX CARRIER-PHASE AMBIGUITIES, *GPS World*.

Tocher, D., 1958. Earthquake energy and ground breakage, *Bulletin of the Seismological Society of America,* 48**,** 147-153.

Utsu, T. & Seki, A., 1954. A relation between the area of aftershock region and the energy of main shock, *J. Seism. Soc. Japan,* 7**,** 233-240.

van Hinsbergen, D.J.J., Hafkenscheid, E., Spakman, W., Meulenkamp, J.E. & Wortel, R., 2005. Nappe stacking resulting from subduction of oceanic and continental lithosphere below Greece, *Geology,* 33**,** 325.

Vernant, P., Nilforoushan, F., Hatzfeld, D., Abbassi, M.R., Vigny, C., Masson, F., Nankali, H., Martinod, J., Ashtiani, A. & Bayer, R., 2004. Present-day crustal deformation and plate kinematics in the Middle East constrained by GPS measurements in Iran and northern Oman, *Geophysical Journal International,* 157**,** 381-398.

Walters, R.J., Holley, R.J., Parsons, B. & Wright, T.J., 2011. Interseismic strain accumulation across the North Anatolian Fault from Envisat InSAR measurements, *Geophysical research letters,* 38**,** L05303.

Wang, J.H. & Ou, S.S., 1998. On scaling of earthquake faults, *Bulletin of the Seismological Society of America,* 88**,** 758-766.

Wdowinski, S., Bock, Y., Baer, G., Prawirodirdjo, L., Bechor, N., Naaman, S., Knafo, R., Forrai, Y. & Melzer, Y., 2004. GPS measurements of current crustal movements along the Dead Sea Fault, *J. geophys. Res,* 109.

Wells, D.L. & Coppersmith, K.J., 1994. New empirical relationships among magnitude, rupture length, rupture width, rupture area, and surface displacement, *Bulletin of the Seismological Society of America,* 84**,** 974-1002.

Wesnousky, S.G., 1986. Earthquakes, Quaternary faults, and seismic hazard in California, *J. geophys. Res,* 91**,** 12587-12631.

Westaway, R., 1994. Present-day kinematics of the Middle East and eastern Mediterranean, *Journal of Geophysical Research,* 99**,** 12071-12012,12090.

Westaway, R., 1995. Deformation around stepovers in strike-slip fault zones, *Journal of Structural Geology,* 17**,** 831-846.

Westaway, R., 2003. Kinematics of the Middle East and eastern Mediterranean updated, *Turkish Journal of Earth Sciences (Turkish J. Earth Sci.),* 12**,** 5-46.

Westaway, R., 2004. Kinematic consistency between the Dead Sea Fault Zone and the Neogene and Quaternary left-lateral faulting in SE Turkey, *Tectonophysics,* 391**,** 203-237.

Westaway, R.O.B. & Arger, J.A.N., 1996. The Golbasi basin, southeastern Turkey: a complex discontinuity in a major strike-slip fault zone, *Journal of the Geological Society,* 153**,** 729.

Wilson, J.T., 1965. A new class of faults and their bearing on continental drift, *Nature,* 207**,** 343-347.

Yurtmen, S., Guillou, H., Westaway, R., Rowbotham, G. & Tatar, O., 2002. Rate of strike-slip motion on the Amanos Fault (Karasu Valley, southern Turkey) constrained by K-Ar dating and geochemical analysis of Quaternary basalts, *Tectonophysics,* 344**,** 207-246.

Yurtmen, S., Rowbotham, G., bler, F. & Floyd, P.A., 2000. Petrogenesis of basalts from southern Turkey: the Plio-Quaternary volcanism to the north of Iskenderun, in: Bozkurt E., Winchester

J.A., Piper J.D.A. (Eds.), Tectonics and magmatism in Turkey and the surrounding area, *Geological Society, London*, 489-512.

Yurur, M.T. & Chorowicz, J., 1998. Recent volcanism, tectonics and plate kinematics near the junction of the African, Arabian and Anatolian plates in the eastern Mediterranean, *Journal of Volcanology and geothermal Research,* 85, 1-15.

Zange, H., 1998. Late Pleistocene and Holocene slip rate of the Northern Wadi Araba Fault, Dead Sea Transform, Jordan, *Master Thesis, University of Issouri - Kansas City, PP.128*.

Zhang, J., Bock, Y., Johnson, H., Fang, P., Williams, S., Genrich, J., Wdowinski, S. & Behr, J., 1997. Southern California Permanent GPS Geodetic Array: Error analysis of daily position estimates and site velocities, *JOURNAL OF GEOPHYSICAL RESEARCH-ALL SERIES-,* 102, 18-18.

Zilberman, E., Amit, R., Porat, N., Enzel, Y. & Avner, U., 2005. Surface ruptures induced by the devastating 1068 AD earthquake in the southern Arava valley, Dead Sea Rift, *Tectonophysics,* 408, 79-99.